ISSN 0974 - 8725

CSVTU Research Journal

(Bi-Annual Publication)

Vol. 4, No. 1 2011

CONTENTS

CHHATTISGARH SWAMI VIVEKANAND TECHNICAL UNIVERSITY, BHILAI

Chhattisgarh Swami Vivekanand Technical University
Research Journal

Published By:
Dr. Ashok Kumar Dubey, Registrar
Chhattisgarh Swami Vivekanand Technical University, Bhilai

FOREWORD

The state of Chhattisgarh has made considerable progress in the field of engineering and technical education during the last decade. Technical education is the backbone for economic progress and development of any state as well as the nation. Hence it is essential to see that the quality in technical education is induced and sustained. We are exposed to globalization in technical education. Now, foreign universities are at liberty to open their branches of educational institutes in our country. This coupled with privatization of technical education has created a tough competitive situation. Under this scenario, a Technical Institution can survive only through the quality in education.

Quality of technical education is a measure of development of any state as it plays a vital role to produce good engineers for the state. Engineering education has been expanding very rapidly in recent years in the state of Chhattisgarh. Approximately 89 professional institutions consisting of government, self financing institutions and private colleges are in existence. Nearly 21,620 students are being admitted every year in the disciplines of engineering, pharmacy, management, architecture etc. It is not sufficient for the engineering institutions just to have the infrastructural facilities but it is essential to have strong, trained, quality dedicated faculty members to produce the engineers of expected quality. However, there is a dearth of large number of well qualified teachers.

The enrollment of students recorded an increase of 162.5% over a period of 5 years. Similarly total affiliated institutions showed a growth of 157% i.e. 35 institutions in the year 2005-06 increased to 89 institutions in the year 2010-11. For imparting quality education, curriculum development & upgradation, teachers' training programmes, academic inspection of colleges etc. are taken up regularly. Research is an important component in the academics. A faculty or a senior student can develop innovative ideas only through research activities. Research also helps the faculty members to update their knowledge in the fast changing world of knowledge. During the last one and half years, nine faculty members completed their Ph.D. degree from this university and quite a few of them are about to complete.

To encourage the faculty members to take up research and provide an avenue to publish their research findings, the University has been publishing CSVTU Research Journal for the last three years. Research papers contributed by the faculties from various disciplines such as applied sciences, computer science & engineering, mechanical engineering, civil engineering, electrical engineering, electronics and telecommunication engineering, management etc. are embodied in the journal.

We are making an endeavour to reach wide cross section of the academia engaged in research activities, especially, in the fields of engineering and technology and get their comments about the research papers published in this journal. I wish that the readers will send their comments to the editor of the journal which may be helpful to improve the quality of the journal in future.

Finally, I congratulate all the researchers who made efforts for publication of their papers in this journal and whose papers were accepted for publication.

Prof. B. C. Mal
Vice-chancellor

Development of A Spreadsheet Model For Evaluation of Nitrogen Dynamics In Intensive Shrimp Culture Pond

Sanjib Moulick
Agricultural and Food Engineering Department,
Indian Institute of Technology
Kharagapur, India

Neenu Peter
Agricultural and Food Engineering Department,
Indian Institute of Technology
Kharagapur, India

B C Mal
Chhattisgarh Swami Vivekanand Technical University,
Bhilai, India

Abstract

Fishery sector worldwide caters to the major portion of protein requirement in the human diet. The declining natural reserves of fish species have led to the faster growth of aquaculture sector which is capable of mitigating nutritional deficiencies and food insecurity to a possible extend. Shrimp culture has expanded as a large scale business and technological advances have led to intensive culture. The fish feed, being highly proteinaceous in nature, becomes the primary source of nitrogen (N) accumulation in the pond. The left over portion of the N input which is not incorporated into shrimp tissues, is either taken up by phytoplankton or goes as uneaten feed which ultimately, settles on the sediment as particulate organic N. As a result, anoxic sludge gathers in the pond bottom and a part of it remineralizes to enter the water column as harmful total ammoniacal nitrogen (TAN) and may have a devastating impact on the shrimp or on the adjacent aquatic environment when water is discharged from ponds. To predict the concentrations of the nitrogenous compounds and chlorophyll a (CHL) in shrimp ponds, a user-friendly spreadsheet model is developed by which effective management strategies like sludge removal or water exchange can be adopted as and when needed. The model was calibrated and successfully validated for an intensive shrimp (*Penaeus monodon*) culture pond.

Keywords- Nitrogen dynamics; Spreadsheet modelling; Shrimp culture

Broad Area- Environmental Engineering

1. Introduction

Decision makers at regional, national and global levels have been monitoring the causes for food insecurity and trying out possible solutions to handle this vulnerable situation. Aquaculture, the farming of aquatic organisms, including fish, molluscs, crustaceans and aquatic plants, is often cited as one of the means of efficiently increasing food production. Large scale commercial aquaculture, practised in many developing countries, can enhance the production for domestic and export markets bringing much needed foreign exchange, revenue and employment, thereby contributing to food security (Ridler and Hishamunda, 2001). India is experiencing a boom in shrimp culture because of economic liberalization, high profitability and a good international market. With government support, shrimp culture has now emerged as a global industry and technological advances have led to intensive culture. Highly proteinaceous feeds are generally provided for the aquatic animals, which finally become source for nitrogen (N) in the pond (Lorenzen et al., 1997).

N plays a major role in the dynamics of intensive aquaculture systems. Much of the N input not incorporated into shrimp tissue enters the water column as total ammonia nitrogen (TAN) and is taken up by phytoplankton and settles on the sediment as particulate organic N. This creates a pile of anoxic sludge with a high organic loading. Alternatively, N input is deposited directly as uneaten feed or faeces. A part of the sludge N is remineralized to enter the water column again as TAN (Burford and Lorenzen, 2004). The nitrogenous compounds in high concentrations can become a threat to the shrimp under culture or pose danger to aquatic life if these untreated compounds reach natural water bodies while being discharged from the culture pond. In order to take care of the water quality parameters from exceeding their permissible limits, a user-friendly spreadsheet model is developed to predict the concentrations of TAN, nitrite/nitrate (NOX) and chlorophyll a (CHL) and the sediment nitrogen pool.

2. Materials and methods

2.1 Model Formulation

A mathematical model to investigate the nitrogen dynamics in intensive shrimp culture pond was formulated by Burford and Lorenzen (2004). In the present study, a user friendly spreadsheet was developed to solve the model expressions. The conceptual model of N input, transformation and removal in intensive shrimp ponds is shown in Figure 1. In this model, the source for N input is assumed to be solely from formulated feed. The process of denitrification was ignored as many studies showed it to be negligible. Dissolved organic N (DON) is produced in significant quantities in shrimp ponds as a result of the addition of shrimp feed. However, much of it is not readily utilized by the natural biota, and therefore is shown as an isolated pool in the model.

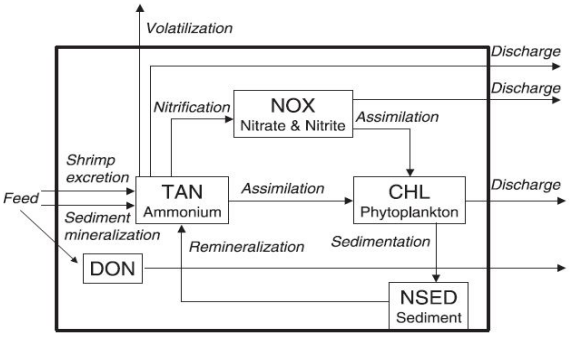

Figure 1. Conceptual model of N input, transformation and removal in intensive shrimp ponds (source: Burford and Lorenzen,2004)

2.2 Mathematical model

The model has five state variables representing the main N components: TAN, NOX, DON, NSED and particulate N in the form of phytoplankton, expressed as units of CHL. The N dynamics model is given by the following set of coupled differential equations for the five state variables:

$$\frac{dC_{TAN}}{dt} = q.A_t + r.M_{NSED} - (n+v+f).C_{TAN} - g.c.C_{CHL}.\left\{\frac{C_{TAN}}{C_{TAN}+C_{NOX}}\right\} \quad \ldots (1)$$

$$\frac{dC_{NOX}}{dt} = n.C_{TAN} - f.C_{NOX} - g.c.C_{CHL}.\left\{\frac{C_{NOX}}{C_{TAN}+C_{NOX}}\right\} \quad \ldots (2)$$

$$\frac{dC_{CHL}}{dt} = g.C_{CHL} - (f+s).C_{CHL} \quad \ldots (3)$$

$$\frac{dM_{NSED}}{dt} = s.c.C_{CHL} - r.M_{NSED} \quad \ldots (4)$$

$$\frac{dC_{DON}}{dt} = (1-q).A_t - f.C_{DON} \quad \ldots (5)$$

Where, C_{TAN} = TAN concentration (mg/L); t = time (day); q = proportion of N waste entering the water as TAN (with the remainder entering the water as DON); A_t = total N waste input per unit time (mg/L/day); r = remineralization rate of TAN in the mud of pond bottom (day^{-1}); MNSED = mass of N (mg) in the sludge per L of pond water; n = nitrification rate (day^{-1}); v = volatilization rate of ammonia (day^{-1}); f = water exchange rate (day^{-1}); g = phytoplankton growth rate (day^{-1}); c = N/CHL ratio of phytoplankton; C_{NOX} = NOX concentration (mg/L); C_{CHL} = CHL concentration; s = sedimentation rate of phytoplankton (day^{-1}); C_{DON} = DON concentration (mg/L).

The total N waste input A_t was assumed to be proportional to the metabolism of the shrimp population:

$$A_t = a\ .N_t\ W_t.b \quad \ldots (6)$$

Where, a is the N waste produced by one shrimp at unit weight (mg/g/day) and b is the allometric scaling factor of metabolism. The number N_t, of shrimp is given by an exponential mortality model:

$$N_t = N_0\ e^{-Mt} \quad \ldots (7)$$

where, N_0 = initial stocking density (L^{-1}) and M the natural mortality rate (day^{-1}) of shrimp.

Shrimp mean weight Wt is given by a von Bertalanffy growth function:

$$W_t = [W_\infty^{1/3} - (W_\infty^{1/3} - W_0^{1/3})\ e^{-Kt}]^3 \quad \ldots (8)$$

where, W∞ (g) and K (day-1) are the von Bertalanffy growth parameters and W0 (g) is the weight at stocking.

The growth rate g of phytoplankton is defined as:

$$g = g_{max}.\ L_{light}t\ .LN \quad \ldots (9)$$

where gmax (day^{-1}) is the maximum growth rate in the absence of limitation, and L_{light} and LN are the light and TAN plus nitrate limitation coefficients, respectively. It was

assumed that phosphate was not limiting to growth. The light limitation coefficient is given by the integral of Steele's (1962) light inhibition model over the water column, with light conditions defined by the Lambert–Beer law:

$$L_{light} = \left(\frac{e}{k}\right).\left[\exp\left\{\left(-\frac{I_o}{I_{sat}}\right).\exp(-kz)\right\} - \exp\left(-\frac{I_o}{I_{sat}}\right)\right] \quad \ldots (10)$$

Where, $\frac{I_o}{I_{sat}}$ is the ratio of the surface light intensity to the saturating light intensity, k is the extinction coefficient (m^{-1}) and z is the pond depth (m). The extinction coefficient is the sum of extinction due to CHL and extinction due to other sources:

$$k = k_{CHL}.C_{CHL} + k_{other} \quad \ldots (11)$$

Where, k_{CHL} is the extinction per unit CHL concentration (m^{-1} mg^{-L}) and k_{other} is the extinction due to other sources. Nitrogen limitation is defined by the Michaelis–Menten model:

$$LN = \frac{(C_{TAN} + C_{NOX})}{[(C_{TAN} + C_{NOX}) + k_{SN}]} \quad \ldots (12)$$

where k_{SN} (mg/L) is the half-saturation constant for nitrogen.

Phytoplankton was assumed to assimilate both TAN and NOX in proportion to their relative concentrations in the water column. Nitrification, volatilization, sedimentation, remineralization and discharge of N were described as first-order rate processes.

2.3 Data used for model

The model was calibrated and validated for black tiger shrimp (*Penaeus monodon*) culture based on data obtained from Oshadira Aquaculture system Pvt. Ltd. Sulerikaddu, Chennai. The TAN, NOX and chlorophyll of the culture water for six months were analysed of which the first three months data was used for calibration of model and the later data for validating the model.

2.4 Modelling technique using Microsoft Excel

Substituting the values of A_t (Eq.s 6 - 8) and g (Eq.s 9 – 12) in Eq.s 1- 5, wherever they appear, and using forward finite difference technique, Eq.s 1 – 5 can be rewritten as follows:

$C_{TAN}^{(i+1)}$

$= C_{TAN}(i) + (t_{i+1} - t_i) \times [q\ a\ N_0\ e^{-Mt(i)}\ [\{W_\infty^{1/3} - (W_\infty^{1/3} - W_0^{1/3})\ e^{-Kt(i)}\}^3]^b + r \times C_{NSED}(i) - (n + v + f)C_{TAN}(i) - g_{max}\ (\exp(1)/k) \times [\exp\{(-I_0/I_{sat}) \times \exp(-kz)\} - \exp(-I_0/I_{sat})] \times (C_{TAN}(i) + C_{NOX}(i))/[(C_{TAN}(i) + C_{NOX}(i)) + Ks_N] \times c \times C_{CHL}(i)\{C_{TAN}(i)/(C_{TAN}(i) + C_{NOX}(i))\}\ ]$

... (13)

$C_{NOX}^{(i+1)}$

$= C_{NOX}(i) + (t_{i+1} - t_i) \times [n\ C_{TAN}(i) - f\ C_{NOX}(i) - g_{max}\ (\exp(1)/k) \times [\exp\{(-I_0/I_{sat}) \times \exp(-kz)\} - \exp(-I_0/I_{sat})] \times (C_{TAN}(i) + C_{NOX}(i))/[(C_{TAN}(i) + C_{NOX}(i)) + Ks_N] \times c \times C_{CHL}(i)\{C_{NOX}(i)/(C_{TAN}(i) + C_{NOX}(i))\}]$

... (14)

$C_{CHL}^{(i+1)}$

$= C_{CHL}(i) + (t_{i+1} - t_i) \times [g_{max}\ (\exp(1)/k) \times [\exp\{(-I_0/I_{sat}) \times \exp(-kz)\} - \exp(-I_0/I_{sat})] \times (C_{TAN}(i) + C_{NOX}(i))/[(C_{TAN}(i) + C_{NOX}(i)) + Ks_N] \times C_{CHL}(i) - (f + s)\ C_{CHL}(i)]$

... (15)

$C_{NSED}^{(i+1)}$

$= C_{NSED}(i) + (t_{i+1} - t_i) \times [s\ c\ C_{CHL}(i) - r\ C_{NSED}(i)]$

... (16)

$C_{DON}^{(i+1)}$

$= C_{DON}(i) + (t_{i+1} - t_i) \times [(1 - q)\ a\ N_0\ e^{-Mt(i)}\ [\{W_\infty^{1/3} - (W_\infty^{1/3} - W_0^{1/3})\ e^{-Kt(i)}\}^3]^b - f\ C_{DON}(i)]$

... (17)

Assuming $(t_{i+1} - t_i) = 1$ day and knowing the initial values of TAN, NOX, CHL, NSED and DON, the concentration values of the five state variables can be predicted at different times.

2.5 Model Calibration

The model parameters that could be estimated directly like shrimp growth, mortality rate and nitrogen waste input were determined during the culture period. The other nitrogen dynamics parameters (flux rates) were estimated by fitting the model to observed water quality parameters.

2.6 Model Validation

The model was evaluated using two criteria: (i) Root Mean Square Error (RMSE) which can be expressed as

$$RMSE = \sqrt{\frac{1}{N}\sum_{i=1}^{N}(O(i)-S(i))^2} \quad \text{..... (18)}$$

and (ii) Coefficient of Determination (R^2) which is given by

$$R^2 = \left\{ \frac{\sum_{i=1}^{N}[O(i)-O_{Avg}][S(i)-S_{Avg}]}{[\sum_{i=1}^{N}(O(i)-O_{Avg})^2]^{0.5}[\sum_{i=1}^{N}(S(i)-S_{Avg})^2]^{0.5}} \right\}^2 \quad \text{..... (19)}$$

where, O(i) = i^{th} observed value; O_{avg} = mean of the observed values; S(i) = i^{th} simulated value; S_{avg} = mean of the model simulated values and N = total no. of events.

3. Results and Discussion

The data obtained on the culture of tiger shrimp in the aquaculture farm under study was calibrated and validated using the spreadsheet developed. The measured values of TAN, NOX and CHL concentrations during the first 90 days of culture were used for model calibration. The observed values of the above mentioned water quality parameters during the last 90 days of culture period were used for evaluating the model's performance. The manual calibration based on the trial and error process of parameters' adjustments was used and several simulations were performed by changing the model parameters. After adjustment of each parameter, the simulated and measured values of the water quality parameters were compared to judge the improvement in the model prediction. The calibrated values of the model parameters are as shown in Table 1.

Table 1. Model parameters

Parameter	Values
Proportion of N entering as TAN, q	0.8
Waste N input, a (mg g^{-1} day^{-1})	3
Allometric scaling of TAN excretion, b	0.75
Shrimp growth rate, K (day^{-1})	0.0055
Shrimp maximum weight ,W_∞ (g)	70 g
Shrimp stocking weight ,W_0 (g)	0.005
Initial stocking density, N_0 (L^{-1})	0.051
Shrimp mortality, M (day^{-1})	0.0055
Pond depth, z (m)	1
Extinction coefficient Non-Chl a, k_{other} (m^{-1})	3
Extinction coefficient Chl a ,kCHL(m^{-1} mg^{-1} L^{-1})	11.9
Ratio surface/saturating light intensity, I_0/I_{sat}	2.4
Sludge remineralization rate, r (day^{-1})	0.06
Nitrification rate, n (day^{-1})	0.2
Volatilization rate, v (day^{-1})	0.05
Water exchange, f (day^{-1})	0 for Day 1 – 65 0.065 Day 65 onwards
Phytoplankton growth rate, g_{max} (day^{-1})	1.4
N/CHL ratio of algae, c	3.2
Sedimentation rate, s (day^{-1})	0.8
N half-saturation, K_{SN} (mg L^{-1})	0.03

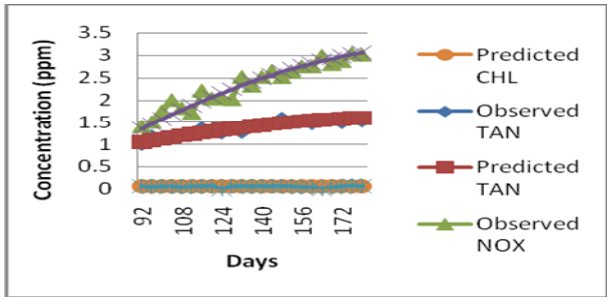

Figure 2. Predicted and observed concentrations of TAN, NOX and CHL

The predicted and observed values of concentration of TAN, NOX and CHL during validation of model are plotted in Figure 2. From equations (18), the values of RMSE for TAN, NOX and CHL were found to be.05, 0. 0132 and 0.017 mg/L respectively and from (19) the corresponding R^2 values were 0.90, 0.94 and 0.006. The higher R^2 values

ensure effectiveness of the model in predicting the concentrations of TAN and NOX in shrimp culture and the lower R^2 value for CHL indicates that the model could not successfully predict CHL concentration. However, the lesser RMSE value for CHL ensures that the models for TAN and NOX do not get affected.

4. Conclusions

A spreadsheet model has been developed to predict the harmful nitrogenous compounds in intensive shrimp aquaculture pond. The user-friendly format makes it convenient for the users to use the model for predicting the concentrations of water quality parameters in culture water. This in turn enables the user to go for timely adoption of management programmes which are otherwise difficult to decide. This is essentially helpful for farmers and entrepreneurs who do not have access to daily water quality measurement facilities. Once the model is calibrated and validated for a particular culture pond, it serves as a useful predictive tool in deciding the water quality management practices like water exchange or sludge removal to be adopted when the concentrations of parameters reach their permissible limits.

References

[1] Burford, M.A. and Lorenzen, K., 2004. Modelling nitrogen dynamics in intensive shrimp ponds: the role of sediment remineralization. Aquaculture, 229(1-4), 129–145.

[2] Lorenzen, K., Struve, J., Cowan, V.J., 1997. Impact of farming intensity and water management on nitrogen dynamics in intensive pond culture: a mathematical model applied to Thai commercial shrimp farms. Aquaculture Research, 28(7), 493–507.

[3] Ridler, N. & Hishamunda, N., 2001. Promotion of sustainable commercial aquaculture in sub-Saharan Africa. Volume I: policy framework. FAO Fisheries Technical Paper No. 408/1. FAO, Rome.

Remediation of Acid Mine Drainage through Permeable Reactive Barrier Using Waste Materials from Integrated Steel Plant: A Column Mode Simulation Study

Piyush Kant Pandey
Bhilai Institute of Technology
Kendri, Raipur, C.G., India
drpiyush_pandey@yahoo.com

Richa Deshmukh
Department of Applied Chemistry
Bhilai Institute of Technology
Durg, C.G., India
deshmukh_richa2007@yahoo.com

Madhurima Pandey
Department of Applied Chemistry
Bhilai Institute of Technology
Durg, C.G., India
drmadhurima_pandey@yahoo.com

Abstract

Acid mine drainage (AMD) is considered as one of the biggest non point source water pollution problem, generated due to mining activity. Use of permeable reactive barrier (PRB) for treatment of water impacted by AMD is considered in this paper. Laboratory column test was performed using four different integrated steel plant waste materials as Reactive barrier material (RBM). The alkaline fly ash (AFA) from a particular gas cleaning plant (GCP stack dust) was identified as the best RBM for acidity neutralization as well as metals removal. Laboratory column tests were further conducted to study the efficiency of AFA in removing heavy metal ions; such as Cu, Mn, Fe, Cr, Cd, and Zn, from acidic lechate. AFA also gave highest removal capacity for all metals except for iron. The Blast Furnace slag (BFS) gave highest removal capacity for iron i.e., 70.59 mg/gm. The removal capacity (mg/gm) of AFA for metals was Cu-54.54, Mn-44.90, Fe-54.51, Cr-18.20, Cd-45.85 and Zn-45.77. The high uptake capacity and stable behaviour can be attributed to the high alkaline chemical composition of this RBM.

Keywords- Acid mine drainage (AMD), Permeable reactive barrier (PRB), Reactive barrier material (RBM), steel slag, alkaline fly ash (AFA).

Broad Area- Applied Chemistry.

1. Introduction

Acid mine drainage (AMD) or acid rock drainage (ARD) generated from mining activities is a well-recognized source of environmental contamination worldwide. Acid mine drainage produced form the exposure of iron-sulphur mineral to atmospheric oxygen and water, resulting $Fe(OH)_2$ and sulphuric acid (H_2SO_4). Due to acid formation toxic metals can leach in water stream. AMD is characterized by yellowish-orange colored water, with low pH and high metallic content. AMD is considered as one of the biggest non point source pollution problem, which irreparably damaging waterways and vegetation. Although AMD is naturally occurring but mining activities greatly accelerate its production.

In the last years, the use of permeable reactive barriers (PRB) for the decontamination of waters impacted by AMD has been well documented [1-4]. PRBs are able to remove multiple contaminants present in water depending on the reactive medium used for their construction [5]. Permeable reactive barriers are subsurface barrier placed in path of contaminated plume, which are capable to remove contaminants.

Industrial waste materials, such as fly ash, bottom ash, and granulated slag of steel plants, have been studied as possible cost-effective and convenient adsorbents for the treatment of wastewater containing heavy metals [6]. Converter slag has a higher capacity for pH increase and removal of Fe, Al, and other heavy metals in acid mine drainage than limestone [7]. Converter slag composed of magnetite (Fe_3O_4) has been known to be suitable for use as a metal adsorber in wastewater treatment. There is a considerable effort for the use of low-cost industrial by-products as reactive media [8-9].

The main objective of this study was to evaluate the efficacy of different steel waste materials such as slag, sludge and fly ash to treat mixed toxic metallic contaminants present in acidic mine drainage. This study was carried out to evaluate the efficiency of various waste materials for treatment of acidity as well as metals contamination. For evaluation of removal capacity laboratory column studies was carried out.

Emphasis was placed on determining which steel waste material is effective as both neutralizing agent and heavy metal adsorber in dynamic flow condition. The most effective material for acidity neutralization was studied further for its trace element sequestration capability.

2. Material and method

For laboratory based column study, four types of waste materials were used. These materials were collected from an integrated steel plant. Waste materials analyzed include- blast furnace slag (BFS), gas cleaning plant sludge (GCPS), basic oxygen furnace slag (BOFS) or LD converter slag (LDS) and alkaline fly ash (AFA). Before column studies the waste materials were analyzed for composition determination and batch tests were also conducted, as described in previous paper [10]. GCPS and LDS were crushed before use because these were obtained in a form of very large size. BFS and AFA were available in granulated and ash form respectively; hence these were used as it was obtained.

2.1 Column test

Two different sets of column test were carried out. First set involved four different waste materials- BF slag (BFS), GCP sludge (GCPS), LD slag (LDS) and alkaline fly ash (AFA). This study was carried out to evaluate the efficiency of four different materials, as RBM. The efficiency of Waste material as RBM was selected on the basis of pH of outlet solution. Second set of experiment was performed using that material which gave the best result during first set of experiments. This study observes the effect of different active bed height on removal capacity of trace elements. An upward flow of synthetic acidic solutions spiked with high concentrations of contaminants was maintained in order to simulate field flow rates. Schematic diagram of laboratory upflow column set up is depicted in (Figure 1)

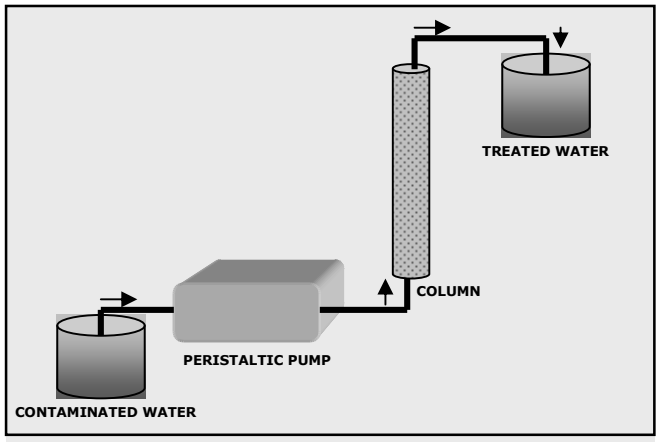

Figure 1. Schematic of laboratory column set up

2.2 Synthetic acidic mine water

A synthetic acid mine water (pH 2, with sulphuric acid) was prepared in laboratory for column tests. Characteristic of synthetic mine water was low pH (~2) and high metals concentration (Table 1). This synthetic solution contained trace elements viz. Cu, Mn, Fe, Cr, Cd, and Zn. The metals were taken in such combination because these metals are most abundant in acid mine drainage.

Table 1. Synthetic acid mine water composition and corresponding chemicals

Contaminants	Concentration in mg/l	Used compound
Cu	100	$CuSO_4 \cdot 5\ H_2O$
Mn	100	$MnSO_4 \cdot\ H_2O$
Fe	100	$(NH_4)_2SO_4.FeSO_4.6H_2O$
Cr	100	$K_2Cr_2O_7$
Cd	100	$CdCl_2 \cdot H_2O$
Zn	100	$ZnSO_4 \cdot H_2O$
pH	2.63	H_2SO_4

2.3 Investigation on efficiency of waste materials as RBM

First set of Column test was conducted using four waste materials including BF slag, GCP sludge, LD slag and AFA. This study was conducted to analyze the metal removal and acidity neutralization capacity of material in continuous flow through column. The summary of column characteristics for this study is shown in Table 2. A set of 4 columns (diameter 1.5 cm, height 65 cm) was installed. Each column was filled with different material with same active bed height. Material was filled between two layers of silica (2 cm each layer), for packing as inert material. The synthetic acid mine water that was prepared in laboratory was used for column test. Acidic solution was passed through packed column in up flow mode by using peristaltic pump (ISMATEC). The flow rate was kept constant at 5 mL/min. 4 columns were run simultaneously and continuously. Definite volume of outlet solution was collected from each column. These collected samples were analyzed immediately for residual metals and pH. This procedure was continued till the exhaustion of column. Analysis of metals concentration was done using Atomic Absorption Spectrophotometer (Varian AA240FS). Although outlet solution was analyzed for pH and all metal concentration, present in acidic metal solution, but only pH value is taken into consideration for selection of RBM through this study for further detailed analysis.

2.4 Detailed investigations on selected RBM

Second Column test was conducted using alkaline fly ash (AFA) sample, because this material was giving best result for metal removal and acidity neutralization during first column test. Set of 5 columns (same as first set) was installed. Table 3 is showing column characteristic for this study. Each column was filled with AFA material with different active bed heights. Objective of taking different bed height columns was to evaluate the effect of height on removal capacity. Acidic solution was passed in up flow mode by peristaltic pump with a flow rate of 13 mL/min. 5 columns with different active bed height were run simultaneously. A definite volume (200 mL) of solution was collected from each column. These collected samples were analyzed immediately for residual metals and pH.

Table 2. Summary of the column characteristics for First set (different material column)

COLUMN	1	2	3	4
Material	BFS	GCPS	LDS	AFA
Flow rate (mL/min.)	5	5	5	5
Weight of material (gm)	50	50	50	50
Height of active bed (cm)	40	40	40	40
1 Bed Volume (mL)	70.65	70.65	70.65	70.65
EBCT[a] (min)	14.13	14.13	14.13	14.13
Total volume passed (mL)	2575	2275	1375	2775
No. of Total Bed Volume passed	36.45	32.20	19.46	39.29
Average inlet pH	2.63	2.63	2.63	2.63
Average outlet pH	3.98	5.77	2.83	9.21

[a]EBCT= **Empty Bed Contact Time**

3. Result and discussion

3.1 Investigation on efficiency of waste materials as RBM

3.1.1 Effect of waste materials on pH

The pH and residual metal concentration vs. solution passed (mL) was plotted for each column in each study. The change in pH value with solution passed through different material columns is shown in Figure 2.

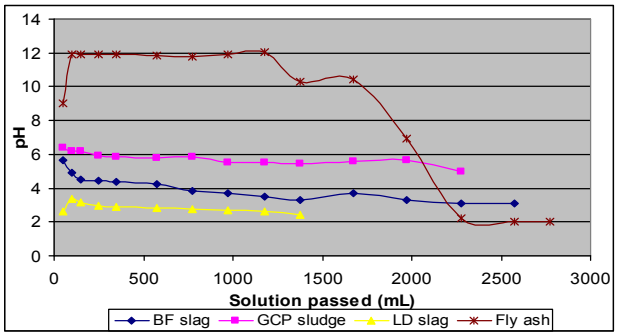

Figure 2. Effect on pH with solution passed from different material column

Table 3. Summary of the column characteristics for Second set (Alkaline fly ash columns)

COLUMN	1	2	3	4	5
Material	AFA	AFA	AFA	AFA	AFA
Flow rate (mL/min.)	13	13	13	13	13
Weight of material (gm)	10	20	30	40	50
Height of active bed (cm)	8	16	23	31	38
1 Bed Volume (mL)	14.13	28.26	40.62	54.75	67.12
EBCT[a] (min)	1.09	2.17	3.12	4.21	5.16
Total volume passed (mL)	1000	1000	1000	1000	1000
No. of Total Bed Volume passed	70.77	35.38	24.62	18.26	14.90
Average inlet pH	2.63	2.63	2.63	2.63	2.63
Average outlet pH	4.32	6.87	6.45	7.5	7.6

[a]EBCT= **Empty Bed Contact Time**

It was evident from the result obtained that the acid neutralization capacity of the three studied RBMs i.e., BFS, GCPS, LDS was not very high (Figure 2). But in case of AFA column there was a sharp change in pH from the very beginning and the change noted was up to pH 9 from 2. The pH was then remained constant between 11.9-11.8 till the passage of about 1L of solution. Beyond 1 L the treatment efficiency started to decrease and became nil after treating about 2-L of acidic water. It is observed from the result that fly ash column is giving best result for neutralization of acidity by increase in pH. The higher capacity of neutralization by increasing pH to such extent can be explained due to higher alkaline characteristic of AFA. Alkaline property of this material is due to maximum CaO content, which was found to be more than 85%. The percentage composition of all the four studied material is shown in Table 4. The CaO content was highest in AFA, it attributes higher alkaline characteristics. Metals precipitate at higher pH hence fly ash also decrease metals concentration from solution (Figure 3).

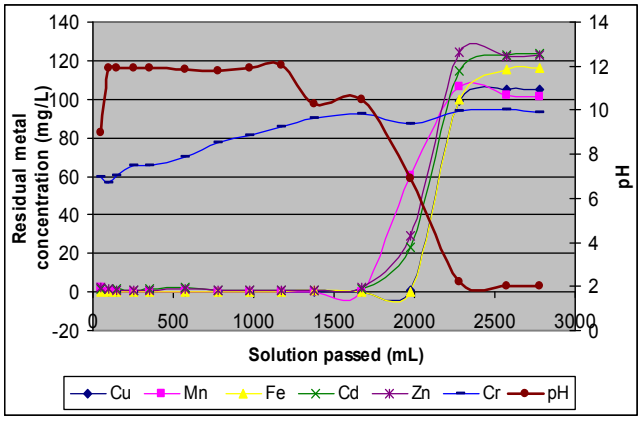

Figure 3. Effect on pH and metal concentration (Cu, Mn, Fe, Cd, Cr and Zn) with solution passed from alkaline Fly ash (AFA) column.

3.1.2 Removal capacity

Removal capacity q (mg metal/gm material) was calculated for all of the four materials. For calculation of removal capacity q (1) was used.

$$q = \frac{(C_I - C_F)V}{M} \qquad (1)$$

Where, q is Removal capacity (mg metal/gm material), C_I= Initial metal concentration (mg/L)

C_F= Final metal concentration (mg/L), V= Volume of effluent collected upon exhaustion of the bed (L), M= Mass of material filled in column (gm).

The value of removal capacity is shown in Table 5. In case of iron removal BFS and GCPS was giving very good removal capacity i.e. 70.59 mg/gm and 58.99 mg/gm respectively, these values are more than that of AFA (Figure 4). Hence these materials can be utilized as RBM for treatment of iron containing effluent. From Figure 4 it is clear that BFS is showing highest removal capacity, while not found good for other metals. The over all removal capacity was the maximum in case of AFA. Hence, the AFA can be selected as RBM for metals containing AMD.

Table 5. Removal capacity q (mg metal/gm material)

METAL	BF SLAG	GCP SLUDGE	LD SLAG	AFA
Cu	0.98	32.00	0.03	54.54
Mn	0.22	1.47	0.02	44.90
Fe	70.59	58.99	1.34	54.51
Cr	6.32	12.71	3.44	18.20
Cd	0.27	2.38	0.19	45.85
Zn	0.01	1.82	0.05	45.77

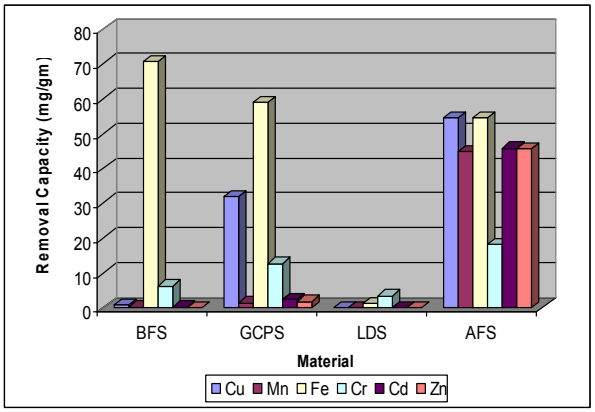

Figure 4. Removal capacity q (mg metal/gm material)

3.1.3 Metals removal by AFA column

The result of metals removal with pH, by fly ash column during first set is shown in Figure 3. Figure 3 shows the results of such experiments using AFA. Removal of metals (Cu, Mn, Fe, Cd, and Zn) form solution showing almost similar pattern except Cr in case of AFA column (Figure 3). Up to passing 1975mL of solution, metals Cu, Mn, Fe, Cd, and Zn was completely removed, with a sudden increase in pH. After passing further solution through the column, the residual metal concentration increases in outlet solution. The pH of outlet solution decreases with the passage of acidic influent.

3.2 Detailed investigations on alkaline fly ash (AFA)

To study the operational parameters a detailed column study was carried out with different active bed height. The result of second set of column using AFA is shown in Figure 5 (a-g). Effect of different bed height on pH is shown in Figure 5a. The effect of different active bed height on behavior of metal removal is almost similar in case of Cu, Cd and Zn. From graph it is clear that with increase in active bed height the metal removal capacity also increases. While considering Cu removal (Figure 5b), column 4 and column 5 with active bed height 31cm and 38cm respectively, are showing almost similar pattern of metal removal. In case of column 1 with active bed height 8 cm the residual Cu concentration increases with solution passed and reaches upto 100 mg/L when 1000 mL solution passed. Column 1 exhausted upto passing 1000 mL of solution, while other column with higher active bed was still removing Cu. This material was not found very good for removal of Cr, even when active bed height was increased (Figure 5e).

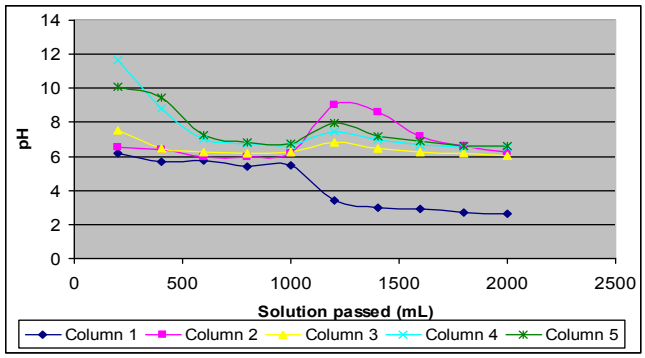

a) pH.

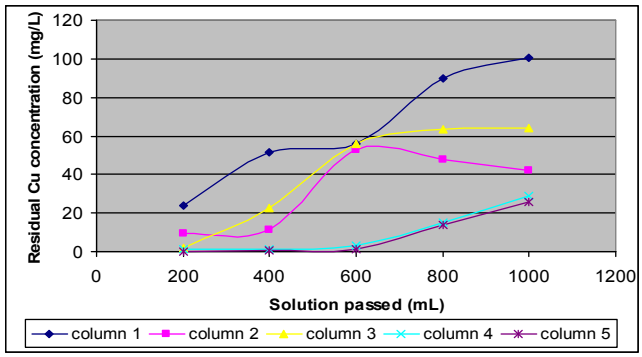

b) Cu

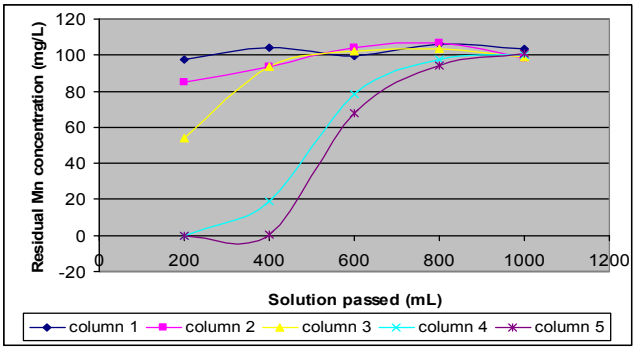

c) Mn

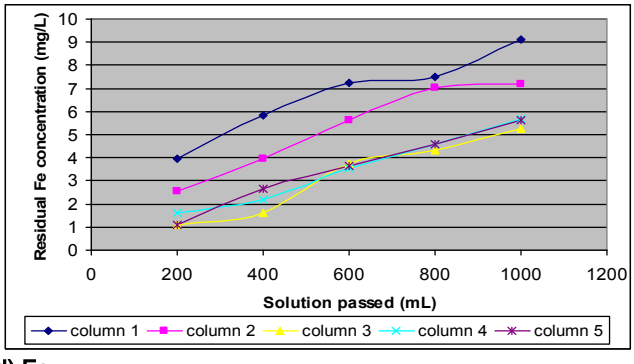

d) Fe

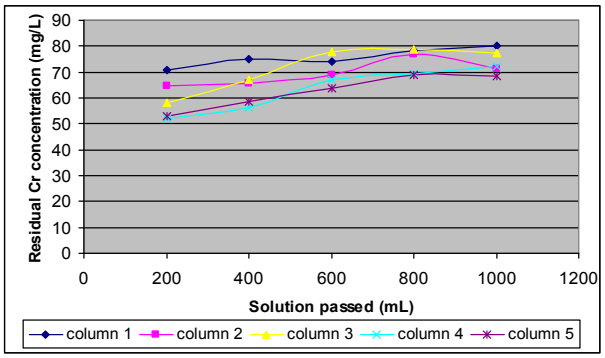

e) Cr

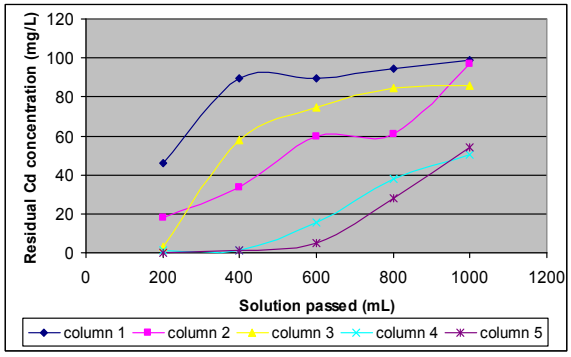

f) Cd

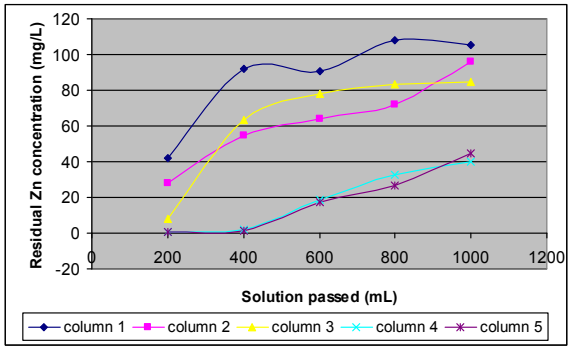

g) Zn

Figure 5. (a-g). Effect on pH and metal concentration (Cu, Mn, Fe, Cr, Cd, and Zn) with solution passed from alkaline fly ash (AFA) columns with different active bed height.

4. Conclusion

The experiments conducted show that the alkaline fly ash (AFA) containing higher calcium oxide content was most effective in treating acidity of water and the removal of metallic elements, particularly copper and iron, with removal capacity 54.54 (mg/gm) and 54.51 (mg/gm) respectively. The order of the removal capacity for AFA was Cu>Fe>Cd>Zn>Mn> Cr. Hence, it appears that the calcium content of waste material

provides alkalinity in the system raising pH to strongly alkaline values (~12) and precipitative removal of metallic elements. Permeable Reactive Barriers, constructed from such alkaline fly ash can be emerging and innovative technology that can be effective in removing heavy metals from acidic leachates or contaminated groundwater in an economically feasible manner. This waste steel sludge and converter slag are inexpensive and abundant, therefore, can be use as ideal and low-cost reactive materials for leachate treatment generated from mining activities.

Table 4. Composition of metallurgical waste materials (in percentage %, BDL = below detection limit)

SN	Metallurgical waste materials	CaO	MgO	Si	Fe	Al	Pb	Mn	Zn	Cu	Cr	Ni
1	Blast furnace slag (BFS)	43	8	29	0.37	19.6	0.003	0.16	0.002	BDL	BDL	BDL
2	Gas Cleaning Plant sludge (GCPS)	11	4.4	6	8.75	17	0.01	BDL	0.007	BDL	BDL	BDL
3	LD converter slag (LDS)	58	3	15	20.5	6	0.007	1.70	0.003	BDL	BDL	BDL
4	Alkaline Fly ash (AFA)	83	4.2	3	0. 48	9.5	0.01	0.02	0.006	BDL	BDL	BDL

Reference

[1] P.W. Amos, and P.L. Younger (2003) "Substrate characterisation for a subsurface reactive barrier to treat colliery spoil leachate," Water Resources; vol. 37(1): pp. 108–120.

[2] S.G. Benner, D.W.Blowes, and C.J. Ptacek (1997) "Full-scale porous reactive wall for the prevention of acid mine drainage," Ground Water Monitoring and Remediation; vol. 17: pp.99–107.

[3] D.W. Blowes, C.J.Ptacek, S.G.Benner, C.W.T. McRae, T.A. Bennett, and R.W. Puls, (2000) "Treatment of inorganic contaminants using permeable reactive barriers," Journal of Contaminant Hydrology; vol. 45: pp.123–137.

[4] K.R. Waybrant, D.W. Blowes, and C.J.Ptacek (1998) "Selection of reactive mixtures for use in permeable reactive walls for treatment of mine drainage," Environmental Science and Technology; vol. 32: pp. 1972–1979.

[5] D. H. Snow (1999) "Overview of Permeable Reactive Barriers," Civil engineering Dept.; BYU.

[6] N.Ortiz, M. A. F. Pires, and J. C. Bressiani, (2001) "Use of steel converter slag as nickel adsorber to wastewater treatment," Waste Management; vol. 21: pp. 631–635.

[7] S.D. Kwon, and S.J. Kim, (1999) "A study on the treatment of the acid mine drainage using the steel mill slag," Journal of Korean Society for Groundwater Environment; vol. 6: pp.206–212 (in Korean with English abstract).

[8] S. Bailey, T. Olin, M.Bricka, and D. Adrian, (1999) "A review of potentially low-cost sorbents for heavy metals," Water Research; vol. 33(11): pp. 2469–2479.

[9] T.Y.Lee, J.W.Park, J.H.Lee, (2004) "Waste Green Sands as Reactive Media for the Removal of Zinc from Groundwater," Chemosphere; vol. 56(6): pp. 571–581.

[10] P.K.Pandey, R.Deshmukh, H.Zankyani, and M.Pandey, (2009) "Reactive barrier material for treating acid mine drainage using metallurgical waste materials," Environmental pollution control journal; vol. 12(4): pp. 66-70.

Bimetallic Zn(II) Complexes of Organoselenium Substituted Macroacyclic Ligands: Synthesis and Characterization

Ashish K. Asatkar
Dept. of Chemistry
Disha Institute of Management & Technology
Raipur (C.G.), India
ashishasatkar007@rediffmail.com

Vinay K.Verma
Dept. of Chemistry
Disha Institute of Management & Technology
Raipur (C.G.), India
verma_vinay2002@rediffmail.com

Tripti A. Jain
Dept. of Chemistry
Disha Institute of Management & Technology
Raipur (C.G.), India
tripti323@yahoo.com

Abstract

The reactions of organoselenium substituted macroacylic Schiff-base ligands L_aH and L_bH with Zn(II) ions at room temperature under argon atmosphere produce bimetallic complexes 1: $[\{C_6H_2(O)(4\text{-}CH_3)(PhC{=}NCH_2CH_2SePh)(PhC{=}O)\}_2Zn_2Cl_2]$ and 2: $[\{C_6H_2(O)(4\text{-}CH_3)(PhC{=}NCH_2CH_2CH_2SePh)(PhC{=}O)\}_2Zn_2Cl_2]$, with the partially hydrolyzed ligand molecules. Each molecule of such partially hydrolyzed ligands behave in tridentate (NOO) fashion and two such molecules coordinate with two Zn atoms through imino N, benzoyl O and phenolic O; the phenolic 'O' bridges the two Zn(II) atoms. Further, each metal ion is bonded with a Cl atom and thereby adopts a square pyramidal geometry in the complexes. Complexes were characterized by elemental analysis, ESIMS, FTIR, UV-Visible spectroscopy and conductance measurement.

Keywords- Hybrid ligands, Bimetallic Zn(II) complexes

Broad Area- Chemistry, Material Science

Sub-Area- Coordination Chemistry, Organometallic Chemistry

1. Introduction

The coordination chemistry of organoselenium ligands is an area of growing interest [1-7]. Increased interest in this area is due to the potential applications of their complexes as single source molecular precursors for the generation of metal selenide nano materials by Chemical Vapour Deposition (CVD) technique [8-13]. Because of the presence of broad range of energy band gap, these materials are technologically important candidates with their uses in a range of electronic devices like light emitting diodes, photovoltaic materials as well as their applications as a cathode materials in rechargeable batteries and high temperature lubricants [14-25].

As part of our research into design and synthesis of novel selenium bearing hybrid ligands, we recently reported the synthesis and characterization of organoselenium substituted hybrid macroacyclic Schiff base ligands $\mathbf{L_aH}$ and $\mathbf{L_bH}$ (Figure 1.) and their Cu(II) complexes [26]. Herein, we report the synthesis and characterization of two new bimetallic Zn(II) complexes **1**: $[\{C_6H_2(O)(4\text{-}CH_3)(PhC{=}NCH_2CH_2SePh)(PhC{=}O)\}_2Zn_2Cl_2]$ and **2**: $[\{C_6H_2(O)(4\text{-}CH_3)(PhC{=}NCH_2CH_2CH_2SePh)(PhC{=}O)\}_2Zn_2Cl_2]$ obtained by the reactions of the ligands $\mathbf{L_aH}$ and $\mathbf{L_bH}$ with $ZnCl_2$.

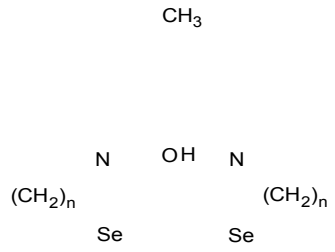

Figure 1. L_a.H (n=2); L_b.H (n=3)

2. Experimental

All the chemicals used were of reagent grade. Solvents were purified by standard methods [27] and freshly distilled prior to use. All the reactions were performed under argon atmosphere. Chlorine was quantitatively estimated by Mohar method.

2.1 Physical measurements

Melting points of the compounds in the capillary tubes were recorded and are reported as such. CHN analyses were carried out on a Carlo-Erba Model DP 200 analyzer. Quantitative estimation of zinc was carried out on Varian Atomic Absorption Spectrophotometer AA240FS. The electrospray ion mass spectra (ESIMS) were recorded on a WATERS- HAB 213 triple quadrupole mass spectrometer. The ESI capillary was set at 3.5 kV and the cone voltage was 40 V. Infrared spectra were recorded in the range of 4000-400 cm^{-1} by a Shimadzu IR Prestige-21 FT spectrophotometer on a KBr disc. Electronic spectra were obtained by the use of a Perkin Elmer Lambda 35 UV-VIS spectrophotometer. Conductance values were measured using Global DCM-900 digital conductivity meter in acetonitrile at 273K.

2.2 Reaction of $ZnCl_2$ with Ligands L_aH and L_bH

10 mL methanolic solution of $ZnCl_2$ (0.136 g, 1.0 mmol) was added dropwise to a degassed 60 mL methanolic solution of ligands **L_aH** (0.680 g, 1.0 mmol)/ **L_bH** (0.708 g, 1.0 mmol) at room temperature. The reaction was carried out under argon atmosphere with vigorous stirring. Precipitation of yellow solid started after 10 minutes of mixing of the reactants. The progress of reaction was monitored by TLC. After stirring of the reaction mixture for 12 h, the precipitated solid was filtered and washed several times with methanol. Complexes were dried under vacuum.

[{C_6H_2(O)(4-CH_3)(PhC=NCH_2CH_2SePh)(PhC=O)}$_2$$Zn_2$ Cl_2]; 1

Colour and state: yellow powder; yield: 0.425 g (72 %). M.p.: 225 °C. Anal. Calc. for $C_{58}H_{48}N_2O_4Se_2Zn_2Cl_2$: C, 58.21; H, 4.04; N, 2.34; Zn, 10.93; Cl, 5.93 %. Found: C, 57.66; H, 4.42; N, 2.51; Zn, 10.76; Cl, 5.61 %. Positive ESIMS: m/z 1159 [**1**-Cl]$^+$, 1097, 1061, 500. FTIR (KBr disc, cm^{-1}): ν(C=O) 1610, ν(C=N) 1532, ν(C−O) 1248. UV−Vis (λ/nm, ε/$M^{-1}cm^{-1}$, CH_3CN): 250 (15427), 344 (3062), 416 (2031). Λ_M (10^{-3} M, CH_3CN, 298 K): 20 S cm^2 mol^{-1}.

[{C_6H_2(O)(4-CH_3)(PhC=N$CH_2CH_2CH_2$SePh)(PhC=O)}$_2$ Zn_2Cl_2]; 2

Colour and state: yellow powder; yield: 0.465 g (76 %).M.p.: 229 °C. Anal. Calc. for $C_{60}H_{52}N_2O_4Se_2Zn_2Cl_2$: C, 58.84; H, 4.28; N, 2.29; Zn, 10.68; Cl, 5.79 %. Found: C, 58.47; H, 4.25; N, 2.96; Zn, 10.33; Cl, 5.32 %. Positive ESIMS: m/z 1187 [**2**-Cl]$^+$, 1125, 1089, 514. FTIR (KBr disc, cm^{-1}): ν(C=O) 1611, ν(C=N) 1531, ν(C−O) 1247. UV−Vis λ_{max}/nm (λ/nm, ε/$M^{-1}cm^{-1}$, CH_3CN): 248 (15638), 345 (3126), 412 (2431). Λ_M (10^{-3} M, CH_3CN, 298 K): 22 S cm^2 mol^{-1}.

3. Results and Discussion

The isolated solids exhibit good solubility in chloroform, dichloromethane and acetone but very poor solubility in methanol and diethyl ether.

The ESI mass spectra of the complexes **1** and **2** show parent ion peaks at m/z 1159 and 1187 corresponding to [{C_6H_2(O)(4-CH_3)(PhC=NCH_2CH_2SePh)(PhC=O)}$_2$$Zn_2Cl$]$^+$ and [{C_6H_2(O)(4-CH_3)(PhC=N$CH_2CH_2CH_2$SePh)(PhC=O)}$_2$ Zn_2Cl_2]$^+$, respectively, *i.e.* mass of two molecules of partially hydrolyzed ligands, two atoms of Zn and one atom of Cl. Various other peaks of selenium containing fragments appeared in mass spectrum of **1** at m/z 1097, 1061 and 500 were assigned to [{C_6H_2(O)(4-CH_3)(PhC=NCH_2CH_2SePh)(PhC=O)}$_2$ZnCl]$^+$, [{C_6H_2(O)(4-CH_3)(PhC=NCH_2CH_2SePh)(PhC=O)}$_2$Zn]$^+$ and [C_6H_2(O)(4-CH_3)(PhC=NCH_2CH_2SePh)(PhC=O)]$^+$, respectively, and the peaks in mass spectrum of **2** at m/z 1125, 1089 and 514 were attributed to [{C_6H_2(O)(4-CH_3)(PhC=N$CH_2CH_2CH_2$SePh)(PhC=O)}$_2$ZnCl]$^+$, [{C_6H_2(O)(4-H_3)(PhC=N$CH_2CH_2CH_2$SePh)(PhC=O)}$_2$Zn]$^+$ and [C_6H_2(O)(4-CH_3)(PhC=N$CH_2CH_2CH_2$SePh)(PhC=O)]$^+$, respectively.

In the IR spectra of these complexes, the bands at 1532 cm^{-1} in **1** and 1531 cm^{-1} in **2** are attributed to ν(C=N) stretching frequencies which are shifted to lower frequency side by the order of about 60 cm^{-1} with respect to those of free ligands **L_aH** and **L_bH**. The red shift in this band suggests the coordination of imine N atoms with Zn atom. In addition to ν(C=N) band, appearance of band at 1610 cm^{-1} in **1** and 1611 cm^{-1} in **2**, suggest hydrolysis of one imine group of the ligand molecules which results in the formation of C=O at one arm. However, this band is shifted to lower frequency side by the order of about 50 cm^{-1} as compared to the 4-methyl-2,6-dibenzoylphenol which strongly suggests the coordination of benzoyl O with the metal ion. The disappearance of broad bands around 3500 cm^{-1} [ν (O-H)] in both the spectra suggest the binding of phenolic proton with the chloride ion of the $ZnCl_2$ and thus Zn(II) ion coordinates with the phenolic O atom.

Molar conductance values of 20 and 22 S cm^2 mol^{-1} of complexes **1** and **2**, respectively, in the acetonitrilic solutions show non-electrolytic nature of the complexes and eliminate the possibility of products to be ionic.

The electronic absorption spectra of acetonitrilic solutions of the complexes **1** and **2** showed the maxima at 344 and 345 nm, respectively, which can be assigned to the $\pi\rightarrow\pi^*$ transitions in ligand frameworks. The weak bands at 416 and 422 nm in the spectra of **1** and **2** respectively, are attributed to the $n\rightarrow\pi^*$ transition in ligand moieties.

Formulas of the complexes **1** and **2** assigned on the basis of their analytical data are [{C_6H_2(O)(4-CH_3)(PhC=N

$CH_2CH_2SePh)(PhC=O)\}_2Zn_2Cl_2]$ and $[\{C_6H_2(O)(4\text{-}CH_3)(PhC=NCH_2CH_2CH_2SePh)(PhC=O)\}_2Zn_2Cl_2]$, respectively, which are in good agreement with the composition as obtained from elemental analysis (C, H, N, Zn and Cl). In these complexes two molecules of partially hydrolyzed ligand are in association with two atoms of Zn(II). Based on the spectroscopic data it can be inferred that each molecule of partially hydrolyzed ligand coordinates in a tridentate fashion through benzoyl 'O', imine 'N' and phenolic 'O'; the latter bridges the two Zn(II) ions (leaving the 'Se' uncoordinated). Further, in view of the fact that the compounds are nonionic in nature, each metal atom is directly bonded to a chlorine atom thus, the Zn(II) adopts the square pyramidal geometry in the complex. A tentative structure of these complexes is depicted in Figure 2..

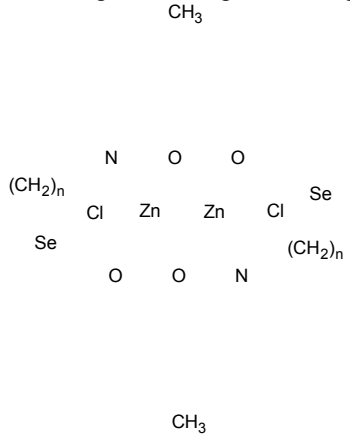

Figure 2. 1(n=2); 2(n=3)

4. Conclusion

The reactions of ligands $\mathbf{L_aH}$ and $\mathbf{L_bH}$ with $ZnCl_2$ led to the formation of bimetallic complexes **1**: $[\{C_6H_2(O)(4\text{-}CH_3)(PhC=NCH_2CH_2CH_2SePh)(PhC=O)\}_2Zn_2Cl_2]$ and **2**: $[\{C_6H_2(O)(4\text{-}CH_3)(PhC=NCH_2CH_2CH_2SePh)(PhC=O)\}_2 Zn_2Cl_2]$, with the loss of phenylselenato(alkyl)amine and HCl. The acid thus liberated probably catalyzes the hydrolysis of one arm of the ligand at the C=N position. Thus, each Zn atom adopts square pyramidal geometry with the O_3NCl coordination sphere.

Acknowledgements

We are thankful to Disha Institute of Management & Technology, Raipur, for providing the laboratory facilities. We are also grateful to DRDO, New Delhi for the financial assistance and for the award of fellowship to Ashish Asatkar We thank Prof. B.L. Khandelwal, DIMAT, Raipur for useful discussion, Prof. Sandeep Verma, IIT Kanpur for Mass spectra and Prof. S.K. Gupta, Giwaji University, Gwalior for IR spectra.

References

[1] M. Minoura, V.K. Landry, J.G. Melnick, K. Pang, L.Marchio` and G. Parkin, Chem. Commun. 2006, 3990–3992.
[2] S. Tripathi, S. Mishra, M. Nasim, B.L. Khandelwal, Phosphorus, Sulphur and Silicon and Related Elements, 180 (3&4) 2005, 1019-1034.
[3] M.D. Milton, J.D. Singh, B.L. Khandelwal, P. Kumar, T.P. Singh and R.J. Butcher, Phosphorus, Sulphur and Silicon, 172, 2001, 231-238.
[4] M.D. Milton, Sabana Khan, J.D. Singh, V. Mishra, B.L. Khandelwal, Tetrahedron, 46, 2005, 755-758.
[5] J.D. Singh, M.D. Milton, G. Bhalla, B.L. Khandelwal, S. Karthikeyan, P. Kumar, T.P. Singh and R.J. Butcher, Phosphorus, Sulphur and Silicon, 172, 2001, 223-230.
[6] S. Panda, H.B. Singh and R.J. Butcher, Chem. Commun., 2004, 322-323.
[7] N.J. Hill, W. Levason, R. Patel, G. Reid and M. Webster, Dalton Trans. , 2004, 980-981.
[8] J.S. Ritch, T. Chivers, M. Afzal and P. O'Brien, Chem. Soc. Rev., 36, 2007, 1622-1631.
[9] L.B. Kumbhare, V.K. Jain and B. Varghese, Inorg. Chem. Acta, 359 (2) 2006, 409-416.
[10] Dey, V.K. Jain, B. Varghese, T. Schurr, M. Niemeyer, W. Kaim and R. J. Butcher, Inorg. Chem. Acta, 359 (5) 2006, 1449-1457.
[11] S. Schulz, E.G. Gillan, J.L. Ross, L.M. Rogers, R.D. Rogers and A.R. Barron, Organnometallics, 15, 1996, 4880-4883.
[12] D. Selvakumar, S.K. Tripathi, R. Singh and M. Nasim, Chemistry Letters, 37 (1) 2008, 34-35.
[13] C.T. Chen, V.D. Pawar, Y.S. Munot, C.C. Chen and C.J. Hsu, Chem. Commun., 2483-2485, 2005.
[14] Lithium Batteries, ed. J. P. Gabane, Academic Press, London, 1983.
[15] B. Scrosati, Electrochim. Acta, 26 (11) 1981, 1559-1567.
[16] R. H. Friend and A. D. Yoffe, Adv. Phys., 1987, 361-94.
[17] M. Bochmann, Chemica Vapour Deposition, 2 (3) 1996, 85-96.
[18] L. Ren, H. Zhang, P. Tan, Y. Chen, Z. Zhang, Y. Chang, J. Xu, F. Yang and D. Yu, J. Phys. Chem. B., 108 (15) 2004, 4627-4630.
[19] M. Afzaal and P. O'Brien, J. Mater. Chem., 16, 2006, 1597-1602.
[20] O.C. Monteiro, T. Trindade, F.A. Almeida Paz, J. Klinowski, J. Waters and P. O'Brien, J. Mater. Chem., 13, 2003, 3006-3010.
[21] V. M. Pathak, K. D. Patel, R. J. Pathak and R. Srivastava, Sol. Energy Mater. Sol. Cells, 73, 2002, 117-123.
[22] M.S. Whittingham, J,D, Guo, R. Chen, T. Chirayll, G. Janauer and P. Zavalij, Solid State Ionics, 75, 1994, 297.
[23] Y. Zhu and X. Hu, Meter. Lett., 58, 2004, 1234-1236.
[24] S.T. Lakshmikvmar, Sol. Energy Mater. Sol. Cells, 32, 1994, 7-19.
[25] W.U. Huynh, J.J. Dittmer, A.P. Alivisators, Science, 295, 2002, 2425-2427.
[26] V.K. Verma, A.K. Asatkar, T.A. Jain, S.K. Tripathi, R. Singh, P.B. Hitchcock, S. Nigam, S.K. Gupta, Polyhedron 28, 2009, 2591–2598.
[27] W.L.F. Armarego, D.D. Perrin, Purification of Laboratory Chemicals, 4th edition, Pergamon Press, Oxford,1997.

Spectrophotometric Determination of Uranium with Thiocyanate

S.Ganesh
Indira Gandhi centre for Atomic Research
Kalpakkam – 603 102, India
Email: gans@igcar.gov.in

Fahmida Khan
Department of Chemistry,
National Institute of Technology,
Raipur, 492010, INDIA
E mail: fkhan.chy@nitrr.ac.in

Sonalika Agrawal
Department of Chemistry,
National Institute of Technology
Raipur, 492010, INDIA
E mail: sagrawal.chy@nitrr.ac.in

M.K Ahmed
Indira Gandhi centre for Atomic Research Kalpakkam – 603 102, India
Email: ahmed@igcar.gov.in

Shashi Krishna Pandey
National Institute of Technology
Raipur – 492010, India
Email: dir@nitrr.ac.in

Abstract

A simple spectrophotometric method is developed for the determination of low concentration of uranium in process samples. The method is based on the formation of complex with added ammonium thiocyanate in aqueous nitric acid or in presence of ethanol and ethyl acetate. Uranium and thiocyanate ions combine to give yellow colour due to formation of complex of uncertain composition. The intensity of yellow colour is proportional to the amount of uranium, the resulting yellow complex exhibits maximum absorption at 375 & 420 nms. The system obeys Lambert-Beer's law at 375 & 420 nm in the concentration range of 2 - 50 ppm & 100 – 500 ppm of uranium. Molar Absorptivity was determined to be 3.35 x10^3 L.mol^{-1}.cm^{-1} at 375 nm and 0.84 x 10^3 L.mol^{-1}.cm^{-1} at 420 nm. The results obtained are reproducible with standard deviation of 1% and relative error less than 2%. The results obtained by the developed procedure are in good agreement with those obtained by the standard procedure. The method is also applicable for the determination of low concentration of uranium in process control samples.

Keywords- Spectrophotometry, ammonium thiocyanate, molar absorbivity, calibration graph

Broad Area- Analytical Chemistry

1. Introduction

Spectrophotometric estimation involves the use of a calibration curve (generally linear) to estimate the concentration of an unknown. The characteristics of the calibration curve are determined by linear regression on the absorbance measurements of a finite number of standards. Accurate determination of uranium in trace level is important to evaluate the performance of various nuclear processes. Its determination in environmental samples is also important for reasons of safety. Numerous methods have been reported for determination of uranium in samples of various compositions. Spectrophotometric methods are widely used for trace analysis of uranium because of relative simplicity and better accuracy [1]. Many of the more sensitive chromogenic reagents such as dibenzomethane, PAR, oxime and arsenazo are nonselective, while thiocyanate and hydrogen peroxide, which are quite selective, are relatively insensitive [2]. The thiocyanate method as developed by Currah and Beamish [3] and other [4] has relatively high sensitivity and freedom from cation interferences. However, anion interferences have severely limited the applications of this method. Other spectrophotometric methods for uranium are required excellent separations of ions. The use of the thiocyanate acetone media has eliminated the majority of the anionic interferences of aqueous thiocyanate method, increased the sensitivity, increased the stability of the colour and mad the correct colour development independent of pH in the acid region [5-]. Hence the alcoholic ammonium thiocyanate method is well suited for the process control analysis of uranium. The molar extinction coefficient of about 3.35x 10^3 for 375nm and 0.84 x 10^3 for 420 nm made it possible to work with dilution factors high enough to give required reduction of the dilution. This method is applicable

for the micro quantities of uranium 0.1 to 5.0 mg of uranium in 25 ml.

1.1 Principle

The uranyl ions for a series of complexes of intense yellow colour with ammonium thiocyanate in aqueous nitric acid medium or in presence of ethanol and ethyl acetate. The complexes formed are as, follows: $[UO_2 (CNS)]^+$, $[UO_2 (CNS)_2]$, $[UO_2 (CNS)_3]^-$. The yellow colour is reproducible for analytical control process. The absorption of the complex increase rapidly with decreasing wavelength below 400 nm. Reagent also, absorb strongly below 360 nm. The stability of the complex is also extremely poor in aqueous medium. Non-linearity between concentration of uranium and the extinction of the complex at lower wavelengths warrants measurements of absorbance at wavelengths near 400 nm at the expense of sensitivity. Alcoholic medium eliminates majority of the anionic interferences encountered in the aqueous system. It increases the sensitivity and enhances the stability of the colour complex to more than 24 hours. It also makes the colour development independent of pH in the acid region. Addition of ethyl acetate to the alcoholic medium permits organic samples to be analyzed by the same procedure since organic is miscible in ethyl acetate. The maximum absorbiviity in the alcoholic medium is at 375 nm and 420 nm are chosen for absorbance measurement because of the tendency of ammonium thiocyanate to fluorescence at lower wavelengths.

2. Experimental

2.1 Instrumentation

The Beckman Model spectrophotometer is an accurate, easy to operate instrument specifically designed for rapid transmittance and absorbance measurements in the 320 – 1000 nm spectral range. All the absorbance measurements were recorded by placing the sample tube containing the solution.

2.2 Reagents

All reagents should be analytical grade.
1. Stannous chloride (10% w/v): Dissolve 10 g of hydrated stannous chloride in 10 ml of 11M hydrochloric acid and diluted to 100 ml with distilled water.
2. Ammonium Thiocyanate (50% w/v): Dissolve 50 g ammonium thiocyanate in distilled water, made up to 100 ml. Add 10 g of activated alumina to declourize, shake and allow to stand. Filter before use.
3. 2 M Hydrochloric acid
4. Ethyl acetate, reagent grade, Fisher Scientific
5. Acetone, reagent grade, Fisher Scientific
6. Aluminum nitrate: saturated $Al(NO_3)_3.9H_2O$ solution
7. Standard Uranium solution: Dissolve 0.1179 g of pure U_3O_8 in 25 ml of 8M nitric acid and dilute to 500 ml with water to give a solution, 1 ml contained 200 g Uranium. Standardize the solution by Davis Gray method [6].

2.3 Procedure

Weigh out from a polythene weight burette the required quantity of uranium into 25 ml standard flask. Add 2 ml of 2M hydrochloric acid. Add 10 drops (~ 0.1 ml) of stannous chloride solution. Pipette out 10 ml of the ammonium thiocyanate solution and made up to 25 ml flask and shake well before measuring absorbance at 375 nm and 420 nm. Prepare a blank in the same fashion but without uranium. Measure optical density against distilled water of the blank and standard and take the difference.

Range
1. 1 – 10 ppm of uranium – 5 cm cell –OD at 375nm
2. 10 -50 ppm of Uranium – 2 cm cell – OD at 375 nm
3. 50 -500 ppm of uranium – 1 cm cell – OD at 420 nm
4. 500 – 2000 ppm of uranium – 1 cm cell – OD at 460 nm

Note: Absorbance measured within 15 min of preparation of complex. Calculate the Uranium concentration of the unknown samples from the calibration graph.

If uranium samples containing interfering cations. The method consists of an extraction of the uranium into ethyl acetate. To an aliquote of no more than 2ml of uranium samples in an extraction vial, add 15 ml of saturated aluminum nitrate. Add 20 ml of ethyl acetate, shake for two minutes, and centrifuge to separate the phases. Pipette off 10 ml of the organic phase into another vial. Add 15 ml of 50% ammonium thiocyanate, 10% stannous chloride in acetone. Mix the solution and measure the colour against a blank prepared in the same manner without sample.

3. Result and Discussion

Figure 1. refers to a typical calibration graph obtained using Uranium with thiocyanate at 375 nm for the uranium standards in the concentration range of 2-12 ppm. The calibration graph is linear with a correlation coefficient of 0.099. By using this calibration graph, the concentrations of uranium present in the unknown samples were calculated.

Figure 2. refers to a typical calibration graph in the range of 5- 10 ppm (2cm path length) showing the accuracy for the determination of Uranium as thiocyanate. The graph obtained was linear with correlation coefficient of 0.00622.

Figure 3. refers to a typical calibration graph obtained using Uranium with thiocyanate at 420 nm for the uranium standards in the concentration range of 5-50 ppm using 1 cm path length. The calibration graph is linear with a correlation

coefficient of 0.062. By using this calibration graph, the concentrations of uranium present in the unknown samples were calculated.

Figure 4. refers to a typical calibration graph in the range of 500 -2000ppm (1cm path length) showing the accuracy for the determination of uranium with thiocyanate at 460nm. The graph obtained was linear with correlation coefficient of 0.015

Molar absorptivities determined at various wavelengths (375nm, 420nm & 460 nm) recorded in tables 1-4.

The interference of anions around 375 nm, which was not too serious when the thiocyanate was fresh but became large and rapid in forming as the thiocyanate solution aged. In aqueous solution reducing agents stronger than stannous chloride generally react more rapidly with the thiocyanate and cannot be used to remove the iron interferences. Fortunately, in acetone medium the attack of thiocyanate by the stannous chloride was greatly inhibited and its use is recommended. The major difficulties with the aqueous thiocyanate method are the rather poor colour stability and the large number of anion interferences. Thus, for the purpose of obtaining a medium which would eliminate the anion interference and yet retain the original sensitivity and freedom from the cation interference turned to a system of lower dielectric constant in which the ionization of the large majority of weakly acidic anions is greatly suppressed. The use of the thiocyanate acetone media has eliminated the majority of the anionic interferences of aqueous thiocyanate method. The ammonium or sodium salt of thiocyanate is recommended over the potassium salt, as these salts caused no insoluble salt formation at the high acetone water ratios used in the procedure [7]. Typical results obtained by using this methodology and instrumentation for the determination of uranium in process samples generated results are reported in Table 5. The results obtained are reproducible with standard deviation 1% and relative error less than 2%.

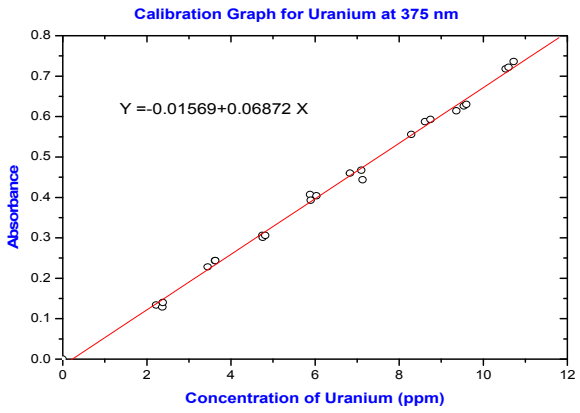

Figure 1. Calibration graph for Uranium with thiocyanate at 375 nm - Concentration of Uranium (VI) 2 ppm – 12 ppm

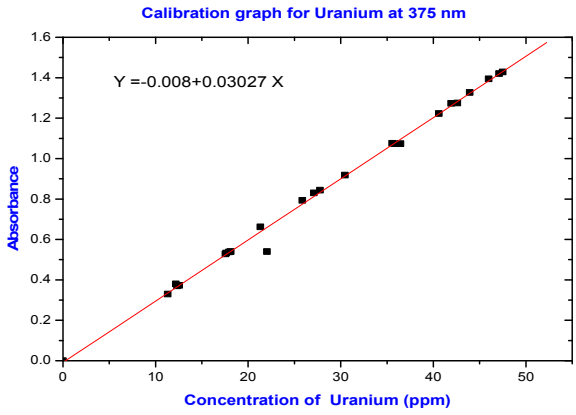

Figure 2. Calibration graph for Uranium with thiocyanate at 375 nm - Concentration of Uranium (VI) 10 ppm – 50 ppm

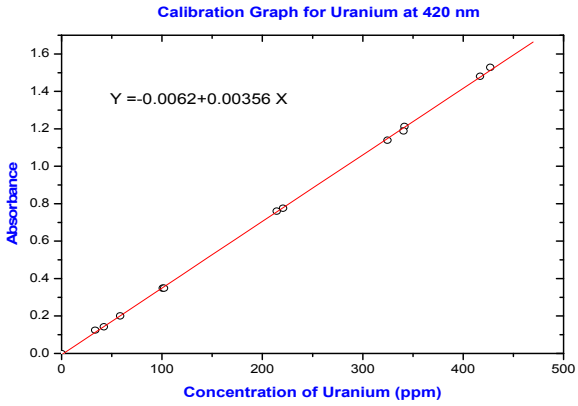

Figure 3. Calibration graph for Uranium with thiocyanate at 420 nm - Concentration of Uranium (VI) 50 ppm – 500 ppm

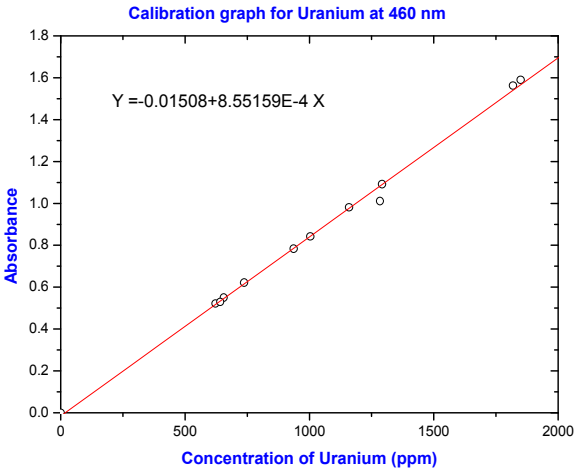

Figure 4. Calibration graph for Uranium with thiocyanate at 420 nm - Concentration of Uranium (VI) 500 ppm – 5000 ppm

Table.1 Molar absorption coefficient determined for U (IV) at 375 nm (path length 5 cm)

S. No	Conc of U(VI) (g/ml)	Absor bance	Specific Absorbance	Molar Absorptivity ($L.Mol^{-1}.cm^{-1}$)
1	0.00237	0.134	11.308	2691.304
2	0.00222	0.129	11.622	2766.036
3	0.00238	0.140	11.765	2800.070
4	0.00345	0.228	13.392	3187.296
5	0.00362	0.244	13.466	3204.908
6	0.00475	0.306	12.884	3066.392
7	0.00476	0.301	12.647	3009.986
8	0.00588	0.393	13.367	3181.346
9	0.00603	0.404	13.392	3187.296
10	0.00713	0.443	12.426	2957.388
11	0.00683	0.460	13.470	3205.860
12	0.00861	0.587	13.635	3245.130
13	0.00875	0.593	13.553	3225.610
14	0.00829	0.564	13.605	3237.990
15	0.00936	0.614	13.120	3122.560
16	0.00960	0.630	13.125	3123.750
17	0.01604	0.722	13.618	3241.084
18	0.01727	0.736	13.722	3265.836
Average				3095.547

Table.2 Molar absorption coefficient determined for U (IV) at 375 nm (path length 2 cm)

S.No	Conc of U(VI) (g/ml)	Absor bance	Specific Absorbance	Molar Absorptivity ($L.Mol^{-1}.cm^{-1}$)
1	0.0113	0.330	14.576	3469.088
2	0.0123	0.387	15.706	3738.028
3	0.0125	0.373	14.860	3536.680
4	0.0122	0.370	15.164	3609.032
5	0.0176	0.533	15.099	3593.562
6	0.0179	0.538	14.982	3565.716
7	0.0181	0.540	14.892	3544.296
8	0.0220	0.662	15.025	3575.950
9	0.0213	0.642	15.050	3581.900
10	0.0225	0.676	15.070	3586.660
11	0.0278	0.642	15.049	3581.662
12	0.0271	0.834	15.022	3575.236
13	0.0346	0.918	15.069	3586.422
14	0.0356	1.075	15.318	3645.684
15	0.0364	1.100	15.089	3591.182
16	0.0406	1.223	15.065	3585.470
17	0.0419	1.273	15.176	3611.888
18	0.0426	1.275	14.968	3562.384
19	0.0439	1.327	15.104	3594.752
20	0.0460	1.394	15.155	3606.890
21	0.0471	1.420	15.068	3586.184
22	0.0475	1.428	15.031	3577.378
Average				3586.638

Table 3. Molar absorption coefficient determined for U (IV) at 420 nm (path length 1 cm)

S.No	Conc of U(VI) (g/L)	Absor bance	Specific Absorbance (Abs/ g/L)	Molar Absorptivity (L.Mol-1.cm-1)
1	0.0335	0.124	3.70	881.31
2	0.0313	0.112	3.58	852.04
3	0.0422	0.145	3.44	818.72
4	0.0583	0.200	3.43	815.86
5	0.1009	0.348	3.45	821.10
6	0.1021	0.348	3.41	811.58
7	0.2206	0.776	3.52	837.76
8	0.2143	0.760	3.55	844.90
9	0.3245	1.139	3.51	835.38
10	0.3451	1.212	3.55	844.90
11	0.3274	1.168	3.57	848.95
12	0.3406	1.188	3.49	830.62
13	0.4170	1.480	3.55	844.90
14	0.4269	1.528	3.58	852.04
Average				838.58

Table.4 Molar absorption coefficient determined for U (IV) at 460 nm (path length 1 cm)

S.No	Conc of U(VI) (g/L)	Absorba nce	Specific Absorbance	Molar Absorptivity ($L.Mol^{-1}.cm^{-1}$)
1	0.6225	0.521	0.8368	199.1584
2	0.6417	0.530	0.8259	196.5642
3	0.6558	0.550	0.8387	199.6106
4	0.7377	0.622	0.8432	200.6816
5	0.9364	0.783	0.8361	198.9918
6	1.0042	0.842	0.8385	199.563
7	1.1592	0.981	0.8627	205.3226
8	1.2839	1.102	0.8627	205.3226
9	1.2925	1.092	0.8448	201.0624
10	1.8189	1.562	0.8587	204.3706
11	1.8498	1.590	0.8596	204.5848
Average				201.3848

Table.5 Typical results obtained from process samples using this present method

S.No	Absorbance	Conc of U(VI) (g/mL)
1	0.718	0.0154
2	0.244	0.0036
3	0.528	0.0175
4	0.626	0.010
5	0.306	0.0048
6	1.074	0.0358
7	0.528	0.0259
8	0.677	0.0225

9	1.079	0.0352
10	0.467	0.0071
11	0.407	0.0059

Acknowledgment

Authors wish to express their sincere thanks to Dr. Baldev Raj, Director, IGCAR for motivating them to excel. The authors are also thankful to Shri. R. Natarajan, Director, RpG, Dr. U. Kamachi Mudali, Head, RR&DD, Shri. M.Venkataraman, Head, RPOD, Shri. R.V.Subba Rao for the encouragement provided during the course of this work. The authors are also thankful to Smt.R.Geetha for her guidance and help in preparation of manuscript.

References

[1] A. Suresh, D. K. Patre, T. G. Srinivasan and P. R. Vasudeva Rao, Spectrochemica Acta, Part A 58 , 341 (2002)

[2] E. B. Sandell, "Colorimetric metal analysis", 3rd ed. Interscience, New York, 1959

[3] J. E. Currah and F. E. Beamish, "Colorimetric Determination of Uranium with Thiocyanate," Anal.Chem. 19, 8, 609 (1947).

[4] C. E. Crouthamel and C. E. Johnson, ANL – 4750, 1952 and Anal.Chem. 24, 1780 (1952)

[5] T. M. Florence and Y. Farrar, Anal. Chem, 11, 35, 1952 pp 1613

[6] C. J. Rodden, "Analytical chemistry of the Manhattan Project", New York, McGraw-Hill Book Co., 1950

[7] H. P. Tucker., "The Absorptiometric Determination of Uranium in Solution by an improved Thiocyanate Method," Analyst, 82,976,529(1957).

[8] M. A. De Sesa and O. A. Nietzel, "Spectrophotometric Determination of Uranium with Thiocyanate." U. S. Atomic Energy Comm. Rpts, 1954, ACCO-54, 194 .

[9] O. A. Nietzel and M. A. De Sesa, "Spectrophotometric Determination of Uranium with Thiocyanate in Butyl Cellosolve-isobutyl Methyl Ketone-water Medium", Anal.Chem., 29(5), 756(1957)

[10] M. Gerhold and F. Hecht, "Photometric Determination of Small Quantities of Uranium with Potassium Thiocyanate. Microchemie Ver. Mikrochim. Acta, 37, 1100(1951).

[11] A. Madhusudan and R. K. Iyer, "Determination of low concentrations by spectrophotometry; Uranium-thiocyanate system", Proc. Indian Acad. Sci(Chem.Sci) Vol.101, 3 (1989) pp 227

[12] K. S. Koppikar, V. G. Korgaonkar, T. K. S. Murthy, " Spectrophotometric Determination of Uranium Application of The Method to the Analysis of leach Solutions and Monazite. Anal. Chim. Acta, 20, 366 (1959).

[13] S. Vladan, Jovanovic and Eva F. Zucker., "Colorimetric Determination of Uranium with Ammonium Thiocyanate. Bull. Inst. Nuclear Sci. "Boris Kidrich", 4, 111--18 (1954) , in English.

[14] H. I. Feinstein, "Spectrophotometric Determination of Uranium in Ores. U. S. Atomic Energy Comm., Rep., TEL--555, 1955, 16 pp.

[15] J. Clinch and M. J. Guy, The Extraction and Absorption Spectrometric Determination of Uranium as Thiocyanate. Analyst, 82, 800 (1957).

[16] P. N. Paley, USSR, "Determination of Small Quantities of Uranium in Ores. Proceedings of The International Conference on the Peaceful Uses of Atomic Energy, Vol. 8 . 225 (1956).

[17] I. M. Kolthoff and P. J. Elving, "Treatise on analytical Chemistry" Part II, Vol.9, pp 74 (1962).

[18] R. M. Dyck and D. G. Boase, "Fuel Reprocessing with tertiary amine extractants – Part 2: A manual of analytical methods", AECL – 4214, pp31-32

Hardness Studies of Magnetron Co-sputtered Coated Nano-scale Multilayered Structure of TiAlN films

Dilip Kumar Sahu
Department of Physics
Parthivi College of Engg. & Management
Bhilai-3, 490021, C.G, India
E–mail: dilip.physics@gmail.com

Sadhana Agrawal
Department of Physics
National Institute of Technology
Raipur 491001, C.G, India
E–mail: agrawaldrs@rediffmail.com

Janita Saji
Department of Physics
National Institute of Technology
Raipur 491001, C.G, India
E–mail: janita.saji@rediffmail.com

Abstract

For engineering applications of thin films, appropriate combination of high hardness with other properties. $Ti_{1-x}Al_xN$ films were synthesized by reactive magnetron co–sputtering with different aluminum compositions which appear to be appropriate for engineering applications. XRD, SIMS, Nanoindentation techniques were used to analyze these films. The as-deposited films were found to be crystalline for Al concentrations of 35, 40, 55 and 64% and became amorphous at 81%. The nanoindentation hardness increases with increase in concentration of Al up to 64% and starts decreasing beyond 81%. Continuous Multi-Cycle indentation technique is used to analyze the failure mode of the film with highest hardness.

Keywords- Magnetron sputtering; Profilometry; Secondary ion mass spectroscopy (SIMS); Nano-indentation.

Broad Area- Nanotechnology.

Sub-Area- Hardness of thin films.

1. Introduction

Coating materials that should withstand cyclic loading during high speed cutting without failure are required for high performance of protective thin films for wear and tribological applications [1].Several transition metal nitride films, especially TiN is an important material for protective coatings and several other functional applications [2, 3]. However for wear protection, now-a-days metastable solid solution phase based on $Ti_{1-x}Al_xN$ with cubic structure is preferred due to its oxidation resistance and higher hardness [4-7]. The high hardness of these films is due to the compressive stress in the film by the substitution of smaller atomic radius Al in the place of Ti. High temperature oxidation resistance of these films increase with Al concentration, as it arises from protective and dense Al_2O_3 scale on surface [8].

$Ti_{1-x}Al_xN$ is a metastable solid solution and can be synthesized through Physical Vapor Deposition (PVD) techniques. There are many reports about different ways of preparation, such as sputtering [8-11], cathodic arc evaporation [7, 12], Chemical Vapor Deposition (CVD) [13, 14] and Pulsed Laser Deposition (PLD) [15]. Amongst these, reactive magnetron co-sputtering is an important method to prepare $Ti_{1-x}Al_xN$ films because of ease of control on concentration of titanium, aluminum and nitrogen [10, 11].

The cyclic nanoindentation tests have been carried out for phase transformation studies on the thin films and confirmed by Raman microspectroscopy [16]. These tests can be used to study the buckling, delamination of the film and the interfacial strength between the film and the substrate [17]. In this paper, we are reporting the reactive magnetron co-sputtering deposition of $Ti_{1-x}Al_xN$ films with different Al concentrations and their nanomechanical properties with the help of a Continuous Multi-Cycle (CMC) loading indentation.

2. Experimental Procedure

$Ti_{1-x}Al_xN$ films were deposited on SS 304 LN (10 mm × 10mm) substrate by reactive magnetron co-sputtering technique, using MECA 2000 (France) sputtering system. Prior to deposition, the substrates were cleaned in-situ by

Ar^+ ion bombardment. The targets were also sputter cleaned before deposition. The base pressure of the chamber was 1×10^{-6} mbar. The target to substrate distance was maintained at 100 mm. A constant pressure of 1×10^{-2} mbar and substrate temperature of 773 K was maintained through out the deposition process. The total gas pressure of Ar to N_2 was kept constant as 3:1 for all coatings. By varying the power of both targets, $Ti_{1-x}Al_xN$ films having different Ti/Al ratio were synthesized. With these conditions 1.4 μm thick films were prepared. The parameters for the synthesis of $Ti_{1-x}Al_xN$ films by reactive processing and their corresponding Al percentage was obtained from EPMA. These are given in Table I.

Table 1. Target power & their corresponding Al concentrations

S. No	Al target DC Power (W)	Ti target RF Power (W)	Al %
1	120	300	35
2	150	300	40
3	180	300	55
4	200	200	64
5	180	100	81

Identification of crystalline phases and the corresponding crystal structure were carried out by a STOE diffractometer in the Glancing Incidence X-ray Diffraction (GIXRD) mode at a glancing angle of 1º. Compositional homogeneity with respect to depth was studied by Secondary Ion Mass Spectrometry (SIMS) using IMS 4F (Cameca, France) instrument. The depth profiles up to the substrate interface were obtained using Cs^+ primary ions. The depth calibration of the SIMS profile was achieved by measuring the crater depth using a Dektak 6M (VEECO, US) surface profiler.

The depth dependant hardness studies were carried out using nanoindentation system (CSM open platform, Switzerland) using a Berkovich diamond indenter. The hardness values were obtained from load displacement curve with the help of Oliver and Pharr technique [18]. We have used Continuous Multi-Cycle (CMC) mode with a load range of 10 to 100 mN, 200 mN and 300 mN with a progressive load increment of 10 mN. The unloading was allowed up to 5% of the corresponding applied load. Time period of loading and unloading was maintained at 60 sec each.

3. Results and Discussion

Figure1. shows the normalized GIXRD profiles of as deposited $Ti_{1-x}Al_xN$ films with different Al concentrations. The reactions were completed in every case and the XRD profile shows peaks only corresponding to TiN with peak shift and broadening. With lower Al concentration, $Ti_{1-x}Al_xN$ films were formed with single phase NaCl structure and these are highly oriented (200). The increase in Al concentration increases the width of the peaks corresponding to the $Ti_{1-x}Al_xN$ (200) with a shift towards higher angle (2θ). At 55% Al content, a peak for (111) has formed, whereas at either side of the Al concentrations this peak disappears. These films become amorphous when the Al concentration exceeded 81%, this can be understood from the XRD profile.

The grain size was calculated from the FWHM of the (200) peak using Debye Scherrer formula .The grain size of the films decrease with the increase in Al concentration and these ultimately become amorphous. The change in the roughness of the films is very small with the increase in Al concentration. The decrease in the grain size with the Al content during deposition can be explained by the following reasons: (a) the addition of Al to TiN may change the surface diffusion behavior of Ti and N atoms and (b) the grains of disordered or amorphous AlN prevents the growth of TiN phase [11]. When Al concentration varies above 64% to below 81 % films were formed two phases with the cubic B1 structure and the hexagonal B4 structure were detected.

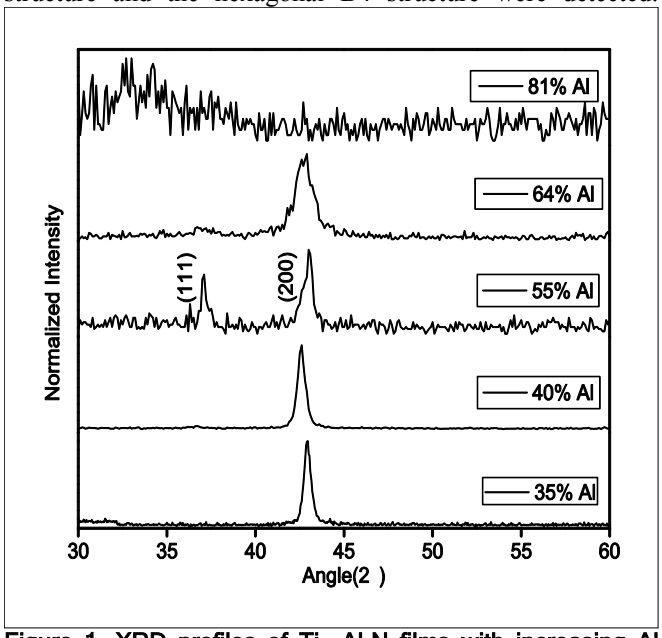

Figure 1. XRD profiles of $Ti_{1-x}Al_xN$ films with increasing Al concentrations.

For Al concentration varies above 81 % of $Ti_{1-x}Al_xN$ films were formed only a single phase with the hexagonal B4 structure was observed so these reasons we have study only the Al concentration in 64% and 81% of $Ti_{1-x}Al_xN$ in this paper.

For clarity and being concise, we have discussed the SIMS profile of $Ti_{1-x}Al_xN$ film with 64% Al alone and it is shown in the Figure 2. SIMS intensity of an element depends on its concentration, isotopic abundance and its relative sensitivity factor. Hence the absolute conversion of SIMS intensity to its concentration is difficult. The relative isotopic abundances for ^{27}Al and ^{46} Ti are 100% and 8% respectively. The concentrations of Al, Ti and N in the film throughout the thickness are uniform. The concentration of nitrogen is found to be proportional to the titanium to aluminum ratio. This is an indirect measure of stoichiometry of films that remains constant throughout the depth. The outer most layer

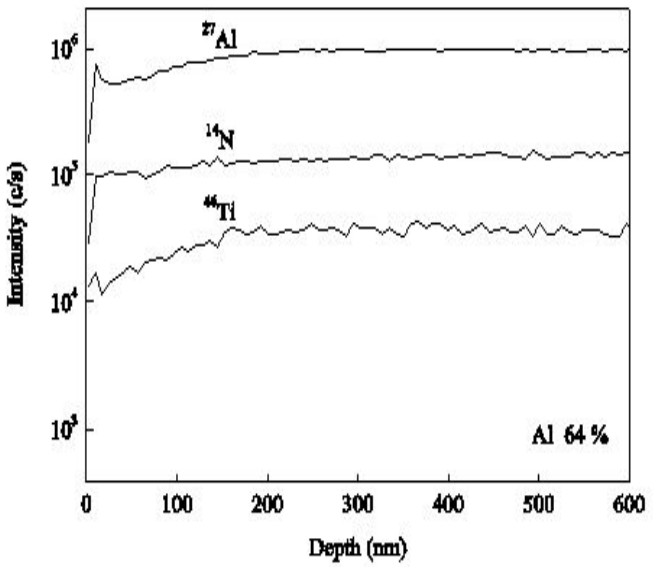

Figure 2. SIMS profile of Ti1-xAlxN films with 64% Al.

intensities are affected by contamination and non steady state sputtering. It has been found that the total metal (Al + Ti) to nitrogen ratio remains almost constant for all the samples of $Ti_{1-x}Al_xN$.

The measured values of nanoindentation hardness of $Ti_{1-x}Al_xN$ films at the surface are mentioned in Table. II. Nano hardness of the films increase with the increase of Al content up to 64% and then decreases beyond 81% of Al. Cubic NaCl structured $Ti_{1-x}Al_xN$ with 64% Al exhibited highest hardness of 37 GPa whereas one with 81% had the hardness of 12 GPa. This value is almost similar to the bulk AlN. The compressive stress occurring from substitution of small aluminum atoms by titanium and the subsequent reduction in the grain size contributed to the increase in the hardness.

In CMC mode, the specimen is loaded to a specific value, then unloaded and immediately reloaded at the same place; a cyclic nanoindentation curve is generated. The unloading and reloading paths do not overlap necessarily in all materials.

Therefore, sensitive dislocation-microstructure interactions may be detectable in the unloading-reloading curves during cyclic indentation. We have selected the hardest film (64% Al) for CMC studies to understand the crack formation and the interfacial strength existing between film and the substrate. CMC tests carried out on the substrate and $Ti_{1-x}Al_xN$ film are shown in Figure3 (a) and 3(b) respectively.

Table 2. Grain size and hardness of thin films with different Al concentrations

Al concentration (%)	Grain size (nm)	Indentation Hardness (GPa)
35	37	16.5
40	25	21.5
55	18	25
64	8	37
81	-	12

The hardness of the substrate does not vary with the increase in progressive load. The surface preparation technique followed for the substrate has increased the surface hardness minimally. The slope of the unloading curve remains same. This is an indication of constant modulus which is less susceptible to variation.

4. Conclusions

$Ti_{1-x}Al_xN$ films with increasing Al concentration have been deposited on SS substrates by reactive magnetron processing. 64% Al films exhibited a higher indentation hardness of 37 GPa compared to other compositions.

Nanoindentation hardness increases with the increase of Al percentage and decreases beyond 81% of Al, where the film becomes amorphous. Amorphous nature of this TiAlN film is due to the disassociation of single phase compound to two

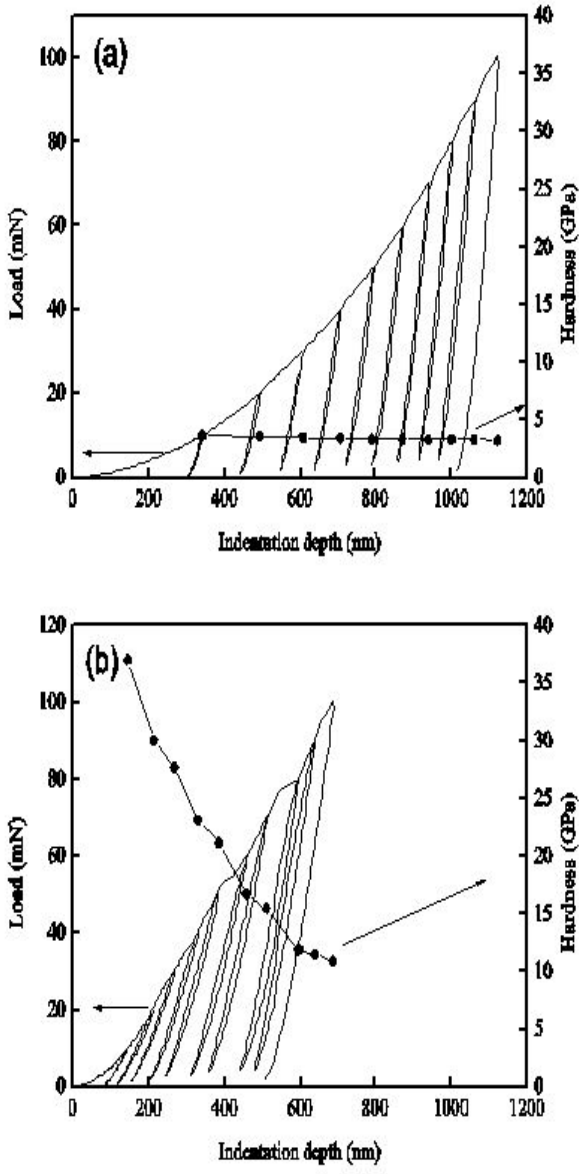

Figure 3. CMC loading and unloading profiles of (a) substrate SS-304LN and (b) the Ti1-xAlxN film with 64% Al.

structurally separate phases ie AlN and TiN. Grain size and roughness of these films support the increase in the hardness value. CMC loading clearly brought out the strain hardening effect. This along with the contribution from substrate effect influences hardness of the film. The hardness properties of the TiAlN coating make it suitable for high temperature cutting operations with minimum use of lubricant or dry machining.

Acknowledgements

Authors thank Indira Gandhi Center for Atomic Research, Kalpakkam for support during this work. The authors acknowledge Dr. Sitaram Dash for sustained encouragement.

References

[1] Y.Tanaka, N. Ichimiya, Y. Onishi and Y. Yamada, "Structure and properties of Al-Ti-Si-N coating prepared by the cathodic arc ion plating method for high speed cutting applications, "Surf. Coat. Technol., 146-147 215-221 (2001).

[2] C–H Ma, J–H. Hung and Haydn Chen, "Nanohardness of nanocrystalline TiN thin films," Surf. Coat. Technol., 200 3868-3875 (2006).

[3] I. Iliuc, "Wear and micropitting of steel ball sliding against TiN coated steel plate in dry and lubricated conditions," Tribol. Int., 39 607-615 (2006).

[4] F. Esaka, K. Furuya, H. Shimada, M. Imamura, N. Matsubayashi, T. Sato, A. Nishijima, T. Kikuchi, A. Kawana and H. Ichimura, "Depth profiling of surface oxidized TiAlN film by synchrotron radiation excited X – ray photoelectron spectroscopy," Surf. Sci., 377 – 379 197-200 (1997).

[5] Paul H Mayrhofer, Christian Mitterer, Lars Hultman and Helmut Clemens, "Microstructural design of hard coatings," Progress. Mater. Sci., 51 1032-1114 (2006).

[6] A. Horling, L. Hultman, M. Oden, J. Sjolen and L. Karlsson, "Mechanical properties and machining performance of $Ti_{1-x}Al_xN$ coated cutting tools," Surf. Coat. Technol., 191 384-392 (2005) .

[7] Mayrhofer PH, Horling A, Larlsson L, Sjolen J, Mitterer C and Hultman L, "Self-organized nanostructures in the Ti-Al-N system," Appl. Phys. Lett., 83 2049 -2051 (2003).

[8] P.W. Shum, K.Y. Li, Z. F. Zhou and Y.G. Shen, "Structural and mechanical properties of titanium-aluminum-nitride films deposited by reactive close-field unbalanced magnetron sputtering," Surf. Coat. Technol., 185 245-253 (2004).

[9] M. Beckers, N. Schell, R.M.S. Martins, A. Mucklich, W. Moller and L. H ultman, "Nucleation and growth of Ti_2AlN thin films deposited by reactive magnetron sputtering onto MgO(111)," J. Appl. Phys., 102 74916 (2007).

[10] M. Beckers, N. Schell, R.M.S. Martins, A. Mucklich and W. Moller, "In Situ x-ray diffraction studies concerning the influence of Al concentration on the texture development during sputter deposition of Ti-Al-N thin films," J. Vac. Sci. Technol. A, 23[5] 1384-1390 (2005).

[11] Liu, P.W. Shum, K.Y. Li and Y.G. Shen, "Roughing kinetics of reactively sputter-deposited Ti-Al-N films on Si(100)," Phil. Mag. Lett., 83 [10] 627-634 (2003).

[12] J. Bujak, J. Walkowicz and J. Kusinski, "Influence of the nitrogen pressure on the structure and properties of (Ti,Al)N coatings deposited by cathodic vacuum arc PVD process," Surf. Coat. Technol., 180 – 181 150 -157 (2004).

[13] J. Shieh and M. H. Hon, "Nanostructure and hardness of titanium aluminum nitride prepared by plasma enhanced chemical vapor deposition," Thin Solid Films, 391 101-108 (2001).

[14] S. Menzel, Th. Gobel, K. Bartsch and K. Wetzig,"Phase transitions in PACVD-(Ti,Al)N coatings after annealing," Surf. Coat. Technol., 124 190-195 (2000).

[15] S. Acquaviva, E. Danna, L. Elia, M. Femandez, G. Leggieri, A. Luches, M. Martino, P. Mengucci and A. Zocco, "Characterization of TiAlN films deposited by reactive pulsed laser abalation," Thin solid films, 379 45-49 (2000).

[16] Yury G. Gogotsi, Vladislav Domnich, Sergi N. Dub, Andreas Kailer and Klaus G. Nickel, "Cyclic nanoindentation and Raman microspectroscopy study of phase transformations in semiconductors," J. Mater. Res., 15 [4] 871 – 879 (2000).

[17] P. Bruno, G. Cicala, A. M. Losacco and P. Decuzzi, "Mechanical properties of PECVD hydrogenated amorphous carbon coatings via nanoindentation and nanoscratching techniques," Surface Coatating Technology, 180 – 181 259 – 264 (2004).

[18] W. C. Oliver and G. M. Pharr, "An improved technique for determining hardness and elastic modulus using load and displacement sensing indentation experiments," J. Mater. Res, 7 [6] 1564 – 1583 (1992).

Photoluminescence of ZnS And ZnS: Mn Nanoparticles

Ravi Sharma
Arts & Commerce Girls College Devendranagar,
Raipur,(C.G.) 492001
Email – rvsharma65@gmail.com

B.G. Sharma
Department of Physics and Computer science,
Govt.Science College
Raipur 492010

D.P. Bisen
School of studies in Physics and Astrophysics,
Pt. Ravishankar Shukla University, Raipur, (C.G.) 492010

Abstract

The present paper reports the synthesis and characterization of ZnS and ZnS:Mn nanoparticles. Nanoparticles of ZnS and ZnS:Mn were prepared by chemical precipitation method using the solution of zinc chloride, sodium sulphide, manganese chloride. Mercaptoethanol was used as the capping agent. The particle sizes of such nanoparticles were measured by XRD analysis and it is found that the average particle size is of few nm. For Zns nanoparticles only one peak was found whereas two peaks were obtained in the photoluminescence spectra of ZnS:Mn nanoparticles. The dominant peak lies at 598nm and the low intensity peak lies at 423nm. The XRD pattern indicated the growth of the nanoparticles.

Keywords- Nanophosphor; XRD, Photoluminescence, ZnS, ZnS:Mn

Broad Area- Applied Physics

1. Introduction

Semiconductor nanophosphors are described as a state of matter that is intermediate between individual molecule and bulk. Transition from bulk to nanoparticles lead to the display of quantum mechanical properties and an increased dominance of surface atoms which increases the chemical reactivity of a material. Semiconducting nanocrystalline materials have attracted tremendous attention in electronics and photonics [1–3]. Of the various types of semiconductor nanostructures, zinc sulfide nanoparticles have been extensively studied because of their size or shape dependent electronic and optical characteristics [2, 4–10], which follow quantum confinement effects. Such nanomaterials have been applied to light emitting diodes [11], photovoltaic devices [12], lasers and sensors [13], phosphors in displays and also in biomedical applications for biological labeling [14], diagnostics [15]. Apart from tuning their properties by size and shape, chemical strategies have been developed such as

doping ZnS nanoparticles with manganese or copper. For the effective preparation of high quality ZnS nanoparticles, a number of methods have been reported, such as solgel, precipitation, electrochemical deposition, and microemulsion [6, 12, 16]. They provide nanophosphors with well defined particle size distribution but often require expensive precursors and large volumes of solvent. The incorporation of impurities by capping agents and low production rate limit the large scale application at an industrial level.

Luminescence measurements were identified as one of the most important techniques to reveal the energy structure and surface states of these particles. Localized trap states inside the band gap were studied in detail to recognize the sub-band gap energy levels. It was found that the defect levels play an important role in determining the luminescence characteristics of the ZnS nanoparticles. Numerous researchers have investigated the structural and luminescent properties of doped phosphor nanoparticles, especially $Mn2^{+}$ doped ZnS nanocrystals, as ZnS can be doped with Mn very easily. This doping causes a visible orange luminescence at about 585 nm. It is well known that ZnS doped with Mn exhibits attractive light-emitting properties with increased optically active sites for applications as efficient phosphors [17]. These nanomaterials behave differently from bulk semiconductors as they are influenced by various surface states arising due to quantum confinement effect and large surface-to-volume ratio.

ZnS is semiconducting materials, which has a wide band gap of 3.68eV. It is a very attractive material for optical application especially in nanocrystalline form. ZnS can have two different crystal structures (zinc blende and wurtzite), both of which have the same band gap energy (3.68 eV) and the direct band structure. ZnS has been used for the cathode ray tube, the field emission display, and the scintillator as one of the most frequently used phosphors.

In this work zinc sulfide nanophosphors were prepared by chemical precipitation technique and mercaptoethanol has been used for capping, which modifies surface of nanoparticles and prevents the growth of the particles to larger size. The effect of concentration of mercaptoethenol on the particle size, effect of changes in Mn concentrations on the photoluminescence spectra and on the particle size has been investigated.

2. Experimental

There are various methods supported for synthesis of nanoparticles. In the present investigation chemical deposition technique described by Khosravi is used to synthesize the powder of ZnS nanoparticles [18]. For synthesis, the 1M aqueous solution of $ZnCl_2$ and 1M aqueous solution of Na_2S were mixed in the presence of various concentration of mercaptoethanol (C_2H_5OSH) solution. $MnCl_2$ was also mixed in the solution in ratio 99:1, while stirring the solution continuously, so that solutions are properly mixed. The obtained precipitate was washed thoroughly three to four times in double distilled water and then separated by centrifuge at 3500 rpm, and finally air dried. Different samples of ZnS:Mn were prepared with different Mn concentrations. The sample which is reported here has 10 weight %. Special care was taken to maintain the same physical condition during the synthesis of the sample.

All the samples were characterized at Inter University Consortium (IUC) Indore The morphologies and sizes of the mercaptoethanol capped ZnS:Mn were determined by X-ray diffraction studies with Cu Kα radiation (λ=1.5418 Å). XRD data were collected over the range 20^0-70^0 at room temperature. X-ray diffraction patterns have been obtained by Rigaku Rotating Anode (H-3R) diffractometer. The particle size was calculated using the Debye-Scherrer formula.

The Photoluminescence measurements were carried out by a Shimadzu RF 5301PC Spectroflurophotometer. Xenon arc lamp was used as a excitation source and the detector (PM tube RCA931) has a flat response from 240-1000 nm.

3. Results and Discussion

The XRD patterns for the samples are shown in Figure 1.Three different peaks are obtained at 2θ values of 29.50^0, 48.80^0 and 57.80^0. This shows that the samples have zinc blende structure. The XRD peaks correspond to Bragg diffraction was at (111), (220) and (311) planes for cubic ZnS. Due to size effect, the XRD peak tends to broaden. The broadening of peaks indicates nanocrystalline behavior of the particles. The width of the peak increases as the size of the particle decreases. The size of the particles has been computed from the width of first peak using Debye Scherrer formula [19]. The particle sizes of the ZnS samples were found to be 5-7 nm.

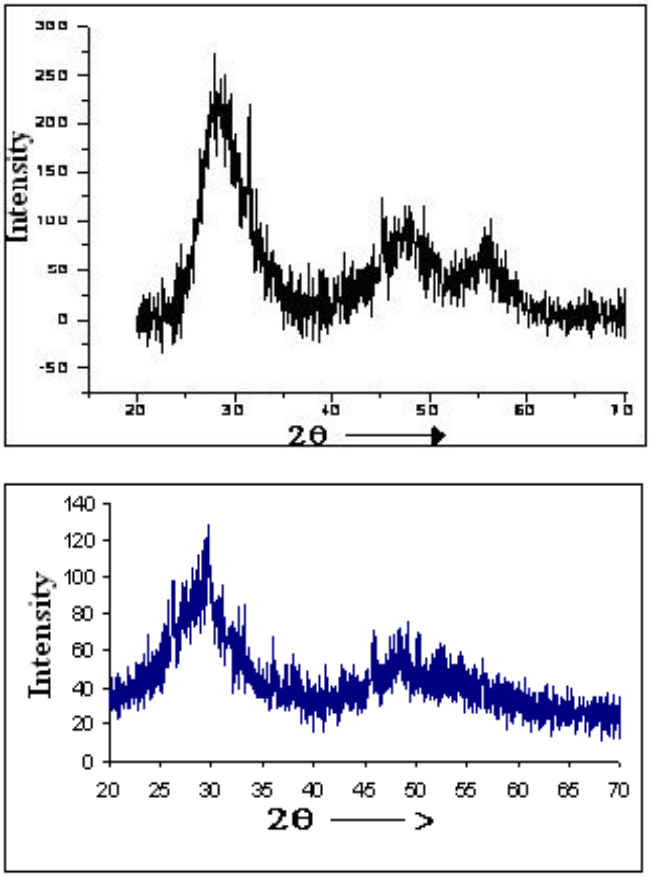

Figure 1 XRD pattern of ZnS and ZnS:Mn nanoparticles.

The XRD spectra of the ZnS:Mn nanoparticles shows that the presence of Mn increases the broadening of the second peak. For Zns:Mn nanoparticles the second and the third peak corresponding to (220) and (311) planes merge into one peak at $2\Theta = 50.80^0$. The broadning of the peak in Mn doped samples are indicative of small crystalline size. The particle size of the sample of Zns:Mn were observed between 3-5 nm.

ZnS has a direct bandgap of 3.67 eV with an effective energy band at wavelength 334 nm at room temperature. On doping zinc sulfide with manganese, the Mn^{2+} ions substitute the Zn^{2+} ions in the ZnS crystal acting as trap sites, where the electrons and holes can be trapped. An electron can undergo photo-excitation process in the host ZnS lattice of nanoparticles and subsequently decay via a nonradiative transition to the $^4T_1$ level to the $^6A_1$ level. The strong emission could be attributed to the radiative decay between these localized states of manganese inside the ZnS bandgap. Figure 2 shows the typical room-temperature PL

spectra from the ZnS nanoparticles and ZnS nanoparticles doped with Mn. The PL emission at around 423 nm is typical luminescence of undoped ZnS resulting from the transition

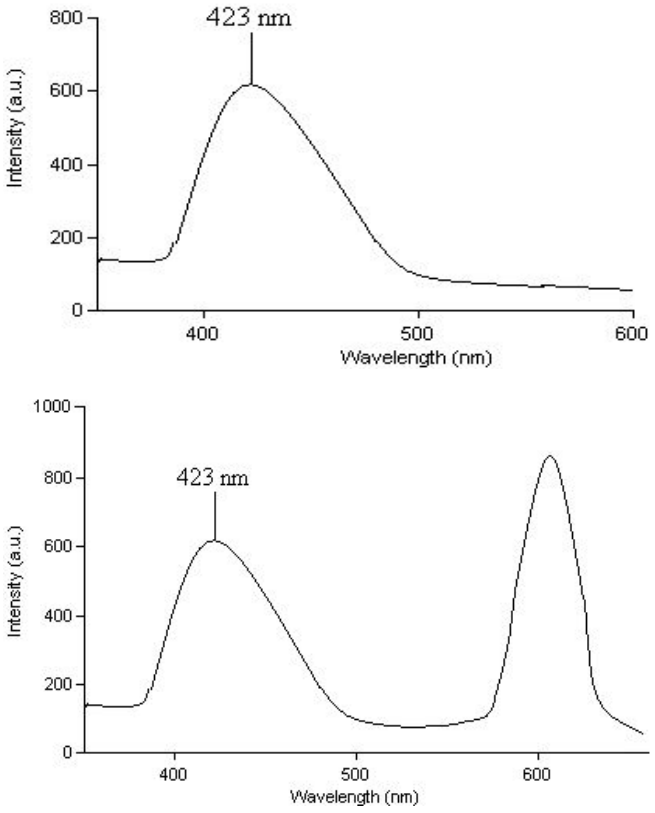

Figure 2. The PL spectra of ZnS and ZnS:Mn nanoparticles

of electrons from shallow traps near the conduction band to sulfur vacancies present near the valence band. This peak occurs because of the self- trapping hole centres in ZnS The PL spectrum of ZnS:Mn has two peaks, one peak at 423 nm and second at 598 nm.. The peak wavelength of ZnS:Mn observed here is the same as that reported by many of the co-workers[20-22]. This is the characteristic emission of Mn^{2+} ($^4T_1$- $^6A_1$) in ZnS lattice. However, the PL peak of the Mn^{2+} transition in the nanocrystal incurs almost no shift when compared to the peak in the bulk sample. The peak at 598nm arises due to the excitation and subsequent de-excitation of mn^{2+} ions. The peak at 423nm occurs because of the self- trapping hole centres in ZnS.

4. Conclusions

The nanoparticles of ZnS and ZnS:Mn were grown by chemical routs in which mercaptoethanol was used as a capping agent . The size of nanoparticle was found to decrease when it is doped with Mn. The XRD pattern indicated the growth of the nanoparticles. The particle size of the sample of ZnS was measured as 7nm and Zns: Mn was measured as 5 nm. The sample which is reported here has 10 weight %. Only one peak was observed in the photoluminescence spectra of ZnS nanoparticles, whereas, two peaks were obtained in the photoluminescence spectra of ZnS:Mn nanoparticles, where the dominant peak lies at 598nm (orange-red colour) and the low intensity peak lies at 423nm (blue colour). Hence it can be concluded that the doping the ZnS nanoparticles with Mn will make them more suitable for the cathodoluminescent devices.

References

[1] Chan W C W and Nie S M , Science 281 2016–8
[2] Han M Y, Gao X H, Su J Z and Nie S 2001 Nat. Biotechnol. 19 631–5
[3] Meng X M, Liu J, Jiang Y, Chen W W, Lee C S, Bello I and Lee S T 2003, Chem. Phys. Lett., 382 434–8
[4] Biswas S, Kar S and Chaudhuri S 2005, J. Phys. Chem. B,109 17526–30
[5] Yu J H, Joo J, Park H M, Baik S I, Kim Y W, Kim S C and Hyeon T 2005 , J. Am. Chem. Soc. 127 5662–70
[6] Lu C L, Cui Z C, Wang Y, Li Z, Guan C, Yang B and Shen J C 2003 ,J. Mater.Chem. 13 2189–95
[7] Belman N, Acharya S, Konovalov O, Vorobiev A, Israelachvili J, Efrima S and Golan Y 2008 , Nano Lett. 8 3858–64
[8] Piret F, Bouvy C and Su B L 2009, J. Mater. Chem. 19 5964–9
[9] Zhang X J et al 2008, Nanotechnology 19 305708
[10] Xiao F, Liu H G, Wang C W, Lee Y I, Xue Q B, Chen X, Hao J C and Jiang J Z 2007 Nanotechnology, 18 435603
[11] Gautam U K, Fang X S, Bando Y, Zhan J H and Golberg D 2008, ACS Nano, 2 1015–21
[12] Breen M L, Dinsmore A D, Pink R H, Qadri S B and Ratna B R 2001, Langmuir 17 903–7
[13] Fang X S et al 2009 , Adv. Mater. 21 2034–9
[14] Yong K T, Roy I, Swihart M T and Prasad P N 2009 J. Mater.Chem,. 19 4655–72
[15] Hu J S, Ren L L, Guo Y G, Liang HP, CaoAM, Wan L J and Bai C L 2005, Chem. Int. Edn, 44 1269–73
[16] Bol A A and Meijerink A 1998, Phys. Rev. B 58 15997–6000
[17]. W. Chen, R. Sammynaiken, Y.Huang, J.O. Malm, R.Wallenberg, J.O. Bovin 2001 J Appl Phys, 1120, 89-97
[18] A.A. Khosravi, M.Kundu, G.S.Shekhawat, R.R.Gupta, A.K.Sharma, P.D.Vyas, S.K.Kulkarni 1995 Appl. Phys. Lett. 67, 2506-11
[19] Sharma R., Bisen, D.P. and Chandra, B.P.,Chalcogenide Letters Vol. 6, No. 6, June 2009, p. 251 - 255
[20] R.Tamrakar, M. Ramrakhiani, B.P. Chandra 2008 Open Nanoscience Journal, 2 12-18.
[21] H.C. Warad, S.C. Ghosh, B. Hemtanon, C. Thanachayanont, J. Dutta 2005 Science and Technology of Advanced Materials 6 296–301
[22] Sharma R., Dhoble S.J.,Bisen, D.P., Brahme N. and Chandra, B.P. (2011), Int. J.Nanoparticles, Vol. 4, No. 1, pp.64–76.

Multi Scale Entropy Analysis of the Sectoral Indices of Indian Stock Market

B.G.Sharma
Department of Physics and Computer science,
Govt.Science College
Raipur
Sharma_balgopal@rediffmail.com

Sadhana Agrawal
Department of Physics
National Institute of Technology
Raipur
agrawaldrs@rediffmail.com

D.P.Bisen
School of studies in Physics,
Pt.Ravishankar Shukla University
Raipur.

Ravi Sharma
School of studies in Physics,
Pt.Ravishankar Shukla University
Raipur

Malti Sharma
WQ-1,Govt. Science College
Raipur

Abstract

There has been considerable interest in quantifying the complexity of the time series of price variations exhibited by stock markets. Different methods have been developed for this purpose. Traditional entropy based algorithms quantify the regularity of the time series. Entropy increases with disorder, however, an increase in entropy may not always be with increase in dynamic complexity. The traditional algorithms may generate misleading results because the algorithms are based on single time scale .However, the multiscale entropy approach measures the complexity of the system taking into account the multiple time scales. This computational tool can be quite effectively used to quantify the complexity of a given time series. In this paper we study the variation in various sectoral indices of Indian stock market using multiscale entropy analysis (MSE).The sample entropies (SampEn) of different sectoral indices are calculated at different ranges of scales and their MSE profiles are compared at different conditions.

Keywords- Entropy, Stock Market data, Multi scale Entropy, index, data Analysis

Broad Area- Applied Physics

1. Introduction

Nonlinear dynamic analysis techniques empowered by progress in the tools of complexity, deterministic chaos and fractals etc. is clearly outperforming the linear methods in analysis of real time series data [1]. Non linear methods consist of an array of toolkits ranging from all kind of correlation dimension calculations, Hurst dimension, Lyapunov exponents, fractal dimensions –both in time as in phase space domain, several types of entropy and complexity measurements and algorithms/methods to estimate the state space embedding dimension ("embedology") and time delays (false nearest neighbors, autocorrelation, mutual information) etc. Yet these approaches might not be without some problem and pitfalls. Hence a cautious approach is required otherwise a blind application of the methodology on non linear signal may give misleading results.

It is estimated that for Grassbergers and Proccacia correlation dimension a long enough data segment is necessary of length N so that $D_2 < 2$ 1ogN [2]. Such long segments will probably contain artifacts and non-stationarities that could jeopardize the whole analysis. Takens Theorem states that if there is deterministic chaos then the fractal attractor can be reconstructed in a time delay space of appropriate dimension constructed from only the one dimensional realization (the signal at hand), this does not imply the reverse[3]. Calculating some non integer dimensionality is evidently no sure proof of existence of deterministic chaos[4]. The linear noise filtering of true random series also suggests the presence of deterministic chaos[5-6]. Hence the correlation dimension can not be used as an absolute detector of chaos. Thus while using these techniques it is imperative to prevent false "positive" conclusions.

Thus it will be useful to focus on model free approach and try to demonstrate alternation in signal complexity using time domain fractal dimension. Multiscale entropy analysis (MSE) is such a technique that is robust, less model dependent (can be applied to deterministic chaos, stochastic as well as periodic signals), can be used on relative short signal segments and is less noise sensitive[7].

This method can effectively be used in measuring the complexity of finite length time series. This computational tool can be applied to various types of physical data sets and can be used with variety of measures of entropy. Whereas traditional methods quantify the degree of regularity of a time series by evaluating the appearance of repetitive patterns, there is no straight forward correspondence between regularity and complexity. Neither completely predictable (e.g. periodic) signal, which have minimum entropy, nor completely unpredictable (e.g. Uncorrelated random) signals which have maximum entropy, are truly complex, since they can be described very compactly. There is no consensus definition of complexity. Intuitively complexity is associated with "meaningful structural richness", which in contrast to the outputs of random phenomena, exhibits relatively higher regularity. Entropy based measures, such as the entropy rate and the Kolmogorov complexity, grow monotonically with the degree of randomness[2]. Therefore their measures assign the highest values to uncorrelated random signals (white-noise), which are highly unpredictable but not structurally "complex" and at a global level, admit a very simple description.

Thus, when applied to a given time-series, traditional entropy-based algorithms may lead to misleading results. For example, they may assign higher entropy value to the data set that generate erratic outputs than to the output of the systems that are exquisitely regulated by multiple interacting control mechanism. Substantial attention, therefore, has been focused on defining a quantitative measurement of complexity that assign minimum values to both deterministic/predictable and uncorrelated random / unpredictable signals. In multiscale entropy analysis the sample entropy of the system is calculated at different scales[9-11]. The Sample Entropy is largely independent of the time series length when the total number of data points is larger than approximately 750[8]. Recently MSE method has been applied successfully to quantify the complexity of many types of time series data[12-13]

This paper is organized as follows: section 2 provides a theoretical background and a review of related previous research. In Section 3 we discuss the methodology applied to different data sets and its analysis. In Section 4 we present the result and the discussion of the study and finally section 5 contains References.

2. Multiscale Entropy Analysis

The MSE method is based on the estimation of sample entropy (SampEn) [8] which is a refinement of the approximate entropy family of statistics introduced by Pincus[14]. Sample entropy is a statistical measure which quantifies the variability of time-series by comparing sequence of consecutive data point. It provides a measure of the regularity or predictability of a time-series (high complexity). Sample entropy is derived from the conditional probability that sequence of data-point is within a certain tolerance range for a number of steps. Sample entropy depends on the length of the series. Though it can't be used to distinguish between signals of similar form but different frequency. A signal which contains noise and has a certain period no more complex than the same quantity of data but with a different periodicity.

*Due to the interrelationship of entropy and scale, which is incorporated in the MSE analysis, the results are consistent with the consideration that both completely ordered and completely random signals are not really complex. In particular, the MSE method shows that uncorrelated random signals (white noise) are less complex than correlated random signal. When the MSE Result for white noise is compared with 1/f noise (pink noise) it is found that for scale one, a higher value of SampEn is obtained for white noise than pink noise. Although the value of entropy for the coarse-grained 1/f noise series remains constant for all scales, the value of entropy for the coarse-grained white noise time series monotonically such that for scales above 4, it becomes smaller than the corresponding value for 1/f noise. In contrast with single-scale entropy based analysis, the MSE results are consistent with the fact that unlike white noise, 1/f noise contains correlations across multiple time scales and is, 1/f therefore, more complex than white noise.

3. Method

MSE method depends on coarse-graining procedure of the given series. It incorporates two steps.
1.Consider a given time series

$$\{x_i\} = \{x_1 x_2 x_3 \ldots \ldots x_n\}$$

The length of the series is N. Then we construct consecutive coarse-grained time series by averaging a successively increasing number of data points in non-overlapping windows. Figure1 shows an schematic illustration of the coarse-graining procedure for scale 2 and 3. Each element of the coarse-grained time series, $y_j^{(\tau)}$ is calculated accordingly to the equation

$$y_j^{(\tau)} = \frac{1}{\tau} \sum_{i=(j-1)\tau+1}^{j\tau} x_i \qquad (1)$$

Where, τ represents the scale the factor and $i \le j \le \frac{N}{\tau}$ The length of each coarse-grained time-series is N/τ. For scale one, the time series $\{y^{(1)}\}$ is simply the original time-series.

2. Finally, we calculate sample entropy (SampEn) for each coarse-grained time-series, and then SampEn is plotted as a function of the scale-facto

Let

$$U_m(i) = \{x_i, x_{i+1} \ldots \ldots x_{i+m-1}\}$$
$$1 \le i \le N - m \quad (2)$$

be vectors of length m. Let $n_{im}(r)$ represent the number of vectors $U_{m(i)}$ Within distance r of $U_{m(i)}$ where j range from 1 to (N-m) and j≠ 1 to exclude self matches.

$$C_i^m(r) = \frac{n_{im}(r)}{N-m-1} \quad (3)$$

Is probability that any vector $U_m(i)$ is within tolerance range r of $U_m(i)$ We then define

$$U^m(r) = \frac{1}{N-m}\sum_{i=1}^{N-m} \ln C_i^m(r) \quad (4)$$

The parameter Sample entropy (Samp En) is defined as

$$SampEn(m,r) = \lim_{N\to\infty}\left\{-\ln \frac{U^{m+1}(r)}{U^m(r)}\right\} \quad (5)$$

For a Time Series of finite length (N), the sample entropy is estimated by statistics,

$$SampEn(m,r,N) = \left\{-\ln \frac{U^{m+1}(r)}{U^m(r)}\right\} \quad (6)$$

Sample entropy is the natural logarithm of the ratio of the total number of two components templates matches to the total number of three components templates matches.

For scale one, the value of entropy is higher for the white noise time series in comparison to the 1/f noise.

This result explains the facts that the 1/f noise contains complex structures across multiple scales in contrast to the white noise.

Scale-1:-

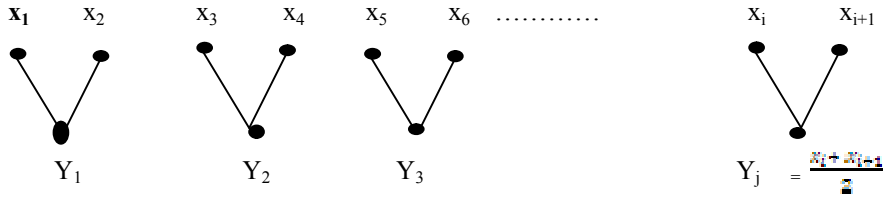

Scale-2:-

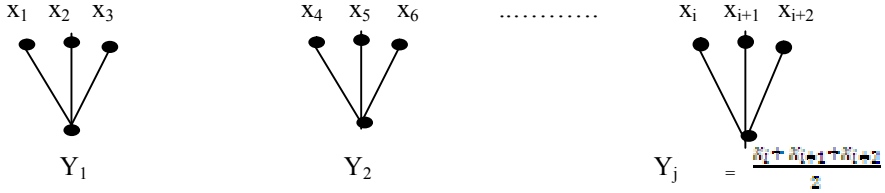

4. Data Analysis

We analyzed the data base of various sectoral indices of National Stock Exchange of India from tt5 (Advance) of India Infoline Sec. Daily closing values of indices are taken from 17th june 2003 to 9th feb 2010. Total no of data points are taken to be 1623. Fig 2(a)-2(b) show the daily variations of various secrtoral indices.

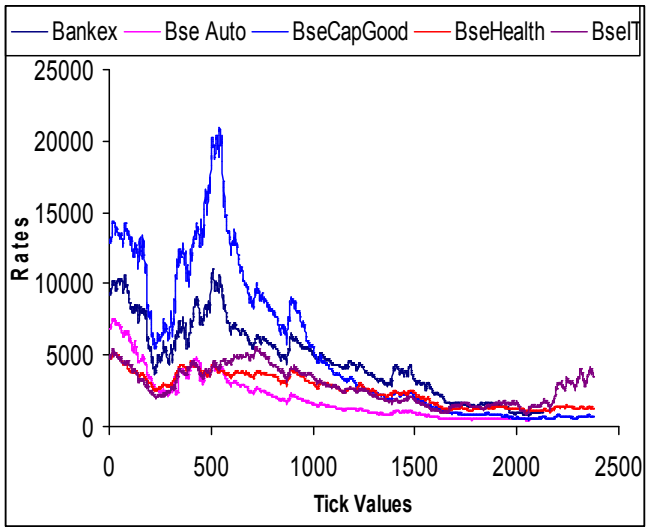

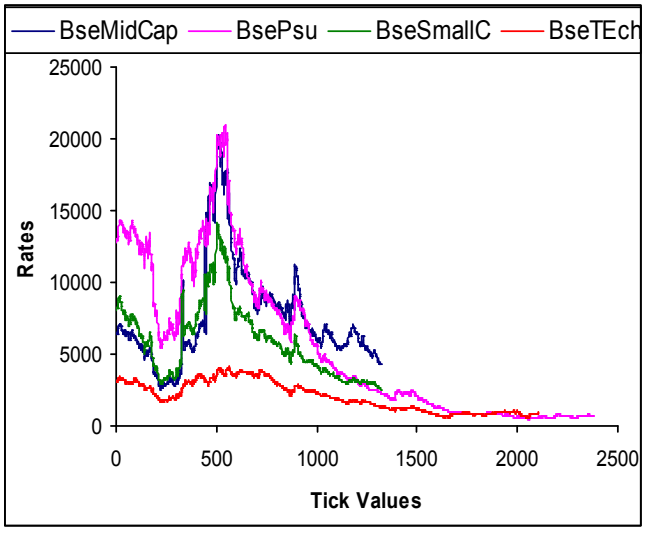

Figure 2(a)-2(b) Graph of Various Sectoral Indices of Nifty

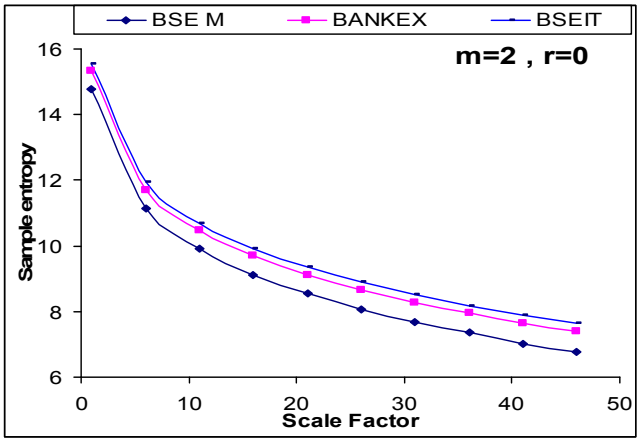

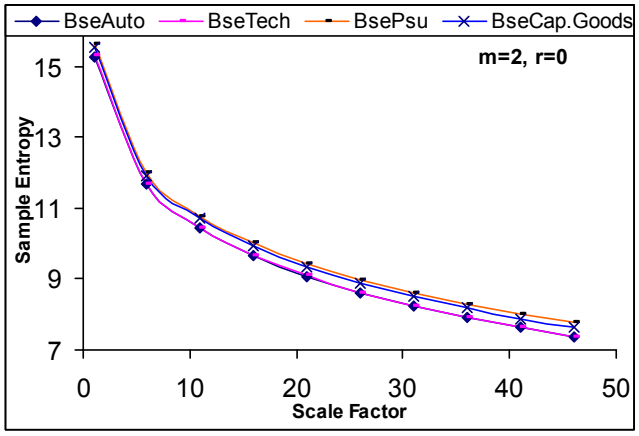

Figure 3(a-b) MSE Profile of Various Sectoral Indices of Bombay Stock Exchange of India

3(a)-3(b) show their MSE profile respectively.

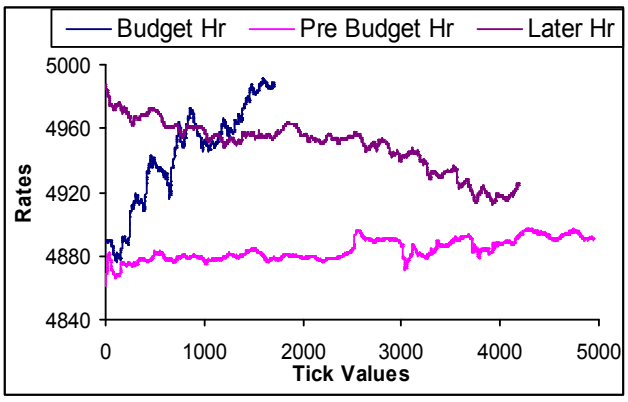

Figure 4. Tick Value of NIFTY for Pre Budget, Budget and post budget hours & Later hours of the Market.

Fig 4 shows the variation of tick value of NIFTY for pre budget hours, just after the budget announcement and at later hours of the market.

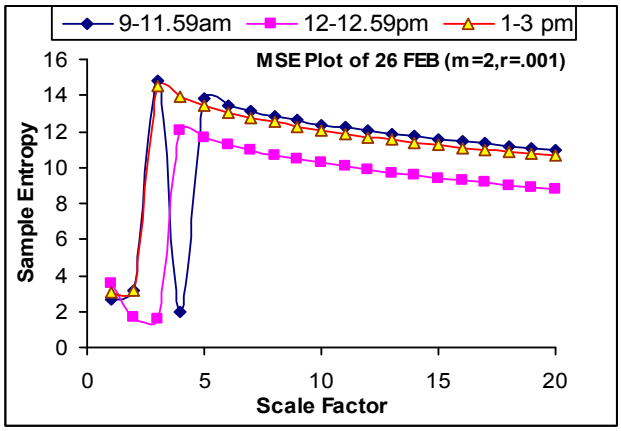

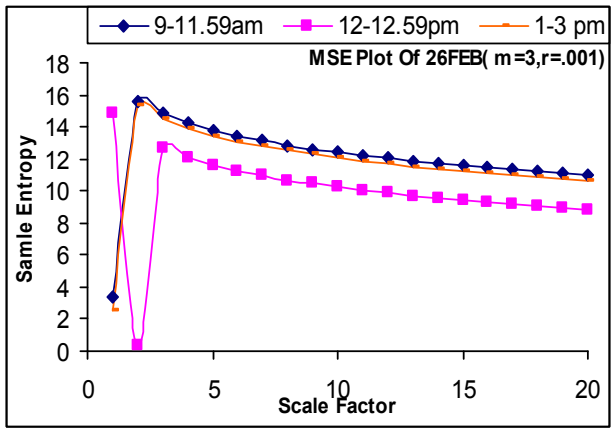

Figure 5(a-b) MSE Profile of Pre Budget, Budget and post budget hours & Later hours of the Market

Fig 5(a) - 5(b) show their MSE profile respectively.

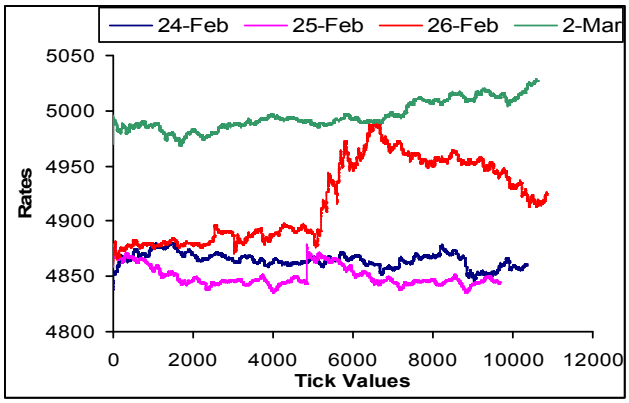

Figure 6(a) Variation in the Tick value of NIFTY for 24th feb 2010 to 2 march 2010

Fig 6(a) shows the variation in the tick value of NIFTY for 24th feb 2010 to 2 march 2010 in which there are two days of pre- budget days, budget day, and one post- budget day.

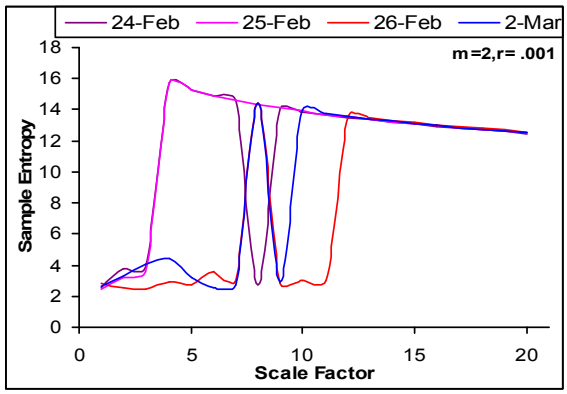

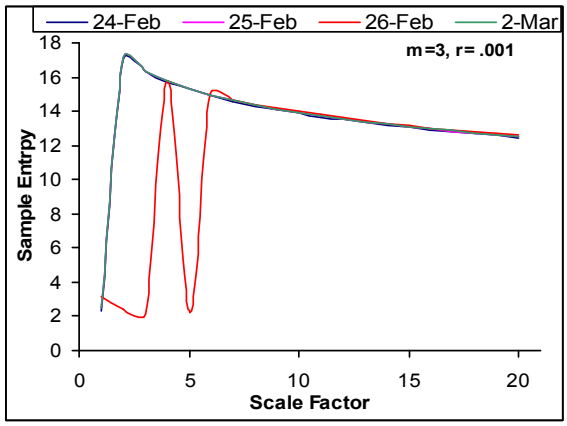

Figure 6(b) MSE Profile of Tick value of NIFTY for 24th feb 2010 to 2 march 2010

5. Result and Discussion

Studies of the MSE profile of daily variations of different indices show that the BSE Metal Index exhibit lower MSE pattern as compared to other sectoral indices. This is due to the cyclical nature of the constituents of the index. Thus a pattern emerging out of the cyclical nature gives rise to a lower MSE pattern at all scales. All other indices show identical MSE pattern indicating equivalent complexity levels of daily data. Similarly NIFTY tick value is studied for pre budget hours, just after budget, and later hours of market timing on the budget day. The MSE profile shows that the entropy of market was the maximum at pre budge hours. The higher entropy profile indicates higher entropy of the data. The index value of the budget and post budget hours shows lower MSE profile showing low complexity, i.e. higher degree of order. As the provisions of the budget were made public market started interacting with the

information showing lower MSE profile indicating higher degree of order (low complexity). Data of later hours again shows higher entropy profile but still having lower values of entropies at different scales than the pre budget hours. However The same study performed on the NIFTY tick value for the period from 24th feb. 2010 to 2nd march 2010 in which there are two days of pre budget, budget day and one post budget day indicates that the difference among their MSE profile disappear and their profiles converge showing the identical behavior. This indicates that the market responds to received information with a higher degree of order and adjust itself interacting with the information. As the information has been received the market behaves like an isolated system with higher entropy.

Thus in conclusion the findings of this study demonstrates that multiscale entropy measurements could be an effective alternative nonlinear approach for analyzing the stock market data [15].

References

[1] Holger Kantz, Thomas Schreiber , Nonlinear Time Series Analysis , Cambridge Press-1999.
[2] Grassberger and Proccacia , Pliysica D 9. (1983), 189-208.
[3] Takens F.,Lect. Notes. Math. 898, (1981) 366-381.
[4] G. Otte, Acta. Neurol. Belg, 107, (2007) 61-62.
[5] Rapp P. E. Biologist,40(1993), 89-94.
[6] Theiler j., Physics Letters A, 196.(1995)335-341.
[7] www. Indiainfoline.com
[8] Richman J. S. and Moorman J. R., Am. J. Physiol., 278 (2000) H2039.
[9] Costa M., Peng C. K., Goldberger A. L., and Hausdorff J. M. Physica A, 330 (2003)53.
[10] Costa M., Goldberger A. L. ., Peng C. K. , Phys. Rev. Lett., 89 (2002)068102.
[11] Costa M., Goldberger A. L. ., Peng C. K., Phys. Rev. E, 71 (2005) 021906.
[12] Li Shuangcheng, Zhou Qiaofu, Wu Shaohong and Dai Erfu, *Int. J. Climatol.* 26 (2006) 2131.
[13] A. Sarkar and P. Barat, arxiv.org/pdf/physics/0604040.
[14] S.M. Pincus, Ann. N.Y. Acad. Sci. 954(2001)245
[15] Part of this paper was presented in "International Workshop on Econophysics of order driven Markets", Saha Institute of Nuclear Physics Kolkata (9 March- 13 March 2010)

Performance of Value Added Multi Model Ensemble Based District Level Weather Forecasts Over Indian Region During Monsoon 2008

M.L. Sahu
Meteorological Centre, Raipur (C.G.)- 492001
Email: mohanlalsahu@rediffmail.com

V.R. Durai
India Meteorological Department,
New Delhi-110003

S.K. Roy Bhowmik
India Meteorological Department,
New Delhi-110003

Abstract

India Meteorological Department has implemented district level quantitative forecasts for the parameters like rainfall, maximum and minimum temperature, relative humidity, cloud and surface wind from 1st June 2008 in real time mode for medium range time scale to meet the requirement of Integrated Agro-advisory Services in India. The forecast is based on three global models namely, ECMWF, JMA and NCEP GFS. A multimodel ensemble technique is developed based on outputs of ECMWF, JMA and NCEP GFS models where weight for each model is assigned on the basis of their past performance. The value addition to the ensemble model forecast is made by regional forecaster on the basis of synoptic analysis, climatology, topography and considering the error structure of previous day's model forecast. Verification of forecasts has been done using various skill scores and categorical statistics for district level forecast. The results of the study shows that MME forecast is capable of capturing the rainfall, maximum and minimum temperature except in the case of extreme values. The output is satisfactory and value addition has improved the accuracy of forecast.

Keywords- Multimodel ensemble technique, Integrated Agro-advisory Services, ECMWF model, JMA model, NCEP GFS model, value addition, skill scores, MME forecast, extreme values

Broad Area- Civil Engineering

1. Introduction

The very specific requirement for the Integrated Agro-advisory Service of the India Meteorological Department is to provide district level quantitative forecasts in the short to medium range time scale.

For generation of district level quantitative forecasts, one has to depend on the forecasts from dynamical Numerical Weather Prediction (NWP) models. As these forecasts are raw direct model outputs, the skill is likely to be poor. The potential approach as emerged in recent studies (Krishnamurti *et al*.,1999, Ebert, 2001; Arribus *et al.,* 2005) is the Multi-Model Ensemble (MME) technique. In the MME approach, forecasts made with different models are combined into a single forecast to partially take into account the uncertainties in the model formulation and initial conditions. This type of ensemble is different from the ensemble forecast of the single model that utilizes a set of different initial conditions where the different initializations constitute the member models (Brooks and Doswell, 1999).

India Meteorological Department (IMD) implemented a MME based district level quantitative forecasts in the operational mode since 1 June 2008, as required for the Integrated Agro-advisory Service of India. The objective of this paper is to document the performance skill of the IMD MME forecasts in spatial and temporal scale during the summer monsoon 2008.

2. Methodology

In the MME forecasting, the main issue relates to the removal of the collective errors of the constituent models. The major drawback of the straight average approach of assigning an equal weight of 1.0 to each model is that it may include several poor models. The mean of these poor models degrades the overall results. To address this problem, in the multimodel super ensemble approach (Krishnamurti *et al*. 1999), weight is assigned to each model based on spatial and temporal performance of respective models. The strategy for the multimodel super ensemble involves two phases. In the first phase, known as training period, which utilizes the direct model outputs and the

corresponding observed fields to derive the weights. In the second phase called the forecast phase, utilizes the multimodel forecasts and aforementioned weights to obtain the final super ensemble forecast.

The NWP models such as, ECMWF, JMA, NCEP GFS, UKMO and NCMRWF T-254 are considered for formulation of the MME based district level 5 days quantitative forecasts for the following parameters:

(a) 24 hours cumulative rainfall of a day

(b) Maximum and minimum temperature (trend)

(c) Morning and evening relative humidity

(d) Total cloud amount of a day

(e) Surface wind speed and wind direction

Out of 5 models, the operational MME for 2008 was prepared based on 3 models namely NCEP, ECMWF and JMA. The outputs of NCEP are available at 1 ^{o} resolution, JMA at 1.2 ^{o} and ECMWF at 0.25 ^{o}. In order to generate district level forecasts, in the first step all the model outputs are statistically down scaled at the 25 km resolution. The weight for each model at each grid point is generated on the basis of the past performance (during monsoon 2007) of these models, using following equation (Roy Bhowmik and Durai, 2008; 2010):

$$W_{i,j,k} = \frac{C_{i,j,k}}{\sum_{k=1}^{3} C_{i,j,k}}, \quad i = 1, 2,\ldots\ldots\ldots, 161;$$

j=1,2,……....,161

C is the correlation coefficient between observed and forecast fields for each model (k) at each grid (i, j). Here i, j = 1,2,..,161, k=1,…,3. Model domain is selected as: Equator to 40^{o} N Latitude and 60^{o} E to 100^{o} E longitude. In the second step, the multimodel forecasts and the corresponding weights are utilized to obtain the final ensemble forecast. For a district value, average value of all grid points falling in a particular district is considered.

The standard procedure (Jolliffe and Stehenson, 2003) for the model verification is to compute spatial pattern of mean errors, root mean square errors (RMSE) and anomaly correlation coefficient.

3. Data

The districtwise daily rainfall, maximum temperature, minimum temperature, morning and evening relative humidity of year 2008 monsoon period data have been used for this analysis. The observed data, Multimodel ensemble forecast data and value added forecast data have been used for analysis and verification of forecast.

4. Result and discussion

4.1. Rainfall Forecast errors

The verification results of MME reveal that, RMSE of daily rainfall of the order of 20-25 mm prevailed over the domain of monsoon trough, particularly along the foot hills of the Himalayas, over the North Bay of Bengal and along the west coast where occasional heavy rainfall occurs. Spatial coverage of errors is found to be considerably reduced in the MME forecasts. RMSE generally remains within 10 mm over the rest of the country. For ECMWF and GFS, RMSE has been of the order of 25 – 30 cm over large areas.

Figure1 presents an inter-comparison of country mean spatial CC of rainfall forecasts by MME and member models. The results show that MME is superior to each member model at all the forecasts (day 1 to day 5).

An inter-comparison of domain mean CC by these models is shown in Table.1. The MME forecasts show higher CC at all the forecast ranges.

Table 1. An inter-comparison of domain mean CC of rainfall

MODELS	DAY1	DAY2	DAY3	DAY4	DAY5
ECMWF	0.90	0.80	0.82	0.83	0.81
NCEP GFS	0.80	0.83	0.73	0.66	0.7
JMA	0.86	0.85	0.80	0.77	0.71
MME	0.92	0.92	0.87	0.85	0.83

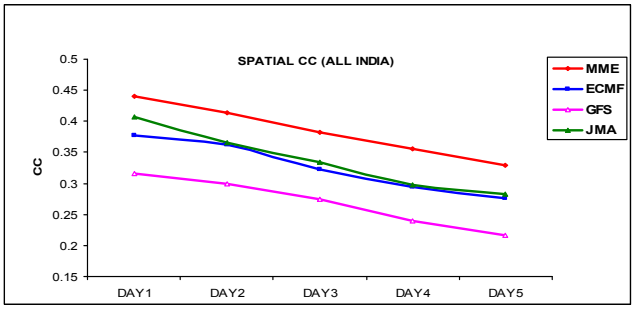

Figure 1. Inter-comparison of country mean spatial CC of day1-day5 rainfall forecasts by MME and member models for the period from 1 June to 30 September 2008

MME based district level forecasts issued by the IMD New Delhi has been disseminated daily to concerned Meteorological Centres spread all over the country. Value additions to the dynamical forecast is made by the concerned Meteorological Centres on the basis of district level synoptic, climatological, and topographical knowledge, and from the consideration of the error structures of the previous day's forecast. The value added district level forecasts are the final forecast product provided for the Integrated Agro-advisory Service. Examples on the performance of the value added district level forecasts of Chhattisgarh are illustrated in Fig .2. and Figure3.

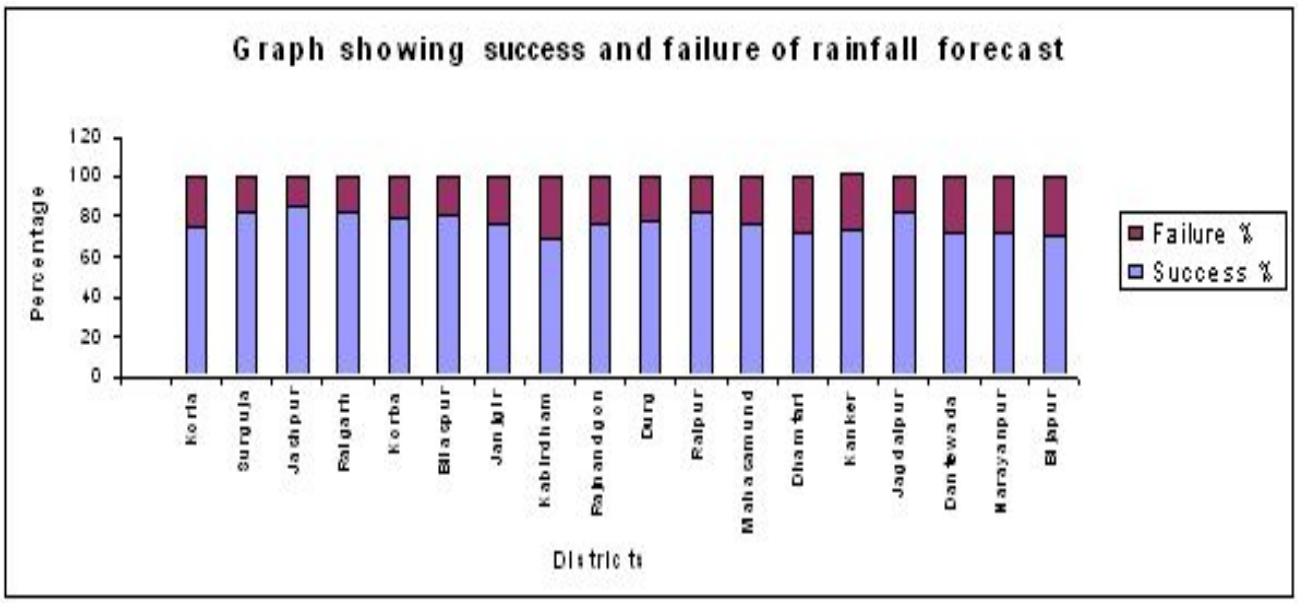

Figure 2. Qualitative verification of district level value added rainfall forecast for Chhattisgarh

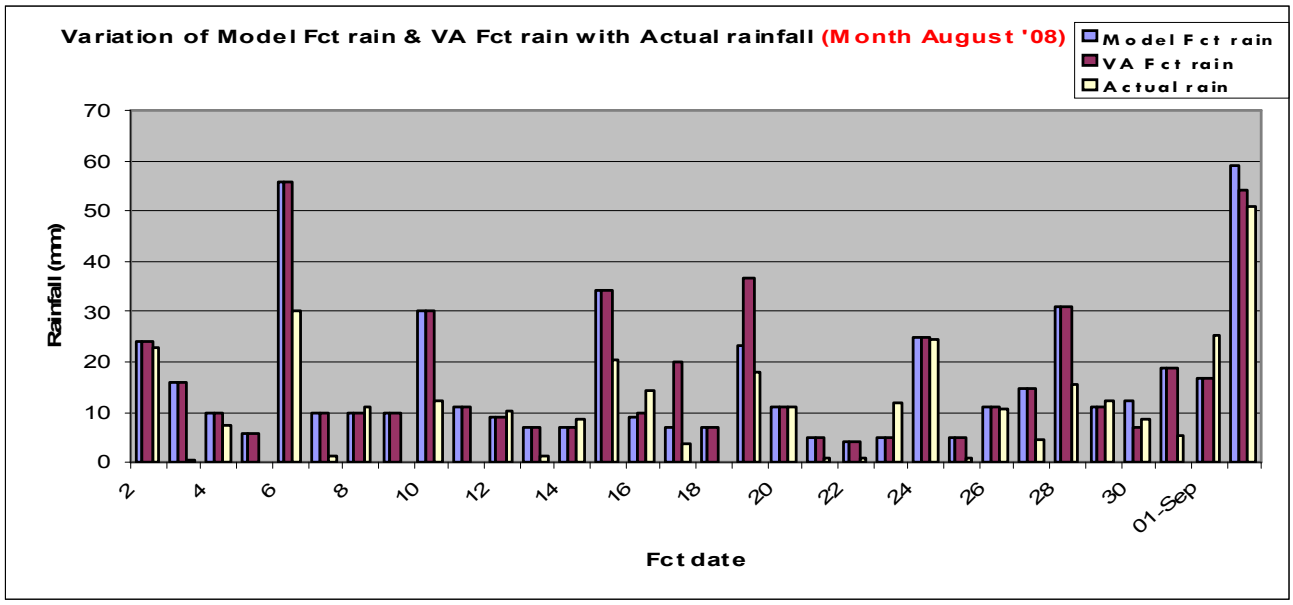

Figure 3. An inter-comparison of district level value added rainfall forecast against MME forecast and observation

4.2. Temperature forecast errors

4.2.1. Minimum temperature

The RMSE for the minimum temperature remains with in 1° to 2° C over most parts of the country, except in the extreme northern India, over the domain of high terrain where RSME becomes 10° C.

4.2.2. Maximum temperature

For the maximum temperature RMSE remains as 2°C over most parts of the country, except over extreme northern India, over the domain of high terrain where RSME becomes as high as 8-10°C. The verification result of Chhattisgarh is shown in Figure4.

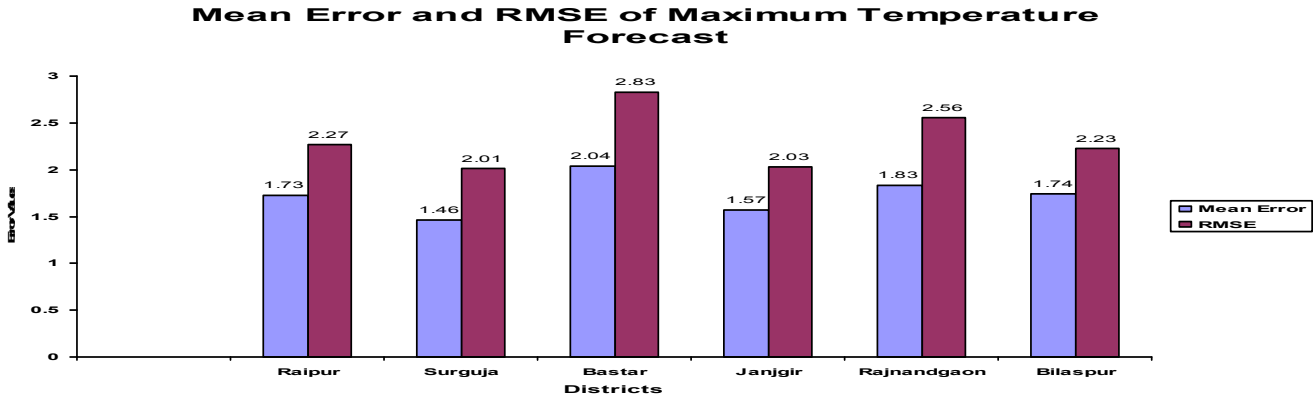

Figure 4. Quantitative verification of district level maximum temperature value added forecasts for Central India (Chhattisgarh)

4.3. Relative humidity forecast errors

4.3.1. Morning relative humidity

Spatial distribution of RMSE of morning relative humidity (%) based on MME forecasts day 1 – day 5 for the period from 1 June to 30 September 2008 remained nearly 10% over most parts of the country.

4.3.2. Evening relative humidity

RMSE of evening relative humidity (%) based on MME forecasts day 1 – day 5 for the period from 1 June to 30 September 2008. RMSE remained nearly 10% over most parts of the country, except northwest India where it has been of the order of 20-30 %.

5. State-wise performance of District Level Forecasts

State-wise performance of district level forecasts for day 1 to day 5 is summarised in Table 2 - 6. Performance index is defined as the % of total districts with threat score more than 0.5 for rainfall thresholds of 2.5 mm, 5 mm, 10 mm and 15 mm. Threat score is defined as number of correct forecasts divided by total forecasts. The threat score ranges between 0 and 1, with 1 as the perfect score. The district level forecast skill is found to be reasonably good over most parts of the country.

Table 2. State-wise District Level Performance Skill of Rainfall Day 1 Forecast (% of districts with threat score 0.5 and above for various rain thresholds)

STATE	TOTAL DIST	2.5 mm	5.0 mm	10 mm	15 mm
ANDAMAN & NICOBAR	2	100	100	100	100
ARUNACHAL PRADESH	13	100	100	92	77
ASSAM	24	100	100	96	63
MAGHALAYA	7	100	100	100	86
NAGALAND	8	100	100	100	13
MANIPUR	9	100	100	100	11
MIZORAM	8	100	100	88	25
TRIPURA	4	100	100	100	50
SIKKIM	4	100	100	100	25
WEST BENGAL	19	100	100	84	58
ORISSA	29	100	100	100	66
JHARKHAND	18	100	100	100	61
BIHAR	37	95	95	92	57
UTTAR PRADESH	70	100	100	90	17
UTTARANCHAL	13	100	100	92	38
HARYANA	19	100	89	32	5
CHANDIGARH	1	100	100	100	5
DELHI	1	100	100	5	5
PUNJAB	17	100	76	18	5
HIMACHAL PRADESH	12	100	100	100	17
JAMMU & KASHMIR	17	100	71	18	5
RAJASTHAN	32	97	78	41	5
MADHYA PRADESH	45	100	100	87	18
GUJARAT	25	92	48	28	12
GOA	2	100	100	100	100
MAHARASHTRA	33	100	94	64	21
CHHATTISGARH	15	100	100	100	53
ANDHRA PRADESH	23	100	87	48	9
TAMILNADU	29	76	21	10	3
KARNATAKA	27	100	93	52	33
KERALA	14	100	100	100	71
LAKSHADWEEP	1	100	100	100	100

Table 3. State-wise District Level Performance Skill of Rainfall Day 2 Forecast (% of districts with threat score 0.5 and above for various rain thresholds)

STATE	TOTAL DIST	2.5 mm	5 mm	10 mm	15 mm
ANDAMAN & NICOBAR	2	100	100	100	50
ARUNACHAL PRADESH	13	100	100	92	77
ASSAM	24	100	100	96	58
MAGHALAYA	7	100	100	100	100
NAGALAND	8	100	100	100	13
MANIPUR	9	100	100	100	11
MIZORAM	8	100	100	88	13
TRIPURA	4	100	100	100	75
SIKKIM	4	100	100	100	25
WEST BENGAL	19	100	100	84	58
ORISSA	29	100	100	97	55
JHARKHAND	18	100	100	100	67
BIHAR	37	95	95	92	57
UTTAR PRADESH	70	100	100	83	11
UTTARANCHAL	13	100	100	92	23
HARYANA	19	100	84	16	5
CHANDIGARH	1	100	100	100	5
DELHI	1	100	100	7	5
PUNJAB	17	100	65	24	5
HIMACHAL PRADESH	12	100	100	92	17
JAMMU & KASHMIR	17	100	65	18	5
RAJASTHAN	32	94	75	41	5
MADHYA PRADESH	45	100	100	89	11
GUJARAT	25	92	56	28	8
GOA	2	100	100	100	100
MAHARASHTRA	33	100	94	55	27
CHHATTISGARH	15	100	100	100	40
ANDHRA PRADESH	23	100	83	35	4
TAMILNADU	29	76	24	7	3
KARNATAKA	27	100	93	52	33
KERALA	14	100	100	100	71
LAKSHADWEEP	1	100	100	100	100

Table 4. State-wise District Level Performance Skill of Rainfall Day 3 Forecast (% of districts with threat score 0.5 and above for various rain thresholds)

STATE	TOTAL DIST	2.5 mm	5 mm	10 mm	15 mm
ANDAMAN & NICOBAR	2	100	100	100	50
ARUNACHAL PRADESH	13	100	100	92	69
ASSAM	24	100	100	96	63
MAGHALAYA	7	100	100	100	86
NAGALAND	8	100	100	100	38
MANIPUR	9	100	100	100	0
MIZORAM	8	100	100	88	50
TRIPURA	4	100	100	100	25
SIKKIM	4	100	100	75	25
WEST BENGAL	19	100	100	79	53
ORISSA	29	100	100	97	45
JHARKHAND	18	100	100	100	56
BIHAR	37	95	95	92	46
UTTAR PRADESH	70	100	100	89	10
UTTARANCHAL	13	100	100	92	15
HARYANA	19	100	89	11	5
CHANDIGARH	1	100	100	100	5
DELHI	1	100	100	5	4
PUNJAB	17	100	59	18	7
HIMACHAL PRADESH	12	100	100	100	17
JAMMU & KASHMIR	17	100	65	24	8
RAJASTHAN	32	97	75	34	5
MADHYA PRADESH	45	100	100	78	13
GUJARAT	25	92	52	24	4
GOA	2	100	100	100	100
MAHARASHTRA	33	100	88	52	21
CHHATTISGARH	15	100	100	100	47
ANDHRA PRADESH	23	100	78	39	4
TAMILNADU	29	76	24	10	3
KARNATAKA	27	100	93	52	33
KERALA	14	100	100	100	79
LAKSHADWEEP	1	100	100	100	100

Table. 5. State-wise District Level Performance Skill of Rainfall Day 4 Forecast (% of districts with threat score 0.5 and above for various rain thresholds)

STATE	TOTAL DIST	2.5 mm	5 mm	10 mm	15 mm
ANDAMAN & NICOBAR	2	100	100	100	100
ARUNACHAL PRADESH	13	100	100	92	85
ASSAM	24	100	100	96	63
MAGHALAYA	7	100	100	100	71
NAGALAND	8	100	100	100	13
MANIPUR	9	100	100	100	2
MIZORAM	8	100	100	88	13
TRIPURA	4	100	100	100	2
SIKKIM	4	100	100	75	25
WEST BENGAL	19	100	95	79	32
ORISSA	29	100	100	97	28
JHARKHAND	18	100	100	100	39
BIHAR	37	95	95	92	49
UTTAR PRADESH	70	100	100	86	13
UTTARANCHAL	13	100	100	92	15
HARYANA	19	100	89	21	5
CHANDIGARH	1	100	100	100	5
DELHI	1	100	100	7	5
PUNJAB	17	100	71	24	5
HIMACHAL PRADESH	12	100	100	100	17
JAMMU & KASHMIR	17	100	65	12	5
RAJASTHAN	32	97	56	22	5
MADHYA PRADESH	45	100	98	80	16
GUJARAT	25	92	28	8	5
GOA	2	100	100	100	100
MAHARASHTRA	33	100	82	42	21
CHHATTISGARH	15	100	100	100	13
ANDHRA PRADESH	23	100	83	26	3
TAMILNADU	29	76	24	7	3
KARNATAKA	27	100	89	52	33
KERALA	14	100	100	100	71
LAKSHADWEEP	1	100	100	100	100

Table 6. State-wise District Level Performance Skill of Rainfall Day 5 Forecast (% of districts with threat score 0.5 and above for various rain thresholds)

STATE	TOTAL DIST	2.5 mm	5 mm	10 mm	15 mm
ANDAMAN & NICOBAR	2	100	100	100	50
ARUNACHAL PRADESH	13	100	92	92	85
ASSAM	24	100	100	96	58
MAGHALAYA	7	100	100	100	86
NAGALAND	8	100	100	100	13
MANIPUR	9	100	100	100	10
MIZORAM	8	100	100	75	13
TRIPURA	4	100	100	100	10
SIKKIM	4	100	100	75	25
WEST BENGAL	19	100	95	84	32
ORISSA	29	100	100	97	31
JHARKHAND	18	100	100	100	39
BIHAR	37	100	97	95	38
UTTAR PRADESH	70	100	100	92	14
UTTARANCHAL	13	100	100	92	15
HARYANA	19	100	84	26	5
CHANDIGARH	1	100	100	100	2
DELHI	1	100	100	7	5
PUNJAB	17	100	71	18	5
HIMACHAL PRADESH	12	100	100	100	25
JAMMU & KASHMIR	17	100	65	24	5
RAJASTHAN	32	97	72	38	3
MADHYA PRADESH	45	100	100	78	7
GUJARAT	25	92	36	4	3
GOA	2	100	100	100	100
MAHARASHTRA	33	100	88	55	21
CHHATTISGARH	15	100	100	100	20
ANDHRA PRADESH	23	100	83	48	0
TAMILNADU	29	76	24	10	3
KARNATAKA	27	100	89	52	33
KERALA	14	100	100	100	79
LAKSHADWEEP	1	100	100	100	100

6. Conclusions

Results of this study showed that value added MME forecast for rainfall RMSE generally remains within 10 mm over the country except in foothills of Himalaya where it is higher. The RMSE in Maximum and Minimum temperature forecast remains within 1°C to 2°C. The RMSE of morning and evening relative humidity (%) based on MME forecasts remained nearly 10% over most parts of the country. All three models (ECMWF, JMA and NCEP GFS models) in general, have the capability to capture large scale rainfall features of summer monsoon, such as heavy rainfall belt along the west coast, over the domain of monsoon trough and along the foothills of the Himalayas. Results of errors statistics have clearly demonstrated the superiority of the MME over the member models. Among the member models ECMWF is found to be the best followed by JMA and NCEP GFS.

Acknowledgments

Authors are grateful to AVM (Dr.) Ajit Tyagi, Director General of Meteorology, India Meteorological Department for his keen interest, encouragement, valuable suggestions, constant support and providing all facilities to complete this research work. Authors also like to thank Dr. L.S. Rathore, Head of Agro-Met, India Meteorological Department for his constant support and valuable suggestions to accomplish the task. Authors thankfully acknowledge the use of model outputs of ECMWF, JMA and NCEP in this work.

References

[1] Arribas, A, Robertson, K.B., Mylne, K.R., 2005. Test of a Poor Man's Ensemble Prediction System for short range probability forecasting. *Monthly Weather Review* , 133, 1825-1839.

[2] Brooks H.E. and Doswell C.A., 1999. New technology and numerical weather prediction. *Weather* 48: 173-177.

[3] Ebert E.E., 2001. Ability of a poor man's ensemble to predict the probability and distribution of precipitation, *Monthly Weather Review* , 129, 2461-2479.

[4] Jolliffe Ian T. and Stehenson B. David, 2003, Forecast Verification – a practitioner's Guide in Atmospheric Science, John Willy and Sons, 240 pp.

[5] Krishnamurti T.N., Kishtawal C.M., Larow T., Bachiochi D., Zhang Z., Willford E.C., Gadgil S. and Surendran S., 1999. Improved weather and seasonal climate forecasts from multimodel super ensemble. *Science* 285: 1548-1550.

[6] Roy Bhowmik S.K. and Durai V.R., 2008. Multimodel ensemble forecasting of rainfall over Indian monsoon region. *Atmosfera*, 21(3): 225-239

[7] Roy Bhowmik S.K. and Durai V.R., 2010, Application of multimodel ensemble techniques for real-time district level forecasts in short range time scale over Indian region, Meteorl and Atmod Phy., 106, 19-35

Modification of Formulation for Rainfall Analysis for Mahanadi Reservoir Project Complex

S. K. Jaiswal
Department of Civil Engg., B.I.T., Durg(C.G.)
Skjaiswal67@yahoo.com

M. K. Verma
Department of Civil Engg., N.I.T.,Raipur(C.G.)
mkseem670@rediffmail.com

Mohan Gupta
Department of Civil Engg, B.I.T., Durg (CG)
info@mohangupta.com

Abstract

As the rainfall over a large area is not uniform the average depth of rainfall over the area is determined. Earlier in Mahanadi Reservoir Project Complex (MRP complex) for calculation of average depth of rainfall for different reservoir basin the records of eight raingauge stations were used. After 1994 records of some raingauge stations are not available. Hence modification of formulation for rainfall analysis for MRP complex basins is required. In this paper different rainfall analysis such as check for consistency of rainfall records, computation of average depth of rainfall for different basins and check for adequacy of raingauge stations have been done for new set of rainfall records. In this paper the different methods of computation of average depth of rainfall over a basin has been compared and the suitable method has been used for calculating the average depth of rainfall to construct the rainfall series for the different reservoir basins of the MRP complex.

Keywords- Average rainfall depth, Thiessen Polygon.

Broad Area- Civil Engineering.

Sub-Area- Water Resources Engineering.

1. Introduction

Rainfall data is of utmost importance to hydrologist as it forms the basis of many hydrological studies such as rainfall-runoff relation etc. Rainfall is measured by a network of raingauge stations established in the basin area of a reservoir. Point rainfall is the rainfall at a single station. For small areas less than 50 km^2 point rainfall may be taken as the average depth over the area. In large areas, there will be a network of raingauge stations. As the rainfall over a large area is not uniform the average depth of rainfall over the area is determined. Since most hydrological problem require knowledge of the average depth of rainfall over a significant area such as river basin, some procedure must be used to connect the rainfall measured at the individual raingauge established in the basin area to the areal averages. It is never possible to determine the exact average depth of rainfall, because the raingauges give, at best, a very small sample. There are three methods of treating the raingauge record to arrive at an approximate answer and in general the three methods give three different approximations. They are (i) Arithmetic mean method (ii) Thiessen polygon method and (iii) Isohyetal method.

In Mahanadi Reservoir Project Complex (M.R.P. Complex) there are three reservoirs, Ravishankar reservoir, Murumsilli reservoir and Dudhawa reservoir. M.R.P. complex consists of Mahanadi river basin. Earlier there were eight rain gauge stations in Mahanadi basin and average rainfall depth for the three reservoir basins were calculated on the basis of these stations. The earlier rain gauge stations are Rudri, Murumsilli, Gattasilli, Keskal, Kanker, Bhanupratappur, Birgudi, and Mahud. After 1994 some raingauge stations were replaced due to nonavailability of records. The raingauge stations Murumsilli, Keskal, Kanker, Bhanupratappur, Birgudi and Mahud are common in old and new system of raingauge network. As the records of Rudri and Gattasilli raingauge stations are not available hence in place of these two stations, Gangrel and Dudhawa raingauge stations have been used in new system. Hence it is required to reconstruct the average depth of rainfall for reservoir basins of MRP Complex on the basis of these new raingauge stations. The location of new raingauge stations have been shown in figure 1.

2. M.R.P. Complex

M.R.P. complex consists of Mahanadi river basin. In MRP complex there are three reservoirs, Ravishankar Sagar Reservoir on Mahanadi river, Dudhawa reservoir on up stream of Ravishankar Sagar Reservoir on Mahanadi river and Moorumsilli Reservoir on Sillari river a tributary of Mahanadi river on upstream of Ravishankar Sagar Reservoir. The total catchment area of MRP complex is

3670 km^2. MRP complex has to meet the demands of municipal uses of Dhamtari and Raipur town, water supply to Bhilai Steel Plant and Irrigation demand in 14810 ha. area. M.R.P. complex is situated in Dhamtari district of Chhattisgarh State. The Index Map of MRP complex and location of raingauge stations are shown in Figure1.

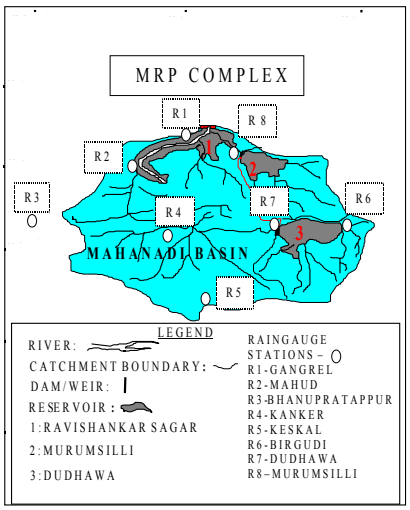

Figure 1. (Index Map of MRP complex)

3. Methods of estimating average depth of rainfall

In a river basin a network of raingauges measures rainfall. Point rainfall is the rainfall at a single station. For small areas less than 50 km^2 point rainfall may be taken as the average depth over the area. In large areas, there will be network of raingauge stations. As the rainfall over a large area is not uniform, the average depth of rainfall over the area is determined. There are three methods of estimating average depth of rainfall.

3.1 Arithmetic average method

This is the simplest of the three methods. It is obtained by simply averaging arithmetically the amount of rainfall at the individual raingauge stations in the basin, i.e.

$$P_{av} = \frac{\sum P}{N}$$

Where Pav = average depth of rainfall over the basin.

$\sum$ P = Sum of rainfall amounts at individual raingauge stations in the basin.

N = Number of raingauge stations in the basin.

If the basin area is flat and gauges are distributed uniformly over the area and if the variation of individual gauge record from mean is not too large, this method is probably as accurate as any other method.

3.2 Thiessen Polygon Method

This method attempts to allow for nonuniform distribution of gauges by providing a weighting factor for each gauge. The stations are plotted on a base map of reservoir basin and are connected by straight lines. Perpendicular bisectors are drawn to the straight lines, joining adjacent stations to form polygons, known as Thiessen Polygon. Each polygon area is assumed to be influenced by the raingauge station inside it i.e. if P_1, P_2, P_3, …….. are the rainfalls at the individual stations and A_1, A_2, A_3, …….. are the areas of the polygons surrounding these stations, respectively, the average depth of rainfall for the entire basin is given by-

$$\mathbf{P_{av}} = \frac{\sum A_1 P_1}{\sum A_1}$$

Where $\sum A_1 = A$ = total area of the basin.

The factors A_1/A, A_2/A, ……. Are called the Thiessen weights. Thus the average depth of rainfall obtained by this method may be interpreted as the sum of the rainfall multiplied by the respective Thiessen weights. This method is fast when once the weights are known. It makes use of the rainfall record of the stations located at a short distance beyond the boundary of the basin and their influence diminishes as their distance from the boundary increases. This is as it should be. On the other hand, in the arithmetic mean method every station is given equal weightage regardless of its location.

3.3 The Isohyetal method

In this method the point rainfalls are plotted on a suitable base map of reservoir basin and the lines of equal rainfall (Isohyets) are then drawn giving consideration to orographic effects and storm morphology. The average rainfall between the sucussesive isohyets taken as the average of the two isohyetal values are weighted with the area between the isohyets added up and divided by the total area which gives the average depth of rainfall over the entire basin i.e.

$$\mathbf{P_{av}} = \frac{\sum A_{1-2}\ P_{1-2}}{\sum A_{1-2}}$$

Where $A_{1\text{-}2}$ = Area between two successive isohyets P_1 and P_2

$$P_{1\text{-}2} = \frac{P_1 + P_2}{2}$$

$\sum A_{1\text{-}2}$ = Total area of the basin

The accuracy of the method is highly dependent upon the skill of the analyst. The method is very slow compared to the previous two.

3.4 Selection of the method to calculate average rainfall depth

Arithmetic mean method is the simplest of the three methods, but in this method the same weightage is given to the rainfall recorded at all the gauges irrespective of their location. The Thiessen polygon method attempts to allow for nonuniform distribution of gauges by providing a weighting factor for each gauge. Hence it is better then the arithmetic mean method. The Isohyetal method is better than the previous two methods, but accuracy of method highly dependent upon the skill of plotting isohyets, which need the knowledge of orographic effects and storm morphology. Comparing the merits and demerits of the three methods it is clear that the Thiessen polygon method is easy to adopt, less time consuming and due to weighting factor gives better result. Central water Commission (CWC) has also recommended the Thiessen polygon method to calculate the average rainfall depth in MRP complex. Hence this method has been selected for the estimation of average rainfall depth for the different reservoir basins of the MRP complex.

4. Estimation of average depth of rainfall for reservoir basins of MRP complex

In MRP complex there are three reservoirs, Ravishankar Sagar reservoir, Murumsilli reservoir, and Dudhawa reservoir. The average depth of rainfall for catchments of these reservoirs have been calculated by constructing separate Thiessen polygon for each reservoir. To construct the Thiessen polygon, raingauge stations have been plotted on a base map of reservoir basin and are connected by straight lines. Perpendicular bisectors are drawn to the straight lines, joining adjacent stations to form polygons, known as Thiessen Polygon. On the basis of these polygons the thiessen weights have been calculated for each raingauge stations by using the procedure as explained in section 4.2. The average depth of rainfall for the catchment of any reservoir can be estimated by taking sum of multiple of rainfall of the different stations and the corresponding thiessen weight of that station.

4.1 Thiessen Polygon for catchment of Ravishankar Sagar Reservoir

The catchment area of Ravishankar Sagar Reservoir is 2559 km^2. Earlier in this reservoir basin the Thiessen polygon was constructed by taking 8 raingauge stations. The name of raingauge stations and the corresponding thiessen weight has been given in Table-1.

Table 1. (Raingauge stations and Thiessen weight in old system)

S.N.	Raingauge Stations	Thiessen weights
1	Rudri	0.014
2	Murumsilli	0.096
3	Gatasilli	0.191
4	Keskal	0.130
5	Kanker	0.212
6	Mahud	0.142
7	Bhanupratappur	0.048
8.	Birgudi	0.227

At present in this catchment there are 7 raingauge stations. New Thiessen polygon has been constructed by taking these 7 raingauge stations. Six raingauge stations are inside the catchment and one raigauge station (Bhanupratappur) is out side the catchment. The name of raingauge and their thiessen weight calculated for the different raingauge stations has been given in table [2].

Table 2. (Raingauge stations and Thiessen weight in new system)

S.N.	Raingauge Stations	Thiessen weights
1	Gangrel	0.052
2	Murumsilli	0.085
3	Dudhawa	0.108
4	Keskal	0.166
5	Kanker	0.333
6	Mahud	0.188
7	Bhanupratappur	0.076

The raingauge stations Murumsilli, Keskal, Kanker, Mahud, and Bhanupratappur are common in old and new system of Thiessen polygon. The raingauge stations Rudri, Gatasilli and Birgudi has been deleted from the old system and two new raingauge stations Dudhawa and Mahud has been

added in the new system. The Thiessen weights of common stations have been compared in table-3.

Table 3. (Comparison of Thiessen weights in old and new system of Thiessen polygon)

S.N.	Raingauge stations	Thiessen Weights in old system	Thiessen Weights in new system
1	Murumsilli	0.096	0.085
2	Keskal	0.130	0.166
3	Kanker	0.212	0.333
4	Mahud	0.142	0.188
5	Bhanupratappur	0.048	0.076

The change in the values of Thiessen weights of the common raingauge stations in old and new system is due to the change in the shape and size of Thiessen polygon corresponding to these raingauge stations, due to change in number of raingauge stations from 8 to 7 in the catchment area.

4.2 Thiessen Polygon for catchment of Murumsilli Reservoir

The catchment area of Murumsilli Reservoir is 486 Km^2. Earlier in this catchment there were three raingauge stations. The thiessen weights were calculated on the basis of these three stations. The name of the raingauge and their theissen weights has been given in table [4].

Table[4]](Old raingauge stations and Thiessen weights)

S.N.	Raingauge Stations	Thiessen weights
1	Murumsilli	0.119
2	Birgudi	0.225
3.	Gattasilli	0.665

In this reservoir basin at present the record of Gattasilli station is not available, hence there are two raingauge stations. The name of raingauge stations and the thiessen weight calculated on the basis of the new thiessen polygon based on these two raingauge stations have been given in table [5].

Table 5. (new raingauge stations and thiessen weights)

S.N.	Raingauge Stations	Thiessen weights
1	Murumsilli	0.42
2	Birgudi	0.58

Two raingauge stations, Murumsilli and Birgudi are common in old and new system of Thiessen Polygon. The data of Gatasilli station is now not available.

4.3 Thiessen Polygon for catchment of Dudhawa Reservoir

The catchment area of Dudhawa Reservoir is 625 Km^2. Earlier in this catchment there was only one raingauge station, Birgudi, hence thiessen weight of this station will be 1. In this catchment, at present the records of two raingauge stations are available hence average depth of rainfall for this catchment have been calculated by constructing thiessen polygon on the basis of these two stations. In this catchment there are two raingauge stations. The name of the raingauge stations and their theissen weights has been given in table [6].

Table 6.

S.N.	Raingauge Stations	Thiessen weights
1	Dudhawa	0.175
2	Birgudi	0.825

5. The consistency of rainfall records

The trend of the rainfall records at a station may slightly change after some years due to a change in the environment or exposure of a station either due to coming of a new building, fence, planting of trees or cutting of forest nearby, which affect the catch of the raingauge due to change in the wind pattern or exposure. In all such cases it is better to test record of any gauge, which is suspected, and adjust the data if required. The consistency of records at the station in question is tested by double mass curve analysis. A certain number of stations (usually 5 as minimum) with reliable data of approximately the same length and in the same climatic region are selected as base stations. In MRP complex there are 8 raingauge stations. The raingauge stations, Gangrel, Muroomsilli, Dudhawa, Kanker, and Mahud have been taken as base stations to check the consistency of the raingauge stations Keskal, Bhanupratappur and Birgudi. The double mass curves to check the consistency of the three stations have been constructed and plotted in the graph and shown in Figure no.2, 3 and 4. For double mass curve analysis rainfall of mansoon months have been taken. From the double mass curve of raingauge stations, Keskal, Bhanupratappur and Birgudi, it is clear that the graph is a straight line hence rainfall records of these raingauge stations of MRP complex are consistent. Hence no correction is required and the rainfall values of these raigauge stations can be directly used for the calculation of average depth of rainfall.

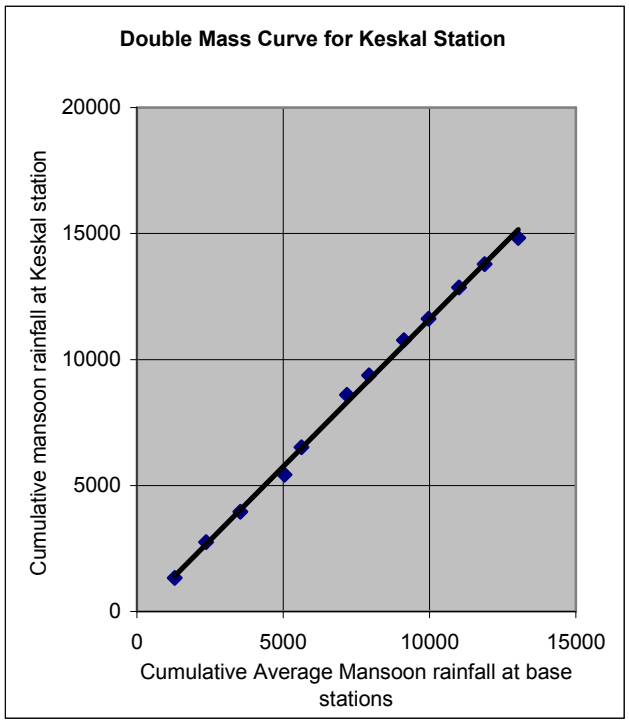

Figure 2.

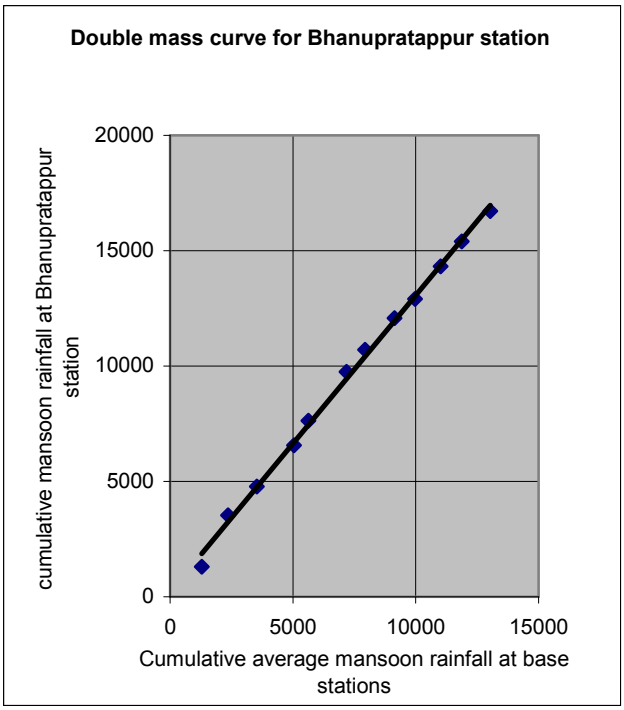

Figure 3.

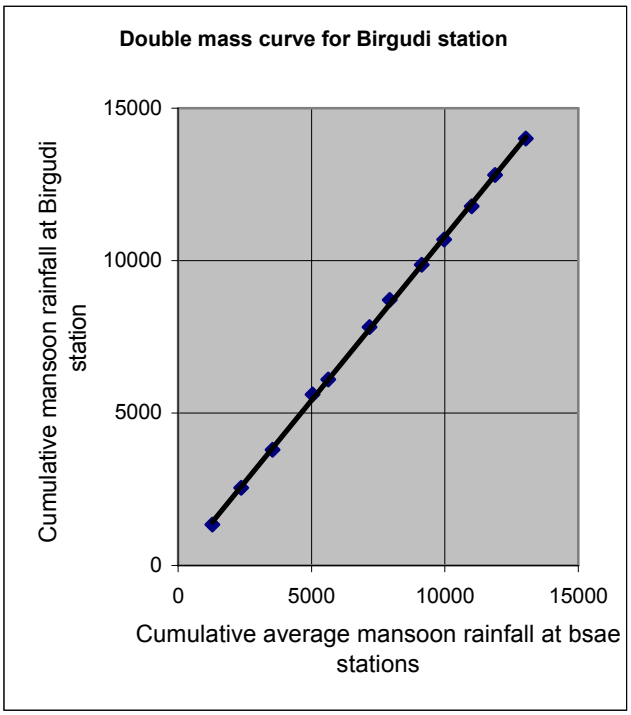

Figure 3.

6. Adequacy of Raingauge stations

The adequacy of the number of gauges in the existing network may be ascertained following the procedure given by Indian Standards. The optimum numbers of raingauges N is given by the equation-

$$N = \left[\frac{Cv}{P}\right]^2$$

where P is allowable degree of error in estimating the average depth of rainfall over the area and C_v is the coefficient of variation of the rainfall recorded at the m existing raingauge stations given by $(S_x / X_{av})X100$. If N<m, the existing network estimates the average depth of rainfall with an error less than the allowable value of P and no more gauges are required. If N>m, the additional gauges required is given by (N-m), rounded off to the next highest integer. In MRP complex there are 8 raingauges, hence m=8, and taking the allowable degree of error P=5%, the calculation for adequacy of number of gauges in the existing network is given below:

The annual average rainfall of the 8 existing raingauge stations of MRP complex are given in following table-

S.N.	Raingauge Station	Annual Rainfall (X)
1	Gangrel	1249.61
2	Mahud	1102.98
3	Murumsilli	1261.83
4	Dudhawa	1159.37

5	Birgudi	1274.75
6	Bhanup.	1427.13
7	Kanker	1042.98
8	Keskal	1257.05

Mean of the rainfall at the existing 8 gauges is given by

$$X_{av} = \frac{1}{m}\sum X$$
$$= 9775.70/8$$
$$= 1221.96$$

The standard deviation of the rainfall is given by

$$S_x^2 = \frac{\sum (X - X_{av})^2}{m-1}$$
$$S_x^2 = 14082.1$$
$$S_x = 118.66$$
$$C_v = \frac{S_x}{X_{av}} \times 100$$
$$= 9.71$$
$$\mathrm{P} = 5\%$$
$$N = \left[\frac{Cv}{P}\right]^2$$
$$= 3.77$$
$$\approx 4$$

as N< m i.e. the number of existing raingauges are more than the optimum number of raingauges hence the number of existing raingauges are adequate.

7. Conclusion

In MRP complex earlier there were eight raingaue stations and the average depth of rainfall was calculated on the basis of these raingauge stations. After 1994 two raingauge stations were replaced due to nonavailability of records. Hence it is required to reconstruct the average depth of rainfall on the basis of new raingauge stations. Out of the three methods of calculating the average depth of rainfall over a catchment the Thiessen polygon method was found suitable and is used for calculating the average depth of rainfall in the catchment of different reservoirs of the MRP complex. The thiessen weight for the raingauge stations in new system has been calculated and shown in table 2, 5, and 6. The change in the thiessen weight of the common raingauge stations in old and new system have been observed which is due to the change in the shape of the thiessen polygon. The rainfall records have been checked for consistency and were found consistent The adequacy of the number of gauges in the existing network have been checked and it was found that the number of gauges are adequate. The new thiessen weight for different raingauge stations calculated in this paper will be used for the generation of rainfall series for the different reservoir basins of MRP Complex.

References

[1] Central Water and Power Research Station, Khadakwasla, Pune (India). "Development of Decision Support System for Mahanadi Project", *Final Report* (Feb. 1994).

[2] Govt. of Madhya Pradesh, "M.P. Major Irrigation Project - Mahanadi Project", Feb. 1990.

[3] Govt. of Chhattisgarh, "Mahanadi Reservoir Project (Major Irrigation Project) – "Water Resources Department", January 2001.

[4] Linsley R.K., Kohler M.A., Applied hydrology, Mc Graw Hill.

[5] K. Subramanya, Engineering hydrology, Tata Mc Graw Hill.

[6] Verma, M. K. (2000), *Ph. D. Desertation,* Devi Ahilyabai University, INDORE (M.P).

[7] Ven Te Chow, Applied Hydrology, Mc Graw Hill.

Laboratory Performance Evaluation of Stabilized Black Cotton Soil with Rice Husk Ash

Laxmikant Yadu
Civil Engineering Department, N.I.T. Raipur, Raipur, India
lkyadu.ce@nitrr.ac.in

Rajesh Kumar Tripathi
Civil Engineering Department, N.I.T. Raipur, Raipur, India
rajesh_tripathi64@yahoo.co.in

Dharamveer Singh
School of Civil Engineering and Environmental Science
University of Oklahoma, Norman, Oklahoma, USA,
dvsingh@ou.edu

Abstract

A laboratory study was undertaken to evaluate the performance of Black Cotton (BC) soil stabilized with Rice Husk Ash (RHA). BC soil, A-7-5 type was collected from borrow area in Raipur District, India. Using various percentages of RHA (3, 6, 9, 11, 13 and 15 %) and employing as criteria California Bearing Ratio (CBR), Free Swell Index (FSI) and Plasticity Index (PI) the optimum amount of RHA (11 %) was obtained. Laboratory test results indicated a tremendous improvement in terms of increase in strength and reduction in expansion characteristics of BC soil with the addition of RHA. In addition, the optimum moisture content (OMC) and maximum dry density (MDD) tests were conducted for different soil-RHA combinations using modified proctor test. It was found that for RHA stabilized soil the OMC increased and the MDD decreased with increasing percentage of RHA. Significant change in the plasticity index has been observed; which shows a manifestation of the ameliorating effects of stabilization. Finally, a cost analysis of pavement was carried out by designing a pavement according to Indian Road Congress (IRC) Rural Road Manual Special Publication (SP): 20 specifications. It is observed that selected optimum amount of RHA (11%) decreases the cost of pavement by approximately 20% per kilometer of length. These findings, by using RHA as a cost effective locally available material, will be useful for highways engineers for construction of pavement.

Keywords- Expansive Soil, Stabilization, Rice Husk Ash, Compaction, California Bearing Ratio.

Broad Area- Civil Engineering.

Sub-Area- Soil Stabilization.

1. Introduction

Use of various waste products in civil engineering construction have attained considerable attention in view of the shortage and high cost of suitable conventional materials. Increasing cost of waste disposal and environmental aspect forced construction Engineers to use various waste products in suitable areas. Rice husk is a major agriculture by-product obtained from the peddy. Rice husk is popularly use as a fuel in small power plants, brick kiln and brick clamps and these are the major source of Rice Husk Ash (RHA). Chemically, RHA consist of more than 80 % of Silica. The high percentage of siliceous materials in the RHA makes it good material for stabilization [1], [6], [10].

Several researchers have conducted laboratory studies on RHA stabilized soils. Muntohar (2002) conducted a series of tests namely physical and index properties, compaction, California bearing ratio (CBR), consolidation, and unconsolidated undrained triaxial test on expansive clay properties of soil to access the effect of RHA (amount varied from 7.5, 10, and 12.5%). RHA was blended with lime as lime pozzolana mix. It was observed that liquid limit decreased whereas, plastic limit increased. RHA-lime mixture achieved considerably reduction of PI and swelling potential. The addition of RHA increased the OMC and diminished the MDD. CBR value increased by addition of RHA but lime has greater potential to increase the CBR.

An experimental investigation was made by Noor et al. (1993) to access the effect of cement – rice husk mixtures on compaction, strength and durability of Melaka series lateritic soil. They observed that OMC increased while MDD decreased with increased content of RHA.

A residual granite soil, typical of Malaysian residual soils was used in the study by Ali et al. (1992) with RHA as an additive to evaluate geotechnical properties of chemically stabilized soils. From the study they concluded that, addition of RHA alone decreases the MDD; whereas it increases the OMC. The development of unconfined compressive strength (UCS) of lime and cement stabilized

residuals soil not only enhanced by adding RHA but also shows higher initial rate of strength development. A stabilized soil should be durable and from their study they observed that addition of RHA with lime produces stronger and more durable samples as compared with those samples treated with lime only.

A study on laterite soil treated with RHA by Alhassan (2008) showed a general decrease in MDD and increase in OMC with increase in RHA content, moreover an improvement in CBR and UCS compared with natural soils was reported. Bhasin et al. (1985) reported an improvement in the soaked CBR of soil on addition of RHA and lime sludge. Rahman (1987) studied the effects of various mix proportions of cement and RHA on geotechnical properties e.g. Atterberg limits, compaction characteristics, UCS, CBR and swelling of lateritic soils. From the test results it was concluded that these lateritic soils stabilized with cement – RHA mixtures can be used in pavement.

Roy and Chattopadhyay (2008) studied the effect of cement on alluvial soil with pond ash and RHA on Atterberg limits, compaction, UCS, unsoaked and soaked CBR, and observed significant improvement in terms of soaked CBR and PI without addition of cement. This is indicated the utilization of maximum quantity of waste materials as a cost effective mix with virgin soil (Roy and Chattopadhyay 2008). Jha and Gill (2006) evaluated the effect of RHA on lime stabilization by conducting compaction, CBR, UCS and durability test and observed considerable improvement of the lime stabilization by using RHA.

All above studies motivated to initiate the laboratory study on BC soil to evaluate the potential of RHA alone as an additive and to find the cost effective mix proportion. Furthermore, the cost analysis of rural road was done by designing pavements using IRC: SP: 20 – 2002.

2. Laboratory Investigations

2.1 Collection of Materials

The raw soil samples collected from borrow area located at Tatibandh–Atari road (District Raipur, Chhattisgarh-India). RHA was obtained from clay brick kiln situated at Village Sarona (District Raipur India), about 1 km. from Tatibandh–Atari road.

The raw soil and RHA properties were evaluated in accordance with the Bureau of Indian Standards (BIS) in laboratory. The raw soil was identified as inorganic fine grained expansive (Free Swell Index value 83%) soil with blackish gray in color. The specific gravity and pH value of raw soil were evaluated as 2.63 and 8.02, respectively. The liquid limit (LL), plastic limit (PL), and plasticity index (PI) of the raw soil were found 47%, 30%, and 17%, respectively. As referred to the Indian Standard and AASHTO, soil classification system the soil was classified as CI-MI and A-7-5 with 4% Group Index (GI) value. Properties of raw soil are given in Table 1. RHA was identified as Non-Plastic (NP) material with 94% LL and having low specific gravity 2.039 but high pH value: 9.20 as compared to raw soil. These properties are tabulated in Table 2.

Table 1. Properties of Raw Soil

Soil Property	Results	Test Procedure
Field Moisture content (%)	2.87	IS : 2720 (Part 2) - 1973
Liquid Limit (%)	47	IS : 2720 (Part 5) - 1985
Plastic Limit (%)	30	IS : 2720 (Part 5) - 1985
Plasticity Index (%)	17	IS : 2720 (Part 5) - 1985
Specific Gravity	2.63	IS : 2720 (Part 3) - 1985
Maximum Dry Density (gm/cm^3)	1.9	IS : 2720 (Part 8) - 1983
Optimum Moisture Content (%)	11.86	IS : 2720 (Part 8) - 1983
California Bearing Ratio (%)	4.08	IS : 2720 (Part 16) - 1987
F S I (%)#	83	IS: 2720 (Part 40) - 1977
pH Value	8.02	IS : 2720 (Part 26) - 1987
AASHTO Classification*	A-7-5 (4)	AASHTO M145-91(2004)
ISSCS Classification**	CI-MI	IS : 1498 - 1970

#FSI – Free Swell Index
*AASTHO -
**ISSCS - Indian Standard Soil Classification System

Table 2. Properties of Rice Husk Ash

Soil Property	Result	Test Procedure
Liquid Limit (%)	93.99	IS : 2720 (Part 5) - 1985
Plastic Limit (%)	NP	IS : 2720 (Part 5) - 1985
Specific Gravity	2.04	IS : 2720 (Part 3) - 1985
Maximum Dry Density (gm/cm^3)	0.71	IS : 2720 (Part 8) - 1983
Optimum Moisture Content (%)	45.52	IS : 2720 (Part 8) - 1983
California Bearing Ratio (%)	15.02	IS : 2720 (Part 16) - 1987
pH Value	9.2	IS : 2720 (Part 26) - 1987

2.2 Moisture Density Relationship

The soil collected from the site was pulverized with wooden mallet to break lumps and then air-dried. Processing of RHA was done on the similar line as that of raw soil. A number of soil-RHA combinations were used to determine the moisture density relationship as shown in Table 3 in accordance with IS:2720 (Part 8) - 1983. From the Table 3, it is conferred that OMC increased and MDD decreased with increasing percentage of RHA which is consistent with observations reported by Ali et al. (1992) and Noor (1993) and recently by Muntohar (2002), Alhassan (2008) and Roy and Chattopadhyay (2008).

Table 3. OMC and MDD of Raw and RHA Stabilized Soil

Additive	Additive (%)	OMC (%)	MDD (gm/cm^3)
Raw Soil	0	11.86	1.9
RHA (%)	3	12.92	1.83
	6	14.83	1.78
	9	15.96	1.75
	11	16.63	1.72
	13	17.24	1.69
	15	19.43	1.63

2.3 Determination of Optimum Amount of RHA

A number of approaches have been used in past to determine the optimum amount of soil additive mixture. Most commonly used approach is acceptable reduction of PI, increase of CBR and swell reduction potential. Optimum amount of soil additive mixture refers the amount of RHA at which it gives the most acceptable stabilization limit in terms of reduction of PI and swelling potential and strength enhancement of raw soil. In the present study, the selection of optimum amount of RHA was based on the strength test (CBR), PI and FSI.

To access the effect of expansive clay properties, the RHA was blended with soil in six different percentages: 3, 6, 9, 11, 13, and 15 %. A series of laboratory tests were conducted namely the physical and index properties, compaction and CBR. Consistency limits of the soil and blended materials were evaluated in accordance with IS: 2720 (Part 5) – 1985. Variation of PI with six different percentages of RHA mixes is shown in Figure 1 which is similar to observation reported by Muntohar (2002) and Roy and Chattopadhyay (2008). Specific Gravity of raw soil and RHA mixes were found in laboratory in accordance with IS: 2720 (Part 3) – 1985 (Figure 2).

Free Swell Index (FSI) and pH value of raw soil and blended material were evaluated in accordance with IS: 2720 (Part 40) – 1977 and IS: 2720 (Part 26) – 1987, respectively as shown in Figure 3 and Figure 4. The FSI decreases with addition of RHA as shown in Figure 3. However, no further reduction in swell index was observed after 11 % of RHA. Similarly, pH value reaches a constant value after 11 % of RHA.

CBR test was conducted on the raw soil as well as on blended material for evaluating the optimum amount of RHA. The CBR tests were conducted on samples compacted at OMC, and soaked for 96 hours in accordance with IS: 2720 (Part 16) – 1987. Variation of the soaked CBR value with RHA mixes is shown in Figure 5 which is consistent with observation reported by Bhasin et al. (1985), Rahman et al. (1987), Muntohar (2002) and Roy and Chhatopadhayay (2008). It was observed that CBR value increases with addition of RHA up to a certain point, after that it starts decreasing. Using FSI, PI and CBR parameters the optimum amount of RHA was chosen as 11 %.

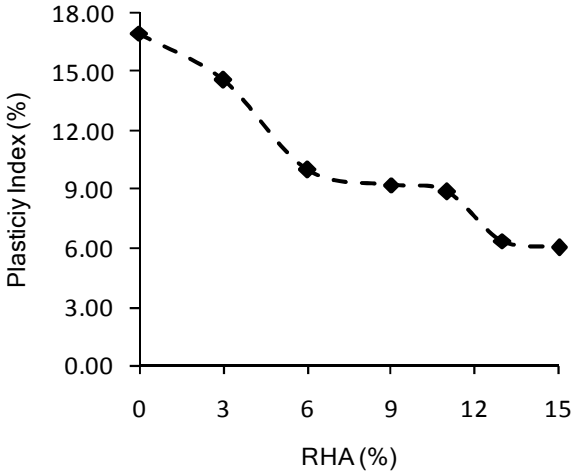

Figure 1. Plasticity Index of RHA Mixes

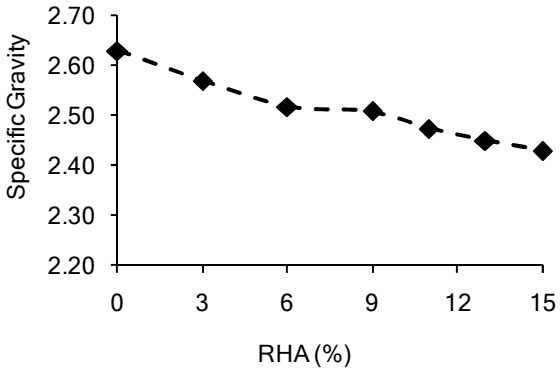

Figure 2. Specific Gravity of RHA Mixes

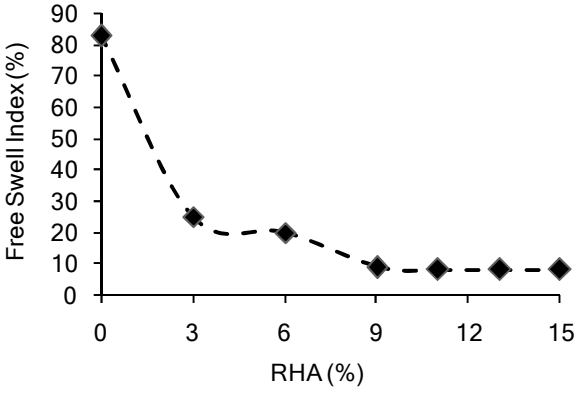

Figure 3. Free Swell Index of RHA Mixes

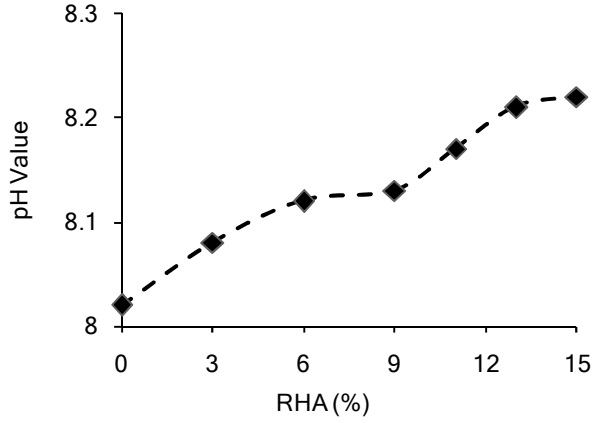

Figure 4. pH value of RHA Mixes

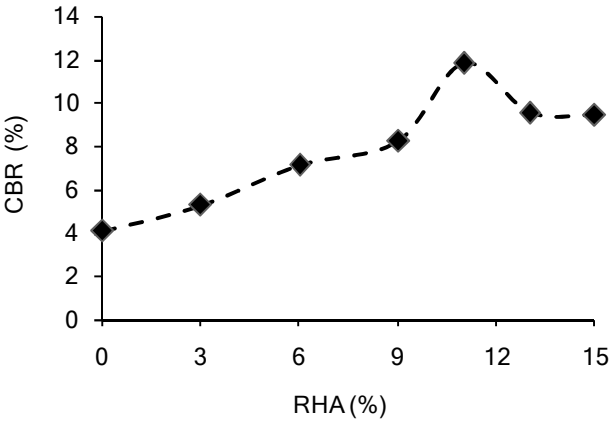

Figure 5. Soaked CBR of RHA Mixes

3. Presentation and Discussion of Results

3.1 Effect of RHA on Physical and Index Properties

As shown in Figure 1, it was inferred that PI decreased from 17% for raw soil to 6 % for 15 % RHA additive which is similar to observation reported by Muntohar (2002) and Roy and Chattopadhyay (2008). Specific gravity of the raw soil was also having the same trend as PI as shown in Figure 2. Since specific gravity of the RHA (2.039) was considerably low as compared to raw soil (2.63) which leads reduction of specific gravity of the blended material. pH value of raw soil and RHA was found 8.02 and 9.20, respectively. Due to higher pH value of RHA, pH value of blended material was increased, corresponding to the increasing proportion of RHA in soil as shown in Figure 4.

3.2 Effect of RHA on Free Swell Index

Figure 3 shows the effect of RHA on free swell index properties of raw soil, which is similar to observation reported by Muntohar (2002). Initially, FSI of raw soil was 83%, after addition of 3% RHA it tremendously reduces to 25%. Further addition of RHA, FSI of soil reduces significantly. FSI reduces significantly at 11 % RHA. After 11% RHA, no reduction was observed in FSI. The reduction in FSI of soil is expected as higher silica content of RHA reacts with calcium hydroxide (CaOH) content of raw soil (Muntohar 2002). Due to reduction in amount of CaOH in soil, FSI of soil reduces significantly.

3.3 Effect of RHA on Compaction Properties and CBR

The variation of MDD and OMC with RHA contents are shown in Table 3. The MDD decreases while the OMC increases with increase in the RHA content. The decrease in the MDD can be attributed to the replacement of soil by the RHA in the mixture which has relatively lower specific gravity (2.039) compared to that of the raw soil which is 2.630 (Ali et al. 1992, Jha and Gill 2006). The decrease in the MDD may also be explained by considering the RHA as filler with lower specific gravity in the soil voids (Alhasan 2008). The increase in OMC due to addition of RHA, may be caused by the absorption of water by RHA (Ali et al. 1992, Jha and Gill 2006). This implies more water is needed in order to compact the soil with RHA mixtures.

CBR is widely used in the design of base and sub base materials for pavement. CBR test is one of the common tests for evaluating the strength of stabilized soils. The variation in CBR value with addition of RHA from 0 to 15% is shown Figure 5. CBR value of raw soil increased from 4.08 % to 11.83 % with addition of 11% RHA. It slightly dropped at 13% RHA and remains constant at 15% RHA. The initial increase in the CBR is expected because of gradual formation of cementitious compounds between the RHA and CaOH present in the soil. The gradual decrease in the CBR after 11% RHA is due to excess RHA that was not mobilized in the reaction, which consequently occupies spaces within the sample and therefore reduces bond in the soil and RHA mixtures (Jha and Gill 2006, Alhassan 2008).

3.4 Effect of RHA on Construction Cost of Pavement

Traffic survey was conducted on the Tathbandh-Atari rural road on the peak season for 24 hours for three days: working day, holiday, and market day for evaluation of design traffic of the road in accordance with IRC: SP: 20 - 2002. Details of the traffic survey are shown in Table 4.

As per IRC: SP: 20-2002 the design traffic was considered in terms of the future traffic to be carried during the design life of the road. Its computation involved estimation of the initial volume of commercial vehicles per day, traffic growth rate and design life in years. In case of rural roads the commercial vehicles will be trucks, buses and tractor-trolley. The traffic for the design life was computed from Equation 1 in accordance with IRC: SP: 20-2002.

$$A = P(1 + r)^{n+x} \quad (1)$$

where,
A = Number of commercial vehicles per day for design
P = Number of commercial vehicles per day at last count
r = Annual growth rate of commercial traffic (%)
x = Design life in years
n = Number of years between the last count and the year of completion of construction

For evaluating the design traffic, parameters were assumed as:

r = 6%,
x = 10 Years (as per IRC SP: 20-2002),

Commercial Vehicle Per Day (CVPD) = 34 Nos.,

n = 2 years

$$A = 34\ (1+0.06)^{10+2} = 68.41 \approx 69 \text{ Nos.}$$

As per number of commercial vehicle per day (69 Nos.), Curve C (range of commercial vehicle per day 45 - 150) was chosen from traffic classification in accordance with CBR curves for flexible design chart IRC SP:20- 2002.

Table 4. Traffic Survey

Period	Fast/Power Driven Vehicles					Remarks
Date	Cars/ Jeep/ Taxies/ Van/ Three Wheelers	Light Commercial Vehicles	Two Axles Truck Tanker	Multi Axles Trucks	Agricultural Tractor	Total
12.04.09	10	5	3	1	15	34
13.04.09	11	4	2	3	14	34
14.04.09	13	5	2	2	12	34
Total Commercial Vehicle Average Per Day = 34 Nos.						

Table 5. Pavement Design and Construction Cost Analysis

Subgrade Type	CBR (%)	Traffic Classification	Total Pavement Thickness (mm)	Thickness of curst (mm)			Cost/ km (Lakhs)
				Sub-base Course	Base course	Surfacing	
Raw Soil	4	Curve C	410	260	150	20	31
Raw soil + 11 % RHA	11.83	Curve C	230	80	150	20	25

Flexible pavement crust was designed for raw soil as a subgrade having CBR 4% and for blended soil with optimum amount of RHA (11 %) as a subgrde having CBR 11.83 % (as shown in Figure 5) in accordance with IRC: SP: 20-2002 guidelines. Total pavement thickness was determined from the CBR curves for flexible pavement design chart with reference to curve C in accordance with IRC: SP: 20-2002 (CBR curves for flexible pavement design chart IRC SP:20-2002 having four curves, namely A, B, C, D according to number of commercial vehicles per day) In the case of raw soil total pavement thickness obtained was 410 mm, while, in case of blended soil with 11% RHA it was 230 mm. Thickness of crest required for both cases were evaluated in accordance with IRC: SP: 20-2002 for traffic classification curve C. Cost analysis were done for both the cases with reference to designed cross-section of the road. Total pavement thickness, thickness of curst required and costs of pavement per km length are shown in Table 5.

From the Table 5, it is evident that optimum amount of RHA (11%) reduces the pavement cost by approximately 20% per km of length; moreover, use of RHA for stabilization of BC soil helps to reduce the adverse impact on the environment and fertility of the adjoining field.

4. Conclusions

Potential of RHA as a stabilizer for a BC soil, A-7-5 types was examined by conducting various tests in laboratory namely atterberg limits, compaction, CBR, swelling potential and pH. Optimum amount of RHA: 11% was found by considering increase in CBR, acceptable reduction of PI and reduction of swelling potential approaches. CBR value increased from 4.08 % of the raw soil to 11.83 % of its stabilized counterpart, and FSI decreased from 83 % to 8%. The change in the plasticity index was observed to be from 17 % to 6 %, a manifestation of the ameliorating effects of stabilization. It indicates a tremendous improvement in terms of increase in strength and reduction in expansion and plasticity characteristics of BC soil. In terms of compaction OMC moved to wet side, and MDD reduced. It inferred that RHA imbibe more water to attain MDD. Finally, from the cost analysis of pavements, it is observed that selected optimum amount of RHA (11%) decreases the cost of pavement by approximately 20% per kilometer. These findings, by using RHA as a cost effective locally available material, will be helpful for highways engineers for construction of pavements. Utilization of waste materials like RHA in bulk quantity in the

construction of road project will be reduced the accumulation hazard and environmental pollution.

Acknowledgment

The authors gratefully acknowledge the contribution of the part time degree course students and technician for their help in conducting laboratory testing.

References

[1] Ali, F.H., Adnan, A., and Choy, C.K. (1992). "Geotechnical Properties of a Chemically Stabilized Soil from Malaysia with Rice Husk Ash as an Additive." Journal of Geotechnical and Geological Engineering, Vol. 10, 117-134.

[2] Alhassan, M. (2008). "Potentials of Rice Husk Ash for Soil Stabilization." AU J. T. 11(4): 246-250.

[3] Bhasin, N.K, Goswami N.K., Oli P., Krishan N., and Lal N.B. (1985). "Utilization of waste material in construction of roads in rural areas." Seminar on road and Road Transport in Rural Area, CRRI, New Delhi. 260-267.

[4] IRC: SP:20 (2002) :- "Rural Roads Manual", Published by the Indian Road Congress, New Delhi, 2002.

[5] Jha, J.N., and Gill, K.S.(2006). "Effect of Rice Husk Ash on Lime Stabilization." Journal of the Institution of Engineers (India), Volume 87, page 33-39.

[6] Muntohar, A.S. (2002). "Utilization of Uncontrolled Burnt Rice Husk Ash in Soil Improvement." Dimensi Teknik Sipil, Vol. 4, No. 2, 100 – 105.

[7] Noor, M. M. J. M., Aziz, A.A., and Suhadi, R.U.R. (1993). "Effect of Cement – Rice Husk Mixtures on compaction, Strength and Durability of Melaka Series Lateritic Soil." The Professional Journal of the Institution of Surveyors Malaysia, Volume 28, No 3.

[8] Rahman, M.A. (1987). "Effects of Cement – Rice Husk Ash Mixtures on Geotechnical Properties of Lateritic Soils." Proceedings of the Japanese Geotechnical Society, Vol.-27, No.-2, 61-65.

[9] Roy, T.K., and Chattopadhyay, B.C. (2008). "A Study on the Effect of Cement on Alluvial Soil Strengthened With Pond and Rice Husk Ash for Construction of Road Subgrade." The 12th International Conference of International Association for Computer Methods and Advances in Geomechanics (IACMAG), Goa, India.

[10] Roy, T.K., and Chattopadhyay, B.C. (2008). "Utilization of Rice Husk Ash and Pond Ash for Improving Subgrade in Road Construction" Journal of Institute of Engineers (India), New Delhi, Vol. - 89, pp 3-6.

Conversion of Domestic Waste Into Fuel By Dry Process - A Case Study

Balasubramanya.N
Professional Institute of Technology, Raipur

Abstract

Human activities generate wastes that are often discarded as they are considered useless. Physically it contains the same materials as that are found in useful products. Hence it is necessary to restore the value so that it terminates to be waste. The experimental study was conducted on a laboratory scale using the pelletisation technique. The pellets were made using corn starch as binder along with varying proportions of vegetable waste, sawdust, leaves litter, coal powder and paper waste. An highest calorific value of 4880 cal/gm with a moisture content of 7.39%, wet bulk density1.11 gm/cc, dry bulk density 1.03gm/cc, durability 92.61%, volatile matter 80.41%, ash content 8%, fixed carbon 4.2% and organic carbon 40.07% was reported. The pellets are modern fuel, bearing reasonably high calorific value which can become a substitution for conventional fuel.

Keywords- Domestic Waste, Dry Process, Conversion, Fuel pellets, ash continents

Broad-Area- Civil Engineering.

1. Introduction

India being a developing country with different life styles, food habits, traditions and socio-economic aspects, is coming out with best disposal options for municipal solid waste. Concerns over consumption of resources have led to calls for, firstly waste minimization or reduction and secondly for ways to recover the materials and energy in the waste, so that they can be reused. The present investigation explores the best energy recovery options available and the technical feasibility for pelletisation of segregated organic waste for Bangalore city.

2. Objectives

The main objective of the present study is to utilize vegetable wastes, dry leaves litter, paper waste, coal powder, saw dust and corn starch which are regarded as useless and convert them into fuel energy by using pelletisation technique. Apart from this, the other objectives include:

a) To minimize the food waste reaching the final destination.

b) To give certain percentage of relief to the energy crisis faced by the community

c) To compare the calorific values obtained from different combination of organic wastes.

d) To study the physical and chemical characteristics of the fuel pellets.

3. Pelletisation technology in India

The conversion of garbage into pellets using the pelletisation technology is gaining more popularity in India. The Indian garbage contains less of plastic, glass, metals as compared to Western and European countries. An informal sector of recycling exists in almost all the cities in India.

A plant of 80 TPD capacity converting garbage to fuel pellets has been constructed at Deonar, Mumbai. The plant is divided into three stages namely, stage1: Sun drying and screening, stage 2: Drying and further separation, stage 3: size reduction, mixing and pelletisation.

4. Material and methods

In the present investigations fuel pellets of 23.5mm. diameter and 27.5mm. height suggested by European Committee for standardisation were used. European Committee for Standardization specifies that the maximum allowable pellet diameter as 25 mm. The diameter of traded pellets is predominantly 6-8 mm. The process of conversion of solid waste into fuel pellets involved drying, removing of non-combustible and recyclable fraction, shredding, mixing with the binder and waste mix was subjected to pelletisation.

5. Results and Discussions

The characteristics namely, mechanical durability, wet and dry bulk densities, ash content, moisture content, volatile

matter, calorific value, fixed carbon, and organic carbon content of fuel pellets were determined.

In all fourteen different combinations of the vegetable waste, saw dust, leaves litter, coal powder, paper waste and binder material, pellets were made and subjected to the characterization of following parameters presented in Table-1.

A detailed study of Table-1 reveals that, highest and lowest calorific values are exhibited by the pellets Di and Dn respectively and they fall in the range of 4880 cal/gm and 4058 cal/gm. The calorific values of fuel pellets were higher than the calorific value of charcoal, reported as 2932 kcal/kg, produced from MSW reported by Bioenergy Lists: Terra Preta. It was also reported by TIDE Technocrats Private Limited that calorific value of fuel produced out of 100% Municipal Solid Waste has almost uniform calorific value of around 3600kcal/kg without adding any additive.

The highest calorific value was observed for the combination De with dry density of 0.62 gm/cc and least density for the combination Dd and Dj with dry density of 0.41gm/cc. The significant variations of calorific values were not observed with the variations of dry bulk density in the dry process.

The mechanical durability varied in a close range of 89.86% to 94.99% for all the pellets, which is an excellent range ensuring that minimum dust emission during handling, transportation and storage. Also there would be least disturbance to the boiler feeding systems and minimum risk to fire and explosion.

Table 1. Characteristics of fuel pellets prepared from dry process.

Sl. no.	Name of pellet	Calorific value cal/gm	Dry bulk density gm/cc	% Durability	% Moisture content	% Volatile matter	% Ash content	% Fixed carbon	% organic carbon
1	Da	4130	0.59	92.63	7.37	59.55	4.81	28.27	46.75
2	Db	4368	0.55	91.58	8.42	72.48	8.90	10.20	51.20
3	Dc	4152	0.48	89.86	10.41	55.66	3.83	30.30	53.43
4	Dd	4515	0.41	92.25	7.75	76.79	6.60	8.86	50.09
5	De	4518	0.62	92.45	7.54	61.91	2.92	27.63	46.75
6	Df	4346	1.02	94.59	5.41	80.59	6.90	7.10	42.30
7	Dg	4552	0.50	94.21	5.79	82.61	7.70	3.90	46.75
8	Dh	4524	0.61	94.89	5.12	82.49	7.20	5.20	42.30
9	Di	4880	1.03	92.61	7.39	80.41	8.00	4.20	40.07
10	Dj	4234	0.41	91.92	8.08	76.92	7.10	7.90	37.85
11	Dk	4184	1.02	94.21	5.79	82.82	9.49	1.90	40.07
12	Dl	4668	1.00	94.62	5.38	85.33	7.50	1.80	42.30
13	Dm	4748	1.06	94.99	5.01	73.55	10.90	10.54	33.40
14	Dn	4058	1.02	92.70	7.30	75.14	9.08	8.48	40.07

The heating value of pellets was further increased to around 4000kcal/kg by adding binder gum additive having higher calorific value.

The highest calorific value was observed for the combination De with dry density of 0.62 gm/cc and least density for the combination Dd and Dj with dry density of 0.41gm/cc. The significant variations of calorific values were not observed with the variations of dry bulk density in the dry process.

The moisture content reported varies in the range of 5.01% to 10.41%. The moisture content determines the quality of the fuel. The present values are fairly low and hence falls under the best quality fuel.

The volatile matter determines the pyrolisis capacity of the solid waste. The high volatile matter content means that most of calorific value would be released due to combustion of volatile matter. The Municipal Solid Waste contains

82.65 wt % volatile matters, paper and cardboards have 88.5 wt% and 73.6 wt % volatile matter respectively. The Peat has 50.3 % volatile matter while plastics volatilized completely in combustor except PVC which has 94.8 wt % volatile matters.

In pellets of different combinations of waste, volatile matter present varies from 55.66% to 85.33%. The Pellet Di with 80.41% of volatile matter has a calorific value of 4880 cal/gm. Therefore pellet Di has high calorific value with higher volatile matter in it. The pellet Dc with volatile matter of 55.66% has a calorific value of 4152 cal/gm. Therefore different pellets of different combinations of waste with high calorific values and with low or high volatile matter can be made to suit the need, to use the pellets as fuel.

The ash is a non-combustible matter and high ash content would result in severe pollution. In the present investigation ash content varies from 2.92% to 10.9%. The pellet De with least ash content of 2.92% gave a calorific value of 4518 cal/gm. The pellet Dm with ash content 10.9% gave a calorific value of 4748% cal/gm. The Municipal Solid Waste with high plastic content consist of 8.76 wt % ash content. The paper and cardboard have 20.2 % and 8.4 % ash content respectively. Coal has 5.7 % ash content. Therefore pellets produced from different combinations of waste produce less of ash thereby causing lesser pollution.

The fixed carbon is the solid combustible residue that remains after a coal particle is heated and the volatile matter is expelled. The fixed carbon varies inversely with volatile matter. The higher percentage of fixed carbon results in the higher calorific value. In the present investigation the percentage of fixed carbon were 28.27%, 30.3%, 27.63% for Da, Dc, and De combinations respectively. The combinations Da, Dc, and De had 59.55%, 55.66% and 61.91% of volatile matter respectively. The calorific values of combinations Da, Dc, &De were 4130cal/gm, 4152cal/gm and 4518 cal/gm respectively. Mumbai pelletisation plant has recorded a fixed carbon of 12.00% - 18.00% and volatile matter 50.00% - 65.00%. Therefore the combinations of pellets in the experiment have higher calorific value and will have better market value.

6. Conclusions

- The calorific values for the pellets tested are very high and can provide relief for the energy crisis.
- The percentage mechanical durability values are very high and hence the pellets can be regarded as high quality fuel with easy handling.
- Volatile matter is high and hence qualities of pellets are suitable for pyrolysis.
- Percentage ash content is reasonable and hence high calorific value, easy to deal the residual product.
- Fixed carbon contents of some pellet combinations are high with high calorific value therefore have better market value.

Acknowledgements

The author appreciates the encouragement& financial assistance received by TEQIP, World Bank (Govt. Of Karnataka) during the course of the investigations.

References

[1] Techno Economic Feasibility report for different Energy Recovery Technologies, December 1999, TIDE Technocrats Pvt. Ltd.

[2] Sylvia Larsson, L.(2008), Doctoral Thesis, “Fuel Pellet Production from Reed Canary Grass” by Sylvia Larsson, Doctoral Thesis, Swedish University of Agricultural Sciences, Umea.

[3] Bioenergy Lists: Terra Preta., April 19, 2007. Conversion of Municipal Solid Waste into Charcoal and Producer Gas submitted by Tom Miles.

[4] Abinayah Shree, M.N., Iyappan.K., Balasubramaniyam, N., and Srinivasa kannan.(2008), Preparation and Chracterisation of Bio Fuel from Industrial Waste.

[5] Sudhir Kumar.(2000), Technology Options of Municipal Solid to Energy Project. June, 2000. TERI Information Monitor on Environment Science 5(1): 1-11.

[6] Nalladurai Kaliyan. & Vance Morey, R.(2009), Factors affecting strength and durability of densified biomass products, Biomass and Bio-energy, 33, 337-359.

[7] http://www.urbanindia.nic.in/quickacess/guidelines of schemes

[8] http://www.wikipedia.org/wiki/fuel pellets

[9] http: // e prints.utm.my/2854/1/75186.pdf

Algorithm for One Dimensional Pattern Matching In DNA Sequences Using Finite Automata

Pawan Kumar Patnaik
Dept. of Computer Science & Engg. BIT, Durg
E-mail: pawanpatnaik@yahoo.com

Jyoti Singh
Chhattisgarh Swami Vivekanand Technical University,Bhiai
Email: jsbhilai@yahoo.com

Manoj Kumar Kowar
Dept. of Electronics & Telecomm. Engg., BIT, Durg
Email: mkkowar@gmail.com

Sanjeev Karmakar
Dept. of Computer Application, BIT, Durg
E-mail: dr.karmakars@gmail.com

Abstract

A new algorithm to search for Pattern matching in DNA sequence using Finite Automata is proposed. The application area of this research work is to develop DNA matching mechanism. DNA is represented in a form of pattern and the main aim is to identify the pattern with the help of Finite automata. Finite automata takes a regular expression and regular expression directly converted to Deterministic Finite Automata (DFA), which will speedup the pattern matching process and reduce execution time. This will also ensure optimum utilization of memory space. The time complexity of the algorithm is O (n*m), but the direct conversion it moves to around θ(n). The algorithm was implemented and compared with some popular pattern matching algorithms and it has shown more enhancement in performance and faster than others.

Keywords- Pattern matching, Deterministic Finite Automata, Execution time, DNA sequence, string matching.

Broad Area- Computer Science & Engineering

1. Introduction

The Finite Automata pattern matching technique can be used in many applications. It is used in DNA fingerprinting, Biometrics and Automatic Speech Recognition (ASR) to find selected patterns. A nucleic acid is that carries the genetic information in the cell and is capable of self-replication and synthesis of RNA. DNA consists of two long chains of nucleotides twisted into a double helix and joined by hydrogen bonds between the complementary bases adenine (A), thiamine (T), cytosine (C) and guanine (G). A succession of any number of nucleotides greater than four is liable to be called a sequence. In the typical case, the sequences are printed abutting one another without gaps, as in the sequence AAAGTCTGAC, going from 5' to 3' from left to right. With regard to its biological function, which may depend on context, a sequence may be sense or anti-sense, and either coding or non-coding. The sequence of nucleotides determines individual hereditary characteristics

A DNA sequence or genetic sequence is a succession of letters representing the primary structure of a real or hypothetical DNA molecule or strand, with the capacity to carry information String searching algorithms, sometimes called string-matching algorithms, are an important class of string algorithms that try to find a place where one or several strings (also called patterns) are found within a larger string or text. Let Σ be an alphabet (finite set). Formally, both the pattern and searched text are concatenations of elements of Σ. The Σ may be a usual human alphabet (for example, the letters A through Z in English). Other applications may use binary alphabet (Σ = {0,1}) or DNA alphabet (Σ = {A,C,G,T}) in bioinformatics. The possible letters are A, C, G, and T, representing the four nucleotide subunits of a DNA strand - adenine, cytosine, guanine, thymine bases covalently linked to phospho-backbone. DNA fingerprint is a method used to identify multilocus DNA banding patterns that are specific to an individual by exposing a sample of the person's DNA to molecular probes and various analytical techniques such as Southern blot analysis. DNA fingerprinting is often used to provide evidence in criminal law cases. Also called genetic fingerprinting. Physiological interaction goes beyond the physical interfaces that a computer has, which would include the input and output devices. Physiological interfaces actually secure and use real body characteristics, including breathing, talking, and height and weight. Some of the top innovations include automatic speech recognition (ASR), virtual reality, cave automatic virtual environments (CAVE), and biometrics Most approximate matchers used for text processing are regular expression matchers.

2.1. String Matching Algorithms

String searching algorithms are an important class of

string algorithms that try to find a place where one or several strings (i.e. patterns) are found within a larger string or text. Let Σ be an alphabet 1(finite set). Formally, both the pattern and searched text are concatenation of elements of Σ. The Σ may be usual human alphabet (A-Z). Other applications may use binary alphabet (Σ = {0, 1}) or DNA alphabet (Σ = {A, C, G, T}) in bioinformatics. Table 1 summarizes the most popular algorithms used for single and multiple pattern matching. Where m is the pattern length and n is the file size. The first thing worth noting is that the relevant body of literature for this problem is the multi-pattern string matching problem, which is somewhat different from the single pattern string matching solutions that many people are familiar with such as Boyer-Moore [1]. For single-pattern string matching, there is a large body of work in which a single string is to be searched for in the text. This processing is used in word processing applications, e.g., in search and-replace operations.

Table 1. String matching algorithm summary

Algorithm	Preprocessing time	Complexity matching time
Naive string search algorithm	0 (no preprocessing)	O((n-m+1) m)
Trie-matching	0 (no preprocessing)	O (m + #pat · n)
Rabin-Karp string search algorithm	θ(m)	O((n-m+1) m)
Finite automata	O(m |Σ|)	θ(n)
Knuth-Morris-Pratt algorithm	θ(m)	θ(n)
Boyer-Moore string search algorithm	O(m)	average O(n/m), worst O(n m)

On the other hand, the multi-pattern string matching problem searches a body of text (in our case an application file such as DNA sequence or a text file regardless it's size) for a set of strings (patterns). One can trivially extend a single pattern string matching algorithm to be a multiple pattern string matching algorithm by applying the single pattern algorithm to the search text for each search pattern. Obviously this does not scale well to larger sets of strings to be matched. Instead, multi-pattern string matching algorithms generally preprocess the set of input strings, and then search all of them together over the body of text. Previous work in precise multi-pattern string matching includes Aho-orasick[2], Commentz- Walter[3], Jan Zdarek and Borivoj Melichar [4], Neetha Sebastian and KAMALA KRITHIVASAN[5].

There has also been even more recent work in imprecise string matching algorithms using hashing and signature based techniques. Although these methods may meet the criteria of having deterministic execution time text, there is a problem of positive matches that must be revivified using a precise string matching algorithm. Thus, the performance of the underlying precise matching algorithm is still important, albeit at a reduced level.

The simplest and least efficient way to see where one string occurs inside another is to check each place that it may contain, one by one, to see if it's there[6] So, first it should be seen if there's a copy of the pattern in the first few characters of the file; if not, we look to see if there's a copy of the pattern starting at the second character of the file; if not, we look starting at the third character, and so forth. In the normal case, we only have to look at one or two characters for each wrong position to see that it is a wrong position, so in the average case, this takes θ(n) steps, where n is the length (size)of the file.

3. The Proposed Algorithm Implementation

In this algorithm directly converting the Regular Expression into DFA, such that due to direct conversion we are able to speed up the pattern matching process and hence also able to optimum utilize the memory space.

3.1 .Description of the algorithm

In this algorithm the four Main functions have been proposed which are important building block of the proposed Algorithm . These functions are :

1.nullable( )

2.firstpos( )

3.lastpos( )

4.followpos( )

These four functions will help us to traverse the syntax tree T . Finally construct DFA from followpos. The functions nullable, firstpos and lastpos are defined on the nodes of the syntax tree and are used to compute followpos , which is defined on the set of positions. Remembering the equivalence between the important Non deterministic Finite Automata (NFA) states and the positions of the leaves in the syntax tree of the regular expression. The ε - transition of the NFA represents some fairly complicated structure of the positions; in particular they encode the information regarding when one position follow the other position. That is, each symbol is input string to a DFA can be matched by certain positions . An input symbol ‘c’ can only be

matched by positions at which there is a 'c', but not every position with a 'c' can necessarily match a particular occurrence of 'c' in the input string . The notion of a position matching an input symbol will be defined in terms of the function followpos() on positions of the syntax tree . If ' i ' is a position, then followpos(i) is the set of positions j such that there is some input string 'cd' such that i corresponds to this occurrence of c and j to this occurrence of d .In order to compute the function followpos , we need to know what positions can match the first or last symbol of a string generated by the given sub expression of a regular expression . If r* is such a sub expression the every position that can be first in r follows every position that can be last in r . Similarly, if rs is a sub expression the every first position of s follows every last position of r . At each node n of the syntax tree of the regular expression we define a function firstpos(n) that gives the set of positions that can match the first symbol of the string generated by the sub expression rooted at n. Likewise we define a function lastpos(n) that can match the last symbol of the string generated by the sub expression rooted at n.

Table 2. Rules for Computing nullable & firstpos

NODE n	nullable(n)	firtspos(n)
N is a leaf labeled ε	true	ϕ
N is a leaf labeled with position i	false	{ i }
	nullable(c1) or nullable(c2)	firstpos(c1) U firstpos(c2)
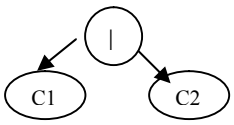	nullable(c1) and nullable(c2)	If nullable(c1) then firstpos(c1) U firstpos(c2) else firstpos(c1)
	true	firstpos(c1)

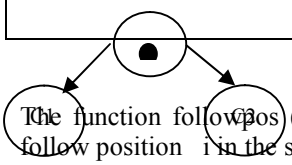

The function followpos (i) tells us what positions can follow position i in the syntax tree. Two rules define all the way one position can follow another.

1. If n is cat node with left child c1 and right c2 , and i is a position in lastpos(c1) then all positions in firstpos (c2) are in followpos(i).
2. If n is a star node and i is a position in lastpos (n) then all positions in firstpos(n) are in followpos(i).

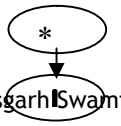

3.1.1 Algorithm For Converting Regular Expression To DFA

Input : A regular expression r .
Output: A DFA that recognizes L(r)
Method :

1. Construct a syntax tree for the augmented regular expression (r)# , where # is a unique end marker appended to (r).
2. Construct the functions nullable , firstpos lastpos and followpos by making depth first traversals of T.
3. Construct Dstates , the set of states of D , and Dtrans , the transition table for D. The states in Dstates are sets of positions ; initially , each state is "unmarked" and a state become marked just before consider its out transitions.

3.1.2 Algorithm For Constructing DFA

Initially, the only unmarked state in Dstates is firstpos(root)
Where root is the root of the syntax tree for (r)# ;
While there is a unmarked state T in Dstate **do begin** Mark T;
For each input symbol a **do begin,** Let U be the set of positions that are in followpos(p)
For some position p in T,
Such that the symbol at position is a ;
If U is not empty and not in Dstate then
Add U as an unmarked state to Dstates;
Dtrans[t,a]:= U
End
End

3.1.3 Algorithm For Construction Of Transition Function

Initially, the only unmarked state in Dstates is firstpos(root)
Where root is the root of the syntax tree for (r)# ;
While there is a unmarked state T in Dstate **do begin**
Mark T;
For each input symbol a **do begin**
Let U be the set of positions that are in followpos(p)
For some position p in T,
Such that the symbol at position is a ;
If U is not empty and not in Dstate then
Add U as an unmarked state to Dstates;
Dtrans[t,a]:= U
End

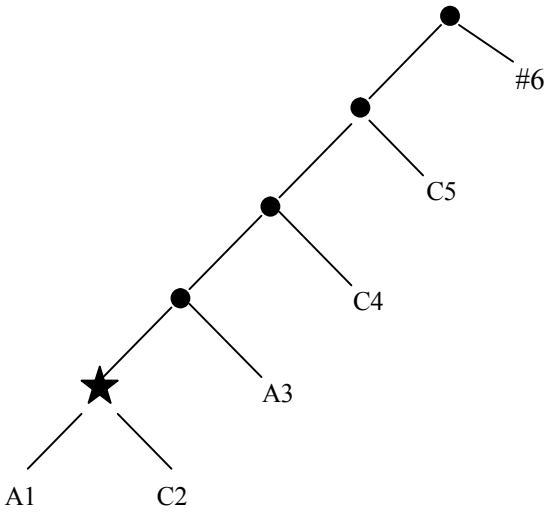

Figure 1. SYNTAX TREE FOR $(A/C)^*$ ACC #

CALCULATION OF THE FOLLOWPOS():

Followpos(1)={1,2,3,}
Followpos(2)={1,2,3,}
Followpos(3)={4}
Followpos(4)={5}
Followpos(5)={6}
Followpos(1)={Φ}
Followpos(1)={1,2,3,}= P

Calculation of the transition function is as follows:

δ(P,A)= δ({1,2,3},A)
= followpos(1) U followpos(3)
={1,2,3) U {4}
={1,2,3,4}= Q

δ(P,C)= δ({1,2,3},C)
= followpos(2)
={1,2,3}=P

δ(Q,A)= δ({1,2,3,4},A)
= followpos(1) U followpos(3)
={1,2,3) U {4}
={1,2,3,4}= Q

δ(Q,C)= δ({1,2,3,4},C)
= followpos(2) U followpos(4)
={1,2,3) U {5}
={1,2,3,5}= R

δ(R,A)= δ({1,2,3,5},A)
= followpos(1) U followpos(3)
={1,2,3) U {4}
={1,2,3,4}= Q

δ(R,C)= δ({1,2,3,5},C)
= followpos(2) U followpos(5)
={1,2,3) U {6}
={1,2,3,6}=S

δ(S,A)= δ({1,2,3,6},A)
= followpos(1) U followpos(3)
={1,2,3) U {4}
={1,2,3,4}= Q

δ(S,C)= δ({1,2,3,6},C)
= followpos(2)
={1,2,3) =P

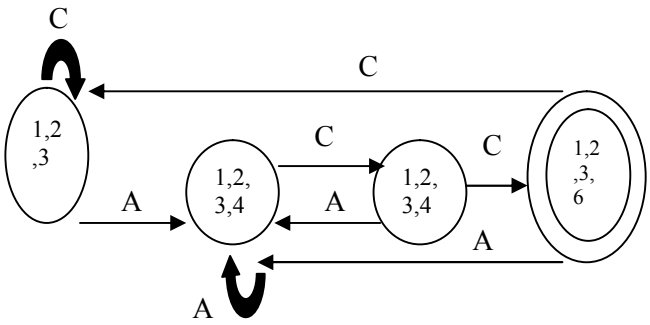

Figure 2. RESULTING DFA

3.1.4 Algorithm For Pattern Matching With The Help Of Finite Automata

Finite Automation Matcher (T,Trans,m)
N←length[T];
Q←0;
For i←1 to n
Do q←trans(q,t[i])
If q=m
Then print " Pattern occurs with shift" i -m

3.2 FA Implementation

The algorithm was implemented using object-oriented programming with C++, and it was tested using different DNA sequence with different filesizes. However, the proposed algorithm is compared with other three algorithms. They are Brute-Force, Trie, and Naïve string search algorithm. These algorithms are selected due to common features with the proposed algorithm as follows:

- Multiple string matching
- No preprocessing operations(and thus no preprocessing time)
- Maintaining different type of files (in contents and sizes).

The implementation and comparison with other algorithms process is carried out When text file size = 1024 bytes, using different patterns and sizes in implementation process. The results are obtained and shown in the following tables.

Authentic DNA Sequences

AGAACGCAGAGACAAGGTTCTCATTGTGTCTCG
CAATAGTGTTACCAACTCGGGTGCCTATTGGCC
TCCAAAAAAGGCTGTTCAACGCTCCAAGCTCGT
GACCTCGTCACTACGACGGCGAGTAAGAACGC
CGAGAAGGTAAGGGAACTAATGACGCGTGGTG
AATCCTATGGGTTAGGATCGTGTCTACCCCAAA
TTCTTAATAAAAAACCTAGGACCCCCTTCGACC
TAGACTATCGTATTATGGACAAGCTTTAACTGT
CGTACTGTGGAGGCTTCAAAACGGAGGGACCA
AAAAATTTGCTTCTAGCGTCAATGAAAAGAAGT
CGGGTGTATGCCCCAATTCCTTGCTGCCCGGAC
GGCCAGGCTTATGTACAATCCACGCGGTACTAC
ATCTTGTCTCTTATGTAGGGTTCAGTTCTTCGCG
CAATCATAGCGGTACTTCATAATGGGACACAAC
GAATCGCGGCCGGATATCACATCTGCTCCTGTG
ATGGAATTGCTGAATGCGCAGGTGTGAATACTG
CGGCTCCATTCGTTTTGCCGTGTTGATCGGGAA
TGCACCTCGGGGACTGTTCGATACGACCTGGGA
TTTGGCTATACTCCATTCCTCGCGAGTTTTCGAT
TGCTCATTAGGCTTTGCGGTAAGTAAGTTCTGG
CCACCCACTTCGAGAAGTGAATGGCTGGCTCCT
GAGCGCGTCCTCCGTACAATGAAGACCGGTCTC
GCGCTAAATTTCCCCCAGCTTGTACAATAGTCC
AGTTTATTATCAAAGATGCGACAAATAAATTGA
TCAGCATAATCGAAGATTGCGGAGCATAAGTTT
GGAAAACTGGGAGGTTGCCAGAAAACTCCGCG
CCTACTTTCGTCAGGATGATTAAGAGTATCGAG
GCCCCGCCGTCAATACCGATGTTCTTCGAGCGA
ATAAGTACTGCTATTTTGCAGACCCTTTGCCAG
GCCTTGTCTAAAGGTATGTTACTTAATATTGAC
AATACATGCGTATGGCCTTTTCCGGTTAACTCC
CTG

The results are obtained and shown in the following tables:

Table 3. pattern= (A/C)* ACC (m=5)

Algorithm	Number of occurrences	Number of comparisons	Comparisons per character
Finite Automata	2	1289	1.187
Brute-Force	2	1388	1.355
KMP	2	1393	1.360
Naïve String Search Algorithm	2	1387	1.354

Table 4 . pattern=(A/G)* CTGG (m=6)

Algorithm	Number of occurrences	Number of comparisons	Comparisons per character
Finite Automata	1	1299	1.156
Brute-Force	1	1409	1.376
KMP	1	1417	1.384
Naïve String Search Algorithm	1	1407	1.374

4. Observation And Result Analysis

After the implementation of the proposed algorithm, the following points could be concluded from the obtained results in table as follows:

- The number of comparisons per character(CPC) which is equal to: (Number of comparisons/file size) can be

used as a measurement factor, this factor affects the complexity time, and when it is decreased the complicity also decreased.

- From the above results we can see that CPC is always around 1, which means that the complexity depends only at the file size. (O (n)).
- If we take in consideration the number of matching (occurrences), we can say that the complexity is less than O(n), since we need less number of comparisons for the second match and less for the third and so on.
- For small, medium and large files complexity remains without changing and still depends on file size.
- The pattern length does not affect the complexity.
- The pattern length and the multiple patterns matching do not negatively affect the algorithm performance.
- The proposed algorithm can suit any type of files with any size.

5. Discussion

5.1 Features Of Proposed Algorithm

The proposed algorithm can be described as quite simple in description and in implementation with following main features:

- The pattern matching process becomes fast as Regular Expression directly get converted to DFA .
- This will also ensure optimum utilization of memory space.
- As compare to other pattern matching algorithms the Time and Space Complexity will be less.
- Good time complexity
- Unlimited size of the pattern.
- Unlimited size of the text file.
- Direct use of Finite Automata technique in the matching process.
- It can be used in different ranges of applications such as: text editors, DNA matching, computer viruses detection, Noise detection (in communication systems).

5.2 Conclusion

A new algorithm to search for pattern matching in DNA sequences using Finite Automata is proposed. The proposed Finite Automata algorithm improves some performance enhancements compared with Brute-Force, Trie- matching, Naïve string algorithms.These enhancements were measured by CPC, and the testing results have shown that Finite Automata algorithm has the minimum value of CPC and less number of comparisons.

References

[1] R. S. Boyer and J. S. Moore. A fast string searching algorithm. Communications of the ACM, 20(10):761–772, 1977.

[2] [Aho, A. V., and M. J. Corasick, ‘‘Efficient string matching: an aid to bibliographic Search,’’ Communications of the ACM 18 (June 1975), pp. 333 340.

[3] Commentz-Walter, B, ‘‘A string matching algorithm fast on the average,’’ Proc. 6th International Colloquium on Automata, Languages, and Programming (1979), pp. 118 132.

[4] Jan Zdarek and Borivoj Melichar, Two-Dimensional Pattern Matching by Finite Automata. LNCS 3845,2008,PP 329-340

[5] Neetha Sebastian and KAMALA KRITHIVASAN Inference of Regular Expressions from a Set of Srings using Pattern Automation, Journal of Combinatorics, Information and System Sciences, Vol 33, Nos. 3-4, pages 307-322, 2008

[6] S.Wu and U. Manber. A fast algorithm for multi-pattern searching. Technical Report TR-94-17, Department of Computer Science, University of Arizona, 1994.

Fractal Image Compression by Multi-Scale Domain Classification Using Fractal Dimension Based On Block Complexity

Amit Kumar Biswas
Bhilai Institute of Technology, Durg (C.G.), India
e-mail: biswas_amit@rediffmail.com

Sanjay Sharma
Bhilai Institute of Technology, Durg (C.G.), India
e-mail: ssharma_bit@yahoo.co.in

Manoj Kumar Kowar
Bhilai Institute of Technology, Durg (C.G.), India
e-mail: mkkowar@gmail.com

Jyoti Singh
CSVTU, Bhilai, India
e-mail: jsbhilai@yahoo.com

Abstract

Fractal Image compression is a relatively new area in the research field and a rapidly growing technique based on the representation of an image by a contractive transform, on the space of images, for which the fixed point (reconstructed image) is close to the original image. The work is intended to provide an approach on this process by introducing the idea of multi-scale Domain-pool classification using Fractal Dimension (FD) based on complexity of the image. A pre-processing analysis of the image by FD to identifies the complexity of each image block for classification. The performance of this idea, evaluated by means of fidelity versus encoding time and amount of compression, and is compared with two image compression method.

Keywords- Fractal Image Compression, Fractal Dimension, Image Encoding, Domain-Pool, Encoding Time.

Broad Area- Computer Engineering

Sub-Area- Image Processing

1. Introduction

Data compression plays an important role in computational practices especially in image analysis and transmission due to heavy memory requirement for storing and retrieving images. The goal of image compression is to reduce storage space and to save transmission time. With the development of multimedia system, Biometric Security system the image database is growing continuously. The growth of the image database and the intense use of internet have enhanced the necessity of efficient storage and fast retrieval of images [1]. There are several methods to compress images and new researches have appeared in this direction. Fractal compression can be considered as one of this new form [2]. A more detailed description of fractal encoding method, the notation used and a description of basic implementations can be found in [3]. In this direction several researches have subjected to improve the Compression Ratio, Time Reduction and Image Fidelity [4]. An attempt has been made through the present work to exhibit that the image fidelity can be improved by considering the local image complexity for domain blocks classification by applying the constant contractive factor. Fractal Dimensions (FD) have been processed to characterize roughness in images. The FD could be used to obtain shape information and to distinguish between smooth (small FD) and sharp (large FD) regions of the image [6]. In other words, pre-processing local FD of the image makes it possible to generate separate sets of domain pools depending on the image complexity. To derive the contractive transformation codes for the encoding process, consider only the elements on domain pool of the same FD as range block and consequently improve the encoding time. Similar ideas are explored in some of the recent works to reduce the encoding time [12] [13] [14].

This communication reports experimental results on commonly used gray scale images: *Lena, Cameraman, Columbia, Goldhill,* and *Couple* by BARNSLEY's algorithm, FISHER's algorithm and the proposed algorithm. Section 2 explains the mathematical foundation of the Fractal coding for the proposed method. Section 3 demonstrates experimental results. Section 4 provides the conclusion.

2. Encoding Using FD

As a model for the gray scale images, a space S of function $f: A \rightarrow G$ has been considered**,** where the set A is taken as

the set of spatial coordinates of the image while *G* represents the set of intensity values of the image. A metric *d* is used such that (*S, d*) is a complete metric space. The fractal coding of an image *F*(*N* x *N*), finds a contractive mapping *T* on *(S, d)* whose fixed point *F = T(F)* exists and is unique (by the contractive mapping fixed point theorem). The fractal encoding process consists of the construction of the operator *T*, which will be defined by matching the better range and domain couple of the original image.

Let *Ri* and *Di* be two subsets on *F*. *Ri* is called Range formed from partitioning (*n* x *n)* non-overlapping region on *A* and *Di* (2*n* x 2*n*) is formed, also by subset of *A* but which may overlap. Let *ti: Di* → *Ri* be a c*ontraction* defined by matching the better *ti* (*Dj*) for each *Ri*, which means that *ti* is chosen such that the distance *d*(*Ri, ti* (*Dj*)) is as small as possible. The operator *T* is given by

$$T = \sum_{i=1}^{(N/n)^2} t_i(F)$$

Considering the contractive factor *s* of the collage theorem **[2]** and fixed point *X* (attractor), then

$$d(F,X) \le \frac{d(F,T)}{1-s}$$

By the Collage theorem an upper limit of the distance between the original image *F* and its reconstructed image *X* is obtained as a function of the contractive factor *s* of *T*. Several researchers have used the scheme where a digital image is partitioned into square range blocks (say *n* x *n* pixels) and larger square domain blocks, probably twice the size of the range blocks [7]. This scheme makes the compression process simple with the contractive factor fixed at s=1/2**.** So by the collage theorem

$$d(F,X) \le 2d(F,T).$$

If the contraction of T is reduced to s=1/3, 1/4, 1/5 or 1/6, then by the above theorem the upper bound to d(F,X) will decrease to

$$d(F,X) \le \frac{3}{2}d(F,T), d(F,X) \le \frac{4}{3}d(F,T)$$

$$d(F,X) \le \frac{5}{4}d(F,T), d(F,X) \le \frac{6}{5}d(F,T)$$

respectively, and it is expected that the attractor *X* should look (each time more) quite like *F*, with these new set of contraction *s*. This is the main idea of the present work and in this paper only the contractive factor *s=1/4* has been considered for different domain classes based on image complexity value. The choice of contractive factor *s=1/4*, gives the average image complexity and equal distribution of domain blocks in each classes. The main idea of this paper is to classify the domain blocks based on image complexity value. Let *D* be a collection of subsets of *Dj* from which the better matching are chosen. *D* consisted of *m* x *m* pixels. The number of elements on *D* determines how much computation time the encoding may take for finding *ti*(*Dj*) for each *Ri*. For encoding, the mapping must be specified and the better domain squares *Dj* must be chosen from a set of potential candidates. The choice of the domain pool as *4n* x *4n* for each *n* x *n* range block, reduced the computation required for a brute force search **[5]** minimizing image quality reduction.

Local FD has been used here to subdivide the domain blocks into classes of complexity (Figure 1). Some methods on FD estimation do not give satisfactory result in all range of FD for images (here consider the range 0 to 2). For fast FD evaluation a simple and efficient algorithm has been used **[6]**. We use four levels of complexity, based on the DF of each image part:

$$0 \le FD \le .5, \quad .5 < FD \le 1$$

$$1 < FD \le 1.5, \quad 1.5 < FD \le 2$$

For the mapping t_i to be specified, domain blocks D_j must be chosen from a class of potential candidates, i.e. a class with same FD of the range. All the images have been treated as ideal fractal models. In the context of this analysis, the corresponding blocks represent semi-fractal behavior. However, the problem of finding the real fractal dimension of the image blocks have not been addressed, it is only a way for classify them by using its local complexity **[10]**.

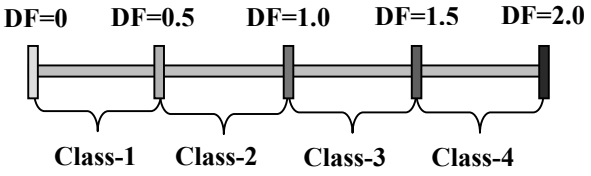

Figure 1. Relating the Domain Pool and FD with the Domain Class

3. Performance Evaluation

The performance of this proposition, evaluated by means of fidelity versus encoding time, is compared with the brute

force algorithm [5], [8] and the adaptive quadtree method [9]. On FISHER's program [9] the default flags (7 bits for the offset factor and 5 bits for the scaling factor), and 4 x 4 Range blocks (no Quadtree scheme) have been used. Figure 2 represents the compressed the image quality on reconstruction of five images, namely Lena, Cameraman, Goldhill, Columbia and Couple using the proposed methodology. Similar results for the other two methods have been presented for comparison (Figure 3 and Figure 4). All images have 128 x 128 pixels and 256 gray levels. For quality verification, the results of subtraction operation between the original image *F* and its reconstructed image *X* have also been presented in these figures. In order to compare the performances of the developed model and the existing models, parameters of the encoding process, viz., Encoding time, the Root Mean Square Error (RMSE), the Signal to Noise Ratio (*SNR)*, the Peak Signal to Noise Ratio (*PSNR)* and the Compression Ratio on bits per pixel of the image have been depicted in the Table 1, Table 2 and Table 3. These parameters are defined as:

$$e(x,y) = F(x,y) - A(x,y)$$

$$RMSE = \frac{1}{N}\sqrt{\sum_{x=1}^{N}\sum_{y=1}^{N}(e(x,y))^2}$$

$$SNR = \frac{\sum_{x=1}^{N}\sum_{y=1}^{N}(A(x,y))^2}{\sum_{x=1}^{N}\sum_{y=1}^{N}(e(x,y))^2}$$

$$PSNR = 20\log_{10}\frac{2^p - 1}{RMSE}$$

where p is the number of bits per pixel of the image.

Table 1. Performance of the proposed method (local Fractal Dimension with blocks of size 4 x 4 and s = 1/4) on the set of test images. Each image is represented by a file with 25600 bits. The compression ratio for all images is 1.5625 *bpp* (bits per pixel)

Image Name	Time (s)	RMSE	SNR	PSNR (dB)
Lena	25.782	14.580	11.703	**35.220**
Cameraman	30.891	17.315	10.123	**36.777**
Columbia	31.906	23.703	8.502	**33.948**
Goldhill	59.563	17.315	12.205	**34.472**
Couple	22.422	20.891	11.913	**32.697**
Average	**34.112**	**18.7614**	**10.889**	**34.623**

Table 2. Performance of BARNSLEY'S PROGRAM [5] for the same images. Each image is represented by a file with 57376 bits. The compression ratio for all images is 3.5020 bpp (bits per pixel)

Image Name	Time (s)	RMSE	SNR	PSNR (dB)
Lena	469.404	7.616	13.347	**30.495**
Cameraman	469.355	14.010	8.188	**23.283**
Columbia	469.385	16.393	5.347	**23.83.7**
Goldhill	469.375	6.797	13.435	**31.483**
Couple	469.313	13.681	8.340	**25.408**
Average	**469.366**	**11.700**	**9.731**	**27.667**

Table 3. Performance of FISHER's program [9] for the same images.

Image Name	Time (s)	RMSE	SNR	PSNR (dB)	Compr -ession
Lena	0.273	10.634	9.736	27.596	**1.4282**
Camera-man	0.212	18.088	6.624	22.982	**1.4058**
Columbia	0.261	17.926	4.917	23.061	**1.4180**
Goldhill	0.262	9.837	9.429	28.273	**1.4360**
Couple	0.248	17.336	6.691	23.351	**1.4375**
Average	**0.251**	**14.764**	**7.479**	**25.053**	**1.4251**

Figure 2. Five test images used in the experiments (First Column); Reconstructed images using Local Fractal Dimension with Range Block of size 4 x 4 pixels, s=1/4 (Second Column); Difference image for quality verification: 5.||e(x; y)|| (Third Column); and ||5. e(x;y)/2 + 127|| (Fourth Column).

Figure 3. Five test images used in the experiments (First Column); Reconstructed images using BARNSLEY's program (Second Column); Difference image for quality verification: 5.||e(x; y)|| (Third Column); and ||5. e(x;y)/2 + 127|| (Fourth Column).

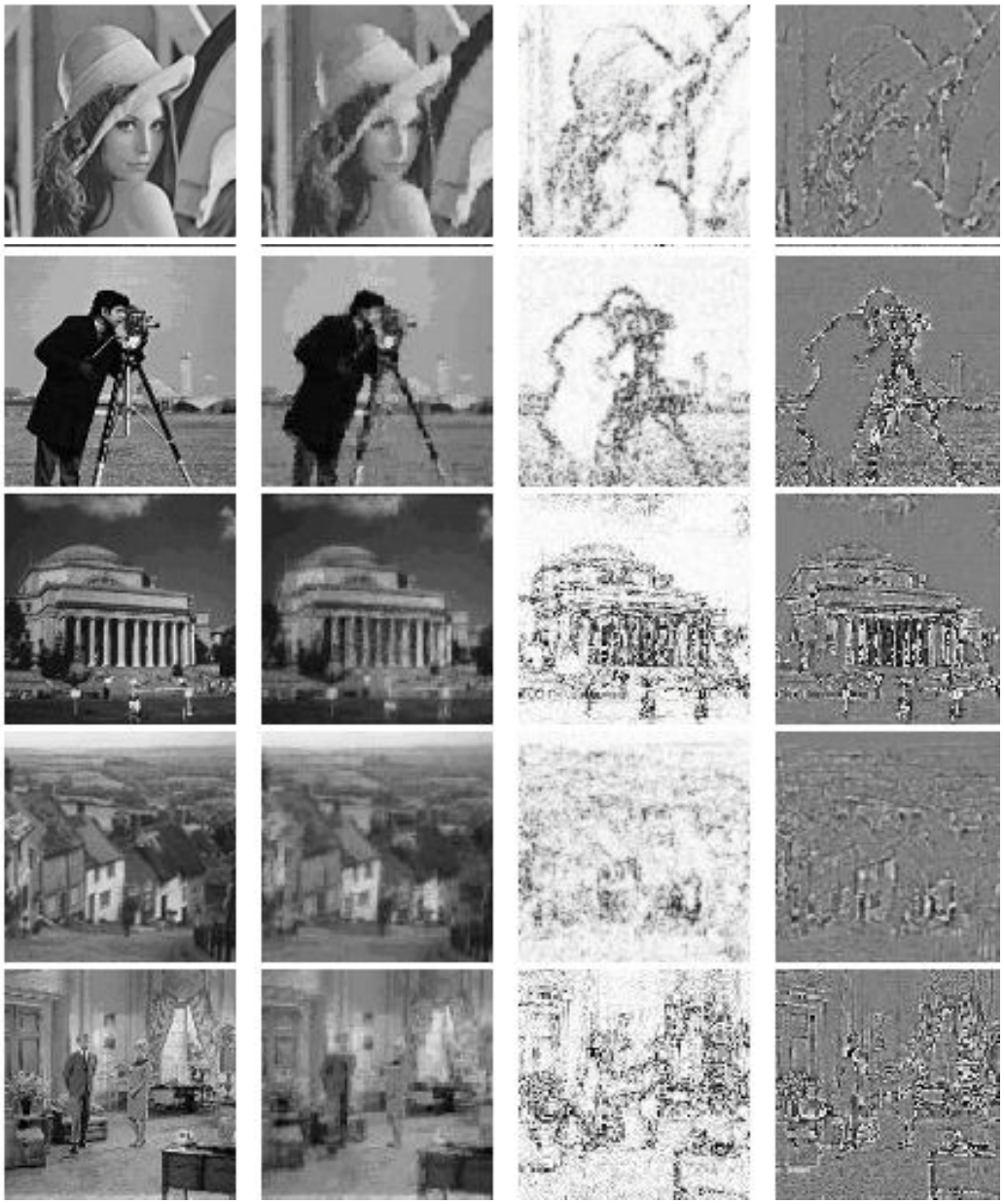

Figure 4. Five test images used in the experiments (First Column); Reconstructed images using Fisher's program (Second Column); Difference image for quality verification: 5.||e(x, y)|| (Third Column); and ||5. e(x,y)/2 + 127|| (Fourth Column).

4. Conclusions

Fractal image compression is relatively developing topic in image processing area. The idea of storing image blocks as a set of transformations is very efficient. However, the speed of encoding process is always a major obstacle in this scheme. This paper discusses a fractal compression scheme adapted with a Fractal Dimension classifier. With this Fractal Dimension classifier, the domain pool used in the encoding processes has significantly reduced the encoding time. The results shows that with suitable classification on range blocks, we can speed up the encoding by about 93% of *BARNSLEY's* approach and also the images on Figure 2, encoded by the proposed approach is slightly better than that on the second column of Figure 3 produced by BARNSLEY's program however, it produces much better results than FISHER's program (Figure 4). However FISHER's program presents minimal encoding time and maximal compression ratio.

References

[1] M. Nappi, G. Polese, G. Tortora, "Fractal Indexing and Retrieval System (FIRST) for Image Databases" Image and Vision Computing Vol.16, pp. 1019-1031, (1998).

[2] M.F. Barnsley: Fractals Everywhere. 2nd ed., Academic Press, New York 1993.

[3] A. Jacquin, "Image Coding Based on a Fractal Theory of Iterated Contractive Image Transformations", IEEE Transactions on Image Processing Vol.1, pp. 18-30, (1992).

[4] Chwen-Jye Sze, Hong-Yuan Mark Liao, Kuo-Chin Fan, Ming-Yang Chern, Chen-Kou Tsaoy, "Fractal Image Coding System Based on an Adaptive Side-coupling Quadtree Structures", Image and Vision Computing Vol. 14, 401-415, (1996).

[5] M.F. Barnsley, L. Hurd, "Fractal Image Compression", Wellesley 1993.

[6] A. Conci, C.F.J. Campos, "An Efficient Box-Counting Fractal Dimension Approach for Experimental Image Variation Characterization" Proceedings of IWSIP'96 3rd International Workshop on Signal and Image Processing, Elsevier Science, Manchester, UK, 665-668 (1996).

[7] J.C. Hart, "Fractal Image Compression and Recurrent Iterated Function Systems, IEEE Computer Graphics and Applications Vol. 16, No. 4, 25-40 (1996).

[8] J. Kominek, "Advances in Fractal Compression for Multimedia Applications. [ftp://links. uwaterloo.ca:/pub/Fractals/Papers/Waterloo/kominek95c. ps.gz] University of Waterloo, Internal Report CS95-28 (1995).

[9] Y. Fisher, "Fractal Compression: Theory and Application to Digital Images", Springer Verlag, New York 1994.

[10] S. Morgan, A. Bouridane, "Application of Shape Recognition to Fractal Based Image Compression", Proceedings of IWSIP'96 3rd International Workshop in Signal and Image Processing, Elsevier Science, Manchester, UK, 23-26 (1996).

[11] D. Saupe, R. Hamzaoui, "A Review of Fractal Image Compression Literature", Computer Graphics, Vol.28, 268-275 (1994).

[12] Tohru Morita, "Fractal Dimension Estimators for a Fractal Process", Journal of the Korean Physical Society, Vol. 46, No. 3, pp. 631-637 (2005)

[13] Aura Conci, Felipe R. Aquino, "Fractal Coding Based On Image Local Fractal Dimension", Computational and Applied Mathematics, Vol. 24, No. 1, pp. 83–98 (2005).

[14] M.L.Valarmathi, K.Anbumani, "Non Iterative Fast Fractal Codec Using Local Fractal Dimension", GVIP Journal, Vol. 6, No. 3(2006).

Effect of Load on Voltage Magnitude and Power-Quality Using Artificial Neural Network

Shubhrata Gupta
Deptt. Of Electrical Engg.,
NIT, Raipur, CG 492010 India
guptashubhrata@rediffmail.com

A.S.Zadgaonkar
Dr. C.V.Raman University,
Kota Bilaspur, CG.

Abstract

The principal objective of a utility is to deliver power to the customer satisfactorily (i.e. with voltage and frequency within limits) and in a manner most economical to the company with respect to transmission and distribution. Increased use of modern sensitive equipments and the increased demands on capacity utilization in the industry not only require an uninterrupted electricity supply but also strict adherence to specified parameters. The goal of power engineers is to provide an uninterrupted supply of high quality power to customers in a secure and economic environment. For reliable and economic operation of power system, it is essential to monitor and control the status of the entire power lines in a control centre.

Presently the power system studies are based on decoupled theory. Accordingly ANN models have been developed and have been reported for power system analysis. In case of decoupled ANN models, different ANN network having the corresponding input/output are required for effective studies.

But in this paper an ANN model based studies are being reported having an integration of both the factors i.e. real and reactive powers, in which only one ANN model is needed and it is able to report the output parameters of the POWER-QUALITY measures e.g. voltage-magnitude.

Keywords- Power quality, reliable and economic operation of power system, Artificial Neural Network.

Broad Area- Electrical.

Sub-Area- Power system, Power quality

1. Introduction

The quality supply means constant voltage and constant frequency power supply under normal operations .Any violation in the above two quantities (V, f) introduce the harmonics in the system. A measure of the harmonic content in a signal is the Total Harmonic Distortion THD. For good quality power the THD is recommended to be less than 3% (Maximum value).

Power-quality monitoring is becoming an essential part of utility services in recent years. All over the world utilities have worked on the improvement of power quality for decades. Even the term Power-Quality has been in use for a rather long time already [1]. A number of approaches have been proposed particularly using ANN [2, 3].

Voltage and frequency are the two important operating parameters of a power-system deciding the quality –power, but majority of events currently of interest are associated with either a reduction (sag) or increase (swell) in the voltage magnitude[4].

The voltage magnitude is split into three regions:

Interruption: the voltage magnitude is zero

Undervoltage: the voltage magnitude is below its normal value

Overvoltage: the voltage magnitude is above its normal value

In duration, a distinction is made between

* very short **:** corresponding to transient and self-restoring events**;**

* short **:** corresponding to automatic restoration of the pre-event situation**;**

* long **:** corresponding to manual restoration of the pre-event situation**;**

* very long **:** corresponding to repair or replacement of faulted components.

In recent years ANN has been developed as an alternative tool for quick assessment of power System parameters, to improve the Power-Quality [5,6]. To assess the power quality, simulation studies are made.

In view of this the best suitable ANN network is developed to assess the power- quality of line e.g. Bus Voltage-magnitude.

2. Power System requirements

In modern power system, networks are complicated with hundreds of generating stations and load centers being interconnected through power transmission lines. Earlier, the main concern of consumers of electricity was the reliability of supply, which is nothing but the continuity of electric supply. However, these days apart from reliability, quality of power too is very important to them. Thus in this changed scenario, the term POWER QUALITY (PQ) attains increased significance [7].

The causes of power quality deteriorating problems are generally complex and difficult to detect. Customers often describe tripping of equipments due to disturbances in the supply voltage as 'bad power quality'. On the other side, utility often view disturbances due to end user equipments as the main power quality problem.

A power system is said to be well designed if it gives a good quality of reliable supply. By good quality is meant the voltage levels and frequency within the acceptable limits. Practically all the equipments on the power systems are designed to operate satisfactorily only when the voltage levels on the system correspond to their rated voltage or at the most the variations are within say 5%. The voltage variation at a node is an indication of the unbalance between the reactive power generated and consumed by that node [8,9]. If the reactive power generated is greater than consumed, the voltage goes up and vice-versa.

Modern power electronic equipments are not only sensitive to voltage disturbances; they also cause power quality problems [10]. The increased use of converter driven equipment has led to a large growth of voltage disturbances [11].

Thus Power-quality monitoring is becoming an essential part of utility services in recent years. A number of approaches have been proposed particularly using ANN [12, 13, 14, 15]. The first prerequisite to perform automatic identification of power quality events is to determine what type of PQ events the system will have to identify. Based on this information, the structure and number of neurons in the ANN are selected and trained with a training data set. At the end of the training session, it is expected that the ANN is capable of identifying the training and testing data set at a desired accuracy rate. If this is not achieved; the structure, the number of neurons or training strategy will be modified to achieve the desired accuracy [16].

3. Problem Formulation

For this purpose an example of IEEE 30-bus system is chosen [17]. The layout of IEEE 30-bus system is shown in Figure 1. Tables 1 to 3 give the data for this system:

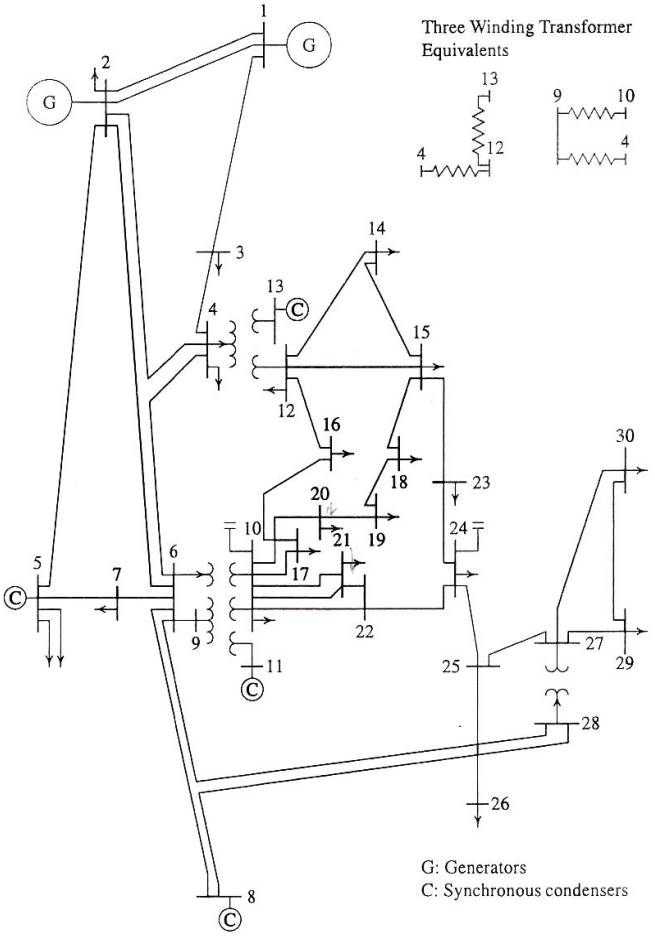

Figure 1.

* Slack bus –No.1

** Voltage controlled (PV, generation) buses- No. 2, 5, 8, 11, and 13

Table 1. Regulated bus Data

Bus No	V mag.	MVar Capacity	
		Max	Min
2	1.043	50	-40
5	1.010	40	-40
8	1.010	40	-10
11	1.082	24	-6
3	1.071	24	-6

The data for injected reactive power due to shunt capacitor is given in Table 2

Table 2.

Injected Q due to capacitors	
Bus No.	Mvar
10	19
24	4.3

Generations and loads at various buses are given in Table 3.

- Code 1 is for the slack bus,
- 2 for the voltage controlled buses and
- 0 is for the load buses.

Table 3. Generations and loads on Buses

Bus Code	Bus No.	Voltage Mag.	Angle Degree	----Load----		----Generation-----		Injected Mvar
				MW	Mvar	MW	Mvar	Mvar
1	1	1.060	0.000	0.000	0.000	260.950	-17.010	0.00
2	2	1.043	-5.496	21.700	12.700	40.000	48.826	0.00
0	3	1.022	-8.002	2.400	1.200	0.000	0.000	0.00
0	4	1.013	-9.659	7.600	1.600	0.000	0.000	0.00
2	5	1.010	-14.380	94.200	19.000	0.000	35.995	0.00
0	6	1.012	-11.396	0.000	0.000	0.000	0.000	0.00
0	7	1.003	-13.149	22.800	10.900	0.000	0.000	0.00
2	8	1.010	-12.114	30.000	30.000	0.000	30.759	0.00
0	9	1.051	-14.432	0.000	0.000	0.000	0.000	0.00
0	10	1.044	-16.024	5.800	2.000	0.000	0.000	19.00
2	11	1.082	-14.432	0.000	0.000	0.000	16.113	0.00
0	12	1.057	-15.301	11.200	7.500	0.000	0.000	0.00
2	13	1.071	-15.300	0.000	0.000	0.000	10.406	0.00
0	14	1.043	-16.190	6.200	1.600	0.000	0.000	0.00
0	15	1.038	-16.276	8.200	2.500	0.000	0.000	0.00
0	16	1.045	-15.879	3.500	1.800	0.000	0.000	0.00
0	17	1.039	-16.187	9.000	5.800	0.000	0.000	0.00
0	18	1.028	-16.881	3.200	0.900	0.000	0.000	0.00
0	19	1.025	-17.049	9.500	3.400	0.000	0.000	0.00
0	20	1.029	-16.851	2.200	0.700	0.000	0.000	0.00

Bus Code	Bus No.	Voltage Mag.	Angle Degree	----Load----		----Generation-----		Injected Mvar
				MW	Mvar	MW	Mvar	Mvar
0	21	1.032	-16.468	17.500	11.200	0.000	0.000	0.00
0	22	1.033	-16.455	0.000	0.000	0.000	0.000	0.00
0	23	1.027	-16.660	3.200	1.600	0.000	0.000	0.00
0	24	1.022	-16.829	8.700	6.700	0.000	0.000	4.30
0	25	1.019	-16.423	0.000	0.000	0.000	0.000	0.00
0	26	1.001	-16.835	3.500	2.300	0.000	0.000	0.00
0	27	1.026	-15.913	0.000	0.000	0.000	0.000	0.00
0	28	1.011	-12.056	0.000	0.000	0.000	0.000	0.00
0	29	1.006	-17.133	2.400	0.900	0.00	0.000	0.00
0	30	0.994	-18.016	10.600	1.900	0.00	0.000	0.00
	Total			**283.400**	**126.200**	**300.950**	**125.089**	**23.30**

As the power system load is gradually increased, the voltages at the load buses decrease until the slope of the voltage power curve becomes infinite. The heavy loading of many power systems has given rise to significant interest and much research regarding the conditions, which may lead to loss of stable condition. As the load powers are increased care must be taken to cover the total load by appropriate generation. A mismatch of a system's reactive power demand and its reactive power resources is the main reason for power system collapses. A reactive power deficit situation is characterized by widespread voltage reduction throughout the transmission network.

With the advent of substation computer systems dedicated to protection, control, data logging functions in a substations and advanced software packages, written in user-friendly high level languages, it becomes possible to develop an algorithm to represent the problem exactly. An appropriate computational tool is then applied to obtain the desired solutions, to obtain a safe and stable limit of operation, with a good POWER-QUALITY.

In this present work Artificial Neural Network (ANN) is used to assess the quality factors and, as an example case study of IEEE 30-Bus system on load conditions has been reported.

The proposed ANN model is shown in Figure2. A multi (Three) layer (including two hidden layers) Feed Forward Network is found to be the most optimally suitable ANN structure for the analysis. The ANNs are trained using fast back propagation learning algorithm. The first hidden layer has 60 neurons, second one has 30 and the output layer has also 30 neurons. Various combination of transfer functions have been taken but the best suited was Tan-Sigmoid (tansig) transfer function for all three-layers, and the training function suited is Gradient Descent (Batch), traingd.

4. Assessment of Voltage magnitude

The ANN model has been used to observe the effect of changes in loads connected at buses 3,7,14,15,16,17,18,19,20,21,23,24,26,29,30.(Their values are mentioned in Table 3);on voltage magnitude .

It is observed that voltage magnitude $|V|$ changes with load variation in above-mentioned buses simultaneously, say: allAL, allRL.

4.1 Effect of change in Active Power Load: allAL

System voltage magnitude variations with active power overloading in all the load buses simultaneously (allAL) are shown in Table 4.

It is observed that individual overloading in any bus even up to 125% does not affect the voltage magnitudes. Also it can be seen from the Table4 that with simultaneous overloading in all the load buses voltage magnitude variations is minor Therefore it may be treated as constant variation with regards to actual power changes.

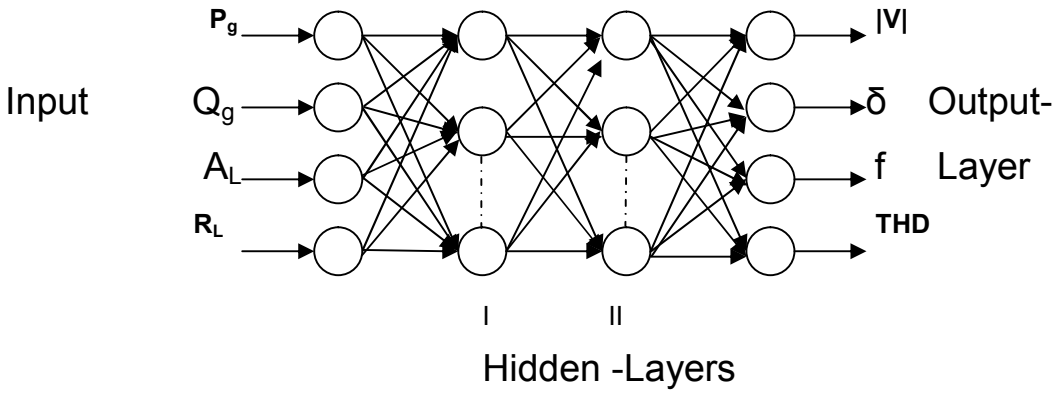

Figure 2. Proposed ANN Model

Table 4. Variation in |V| with allAL

Loading→ Bus no↓	Actual	110	130	150	200
1	1.0668	1.0671	1.0671	1.0671	1.0671
2	1.0409	1.0419	1.0419	1.0419	1.0419
3	1.0217	1.0233	1.0233	1.0233	1.0233
4	1.0134	1.0149	1.0149	1.0149	1.0149
5	1.0087	1.0108	1.0108	1.0108	1.0108
6	1.0118	1.0137	1.0137	1.0137	1.0137
7	1.0033	1.0058	1.0058	1.0058	1.0058
8	1.0099	1.0135	1.0135	1.0135	1.0135
9	1.0489	1.0498	1.0498	1.0498	1.0498
10	1.0442	1.0492	1.0492	1.0492	1.0492
11	1.0799	1.0829	1.0829	1.0829	1.0829
12	1.0568	1.0567	1.0567	1.0567	1.0567
13	1.0703	1.0736	1.0736	1.0736	1.0736
14	1.0414	1.0433	1.0433	1.0433	1.0433
15	1.0372	1.04	1.04	1.04	1.04
16	1.0439	1.0448	1.0448	1.0448	1.0448
17	1.0373	1.0397	1.0397	1.0397	1.0397
18	1.0274	1.0265	1.0265	1.0265	1.0265
19	1.0261	1.0317	1.0317	1.0317	1.0317
20	1.0293	1.0291	1.0291	1.0291	1.0291
21	1.0311	1.0343	1.0343	1.0343	1.0343
22	1.033	1.0344	1.0344	1.0344	1.0344
23	1.027	1.0272	1.0272	1.0272	1.0272
24	1.022	1.0226	1.0226	1.0226	1.0226
25	1.018	1.0219	1.0219	1.0219	1.0219
26	1.0012	1.0021	1.0021	1.0021	1.0021
27	1.026	1.0266	1.0266	1.0266	1.0266
28	1.011	1.01	1.01	1.01	1.01
29	1.0072	1.0088	1.0088	1.0088	1.0088
30	1.0001	0.99909	0.99909	0.99909	0.99909

4.2 Effect of change in Reactive Power Load: allRL

System voltage magnitude variations with reactive power overloading in all the load buses simultaneously (allRL) are shown in Table5. It is observed that individual overloading in any bus even up to 125% is not affecting the voltage magnitudes.

Actual system voltage magnitude is shown in Figure3. Variations in voltage magnitude at bus number 15 with reactive power overloading in all the load buses simultaneously (allRL) is shown in Figure 4 , as a sample.

Table 5. Variation in |V| with allRL

Loading→ Bus no. ↓	Actual	125	140	150	170	200	300
1	1.0668	1.0671	0.97232	0.89338	0.60096	0.31473	0.14425
2	1.0409	1.0419	0.92814	0.81473	0.38553	-0.38476	-0.0059701
3	1.0217	1.0233	1.4815	1.8522	1.4108	-0.14745	-2.0508
4	1.0134	1.0149	1.2323	1.3818	0.74068	-1.0448	-4.322
5	1.0087	1.0108	2.4651	3.6946	7.5034	10.973	10.865
6	1.0118	1.0137	0.5778	0.16938	-0.027615	-1.3331	-6.7623
7	1.0033	1.0058	1.2051	1.3243	2.9089	4.1204	1.4405
8	1.0099	1.0135	0.97634	0.87346	-2.5095	-6.9241	-9.3577
9	1.0489	1.0498	0.675	0.32343	-2.6948	-7.3533	-10.194
10	1.0442	1.0492	1.7135	2.2207	-0.29189	-4.5791	-8.4872
11	1.0799	1.0829	0.58215	0.11576	-4.4929	-9.4623	-10.485
12	1.0568	1.0567	0.97078	0.88128	-1.385	-5.5227	-8.2836
13	1.0703	1.0736	1.1463	1.1305	-3.2412	-8.6487	-10.505
14	1.0414	1.0433	0.62845	0.20992	-0.46091	-1.8162	-5.0908
15	1.0372	1.04	0.29861	-0.35839	-3.6071	-8.372	-10.554
16	1.0439	1.0448	2.3698	3.5201	10.848	22.069	29.969
17	1.0373	1.0397	1.7993	2.3924	6.5919	12.809	17.254
18	1.0274	1.0265	1.3646	1.6526	3.8264	6.5123	12.389
19	1.0261	1.0317	1.2802	1.4005	-0.76763	-4.6912	-9.6013
20	1.0293	1.0291	1.0844	1.1466	3.4744	6.8468	7.7069
21	1.0311	1.0343	2.2545	3.2764	8.9211	17.868	23.058
22	1.033	1.0344	1.8386	2.4825	5.1756	7.6635	11.581
23	1.027	1.0272	0.88176	0.74556	2.4919	3.596	1.2029
24	1.022	1.0226	2.3279	3.4427	11.739	24.938	29.484
25	1.018	1.0219	1.5831	1.9843	-0.36341	-4.1794	-2.9658
26	1.0012	1.0021	1.5184	1.8978	2.9504	2.7062	5.8478
27	1.026	1.0266	1.6457	2.1252	3.2807	3.326	4.8608
28	1.011	1.01	2.0092	2.9033	6.1042	8.8226	20.048
29	1.0072	1.0088	1.9833	2.7668	5.581	7.1763	13.594
30	1.0001	0.99909	1.5701	2.0317	4.4819	5.3793	8.5359

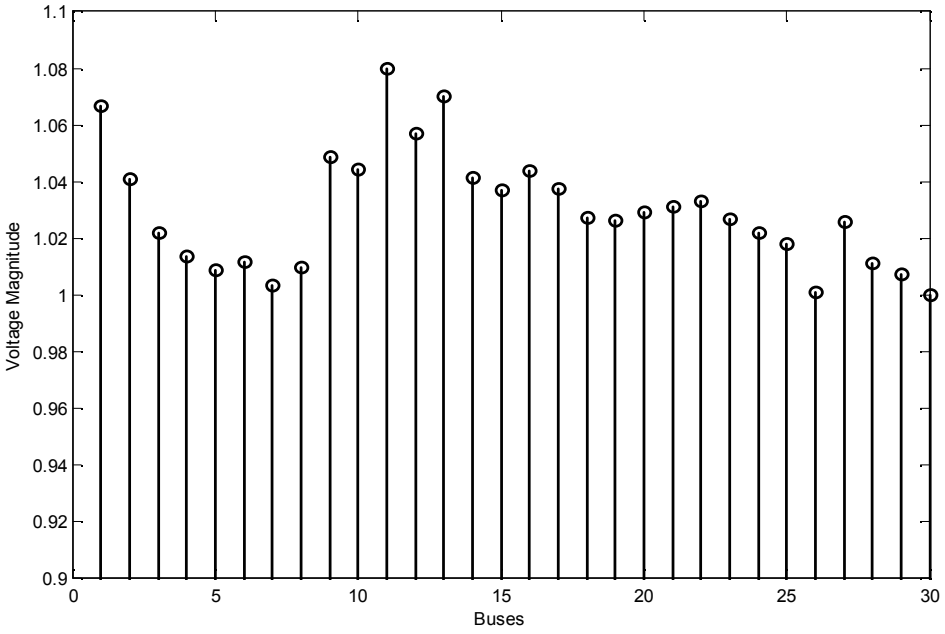

Figure 3. Actual system Voltage Magnitude

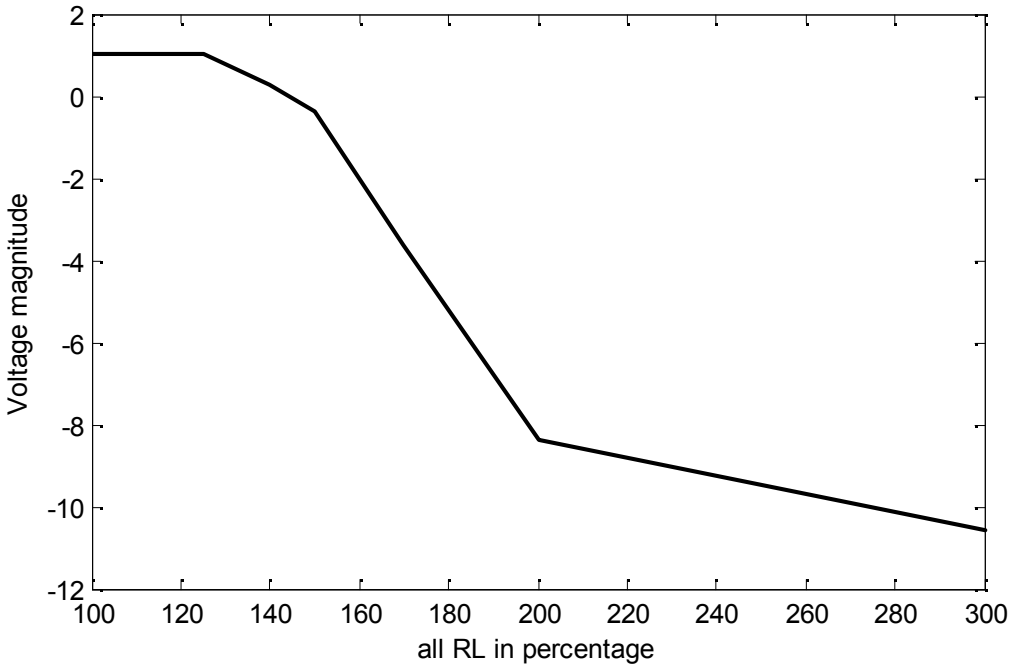

Figure 4. Variation in Voltage magnitude at bus 15 with allRL

5. Test Results and Conclusions

From the Table 3 it can be seen that generator at bus 1 is the main generator supplying 260.95MW and –17.01MVAr (negative sign is showing that this generator is actually absorbing the reactive power). The generator at bus 2 with 40MW and 48.826MVAr and other capacitive reactance (at buses 5, 8, 10, 11, 13, 24) are assisting the main generator.

From the above analysis (shown through Tables and Figures) following conclusions can be made**:**

- With real power variations in all the load buses simultaneously (allAL), system voltage magnitudes remain constant; as real power loading has minor effect on system voltage magnitude.
- With reactive power variations (overloading) in the entire load buses simultaneously (allRL), system voltage magnitudes decreases.
- In actual power- system it is never advised to overload the system more than 10 or at the most 25 %, as it will make the system unstable; so it can be empathetically concluded that studies, which were not possible to realize; could be easily done with this ANN model studies and results in table 5 and figure 4 show that this much overloading is making system Unstable (voltage magnitudes are varying drastically)

6. Discussion

Presently the power system studies are based on decoupled theory. Accordingly ANN models have been developed and have been reported for power system analysis.

In case of decoupled ANN models, different ANN network having the corresponding input/output for real and reactive powers are required for effective studies.

But in the present venture an ANN model based studies are being reported having an integration of both the factors i.e. real and reactive powers.

In the present case only one ANN model is needed and it is able to report the output parameters of the POWER-QUALITY measures e.g. voltage-magnitude.

References

[1] H.H.Kajihara, Quality power for electronics, ElectroTechnology, vol.82, no.5.November1968, p.46.

[2] M.Morcos et al, "Electric power quality and artificial intelligence: Overview and applicability ", IEEE Power engineering review, vol.19, no.6, Jun.'99, pp5-10.

[3] Wael R. "A power quality perspective to system operational diagnosis using fuzzy logic and adaptive technique", IEEE trans.on Power Delivery, vol.18, no.3, July2003, pp903-909.

[4] Sallam A.A., "ANN Application to alleviate voltage instability problem", Large Engg. System Conf. Of Power Engineer2002 (LESCOPE02) pp133-141.

[5] L.L.Lai et al, "Real time frequency and harmonic evaluation using Artificial Neural Network", IEEE trans.on Power Delivery, vol.14, no.1, Jan.'99, pp52-57.

[6] K.Shantiswaroop, "ANN approach assesses system security", IEEE Computer application in Power, July.2002, pp32-38.

[7] R.C.Dugan et al, 'Electrical power system quality', NewYork Mc-graw-Hill, 1996.

[8] K.A.Palaniswamy et al, "Optimum load shedding taking in to account of voltage and frequency characteristics of loads," IEEE trans.on Power Apparatus and Systems, vol.104, no.6, June'85.

[9] C.L.Wadhwa, 'Electrical power system', Wiley eastern ltd., June 1990.

[10] A.K.Ghosh et al, "The classification of power system disturbance waveforms using a Neural Network approach", IEEE trans.on Power Delivery, vol.10, no.1, Jan.'95, pp109-115.

[11] Math H.J.Boolen, 'Understanding power quality problems: voltage sag and interruptions', IEEE press, 2001.

[12] M.Morcos et al, "Electric power quality and artificial intelligence: Overview and applicability ", IEEE Power engineering review, vol.19, no.6, Jun.'99, pp5-10.

[13] S.Gupta et al, "Voltage profile assessment using ANN for improving power quality", XIII NPSC, IIT MADRAS Dec.2004.

[14] A.S.Zadgaonkar et al, "On ANN Model for load management", Proc. of Inter. Conf. On demand side management and energy efficient equipment", IEEMA Journal, Mumbai, Jan.1999.

[15] N.Iwan Santoso, et al, "Neural-Net based real-time control of Capacitors installed on Distribution systems" IEEE trans.on Power Delivery, vol.5, no.1, Jan'89, pp266-272.

[16] Surya Santoso et al, "A scalable PQ event identification system", IEEE trans.on Power Delivery, vol.15, no.2, april.2000, pp738-7433

[17] H. Saadat, 'Power system analysis',TMH, N.Delhi 2002, XI reprint 2007.

Interval Based Differential Evolution Algorithm for Combined Economic Emission Load Dispatch

Archana Gupta
Electrical Engineering Department
Bhilai Institute of Technology,
Durg, India
archana_gupta74@rediffmail.com

Shashwati Ray
Electrical Engineering Department
Bhilai Institute of Technology,
Durg, India
shashwatiray@yahoo.com

Abstract

In this paper we propose an Interval based Differential Evolution algorithm (IDE), an improved version of Differential Evolution algorithm (DE) using interval arithmetic. Initially the IDE algorithm estimates the global minimum roughly, and then it constructs a mechanism which updates the upper and lower bounds of global minimum at each generation and defines an efficient termination criterion. Also the new population is modified using the subset of current population. In this way the extra computational effort is avoided.

The proposed algorithm is applied to Combined Economic Emission Load Dispatch (CEELD) problem which is formulated as a nonlinear optimization problem with both equality and inequality constraints. We choose IEEE 14 bus, three generator system as a test system with and without transmission loss. We obtain lesser fuel and emission costs with lesser computational effort for both the cases as compared to conventional DE algorithm.

Keywords- Interval arithmetic; Differential Evolution; Shrinking box; Fuel cost; Emission level

Broad Area- Global Optimization

Sub-Area- Electrical Power system

1. Introduction

Evolutionary algorithms (EAs) are a class of population based stochastic optimization algorithms that incorporate mechanisms from evolution for optimization processes. Some well-established and commonly used EAs are Genetic Algorithms (GA), Evolution Strategies (ESs), Particle swarm and Differential Evolution.

The Differential Evolution algorithm is a heuristic approach for minimizing nonlinear and non-differentiable continuous space functions. It is an improved version of GA using similar operators: mutation, crossover and selection. The main difference in constructing better solutions is that, GA relies on crossover while DE relies on mutation operation which is based on the differences of randomly sampled pairs of solutions in the population. The algorithm uses selection operation to direct the search towards the prospective regions in the search space. Thus DE is a simple and efficient direct search algorithm for global optimization over continuous spaces [1].

For any optimization process the choice of stopping criteria can significantly influence the duration of an optimization run as well as the global minimum. DE terminates either with user defined number of generations or some error estimate. These criteria are perfectly suitable for comparing the performance of different algorithms, but for solving real world problems they are inefficient.

With predefined number of generations, optimization run might be terminated before the population has converged, or computational resources might be wasted with late termination as the real world problems mostly contain computationally expensive objective functions. Also the maximum number of function evaluations which is highly dependent on the objective function, has to be usually determined by trial-and-error methods. The second criterion requires optimum value which is not possible for an arbitrary function.

As the DE algorithm includes randomness in the optimization process, the number of function evaluations that is needed for convergence is subject to fluctuations. Thus it would be better to use stopping criteria that consider knowledge from the state of the optimization run. Several stopping criteria are reviewed in [2] that are sensitive to the state of the optimization run by observing the improvement, movement or distribution of the population members.

In this paper we propose an Interval based Differential Evolution algorithm that uses interval analysis with conventional DE. Initially the algorithm estimates the initial upper and lower bounds of the objective function using interval arithmetic [3]. Then a mechanism is constructed using interval arithmetic that updates the bounds in each generation, and is able to define an efficient termination criterion [4]. When the criterion is fulfilled, the algorithm converges to the global minimum with certainty. Also to avoid slow convergence near the region of global minimum the next generation population is modified using the subset of current population, which performs with in the current upper and lower bounds of the objective function. The

proposed algorithm is then applied to Combined Economic Emission load dispatch (CEELD) problem.

The purpose of Economic Emission load dispatch (EELD) problem is to obtain the optimal amount of generated power for the fossil based generating unit in the system by minimizing the fuel cost and emission level simultaneously, subject to various equality and inequality constraints of the power system. Different techniques have been reported in the literature pertaining to EELD problem. Abido had pioneered this research by applying three algorithms viz., Non-dominated Sorting Genetic Algorithm (NSGA), Niched Pareto Genetic Algorithm (NPGA) and Strength Pareto Evolutionary Algorithm (SPEA) [5]. A Simulated Annealing based modified approach with a single decision variable was developed to solve the EELD problem [6].

This paper converts the multi objective EELD problem into a single objective problem using price penalty factor, known as Combined Economic Emission Load Dispatch problem [6] and then IDE is applied. The standard IEEE 14-bus 3 generator system is considered as a test system [7]. We consider the system with and without transmission losses [8]. The results obtained are compared with the conventional DE and henceforth the effectiveness of IDE to solve the EELD problem is demonstrated.

This paper is organized as follows: In section 2 we give the basics of Differential Evolution algorithm and interval arithmetic. In section 3 we present our interval based Differential Evolution algorithm. In section 4 we formulate the CEELD problem and define its objective with equality and inequality constraints for two different cases. In section 5 we apply IDE to CEELD problem and compare the results with traditional DE for both the cases. We conclude our study in section 6.

2. Basics of Differential Evolution Algorithm and Interval Arithmetic

2.1 Differential Evolution Method

DE is a population based direct search method. The algorithm initializes the population vector of fixed size randomly. During each iteration a new population of same size is generated using mutation, crossover and selection operators. It uses mutation operation as a search mechanism, which generates new parameter vector by adding a weighted difference vector between two population members to a third member. In order to increase the diversity of the parameter vector, the crossover operation produces a trial vector which is a combination of a mutant vector and a parent vector. Then the selection operation directs the search toward the prospective regions in the search space. In addition, the best parameter vector is evaluated for every generation in order to keep track of the progress that is made during the minimization process. The above iterative process of mutation, crossover and selection on the population will continue until a user-specified stopping criterion, normally, the maximum number of generations or the maximum number of function evaluations allowed is met. The process is assumed to have converged if the difference between the best function values in the new and old population, and the distance between the new best point and the old best point are less than the specified respective tolerances. The other type of stopping criterion could be if the global minimum of the problem is known a-priori. Then DE will be terminated if the difference between the best function value in the new population and the known global minimum is less than the user defined tolerance level [1].

2.1.1 Differential Evolution Optimization Process

The DE optimization process operates on population $\mathbf{P}^{(G)}$ of constant size NP consisting of n dimensional real valued vectors $\mathbf{x}_i^{(G)}$ given by

$$\mathbf{P}^G = [\mathbf{x}_1^{(G)}, \mathbf{x}_2^{(G)}, ..., \mathbf{x}_{NP}^{(G)}],\ G = 1,2,..., G_{\max} \qquad (1)$$

where G is the generation or iteration of the algorithm to which the population belongs, $G_{\max}$ is the maximum number of generations defined by the user and

$$\mathbf{x}_i = [\mathbf{x}_{i1}, \mathbf{x}_{i2}, ..., \mathbf{x}_{in}]^T,\ i = 1,2,..., NP \qquad (2)$$

Also $\mathbf{x}_{ij} \in [\mathbf{x}_{ij}^{(L)}, \mathbf{x}_{ij}^{(U)}]$ where $\mathbf{x}_{ij}^{(L)}$ and $\mathbf{x}_{ij}^{(U)}$ are the lower and upper boundary constraints. The population is initialized randomly by assigning random values to each decision parameter of each individual of population.

$$x_{ij}^{(G)} = x_{ij}^{(L)} + rand[0,1] * (x_{ij}^{(U)} - x_{ij}^{(L)}) \qquad (3)$$

where rand [0, 1] denotes a uniformly distributed random value within [0, 1] that is new for each j. The population is improved by applying mutation, crossover and selection operators.

The mutation operator is in charge of introducing new parameters in to the population. Two vectors $\mathbf{x}_{r1}^{(G)}$ and $\mathbf{x}_{r2}^{(G)}$ are randomly selected from the population and the vector difference between them is established. This difference is multiplied by a scaling factor $\mu \in [0,1]$ (specified at the start and remains unchanged throughout the algorithm) and added to a third randomly chosen vector $\mathbf{x}_{r3}^{(G)}$ from the population. This is known as the differential variation and a mutant vector is generated as

$$\mathbf{v}_i^{(G+1)} = \mathbf{x}_{r3}^{(G)} + \mu * (\mathbf{x}_{r2}^{(G)} - \mathbf{x}_{r1}^{(G)}) \qquad (4)$$

Following the mutation operation, the crossover operator creates the trial vectors, which are used in the selection process. A trial vector is a combination of a mutant vector and a parent (target) vector which is formed based on probability distributions. The purpose of crossover is to inject diversity into the original population in order to avoid being trapped in the local minimum, i.e., searching the entire solution space, including unvisited areas in order to generate solutions that differ from the previous ones. The crossover

probability is determined by the user defined crossover constant $CR \in [0,1]$. For each parameter, a random value based on binomial distribution is generated in [0,1] and is compared against CR . If the value of the random number is less than or equal to the value of the CR , the parameter would be the mutant vector, otherwise the parameter would be the parent vector.

$$u_{ij}^{(G+1)} = \begin{cases} v_{ij}^{(G+1)} \ if \ rand\ [0,1] \le CR \ or \ j = rnbr(i) \\ x_{ij}^{(G)} \qquad otherwise \end{cases} \tag{5}$$

Where $rnbr(i)$ is a randomly chosen index $\in \{1,...,n\}$ which ensures that each individual trial vector $\mathbf{u}_i^{(G+1)}$ differs from its counterpart in the previous generation $\mathbf{x}_i^G$ by at least one parameter.

The selection operator chooses the vectors that are going to compose the population in the next generation. These vectors are selected from the current population and the trial population. Each individual of the trial population is compared with its counterpart in the current population. Assuming that the objective function is to be minimized, the vector with the lower objective function value wins a place in the next generation's population. As a result, all the individuals of the next generation are as good as or better than their counterparts in the current generation.

$$\mathbf{x}_i^{(G+1)} = \begin{cases} \mathbf{u}_i^{(G+1)} \ if \ f(\mathbf{u}_i^{(G+1)}) \le f(\mathbf{x}_i^{(G)}) \\ \mathbf{x}_i^{(G)} \quad otherwise \end{cases} \tag{6}$$

In boundary constrained problem it is essential to ensure that parameter values lie inside their allowed ranges. A simple way to replace parameter values that violate boundary constraints with random values generated within the feasible range is as follows [9]

$$u_{ij}^{(G+1)} = \begin{cases} x_{ij}^{(U)} + rand[0,1]*(x_{ij}^{(G)} - x_{ij}^{(U)}) \ \ if \ u_{ij}^{(G+1)} > x_{ij}^{(U)} \\ x_{ij}^{(L)} + rand[0,1]*(x_{ij}^{(G)} - x_{ij}^{(L)}) \ \ if \ u_{ij}^{(G+1)} < x_{ij}^{(L)} \\ x_{ij}^{(G+1)} \qquad otherwise \end{cases} \tag{7}$$

2.1.2 Differential Evolution Algorithm

Algorithm DE $[f^*, \mathbf{x}^*]$:=D_E $(\mathbf{x}, n, f, \mu, CR, NP, r, \varepsilon_x, \varepsilon_f)$

Inputs: lower and upper boundaries $\mathbf{x}^{(L)}$ and $\mathbf{x}^{(U)}$ respectively, dimension n , function f , scaling factor μ , the crossover constant CR , the population size NP , maximum number of function evaluation f_{eval} .

Outputs: global minimum f^* and real vector $\mathbf{x}^*$ of n dimension at which f^* occurs

BEGIN Algorithm

- {Initialization}
  Create an initial population
- Evaluate each individual in the population
- Find out the vector with the lowest cost
- While the termination criterion not reached do
  - ❖ Mutation
  - ❖ Crossover
  - ❖ Selection
- Evaluate the new individuals
- {Return}
  Output f^* and $\mathbf{x}^*$

END Algorithm

2.2 Interval Arithmetic

Interval arithmetic is an arithmetic defined on sets of intervals, rather than on sets of real numbers. It has been invented by R. E. Moore. The power of interval arithmetic lies in its implementation on computers. In particular, outwardly rounded interval arithmetic allows rigorous enclosures for the ranges of operations and functions. This makes a qualitative difference in scientific computations, since the results are now intervals in which the exact result must lie. It has been used recently for solving ordinary differential equations, linear systems, global optimization, etc. [3]

Let $\mathbf{x} = \{[a,b] \,|\, a \le b, a, b \in R\}$ be a real interval, where a is the infimum and b is the supremum of $\mathbf{x}$. The width of interval is defined as $w(\mathbf{x}) = b - a$. The midpoint of the interval is defined as $m(\mathbf{x}) = (a+b)/2$. For a n dimensional interval vector $\mathbf{x}^n = [\mathbf{x}_1, \mathbf{x}_2, ..., \mathbf{x}_n]$, the midpoint of interval vector $\mathbf{x}^n$ is given by $m(\mathbf{x}^n) = [m(\mathbf{x}_1), m(\mathbf{x}_2), ..., m(\mathbf{x}_n)]$. The width of interval vector $\mathbf{x}^n$ is $w(\mathbf{x}^n) = [w(\mathbf{x}_1), w(\mathbf{x}_2), ..., w(\mathbf{x}_n)]$. Let $\mathbf{x} = [a,b]$ and $\mathbf{y} = [c,d]$ be two intervals. Let $+, -, *$ and $/$ denote the operation of addition, subtraction, multiplication and division, respectively. If $\otimes$ denotes any of these operations for the arithmetic of real numbers x and y , then the corresponding operation for arithmetic of interval numbers $\mathbf{x}$ and $\mathbf{y}$ is

$$\mathbf{x} \otimes \mathbf{y} = \{\mathbf{x} \otimes \mathbf{y} : x \in \mathbf{x}, y \in \mathbf{y}\} \tag{8}$$

The above definition is equivalent to the following rules:

$$\begin{aligned} &\mathbf{x} + \mathbf{y} = [a + c, b + d] \\ &\mathbf{x} - \mathbf{y} = [a - d, b - c] \\ &\mathbf{x} * \mathbf{y} = [min(ad, ac, bc, bd), max(ad, ac, bc, bd)] \\ &\mathbf{x} / \mathbf{y} = [a,b] \cdot [1/d, 1/c] \ \ if \ \ 0 \notin \mathbf{y} \end{aligned} \tag{9}$$

An interval function $F(\mathbf{x}_1, \mathbf{x}_2, ..., \mathbf{x}_n)$ of intervals $\mathbf{x}_1, \mathbf{x}_2, ..., \mathbf{x}_n$ is an interval valued function of one or more variables. $F(\mathbf{x}_1, \mathbf{x}_2, ..., \mathbf{x}_n)$ is said to be an interval

extension of a real function $f(x_1, x_2, ..., x_n)$ if $f(x_1, x_2, ..., x_n) \in F(\mathbf{x}_1, \mathbf{x}_2, ..., \mathbf{x}_n)$, whenever $x_i \in \mathbf{x}_i$ for all $i = 1,2,...,n$. F is said to be inclusion monotonic if

$$x_i \subset y_i \Rightarrow F(\mathbf{x}_1, \mathbf{x}_2, ..., \mathbf{x}_n) \subset F(\mathbf{y}_1, \mathbf{y}_2, ..., \mathbf{y}_n) \quad (10)$$

Also $F(\mathbf{x}_1, \mathbf{x}_2, ..., \mathbf{x}_n)$ contains the range of $f(x_1, x_2, ..., x_n)$.

Interval functions $F(\mathbf{x})$ can be constructed in any programming language in which interval arithmetic is simulated or implemented via natural interval extensions. However, computing an interval bound carries a cost of 2 to 4 times as much effort as evaluating $f(\mathbf{x})$ [3, 10].

3. Proposed Interval based Differential Evolution Algorithm

As discussed in section 2, DE algorithm terminates either with user defined number of generations or the implementation of the algorithm requires some estimate of the global minimum to be provided. Also DE converges slowly as the region of global minimum approaches. Looking in to the above mentioned drawbacks, we propose here an Interval based Differential Evolution Algorithm an improved version of DE which uses interval analysis to define an efficient termination criterion. Using interval arithmetic, it estimates the initial upper and lower bounds of the objective function and then it updates the bounds in each generation by constructing a shrinking box which contains the subset of current population and makes the algorithm able to define an efficient termination criterion [3, 4]. As the algorithm proceeds, the width of shrinking box gets reduced and finally the algorithm terminates with specified tolerance on the width of the shrinking box. As the formation of shrinking box depends on the number of individuals in the subset, it acts as a convergence check for the algorithm. Also the algorithm modifies the new population, which is obtained after mutation, crossover and selection operations, by using a subset of new population. Thus the extra computational work is avoided.

3.1 Bounds Updation

The IDE algorithm finds the initial bounds $F(\mathbf{x})$ of the objective function using the n dimensional domain $\mathbf{x}$ .Then

$$F(\mathbf{x}) = [\underline{F}, \overline{F}] \quad (11)$$

Initially the upper bound $\overline{F}$ is modified using the minimum function value $f_{\min}$ obtained with initial population.

$$\overline{F} = min\{\overline{F}, f_{\min}\} \quad (12)$$

Then after each iteration of mutation, crossover and selection operation the IDE algorithm constructs a shrinking box, denoted by $\mathbf{x}_S$. It is a n dimensional interval vector, which contains the subset S of current population. This subset consists of individuals $\mathbf{x}_1, \mathbf{x}_2, ..., \mathbf{x}_k$ where $k \in NP$, which have the function values between the current upper bound $\overline{F}$ and the current lower bound $\underline{F}$. When the number of individuals k in the subset S exceeds a shrinking constant r, which is a user defined number and $r < NP$, the algorithm forms the shrinking box $\mathbf{x}_S$. Once the shrinking box is constructed, range estimation of $f(\mathbf{x})$ over $\mathbf{x}_S$ is obtained.

$$F(\mathbf{x}_S) = [\underline{F_S}, \overline{F_S}] \quad (13)$$

Finally the current bounds of the global minimum are updated at each generation as follows

$$\begin{aligned} \overline{F} &= min\{\overline{F}, \overline{F_S}\} \\ \underline{F} &= max\{\underline{F}, \underline{F_S}\} \end{aligned} \quad (14)$$

We now represent $F^* = [\underline{F}, \overline{F}]$ which contains the global minimum.

3.3 Population Modification

The population obtained after mutation, crossover and selection operations is modified for next generation using the subset S of population. As the number of individuals in S is smaller than the population size NP, the population is increased by taking sequentially a randomly selected individual within S and adding this to the population. This procedure is repeated till the number of individuals reaches the value NP.

3.4 Termination Criterionation Modification

The algorithm makes the upper and lower bounds of F^* sharper at each generation and terminates if $w(\mathbf{x}_S)$ or $w(F^*)$ are less than their respective tolerances ε_x and ε_f.

As $w(\mathbf{x}_S)$ tends to zero the individuals are accumulated to a point as global minimizers. If $w(F^*)$ tends to zero, then the infimum of this interval is the global minimum f^*.

3.5 IDE Algorithm

Algorithm IDE $[f^*, \mathbf{x}^*] :=$ IDE $(\mathbf{x}, n, f, \mu, CR, NP, r, \varepsilon_x, \varepsilon_f)$

Inputs: the initial box $\mathbf{x}$, dimension n, function f, scaling factor μ, the crossover constant CR, the population size NP, shrinking constant r, ε_x tolerance for $\mathbf{x}^*$ and ε_f tolerance for f^*.

Outputs: the global minimum f^* and the minnimizer $\mathbf{x}^*$.

BEGIN Algorithm

- {Initialization}
  Initialize the population with population size NP
  Initialize the upper and lower bounds
- Evaluate each individual in the population
- While the termination criterion not reached do
  - Mutation
  - Crossover
  - Selection
  - Construct the subset S
  - Update the upper and lower bounds
  - Population modification
- Evaluate each individual in the new population
- {Return}
  Output f^* and $\mathbf{x}^*$

END Algorithm

4. EELD Problem Formulation

The basic objective of Economic Load Dispatch (ELD) of electric power generation is to obtain the optimal amount of generated power for the fossil based generating unit in the system so as to meet the load demand at minimum operating fuel cost, satisfying all unit and system equality and inequality constraints.

Due to growing concern over the increase in the level of pollution, there arises a need to reduce the atmospheric emission. Thus the ELD problem can be formulated as a multi objective optimization problem, in which the emission, in addition to the fuel cost objective, is to be minimized and is known as Economic Emission Load Dispatch (EELD) problem. Here we have reduced the multi-objective problem to a single objective problem known as Combined Economic Emission Load Dispatch (CEELD) problem. The objective function is thus obtained by blending the emission cost function with the fuel cost function through the use of a price penalty factor [6].

4.1Objectives

4.1.1 Fuel cost

The most commonly used objective in the EELD problem formulation is the minimization of the total operation cost of the fuel consumed for producing electric power within a schedule time interval (one hour). The individual costs of each generating unit are assumed to be function, only of real power generation and are represented by quadratic curves. The total fuel cost $C(\mathbf{P})$ for the entire power system can then be expressed as the sum of the quadratic cost model of each thermal generating unit.

$$C(\mathbf{P}) = \sum_{i=1}^{N} C(P_i) \tag{15}$$

where, $\mathbf{P}$ is the vector of real power outputs of generators and is defined as $\mathbf{P} = [P_1, P_2, ...P_N]^T$, N represents the number of on-line generating units and $C(P_i)$ is the fuel cost of i^{th} generator in \$/hr which is given by

$$C(P_i) = a_i + b_i * P_i + c_i * P_i^2 \tag{16}$$

where $a_{i,}$ b_i and c_i are the cost coefficients of the i^{th} generator and P_i is the real power output of the i^{th} generator.

4.1.2 Emission

The emission control cost results from the requirement for power utilities to reduce their pollutant levels below the annual emission allowances assigned for the affected fossil units. The most important emissions considered in the power generation industry due to their effects on the environment are sulphur oxides (SO_x) and nitrogen oxides (NO_x) . To carry out an economic emission load dispatch, these emissions must be modeled through functions that relate emissions with power production for each unit. The total emission $E(\mathbf{P})$ can be expressed in a linear equation as the sum of all the pollutants resulting from each generator.

$$E(\mathbf{P}) = \sum_{i=1}^{N} E(P_i) \tag{17}$$

where $E(P_i)$ is the emission of i^{th} generator in kg/hr

$$E(P_i) = \alpha_i + \beta_i * P_i + \gamma_i * P_i^2 \tag{18}$$

where, $\alpha_{i,}$ β_i and γ_i are emission coefficients of the i^{th} generating unit.

4.2 Constraints

4.2.1 Power balance constraint

The total electric power generation $\sum_{i=1}^{N} P_i$ must cover the total power demand P_D and the real power loss P_{loss} in the transmission line.

$$\sum_{i=1}^{N} P_i - P_D - P_{loss} = 0 \tag{19}$$

The real power transmission loss P_{loss} is given by

$$P_{loss} = [\sum A_i P_i]^2 \tag{20}$$

where A_i is the loss coefficient of i^{th} generator [8].

If the test system is considered to be lossless then the total electric power generation $\sum_{i=1}^{N} P_i$ must equal the power demand P_D.

$$\sum_{i=1}^{N} P_i - P_D = 0 \tag{21}$$

4.2.2 Generation capacity constraint

Each generating unit is constrained by its lower and upper limits of real power output to ensure stable operation.

$$P_i^{\min} \le P_i \le P_i^{\max} \tag{22}$$

where $P_i^{\min}$ and $P_i^{\max}$ are the minimum and maximum real power output of i^{th} generator, respectively.

4.3 Total Objective

In the EELD problem, the aim is to minimize the fuel cost as well as the emission. Hence, the multi-objective function is reduced to a single objective function in CEELD. The objective function $F(\mathbf{P})$ is thus obtained by blending the emission cost function with the fuel cost function through the use of a price penalty factor and the total objective of constrained optimization problem is formulated as [6]

$$F(\mathbf{P}) = \sum_{i=1}^{N} (C(P_i) + h_i * E(P_i)) \tag{23}$$

where h_i is the price penalty factor of i^{th} generator in \$/kg

$$h_i = C(P_i^{\max}) / E(P_i^{\max}) \tag{24}$$

4.4 Problem Formulation

Aggregating the objectives and constraints, the problem can be mathematically formulated as

$$minimize F(\mathbf{P})$$

$$\text{Subject to} \quad \begin{aligned} g(\mathbf{P}) &= 0 \\ h(\mathbf{P}) &\le 0 \end{aligned}$$

where g and h are the power balance equality and generation capacity inequality constraints respectively.

5 Experimental Results

The proposed algorithm IDE has been developed in MATLAB 6.1 using INTLAB toolbox [11]. We investigate the effectiveness of the proposed approach over the conventional DE algorithm by considering the standard IEEE 14-bus 3-generator as a test system [7]. The test system data such as fuel cost coefficients, Emission coefficients, corresponding price penalty factors, generation capacity for all generating units and loss coefficients are given in Tables 1-3. The total power demand P_D is taken as 283.4 MW.

For a fair comparison we executed 20 test runs of both the algorithms on the EELD problem. Let NS be the number of runs out of the 20 runs that succeeded in finding the global minimum f^* within the tolerance $\varepsilon_f = 10^{-2}$. Let NE be the total number of function evaluations for which f^* were obtained during the 20 runs. Then, the Expected Number of Evaluations per Success, $ENES$ represents the mean number of function evaluation needed in order to terminate the algorithms and is computed as $ENES = NE / NS$. If the global minima can not be achieved, then $ENES$ is not defined. MNE is the maximum number of real function evaluations of a particular run, out of total twenty runs of the algorithm. To calculate the total effort we adopt the procedure as given in [4]. Assuming that one interval evaluation is equivalent to two real number evaluation, the total effort $TE = 2*(IFE) + MNE$, where IFE is the total number of interval function evaluations.

For all the optimization runs of both the algorithms, the population size NP was set as 50, mutation scaling factor μ as 0.9 and crossover constant CR as 0.85. For IDE algorithm the tolerance for approximating the minimizer $\mathbf{P}^*$ was taken as $\varepsilon_x = 10^{-2}$ and the shrinking constant r as 10.

Table 1.Fuel Cost Coefficients

Generating unit	Fuel Cost Coefficients		
	a_i \$/hr	b_i \$/MW-hr	c_i \$/MW^2-hr
1	105.0	2.45	0.005
2	44.4	3.51	0.005
3	40.6	3.89	0.005

Table 2. Emission Coefficients & Price penalty factor

Gen. unit	Emission Coefficients			Price penalty factor
	α_i kg/hr	β_i kg/MW-hr	γ_i kg/MW^2-hr	h_i \$/kg
1	22.983	-1.3552	0.01265	3.0821
2	137.370	-1.2489	0.01378	2.9638
3	363.705	0.8051	0.00765	0.9210

Table 3. Loss Coefficients & Generation capacity

Generating unit	Loss Coefficients	Generation capacity	
	A_i	$P_i^{\min}$ MW	$P_i^{\max}$ MW
1	0.014362	50.0	200.0
2	0.007737	20.0	100.0
3	00.04083	20.0	100.0

When IDE is applied to EELD on IEEE 14-bus 3-generator system without P_{loss} we observe that it has succeeded in all the runs as shown in Table 4. And *ENES* could be computed as to be 6900. From this it is evident that an efficient termination criterion has been developed, which is verified in all runs. For each run the maximum number of real function evaluations has been less than or equal to 7200 with $IFE = 286$, making $TE = 7772$.

When DE is applied to EELD with this *TE* it has not succeeded even in a single run, due to which *ENES* could not be computed and it consumes all the trials and terminates without any guarantee that the global minimum has been found.

The fuel cost, emission cost and transmission losses obtained by IDE and DE for the system with transmission losses are shown in Table 5. From Table 5 we observe that for each run the maximum number of real function valuations using IDE is at most 7300 and *ENES* is 6950. Also it gave $IFE = 290$, making $TE = 7880$.

We also observe that the DE algorithm with this *TE* has not succeeded even in a single run. Thus *ENES* could not be defined for it. The results exhibited in Table 5 clearly show that IDI has succeeded in all the rums and found the global minima with certainty. Table 6 shows the output powers in MW of all generators obtained from IDE for both the cases.

Table 4. Comparision of IDE and DE for lossless system

Algorithm	DE	IDE
NS	-	20
ENES	-	6900
MNE	7772	7200
Fuel cost ($/hr)	1129.901	1129.852
Emission cost ($/hr)	618.64	618.42

Table 5. Comparision of IDE and DE for system with loss

Algorithm	DE	IDE
NS	-	20
ENES	-	6950
MNE	7880	7300
P_{loss} (MW)	5.362	5.319
Fuel cost ($/hr)	1158.025	1157.669
Emission cost ($/hr)	845.795	845.374

Table 6. Power outputs of generating units with IDE

Generating unit	Without loss (MW)	With loss (MW)
1	95.640	93.72
2	75.028	75.51
3	85.330	92.077

6 Conclusion

In this contribution an Interval based Differential Evolution Algorithm was presented. Poorly defined termination criterion made the conventional DE computationally expensive and also the global minimum was not guaranteed. The above drawbacks were overcome by the inclusion of interval arithmetic in conventional DE. In the first phase of algorithm, it estimates the initial upper and lower bounds of the objective function using interval arithmetic. Then the upper and lower bounds were updated at each generation. Finally, the algorithm was able to compute the global minimum with certainty. The proposed algorithm became more effective when a new termination criterion based on the concept of shrinking box was used. The extra computational effort was avoided by selecting the next generation from the subset of current population, which performed with in the upper and lower bounds of the objective function. We applied the proposed algorithm to CEELD problem of IEEE 14 bus 3 generator systems. We considered two cases; with and without transmission loss. Then we compared the results with that obtained from conventional DE. We demonstrated that IDE exhibited high performance with a high dimensional problem like CEELD. Hence, we conclude that IDE outperforms conventional DE.

References

[1] R. Storn, "Differential Evolution, A Simple and Efficient Heuristic Strategy for Global Optimization over Continuous Spaces," Journal of Global Optimization, vol. 11, pp. 341– 359, 1997.

[2] K. Zielinski , D. Peters, and R.Laur, "Stopping Criteria for Single-Objective Optimization," in Proceedings of the Third International Conference on Computational Intelligence, Robotics and Autonomous Systems, 2005

[3] R. Moore, Interval analysis. Prentice-Hall, Englewood Cliffs, New Jersey, 1966.

[4] D. G. Sotiropoulos, E. C. Stavropolous, and M. N. Vrahatis, "A New Hybrid Genetic Algorithm for Global Optimization," Journal of Global Optimization, vol. 33, no. 7, pp. 4529–4538, 1997.

[5] Abido, "Multiobjective Evolutionary Algorithm For Electric Power Dispatch," IEEE Transactions on Enolutionary computation, vol 10 no. 3, pp. 315-329, 2006.

[6] J. Sasikala, and M. Ramaswamy, "Optimal λ based Economic Emission Dispatch using Simulated Annealing," International journal of Computer Applications, vol. 01, no. 10, pp. 69–83, 2010.

[7] Nanad, Lakshman Hari & Kothari, "Economic Emission Load Dispatch with line constraints using a Classical technique," in IEE proceedings, Generation Transmission and Distribution, vol. 41,no.1, pp. 01– 10, 1994.

[8] J. Nanad, and P.R. Bijw, "A Novel Approach for Generation of Transmission loss Coefficients," IEEE PES, Summer Meeting, Paper no. A77-599-4, 1977.

[9] J. Lampinen, Global Optimization by Differential Evolution, Technical Report, Lappeenranta University of Technology, Lappeenranta, Finland, 1999.

[10] E. Hansen, Global optimization using interval analysis. Dekker, New York, 1992.

[11] S.M.Rump, INTLAB- INTerval LABoratory, Developments in Reliable Computing, Tibor Csendes, Kluwer Acadmic Publishers, Dordrecht, pp. 77–104, 1999.

Heat Transfer Characteristics of Diffusion Flames Impinging Upwards to Plane Surfaces Held Normal to Flame Jet Axis

G. K. Agrawal
Dept. of Mechanical Engg.
Govt. Engineering College
Bilaspur (C. G.), India
gka1966@yahoo.com

S. K. Som
Dept. of Mechanical Engg.
Indian Institute of Technology
Kharagpur (W. B.), India
sksom@mech.iitkgp.ernet.in

Suman Chakraborty
Dept. of Mechanical Engg.
Indian Institute of Technology
Kharagpur (W. B.), India
suman@mech.iitkgp.ernet.in

Abstract

A theoretical model of diffusion turbulent flames impinging normally on a plane circular target plate has been developed to predict the influences of jet Reynolds number, ratio of plate separation distance to nozzle diameter, and equivalence ratio on plate heat transfer characteristics. The model is based on the numerical solution of equations for conservation of mass, momentum and energy. Methane and air have been considered as fuel and oxidizer respectively. Global two-step irreversible reaction kinetics has been employed for the oxidization of methane. The RNG k-ε model has been used to compute the turbulence, and the Discrete Ordinate model has been used for radiative transfer in the flame. It is revealed that the plate surface heat flux attains a maximum value at a location little away from stagnation point and then decreases gradually with the radial distance from the plate centre. There is a monotonic increase in $\overline{Nu}$ with a decrease in H/d from 15 to 4 at all values of Re.

Keywords- Flame impingement, Heat transfer, Diffusion flame

Broad Area- Mechanical Engineering

Sub-Area- Combustion, C. F. D.

1. Introduction

Direct gas flame impingement heating using hydrocarbon-air flame is employed in a wide range of industrial heating processes because of rapid and high heating rates. These include shaping of glasses, heating water walls in a boiler furnace, heating metal bars and billets, melting of scrap materials. In the context of today's concern of energy and environment, any industrial process should be energy efficient and eco friendly. A considerable research work has already been carried out in the field of flame impingement heat transfer for last two to three decades, and a host of articles [1-26] is available in the literature today. The most important experimental works in this field are due to Baukal and Gebhart[1-3], Dong et al.[4-5], Fairweather et al. [6-7], Hargrave et al. [8-9] and many others. The major conclusions drawn from these works are that the plate surface heat flux distribution is non-uniform with a maximum which is little away from the stagnation point. The location of the maximum heat flux depends upon the structure of the flame which in turn is influenced by the operating conditions. Dong et al. [4] developed an empirical correlation of average Nusselt number over plate surface with jet Reynolds number, the ratio of separation distance to burner diameter and equivalence ratio. The experimental works pertain mostly to laminar flow and furnish the information that the the average heat flux at plate surface increases with an increase in Reynolds number and a decrease in the ratio of separation distance to burner diameter. A number of review articles relating to some specific aspects of flame impingement heat transfer is also available in literature [10-17]. The most recent and comprehensive review on flame impingement heat transfer is provided by Chander and Ray [17]. The heat transfer due to the impingement of a flame on a target solid surface depends upon the flame structure, the temperature field in the near vicinity of the plate, and both convective and radiative properties of the constituents species of the flame. The flame temperature is influenced by the flow field of impinging jet which comprises the free jet region, stagnation region, and wall jet region. The theoretical studies in flame impingement heat transfer are very few in number[18-26]. Most of them deal with laminar and turbulent premixed flames impinging normally to a flat surface and predict the temperature field, velocity field and heat released near the plate surface. Malikov et al.[18] predicted that the radiative heat flux at the plate surface is only 1/3 of the total flux , while the remaining 2/3 is due to the convection heat transfer from the hot jet impinging on the surface. All the works confirmed a non uniform temperature distribution near the plate surface with a maximum one shifted away from the stagnation point. It appears from the review of

literature that a comprehensive theoretical work is needed for a further generalised understanding of the influences of the pertinent operating parameters like burner geometry, plate separation distance, types of flame (premixed and diffusion) and equivalence ratio on heat transfer characteristics in both normal and oblique impingement of flame on a flat plate. Therefore a numerical model of diffusion flame impinging normally on a flat surface has been developed in the present article to predict the influences of jet Reynolds number, ratio of plate separation distance to nozzle diameter, and equivalence ratio on plate heat transfer characteristics. The model takes account of both convective and radiative heat transfer to the plate.

2. Theoretical Formulation

2.1 Physical Systems and Assumptions

The physical model refers to the impingement of a vertical flame jet on a plane circular horizontal target plate of radius R with normal impingement (Figure 1.) Diffusion flames has been considered. The fuel and oxidizer are considered to be methane gas (CH_4) and air respectively. The diffusion flame is generated by the jet of fuel from a cylindrical nozzle surrounded by a co flowing stream of air through an annulus formed by a concentric outer cylindrical nozzle (Figure 1.). The jet Reynolds number covered in the present work pertains to a turbulent flame. The RNG k-ε model [27] has been used for the computation of turbulent flow. The adoption of the model has been made for accommodating the implications of smaller scales of motion, and also to account for the effects of mean strain rate and mean rotation on turbulent diffusion to give an implicit consideration for the non-isotropic features of the turbulent impinging flows.The following assumptions have been made in the present work:

- The flow is turbulent but steady (based on time mean values of flow parameters).
- The oxidation of methane has been considered by global two-step irreversible reactions with finite rate chemistry.

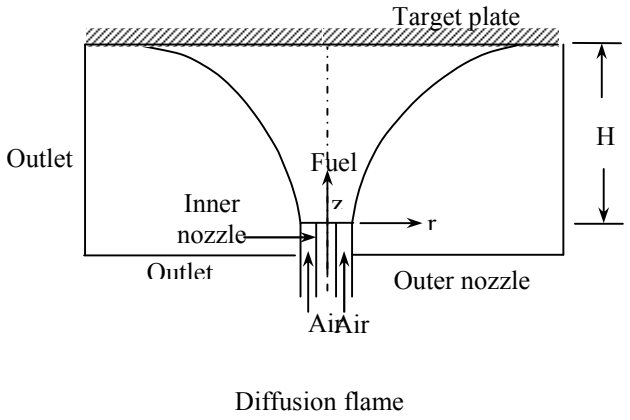

Diffusion flame

Figure 1. Physical model of normal impingement.

- The gas phase comprising air and products of combustion is assumed to obey the ideal gas laws.
- The flow at the outlet of the burner nozzle is considered to be in a plug flow mode i.e. the discharge velocity is uniform.
- The system is assumed to be grey absorbing, emitting medium with respect to radiation characteristics.

2.2 Governing Equations

Conservation of Mass

$$\nabla.\left(\rho v\right)=0 \tag{1}$$

Conservation of Momentum

$$\rho\left[v.\nabla v\right]=-\nabla p+\nabla.\left(\mu_{eff}\nabla v\right)+F_B \tag{2}$$

where

$$\mu_{eff}=\mu+\mu_t=\mu+\rho c_\mu\frac{k^2}{\varepsilon} \tag{2a}$$

Turbulent Kinetic Energy

$$\nabla.\left(\rho vk\right)=\nabla.\left(\frac{\mu_t}{\sigma_k}\nabla k\right)+G_k-\rho\varepsilon \tag{3}$$

Dissipation Rate of Turbulent Kinetic Energy

$$\nabla.\left(\rho v\varepsilon\right)=\nabla.\left(\frac{\mu_t}{\sigma_\varepsilon}\nabla\varepsilon\right)+C_{1\varepsilon}\frac{\varepsilon}{k}G_k-\rho C_{2\varepsilon}\frac{\varepsilon^2}{k} \tag{4}$$

where, v is the Reynolds-averaged velocity, p is the pressure, F_B is the gravitational body force, μ , μ_t , μ_{eff} are respectively the laminar viscosity, turbulent viscosity and effective viscosity, ρ is the density, k and ε are respectively the turbulent kinetic energy and its dissipation rate, and G_k is generation of turbulent kinetic energy due to mean velocity gradients.The values of model constants as evaluated [28] by employing the re-normalization group theory are as follows: $C_\mu=0.0845, C_{1\varepsilon}=1.42,$

$$C_{2\varepsilon}=1.68+\frac{C_\mu n^3\left(1-\left(n/4.8\right)\right)}{1+0.012n^3},\ \sigma_k=\sigma_\varepsilon=0.7194.$$

where n is the ratio of turbulent to the mean strain time scale.

Conservation of Energy

$$\nabla.\left(\rho v h\right) = \nabla.\left(\rho \alpha_{eff} \nabla h\right) - \nabla.q^{r} \tag{5}$$

where, $h = \sum_{k=1}^{N} Y_k \left[h_{f,k}^{0} + \int_{T_{ref}}^{T} c_{p,k} dT \right]$, is the mixture enthalpy, q^r is the radiative component of the heat flux (to be modeled later), h_f^0 is the enthalpy of formation at standard state, T is the temperature, Y_k is the mass fraction of component *k*, and α_{eff} is the effective thermal diffusivity (which takes also the eddy thermal diffusivity into account).

Species Conservation

$$\nabla.\left(\rho v Y_k\right) = \nabla.\left(\rho D_{eff} \nabla Y\right) + S_k \tag{6}$$

where D_{eff} is the effective mass diffusivity (which takes also the eddy mass diffusivity into account), and S_k is the source term for net generation (or depletion) of k[th] species by the chemical reactions.

2.3 Chemical Kinetics

Methane is considered to be the fuel employed for the combustion reaction, and global two-step irreversible reactions for oxidation of methane are considered, as described below.

$$CH_4 + 1.5O_2 = CO + 2H_2O \tag{7}$$

$$CO + \frac{1}{2}O_2 = CO_2 \tag{8}$$

The rate of reaction is found from a comparison of Arrhenius type of kinetic controlled model and the diffusion controlled turbulent eddy dissipation model after Magnussen and Hjertager [29], as elucidated below.

Arrhenius equation:

$$\omega_{fk} = B\left(\rho\right)^{a+b} \frac{Y_f^{a} Y_o^{b}}{M_f^{a} M_o^{b}} \exp\left(-\frac{E}{\bar{R}T}\right) \tag{9}$$

Magnussen and Hjertager equation:

$$\omega_{fd} = A \frac{\rho}{M_f} \frac{\varepsilon}{k} \left[\min\left(Y_f, \frac{Y_o}{\gamma}, \frac{cY_P}{1+\gamma} \right) \right] \tag{10}$$

where ω is the rate of depletion of fuel defining the rate of reaction. The subscripts *fk* and *fd* represent the kinetic controlled and eddy dissipation control model. It has to be mentioned in this context that CH_4 acts as a fuel for reaction given by Eq. (7) while the CO does so for the reaction given by Eq. (8). The values of A and c in Eq. (10) are taken as A=4.0 and c=0.5 [29]. The values of kinetic parameters B, E, a, b are taken from standard literature [30]. Eqs. (9) and (10) are finally utilized to formulate the source term in the species conservation equation, as follows:

$$\omega_f = \min\left(\omega_{fk,} \omega_{fd}\right) \tag{11}$$

$$S_k = \lambda_k M_k \omega_f \tag{12}$$

where λ is stoichiometric ratio and M is molecular weight

2.4 Radiation Model

The present system is assumed to be a gray absorbing-emitting medium. The characteristic physical dimension of the system and the representative values of absorption coefficient of constitutive species make the system to be optically thin to radiation heat transfer. Following the Discrete Ordinate model [31], one can express the equation of radiative transfer in the form

$$\nabla.I\left(s_i\right) + \beta I\left(s, \hat{\mathbf{\Omega}}\right) = kI_b(T) + \frac{\sigma}{4\pi} \int_{4\pi} I\left(s, \hat{\mathbf{\Omega}}'\right) d\Omega' \tag{13}$$

where I is the radiation intensity, subscript '*b*' represents black body, s is the path measured along the direction of propagation, $\hat{\mathbf{\Omega}}$ and s_i are the components of s, Ω is solid angle and β, k, σ are the extinction coefficient, absorption coefficient and scattering coefficient respectively.

The radiative source term in the energy equation (Eq. 5) becomes

$$\nabla.\mathbf{q}^{r} = \int_{4\pi} \nabla.\hat{\mathbf{\Omega}} I d\Omega \tag{13a}$$

The radiation boundary conditions can be formulated by noting that the incident radiation heat flux, q_{in}, at the wall can be described as

$$q_{in} = \int_{s.n>0} I_{in} s.n d\Omega \tag{13b}$$

The radiative flux leaving the surface is given by

$$q_{out} = (1-\varepsilon_w) q_{in} + n^2 \varepsilon_w \sigma T_w^4 \quad (13c)$$

where, ε_w is the emissivity of the plate, n is the refractive index of the medium in the immediate vicinity of the plate and σ is the Stefan-Boltzmann constant . The radiation intensity for all outgoing directions at the plate is given by

$$I_o = q_{out} / \pi \quad (13d)$$

The radiation heat flux at flow inlets and outlets is computed in the same manner as done at plate. The emissivity of all flow inlets and outlets is considered to be 1.0 (black body absorption).

2.5 Heat Transfer Coefficient at Target Plate

The average heat transfer coefficient, $\bar{h}$, is written as

$$\bar{h} = \frac{1}{A} \int h dA \quad (14)$$

where the local heat transfer coefficient, *h*, is given by

$$h = \frac{q_w}{(T_{ad} - T_w)} \quad (14a)$$

where T_{ad} is the adiabatic flame temperature of CH_4

The resultant heat flux q_w is given by

$$q_w = -k \left(\frac{\partial T}{\partial z} \right)_{plate} + q_{rw} \quad (14b)$$

The rate of heat transfer to the plate $Q = \int q_w dA$ (14c)

The non-dimensional heat transfer rate, represented in terms of the average Nusselt number, $N\bar{u}$, is

$$N\bar{u} = \frac{\bar{h}(2R)}{k} \quad (14d)$$

2.6 Numerical Solution

The conservation equations (Eqs.1-6) were solved by employing a fully time implicit finite volume technique. The equations were written in a cylindrical coordinate system with proper matching of the geometry of target plates as one of the boundaries. A coupling between pressure and velocity was accomplished by using the SIMPLE algorithm [32].The spatial derivatives in the diffusion terms were discretized by second order central difference scheme, whereas the advection terms were discretized by first order upwind scheme. A variable size adaptive grid system was considered and variations in the size of grid were affected smoothly, with more densely-spaced grids being skewed close to the target plate. The convergence criterion for the relative errors in all the discretized equations (except the energy equation) was set to 10^{-3}, whereas for the energy equation it was 10^{-6}. Typically, 100 (r) × 40 (z) grid systems were chosen to discretize of *H/d* ratio as 4:1, with proportionate enhancements in the number of grid points along *z* for higher aspect ratios. An optimal size distribution of the numerical mesh to be used, for a given value of *H/d*, was determined from several numerical experiments, which showed that further refinements in grids in either directions did not change the results (maximum change in velocity or any scalar variable) by more than 2%.

2.7 Operating Parameters and Boundary Conditions

For the numerical computations, methane and air were used as fuel and oxidizer, respectively. For a diffusion flame, the diameters of air and fuel nozzles were taken as d_a = 12 mm and d_f = 4 mm, respectively. The temperature of both fuel and air at the exit plane of the burner was considered to be 300 K. The fuel and air flow rates, and vertical distance of the target plate from the burner exit plane were varied to obtain the range of pertinent dimensionless input parameters as follows:

(i) Jet Reynolds number, Re $= \frac{\rho v_i d}{\mu}$: 2000, 6000, 8000, 10000, 15000

(ii) Equivalence ratio, ER $= \frac{(Y_a/Y_f)_s}{(Y_a/Y_f)_a}$: 0.8, 1.0, 1.2, 2.0

where subscripts *s* and *a* stand for stoichiometric and actual mixtures

(iii) The ratio of plate separation distance to nozzle diameter, H/d: 4, 8, 15.

The ranges of input parameters as stated above have been taken in consideration of the typical values used in practice and are also available in literature.

The axial velocity distribution for both fuel and air (in case of diffusion flame) at the exit plane of the nozzle was assumed to be in a plug flow mode (i.e. uniform velocity distribution). No slip, impermeable and isothermal condition was imposed on target plate. The outflow boundary condition was used at the exit plane of the computational domain. Axisymmetric boundary condition was used.

3 Results and Discussion

3.1 Model Validation

In most of the experimental work pertaining to flame jet impingement heat transfer, as reported in literature, the target plates are cooled on the other side of the impingement either by water or air, and the plate temperature is not

specified. The present model, on the other hand, pertains to an isothermal target plate of specified temperature, and therefore it becomes difficult to compare the present model predictions with available experimental work in literature. However, a possible comparison of the results of the present model with those of an experimental work [33] in relation to the stagnation point heat transfer by turbulent flame jet impingement on an isothermal target plate has been made. This is shown in Table 1. A fair agreement is observed between the experimental work and the theoretical predictions of the present model.

Table 1. Comparison of theoretical predictions with experimental work [33]

Fixed input parameters		Variable parameter	Nu (at stagnation point)	
Experim -ental (33)	Present model	H/d	Experim -ental results [33]	Theoretical predictions by present model
Fuel: Mostly methane Flame: Premixed ER=1.0 Re=4226	Fuel: Methane Premixed ER=1.0 Re=4226	2	67.30	60.91
		4	111.82	102.31
		6	113.09	118.74
		8	110.68	99.61

3.2 Diffusion Flame Jet

Figure 1 shows the heat flux distribution at the plate surface for different values of H/d for a given fuel jet Reynolds number of 6000 and an equivalence ratio of 1 based on air flow in the annular nozzle of the burner. It is observed that the surface heat flux attains a maximum value a little away from the stagnation point and then decreases gradually with an increase in the radial distance from the centre of the plate. The heat flux distribution on a target plate by flame impingement is influenced by the shape of the flame and the radial temperature distribution in the near vicinity of plate which, in turn, depend upon the burner geometry, jet Reynolds number and the position of target plate relative to the burner. There is a substantial increase in the heat flux with a relatively flat distribution near the stagnation region.

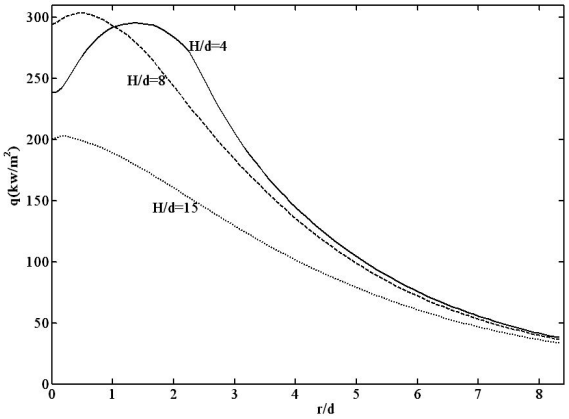

Figure 1. Local heat flux distribution on target plate normal to flame jet axis in diffusion flame, ER=1, Re=6000.

The counter molal diffusion between fuel and air in case of separate fuel and air jet is responsible in preparing the mixture for burning. Therefore the burning zone under this situation gets relatively more lifted from the burner with the appearance of a much thinner flame but with a more radial spread very close to the plate (Figures 2a, 2b, and 2c).

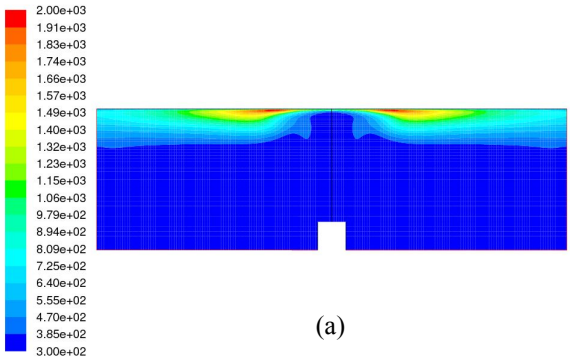

(a)

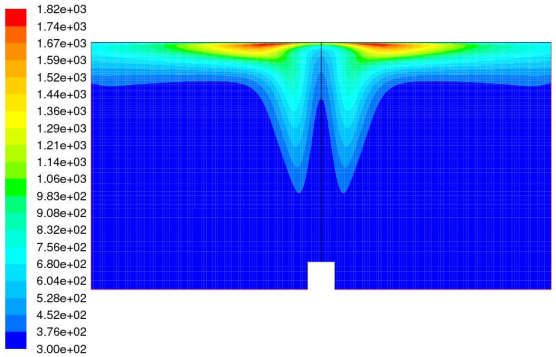

(b)

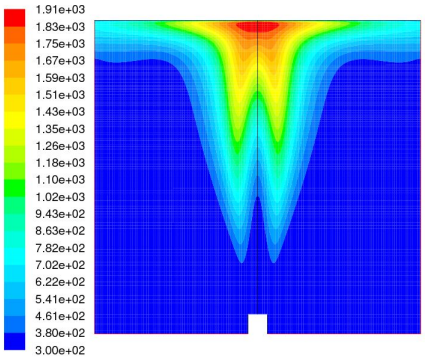

(c)

Figure 2. Temperature contour for diffusion flames, ER=1,Re=6000, (a) H/d=4, (b) H/d=8, (c) H/d=15

With an increase in the value of Re the flame region gets more attached to the plate surface with a relatively larger radial spread of the flame which results in a higher heat fluxes at the plate surfaces (Figure 3a). It is observed from Figure 3b that for a fuel rich mixture (ER=2) in a diffusion flame, the plate heat flux near the stagnation region is reduced as compared to that for ER=1. However the heat flux distribution curve becomes more flat at higher radial location resulting in higher heat fluxes at those locations as compared to that for ER=1.

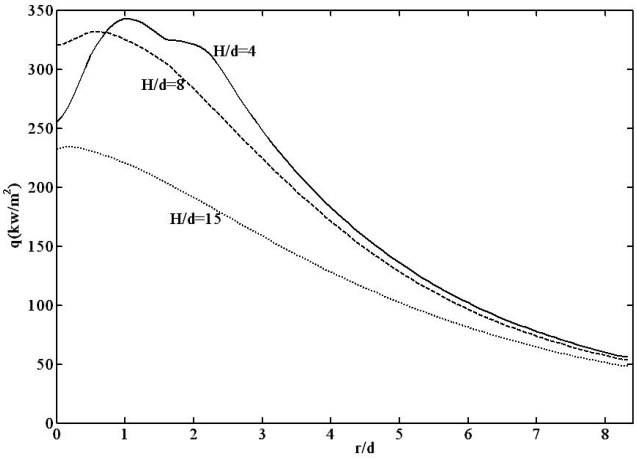

(a)

The average Nusselt number over the plate increases with an increase in Re and a decrease in the value of H/d (Figure 4a). The increase in average Nusselt number is more pronounced for a change in H/d from 15 to 8 as compared to a change from 8 to 4 and that too in the higher range of Reynolds number. This can be attributed to the fact of having a more plate attached flame with lower values of H/d and at higher increase in Re and ER. The increase in the value of Nu is more pronounced in case of higher values of Reynolds

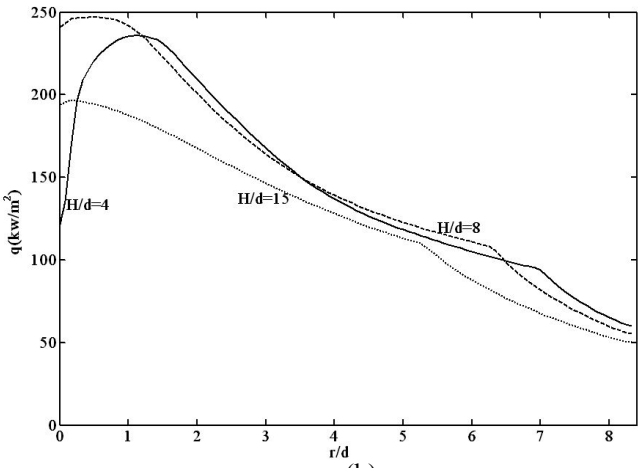

(b)

Figure 3. Local heat flux distribution on target surface in

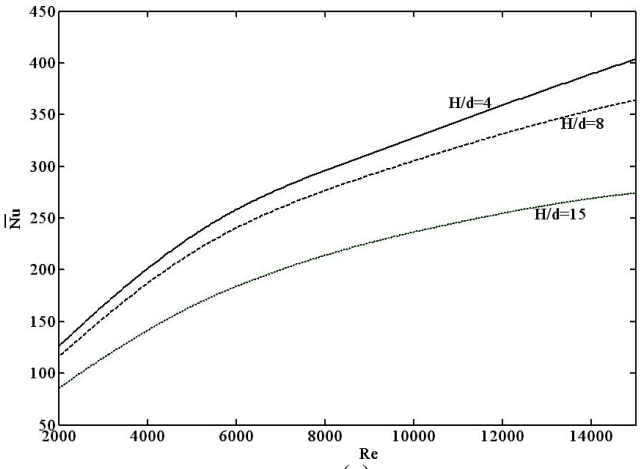

(a)

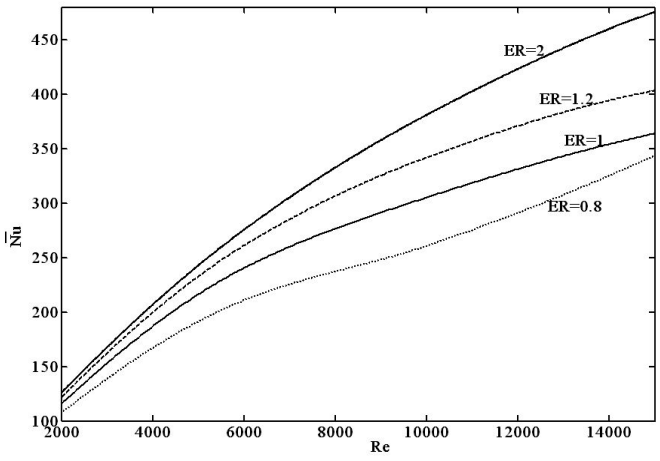

(b)

Figure 4. Variations of $\overline{Nu}$ with Re in diffusion flames, (a) ER=1, (b) H/d=8

number (above Re=6000). An increase in Reynolds number, under the situation, brings about a greater convective effect in reducing both the hydrodynamic and thermal boundary layer at the plate surface finally resulting in an increase in the rate of heat transfer.. Also at ER=2, the value of Nu is higher. Though the mixture is rich near the burner, but due toentrainment of surrounding air, conducive zone of burning is formed near the plate.

4 Conclusions

Numerical predictions have been made on the surface heat flux distributions and average Nusselt number $\overline{Nu}$ in turbulent diffusion flame impingement on plane surfaces held normal to flame jet axis. The main observations of the numerical studies are as follows

- Plate surface heat flux attains a maximum value at a location little away from stagnation point and then decreases gradually with the radial distance from the plate centre. With an increase in the value of separation distance of the plate from the nozzle, the peak in the local heat flux comes closer to the stagnation point.

- For a decrease in the value of H/d from 15 to 8, there is a substantial increase in the surface heat flux at all radial locations. However a further decrease in H/d from 8 to 4 results in a decrease in heat flux near the central region including the stagnation point, but a marginal increase in the same at higher values of r/d.

- The average Nusselt number $\overline{Nu}$ over the plate increases with an increase in Re and ER and a decrease in H/d for diffusion flames. There is a monotonic increase in $\overline{Nu}$ with a decrease in H/d from 15 to 4 at all values of Re. However, the increase in $\overline{Nu}$ is more pronounced for a change in H/d from 15 to 8 and also in the high range of Reynolds number Re

References

[1] C. E. Baukal, B. Gebhart, "Surface condition effects on flame impingement heat transfer", Expt. Thermal Fluid Sci., vol. 15, pp. 323-335, 1997.

[2] C. E. Baukal, B. Gebhart, "Oxygen-enhanced/natural gas flame radiation", Int. J. Heat Mass Transfer, vol. 40(11), pp. 2539-2547, 1997.

[3] C. E. Baukal, B. Gebhart, "Heat transfer from oxygen-enhanced/natural gas flames impinging normal to plane surface", Expt. Thermal Fluid Sci., vol. 16, pp. 247-259, 1998.

[4] L. L. Dong, C. S. Cheung, C. W. Leung, "Heat transfer characteristics of an impinging butane/air flame jet of low Reynolds number", Exp. Heat Transfer, vol. 14, pp. 265-282, 2001.

[5] L. L. Dong, C. S. Cheung, C. W. Leung, "Heat transfer from an impinging premixed butane/air slot flame jet", Int. J. Heat Mass Transfer, vol. 45, pp. 979-992, 2002.

[6] M. Fairweather, J. K. Kilham, S. Nawaz, "Stagnation point heat transfer from laminar high temperature methane flames", Int. J. Heat Fluid Flow, vol. 5 (1), pp. 21-27, 1984.

[7] M. Fairweather, J. K. Kilham, A. M. Ashtiani, "Stagnation point heat transfer from turbulent methane air flames", Combust. Sci. Tech., vol. 35, pp. 225-238, 1984 .

[8] G. K. Hargrave, M. Fairweather, J. K. Kilham, "Forced convective heat transfer from premixed flames-Part 1: Flame structure", Int. J. Heat Fluid Flow, vol. 8 (1), pp. 55-63, 1987

[9] G. K. Hargrave, M. Fairweather, J. K. Kilham, "Forced convective heat transfer from premixed flames-Part 2: Impingement heat transfer", Int. J. Heat Fluid Flow, vol. 8 (2), pp. 132-138, 1987.

[10] R. Viskanta, M. P. Mengüç, "Radiation heat transfer in combustion systems", Prog. Energy Combust. Sci., vol. 13, pp. 97-160, 1987.

[11] R. Viskanta, "Heat transfer to impinging isothermal gas and flame jets", Expt. Thermal Fluid Sci., vol. 6 (2), pp. 111-134, 1993.

[12] C. E. Baukal, B. Gebhart, "A review of flame impingement heat transfer studies Part 1: Experimental conditions", Combust. Sci. Tech., vol. 104, pp. 339-357, 1995 .

[13] C. E. Baukal, B. Gebhart, "A review of flame impingement heat transfer studies Part 2: Measurements", Combust. Sci. Tech., vol. 104, pp. 359-385, 1995.

[14] C. E. Baukal, B. Gebhart, "A review of empirical flame impingement heat transfer correlations" Int. J. Heat Fluid Flow, vol. 17, pp. 386-396, 1996.

[15] C. E. Baukal, B. Gebhart, "A review of semi analytical solutions for flame impingement heat transfer", Int. J. Heat Mass Transfer, vol. 39 (14), pp. 2989-3002, 1996.

[16] R. Viskanta, "Convective and radiative flame jet impingement heat transfer", Int. J. Transport Phenomena, vol. 1, pp. 1-15, 1998.

[17] S. Chander, A. Ray, "Flame impingement heat transfer: A review", Energy Conversion Management, vol. 46(18-19), pp. 2803-2837, 2005.

[18] G. K. Malikov, D. L. Lobanov, K. Y. Malikov, V. G. Lisienko, R. Viskanta, A. G. Fedorov, "Direct flame impingement heating for rapid thermal materials processing", Int. J. Heat Mass Transfer, vol. 44, pp. 1751-1758, 2001.

[19] H. H. Liakos, E. P. Keramida, M. A. Founti, N. C. Markatos, "Heat and mass transfer study of impinging turbulent premixed flames", Heat Mass Transfer, vol. 38, pp. 425-432, 2002.

[20] G. K. Malikov, D.L. Lobanov, Y.K. Malikov, V.G. Lisienko, R. Viskanta, A.G. Fedorov, "Experimental and numerical study of heat transfer in flame jet impingement system", J. Inst. Energy, vol. 72, pp. 2–9, 1999.

[21] H. H. Liakos, M. K. Koukou, M. A. Founti, N. C. Markatos, "Industrial scale processing of granite surfaces by natural gas jet flames", Applied Thermal Engineering, vol. 22, pp. 393-405, 2002.

[22] C. R. Kleijn, "Heat transfer from laminar impinging methane/air flames", in: Proceedings of ASME-PVP Conference, Atlanta, Georgia, USA, 2001.

[23] N. Sullivan, M.C. Branch, M. Strobel, J. Park, M. Ulsh, B. Leys, "The effects of an impinging surface and quenching

on the structure of laminar pre-mixed flames", Combust. Sci. Technol., vol. 158, pp. 115–134, 2000.

[24] H. H. Liakos, K.K. Maria, M.A. Founti, N.C. Markatos, "Effect of varying pressure and impingement angle in flaming process", Can. J. Chem. Engg., vol. 78, pp. 834–41, 2000.

[25] M. Sibulkin, "Heat transfer near the forward stagnation point of a body of revolution", J. Aero. Sci., vol. 19, pp. 570-571, 1952.

[26] G. Malikov, V. Lisienko, Y. Malikov, J. Wagner, H. Kurek, Y. Chudnovsky, R. Viskanta, "Mathematical modeling of direct flame impingement heat transfer", Proceedings of IMECE2006, Chicago, Illinois, USA, November 5-10, 2006

[27] V. Yakhot, S. A. Orszag, S. Thangam, T.B. Gatski, C. G. Speziale, "Development of turbulence model for shear flows by a double expansion technique", Physics of Fluids A, vol. 4, pp. 1510-1520, 1992.

[28] H. H. Liakos, E. P. Keramida, M. A. Founti, N. C. Markatos, "Heat and mass transfer study of impinging turbulent premixed flames", Heat Mass Transfer, vol. 38, pp. 425-432, 2002.

[29] B. F. Magnussen, B. H. Hjertager, "On mathematical modelling of turbulent combustion with specified emphasis on soot formation and combustion", in: 16th symp. (Int'l) on combustion, The combustion institute, Cambridge, MA, USA, pp. 719-729, 1976.

[30] R. W. Perry, D. W. Green, Perry's Chemical Engineers' Hand Book, McGraw- Hill, New York, 1998.

[31] M. N. Ozisik, Radiative Transfer and Interactions with Conductions and Convections, John Wiley and Sons, New York, 1973

[32] S. V. Patankar, Numerical Heat transfer and Fluid Flow, Hemisphere Publishing Company, Washington DC, 1980.

[33] T. H. van der Meer, "Stagnation point heat transfer from turbulent low Reynolds number jets and flame jets", Expt. Thermal Fluid Sci., vol. 4, pp. 115-126, 1991.

Study of Variations in Top Heat Loss Coefficient of Double Glazed Flat Plate Solar Collector with Different Range of Design and Climatic Variables Using MATLAB.

Pooja Tiwari
Govt. Engg. College, Jabalpur-482011,
Madhya Pradesh, India .
Email:pooja_atharva@rediffmail.com

Basant Kumar Chourasia
Department of Mechanical Engg.
Govt. Engg. College, Jabalpur-482011,
Madhya Pradesh, India .
basant_chourasia@rediffmail.com

Abstract

In the present study the estimation of glass cover temperatures, individual heat transfer coefficient, top heat loss coefficient and overall heat loss coefficient at different tilt angles of double glazed flat plate solar collectors has been done. The heat transfer from absorber plate to inner glass cover and from inner glass cover to outer glass cover occurs due to convection and radiation. Under steady state conditions heat transfer rate from plate to inner glass cover, from inner to outer glass cover is same and it is also equal to the rate of heat loss from outer glass cover to ambient. The top heat loss coefficient (U_t) is the result of convection and radiation between parallel plates. The top heat loss coefficient is a measure of thermal performance evaluation of flat plate collector. The methodology to compute the glass cover temperatures is based on the correlations proposed by Akhtar and Mullick [1]. The parameters with affects on the overall heat loss coefficient of a flat plate solar collector are mainly air properties estimation of convective and radiative heat transfer coefficient by Holland's and Buchhberg's equation, heat transfer coefficient of wind, ambient temperature, plate temperature , gap spacing between absorber plate and the glazing cover, emissivity of absorber plate, tilt angle of collector. The results reflect the contribution and significance of Design and Climatic variables to the collector overall heat loss coefficient and shows variations in results due to Eq.1.1 and Eq.1.2.

Keywords- Top heat loss coefficient, Absorber plate, Inner and outer glass cover, Nusselt number.

Broad Area- Mechanical Engineering.

Sub-Area- Renewable Energy.

1. Introduction

Thermal performance of flat plate collector is controlled by Design and Climatic variables. The various design parameters which affect the thermal performance of flat plate collector are : absorber plat temperature (T_p), collector tilt from horizontal (β), air gap spacing between absorber plate and inner glass cover (L_1),air gap spacing between inner and outer glass cover (L_2), emissivity of absorber plate (T_p). Various Climatic Parameters which affect the thermal performance of flat plate collector are: wind heat transfer coefficient (h_w) and Ambient Temperature (T_a) , respectively on the overall heat loss coefficient of the flat plate collector.

Nusselt number (N_u) has been calculated by the following equations suggested by Holland et al [2] Eq-(1.1) & Buchbergs et al [3] Eq-(1.2) and top heat loss coefficient (U_t) is calculated, compared and plotted with different range of design parameters by using MATLAB.

$$N_u = 1 + 1.44\left[1 - \frac{1708(\sin 1.8\beta)^{1.6}}{R_a \cos\beta}\right]^{+}\left[1 - \frac{1708}{R_a \cos\beta}\right]^{+} + \left[\left[\frac{R_a \cos\beta}{5830}\right]^{1/3} - 1\right]^{+}$$

-Eq-(1.1)

Where the + exponent implies that only positive values of the terms in the square brackets should be used (and ignored when they become negative).

$N_u = 1 + 1.446[1-(1708/Ra')]^{+}$ for $1708 < Ra' < 5900$

$N_u = 0.229(R_a')0.252$ for $5900 < Ra' < 9.23x104$

$N_u = 0.157(R_a')0.285$ for $9.23x104 < Ra' < 106$

-Eq-(1.2)

For the estimation of convective heat transfer coefficient the properties of air are to be evaluated at mean temperatures between absorber plate and inner glass cover and between inner and outer glass cover. The following relations have been used in the present work for calculation of air properties[4].

Thermal conductivity (K) :

$K = -3 \times 10^{-8} t_m^{\ 2} + 10^{-4} t_m - 4 \times 10^{-5}$ -Eq-(1.3)

Kinematic viscosity (γ) :

$\gamma = (9 \times 10^{-5} t_m^{\ 2} + 0.040 t_m - 4.17) \times 10^{-6}$ -Eq-(1.4)

Prandtl number (P_r):

$P_r = 1.057 - 0.06 \log t_m$ -Eq-(1.5)

Now Rayleigh Number(R_a')

$$R_a' = 9.8\,(T_p - T_{g1})(L_1)^3(P_r) / \gamma^2(t_m) \qquad \text{-Eq-(1.6)}$$

Here t_m is the mean temperature between two heat transfer surfaces and T_{g1} is temperature of inner glass cover.

Convective heat transfer co-efficient can be calculated by

$$h_{cpg1} = \frac{K_1 \times N_{u1}}{L_1} \qquad \text{-Eq-(1.7)}$$

and radiative heat transfer co-efficient (h_{rpg1}) can be calculated by

$$h_{rpg1} = \left\{\frac{\sigma}{\frac{1}{\epsilon_p} + \frac{1}{\epsilon_g} - 1}\right\}(T_p^2 + T_{g1}^2)(T_p + T_{g1}) \qquad \text{-Eq-(1.8)}$$

here ε_g is emissivity of the glass and ε_p is emissivity of the absorber plate. Similarly $(h_{cg1,g2})\&(h_{rg1,g2}), (h_{rg2a})$ may be calculated between inner glass cover and outer glass cover. Then Overall heat transfer co-efficient can be calculated by following equations .

Between plate and glass cover:-

$$U_{pg1} = (h_{cpg1} + h_{rpg1}) \qquad \text{-Eq-(1.9)}$$

Between inner glass cover and outer glass cover:-

$$U_{g1g2} = (h_{cg1g2} + h_{rg1g2}) \qquad \text{-Eq-(2.0)}$$

Between 2^{nd} glass cover & ambient air:-

$$U_{g2a} = (h_w + h_{rg2a}) \qquad \text{-Eq-(2.1)}$$

Finally top heat loss coefficient U_t can be calculated by the following equation.

$$U_t = \frac{1}{\frac{1}{U_{pg1}} + \frac{1}{U_{g1g2}} + \frac{1}{U_{g2a}}} \qquad \text{-Eq-(2.2)}$$

2. Results and discussion

Table 1. shows the range of variables used in present work.

Variables	Nomenclature	Range
T_p	Absorber plate temperature	333 K to 473 K
β	Tilt angel from horizontal	0^o to 60^o
L_1	Air gap spacing between absorber plate and inner glass cover	10 mm to 90 mm
L_2	Air gap spacing between inner and outer glass cover	10 mm to 50 mm
h_w	Wind heat transfer coefficient	05 W/m^2K to 45 W/m^2K
ε_p	Emissivity of absorber plate	0.1 to 0.9

2.1. Figure 1 shows the variation of Absorber Plate Temperature Vs Top heat loss coefficient. It is observed from the results that U_t varies direct with plate temperature and plot shows the % variation of U_t by using the equations suggested by Eq-(1.1) & Eq(1.2). The maximum % variation in U_t by using Eq-(1.1) & Eq-(1.2) is 0.5% .

Figure 2 shows the tilt angle as it affects the collector overall heat loss coefficient. It shows that the Top heat loss coefficient is insignificantly affected by variation in tilt angle values within the range: 0-60.The maximum % variation in U_t by using Eq-(1.1) & Eq-(1.2) is around 1% .

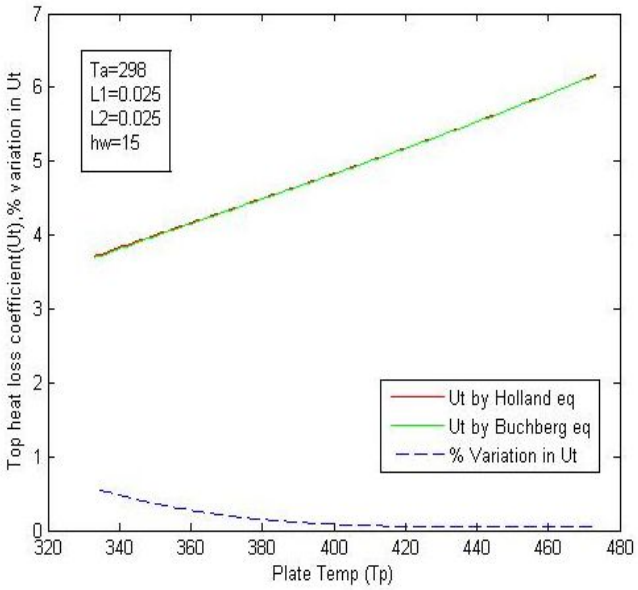

Figure 1. Variation of Absorber Plat Temperature Vs U_t

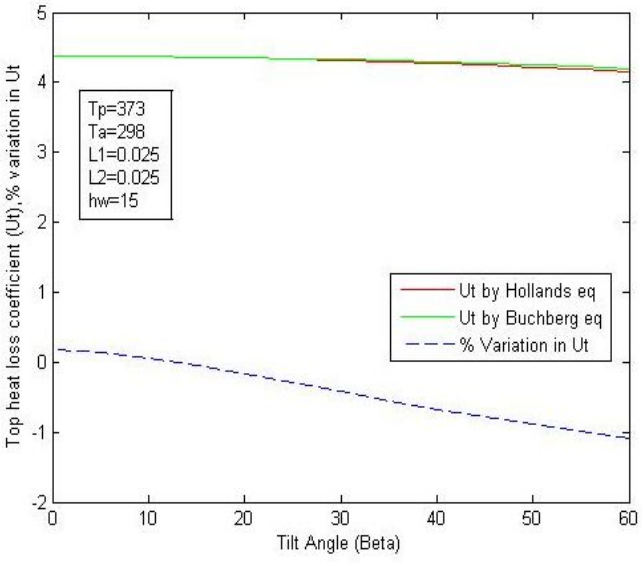

Figure 2. Variation of collector tilt angle Vs U_t

2.2 Figure 3 shows that air gap spacing between the absorber plate and the inner cover is a factor that contributes to the top heat loss co-efficient. The top loss co-efficient decreases as the air gap spacing increases. The % variation in U_t by using Eq-(1.1) & Eq-(1.2) is between 2% to 10%.

Figure 4 shows that it also contributes to top heat transfer coefficient between plate and inner glass cover. As we increase air gap spacing between plate and inner glass it decreases heat transfer coefficient.

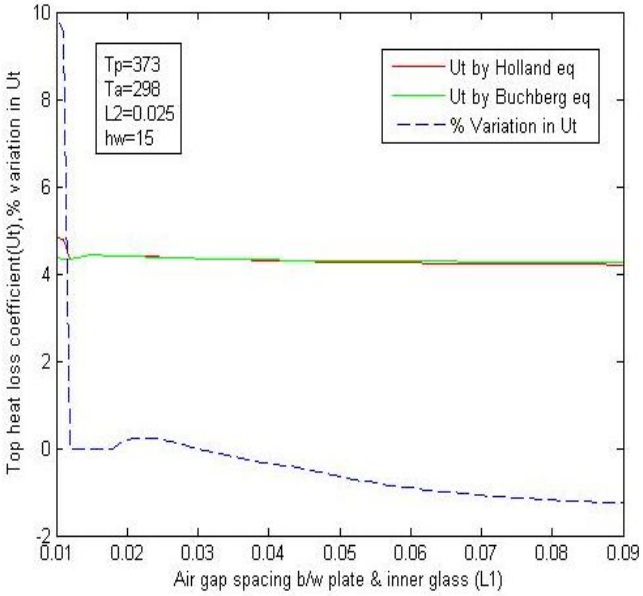

Figure 3. Variation of air gap spacing b/w absorber plat and inner glass cover Vs U_t

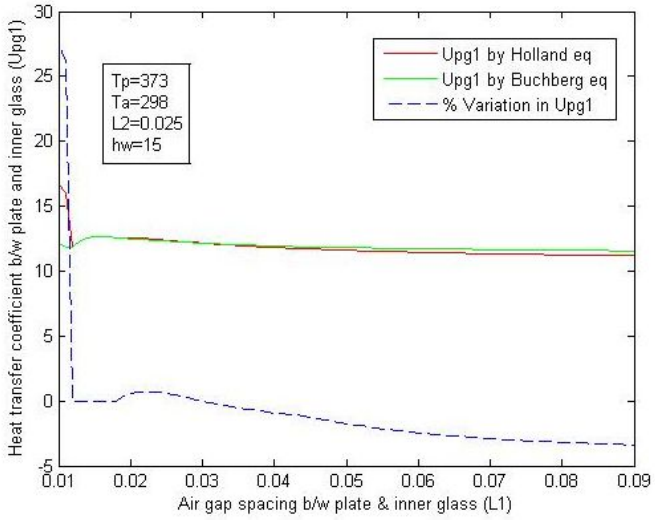

Figure 4. Variation of air gap spacing b/w absorber plat and inner glass cover Vs U_{pg1}

2.3 Figure 5 shows that air gap spacing between the outer and the inner glass cover is a factor that contributes to the top heat loss co-efficient. The loss co-efficient decreases as the air gap spacing increases. The % variation in U_t by using Eq-(1.1) & Eq-(1.2) is between 1% to 2%.

Figure 6 shows that it also contributes to top heat transfer coefficient between outer and inner glass cover. The max % variation in U_t by using Eq-(1.1) & Eq-(1.2) is between 1% to 4%.

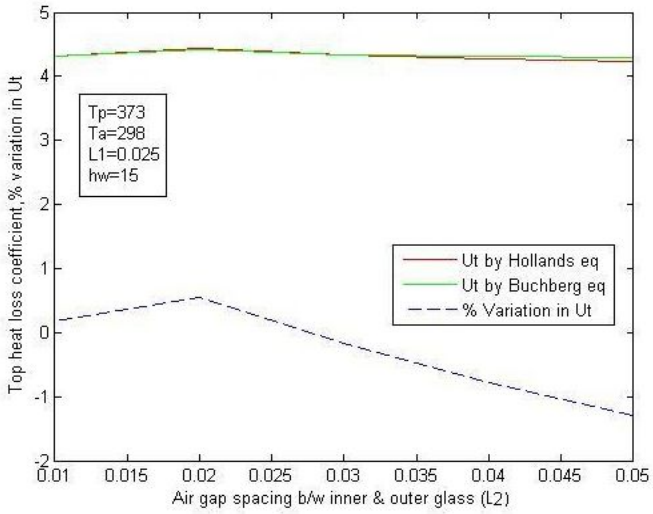

Figure 5. Variation of air gap spacing b/w outer and inner glass cover Vs U_t

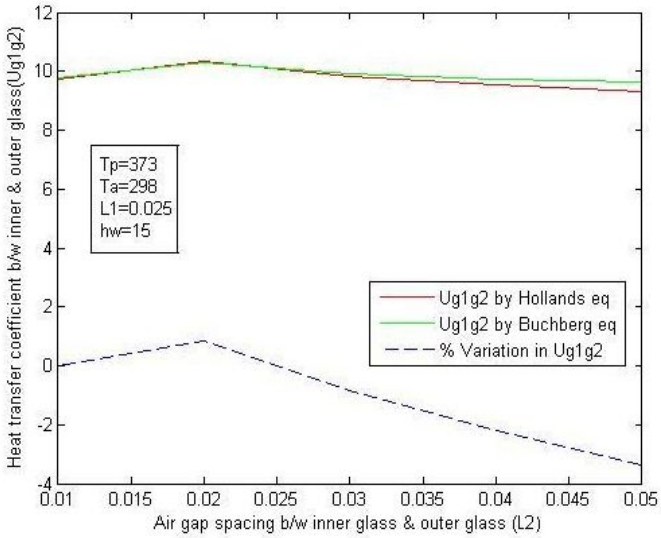

Figure 6. Variation of air gap spacing b/w outer and inner glass cover Vs U_{g1g2}

2.4 Figure 7 shows that absorber plate emissivity is a factor that contributes to the top heat loss co-efficient. It shows the variation of absorber plate emissivity, significantly affects the top heat loss coefficient. The max % variation in U_t by using Eq-(1.1) & Eq-(1.2) is 0.25%.

Figure 8 shows the effect of wind heat transfer coefficient on top heat loss coefficient. The max % variation in U_t by using Eq-(1.1) & Eq-(1.2) is less then 0.5 %. The top loss co-efficient increases as the wind heat transfer coefficient increases.

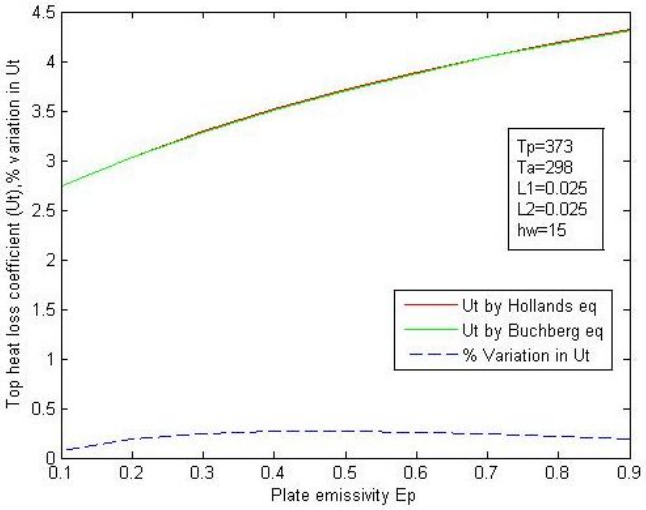

Figure 7. Variation of emissivity of absorber plat and inner glass cover Vs U_t

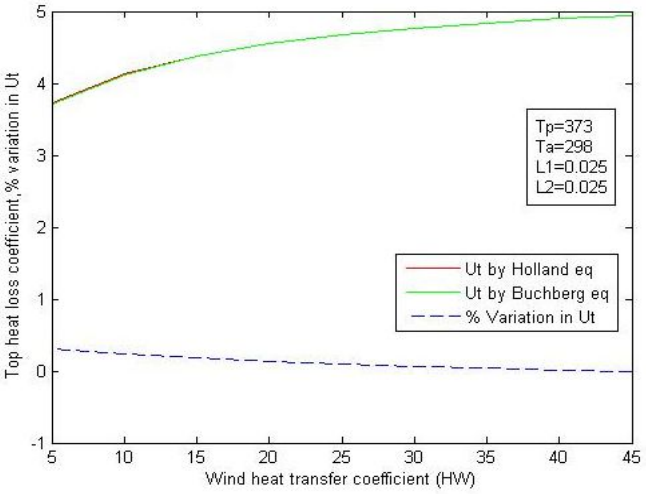

Figure 8. Variation of wind heat transfer coefficient Vs U_t

3. Conclusion

A way to describe the thermal performance of double glazed flat plate solar collectors using numerical computing environment MATLAB has been shown. It has been observed from the results obtained that both Holland's et al and Buchberg's et al relations may be used for the parametric study of design and climatic variables which affects the thermal performance of Flat Plate Solar Collectors.

Acknowledgment

This paper is dedicated to the praise of Almighty Lord Hanuman –the symbol of physical strength and energy, devotion and dedication, for successful completion of the work. I express my deepest sense of gratitude to all the faculty members, staff and friends for their valuable guidance, constant inspiration and continuous encouragement.

References

[1] Akhtar N, Mullick S. C., "Computation of Glass Cover Temperatures and Top Heat Loss Coefficient of Flat Plate Solar Collectors with Double Glazing." Energy 32 (2007),PP.1067-1074.

[2] Hollands K.G.T., Unny T.E., Raithby G.D., Konicek L. "Free Convective Heat – Transfer Across Inclined Air Layers." ASME J heat transfer 98 (1976);PP.189-192.

[3] Buchberg's H, Catton I,Ewards D.K.. "Natural Convection in Enclosed Spaces – A Review of Application to Solar Energy Collection." ASME J heat transfer 98 (1976),PP.182-188.

[4] Duffi J.A. and Beckman W.A.,2006, " Solar engineering of thermal processes ", John Wiley and Sons,New York ,PP. 238-242.

Performance Modeling of Superheater System Using ANFIS Architecture Based on Classification and Regression Trees Algorithm and its Optimization

I.C.Bharti
Department of Mechanical Engg.
Govt. Polytechnic Takhatpur
Takhatpur , India
icb567@rediffmail.com

M.F. Qureshi
Department of Electrical Engg.
Govt. Polytechnic Janjgir Champa
Janjgir Champa, India
mfq_pro@rediffmail.com

Y.P. Banjare
Department of Mechanical Engg.
Govt. Engineering College
Bilaspur, India
yp_banjare@yahoo.co.in

Abstract

This paper presents the performance modeling of superheating system of a 400MW steam generating plant using CART-ANFIS (Classification and Regression Tree based Adaptive neuro-fuzzy inference system). The experimental data are obtained from a complete set of fields experiments under various operating conditions. CART-ANFIS model is constructed for each subsystem of the superheating unit. The CART-ANFIS models are then constructed in a combination of series and parallel units in accordance with real power plant subsystems. Comparing the performance response of CART-ANFIS model of a subsystem with the performance response of a non linear neuro-fuzzy model (proposed by Zaheri M.M. 2007) [1] of a subsystem and also with the performance response of its linear models is more accurate than these two models in the sense that its performance response is closer to the performance response of the actual system.

Keywords- CART-ANFIS, Performance modeling, Superheating system, steam power plant, neuro-fuzzy modeling.

Broad Area- Mechanical Engineering.

Sub-Area- Power plant.

1. Introduction

It is mathematically proved that the least square error (LSE) method is the optimum modeling method for linear systems. For nonlinear plants, in addition to physics based modeling, there are some I/O data based methods, as well. I/O data based methods offer different models, such as CART algorithm based ANFIS model called CART- ANFIS model(J.R.S. Jang, C.T. Sun 2004)[8]. In this paper superheating system of a 400 MW unit of a steam power plant, including seven subsystems is modeled, using CART-ANFIS as a connected set of series and parallel CART-ANFIS models.

The learning rules of ANFIS only deals with parameter identification (J.Vieira et al 2004). A method for structure identification is needed here to determine an initial ANFIS architecture (M.F.Qureshi et al 2008) [11] before any parameter tuning procedures can take over. By having solid methods for both structure and parameter identification CART-ANFIS methods is used for performance modeling of superheater system of a power plant. Structure identification in fuzzy modeling involves some primary issues i.e. (1) selection of relevant input variables (2) determining an initial ANFIS architecture including input space partitioning, number of membership functions for each input, Number of fuzzy IF-Then rules, Antecedent (premise) parts of fuzzy rules and consequent (conclusion) parts of fuzzy rules, (3) choosing initial parameters for membership functions. In this paper the tree partition has been adopted for fuzzy modeling task. Based on the CART (Classification and regression tree) algorithm, this paper introduces a quick method for solving the problem of structure identification. The proposed method generates a tree partitioning of input space, which relieves the "curse of dimensionality" problem (number of rules increasing exponentially with number of inputs) associated with grid partitioning method. Moreover the resulting ANFIS architectures based on CART are more efficient in both training and application because of their implicit weight normalization.

The subsequent sections of this paper includes introduction of decision trees and CART algorithm used to derive them, Transformation of CART derived decision trees into efficient ANFIS structure with implicit weight normalization, modeling of performance of superheater system in power plants.

2. CART Algorithm derived Decision tree:

Decision trees used for classification problems are called classification trees and decision trees used for regression problems are called regression trees.

Fig1 shows the typical binary regression tree with two inputs x and y and one output z. As shown in fig 2, the decision tree (regression tree) partitions the input space into four non-overlapping rectangular regions, each of which is assigned a label f_i , where f_i is either a constant or a equation to represent a predicate output value. Each terminal node has a unique path that starts with a root node and ends at the terminal node; the path corresponds to a decision rule that is a conjunction (AND) of various tests or conditions. For any given input vector, one and only one path in the tree will be satisfied. The number of terminal nodes is always one more than the number of internal nodes.

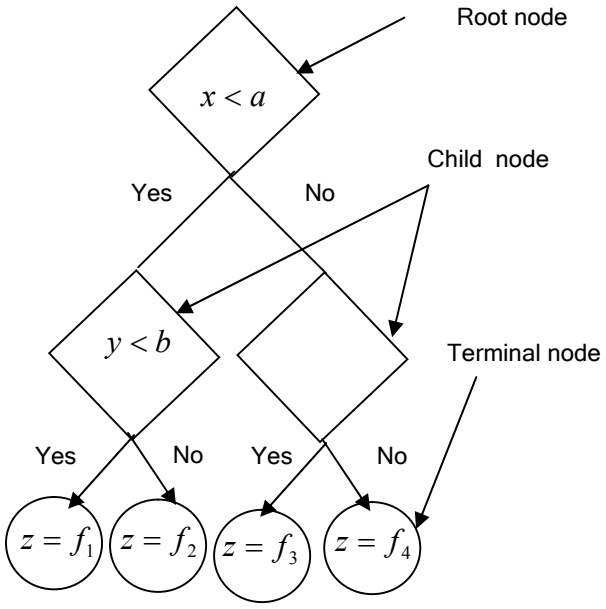

Figure 1 Regression tree with two input x and y and one output z

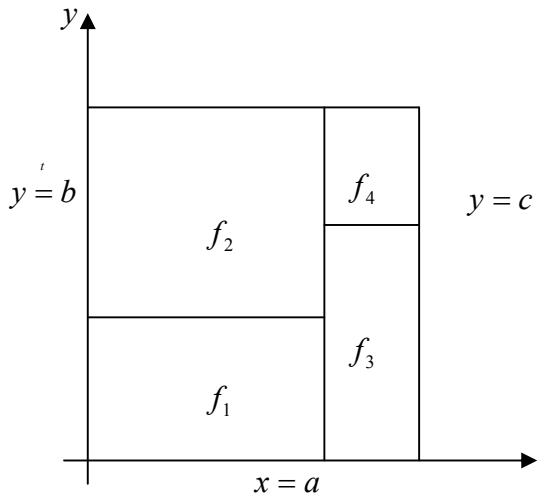

Figure 2 Input space partitioning of figure1 (regression tree)

CART grows a decision tree by determining a succession of splits that partition the training data into disjoint subsets. Starting from the root node that contains all the training data, an exhaustive search is performed to find the split that best reduces an error measures (or cost function). Once the best split is determined, the data set is partitioned into two disjoint subsets, which are represented by child nodes. The recursive procedure terminates when the error measure associated with a node falls below a certain tolerance level, or when the error reduction resulting from further splitting will not exceed a certain threshold value.

Classification trees are used to solve classification problems in which attributes of an object are used to determine what class the object belongs to. To grow a classification tree, an error measure $E(t)$ is needed that quantifies the performance of a node 't' in separating data (or classes) from different classes. This error measure $E(t)$ is also called impurity function. For a given node, $E(t)$ should attain a minimum at zero when the given data all belong to the same class, and reach a maximum when the data are evenly distributed through all possible classes. By using the impurity function ϕ, the impurity measure of a node t is expressed as

$$E(t) = \phi(P_1, P_2, ...P_j) \qquad \text{.....(1)}$$

where P_j is the percentage of cases in node t that belong to class j.

Similarly, the impurity measure of a tree T can be expressed as

$$E(T) = \sum_{t \in T} E(t) \qquad \text{.....(2)}$$

where $\bar{T}$ is the set of terminal nodes in tree T,

The best known impurity functions for a J - class classification tree are the entropy function and Gini diversity index

Entropy function

$$\phi_e(P_1, P_2, ...P_j) = -\sum_{j=1}^{j} P_j \ln P_j \quad \text{.....(3)}$$

Gini function

$$\phi_g(P_1, P_2, ...P_j) = \sum_{i \neq j} P_i P_j = 1 - \sum_{j=1}^{j} P_j^2 \quad \text{....(4)}$$

Since $\sum_{j=1}^{j} P_j = 1$ and $0 \le P_j \le 1$ for all j, the preceding two functions are always positive unless one of P_j is unity and all the others are zero. Moreover they reach their maxima when $P_j = \frac{1}{J}$ for all j.

Given an impurity function for computing the cost of a node, the decision tree growing procedure tries to find an optional way to split the cases (or object) in the node such that the cost reduction is the greatest. The change in impurity due to splitting is given by

$$\Delta E(s,t) = E(t) - P_l E(t_l) - P_r E(t_r) \quad \text{.....(5)}$$

where t is a node being split, $E(t)$ is impurity of the current node t, $E(t_l)$ and $E(t_r)$ are the impurities of the left and right branch nodes, and P_l, P_r are the percentages of cases in node t that branch left and right, respectively. For a split $\overset{*}{s}$ for the root node t_1 such that the split gives the largest decrease in impurity

$$\Delta E\left(\overset{*}{s}, t_1\right) = \max_{s \in S} \Delta E(s, t_1) \quad \text{.....(6)}$$

where S is a set of all the possible ways of splitting the cases in node t_1,

By using the optimal $\overset{*}{s}$, t_1 is split into t_2 and t_3, and same search procedure for the best $s \in S$ is repeated on both t_2 and t_3 separately and so on.

For a regression tree, the error measure of node t is usually taken as the squared error, or residual, of a local model employed to fit the data set of the node

$$E(t) = \min_{\theta} \sum_{i=1}^{N(t)} \left(y_i - d_t(x_i, \theta)\right)^2 \quad \text{.....(7)}$$

where $\{x_i, y_i\}$ is a typical data point, $d_t(x, \theta)$ is a local model for node t and $E(t)$ is the mean squared error of fitting the local model d_t to the data set in the node. IF $d(x, \theta) = \theta$ is a constant function independent of x, then the minimizing θ of the preceding error measure is the average value of the desired output y_i for the node, that is

$$\overset{*}{\theta} = \frac{1}{N(t)} \sum_{i=1}^{N(t)} y_i \quad \text{.... .(8)}$$

Similarly if $d(x, \theta)$ is a linear model with linear parameter θ, then we can always use the least squares methods to identify the minimizing $\overset{*}{\theta}$ and $E(t)$ for a given node t.

For any split S of node t into t_l and t_r, the change in error measure is expressed as

$$\Delta E(s,t) = E(t) - E(t_l) - E(t_r) \quad \text{.....(9)}$$

The best split $\overset{*}{s}$ is the one that maximizes the decrease in the error measure

$$\Delta E\left(\overset{*}{s}, t\right) = \max_{s \in S} \Delta E(s,t) \quad \text{.....(10)}$$

The strategy for growing a regression tree is to split nodes (or data set) iteratively and thus maximize the decrease in $E(T) = \sum_{t \in T} E(t)$, the overall measure (or cost) of the tree. Therefore, the goal of growing either a classification or regression tree is the same i.e. to split nodes recursively and thus minimize a given reasonable error measure in a greedy, single look - ahead manner. Here node means partition data set (or input space).

3. CART based structure Identification in ANFIS

The CART algorithm is powerful non parametric method with the following features (i) conceptual simplicity (ii) computational efficiency (iii) applicability to classification and regression problems (iv) solid statistics foundation, (v) suitability for high - dimensional data, (vi) ability to identify relevant inputs simultaneously.

In this section, it is described how to use CART (J.R.S. Jang, C.T. Sun 2004) [8] for structure identification in ANFIS. CART is used to find the number of ANFIS rules and the initial locations of membership functions before training. For simplicity, our scope is confined to regression problems a similar approach can be also used for classification problems. To construct a regression tree with constant output terminal nodes (see fig1), the CART algorithm described earlier can always identify a right – size tree and determine irrelevant inputs not required by the tree. On the other hand, if the terminal nodes are characterized by linear equations (fig1), more computation is necessary to find relevant inputs. The constants and linear outputs of terminal node may be in the form for example constant input/outputs are $a = 6, b = 3, c = 7, f_1 = 1, f_3 = 5$ and $f_4 = 9$ and that for linear equations for example, $f_1 = 2x - y - 20,$ $f_2 = -2x + 2y + 10,$ $f_3 = 6x - y + 5$ and $f_4 = 3x + 4y + 20,$ respectively.

On way to reduce the computation burden is to employ the least-squares estimator (LSE) method, of particular importance is the LSE that is obtained recursively in accommodating new data and new parameters.

It is obvious that the decision tree in fig1 is equivalent to set of crisp rules,

If $x < a$ and $y < b$, then $z = f_1$

If $x < a$ and $y \geq b$, then $z = f_2$

If $x \geq a$ and $y < c$, then $z = f_3$

If $x \geq a$ and $y \geq c$, then $z = f_4$ ……. (11)

Given an input vector (x, y), only a single rule out of the four will be fired at full strength, while the other three will not be activated at all. This crispness reduces the computation required to construct the tree using CART, but it also gives undesirable discontinuous boundaries in the overall input-output mapping. To smooth out the discontinuity at each split, a natural option is to use fuzzy sets to represent the premise parts of the rules in equation (11), converting equation (11) into a set of Sugeno-style fuzzy if-then rules.

The resultant Sugeno fuzzy inference model (A. Afzalian 2003)[3] can be of zero order if f_i's are constant , or first order if f_i's are linear equations.

To fuzzify the premise (antecedent) part, the statement $y \geq c$ can be represented as a fuzzy set characterized by, for instance, the sigmoidal membership function for $y \geq c$ is,

$$\mu_{y \geq c}(y, \alpha) = Sig(y, \alpha, c) = \frac{1}{1 + \exp[-\alpha(y - c)]} \quad ..(12)$$

where α and c are modified parameters for the membership function. Similarly one can also employ the S membership function to represent the meaning of $y \geq c$.

$$\mu_{y \geq c}(y, \omega) = S(y, (c - \omega), (c + \omega))$$

$$= \begin{cases} 0 & \text{if } x \leq c - \omega \\ 2\left[\dfrac{x - (c - \omega)}{2\omega}\right]^2 & \text{if } (c - \omega) < x \leq c \\ 1 - 2\left[\dfrac{x - (c - \omega)}{2\omega}\right]^2 & \text{if } c < x \leq (c + \omega) \\ 1 & \text{if } (c + \omega) < x \end{cases} \quad \ldots(13)$$

To increase the degree of freedom, we can even use an extended S membership function with an extra parameter γ

$$\mu_{y \geq c}(y, \omega, \gamma) = S_{ext}(y, (c - \omega), (c + \omega), \gamma)$$

$$= \begin{cases} 0 & \text{if } y \leq (c - \omega) \\ \dfrac{1}{2}\left[\dfrac{y - (c - \omega)}{\omega}\right]^{2\gamma} & \text{if } (c - \omega) < y \leq c \\ 1 - \dfrac{1}{2}\left[\dfrac{(c + \omega) - y}{\omega}\right]^{2\gamma} & \text{if } c < y \leq (c + \omega) \\ 1 & \text{if } (c + \omega) < y \end{cases} \quad \ldots(14)$$

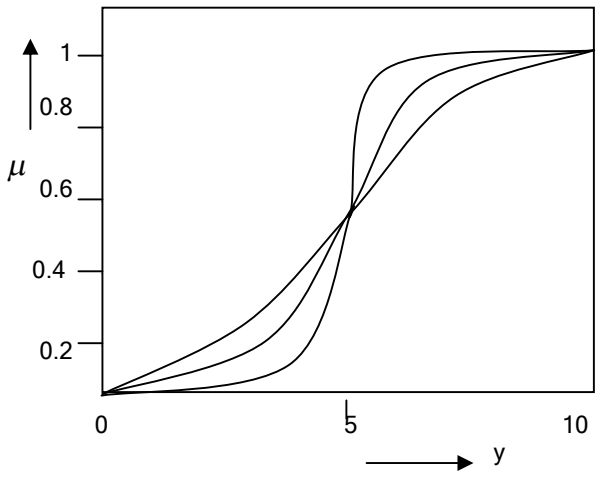

Figure 3 Sigmoidal membership function for x>c , c=5 with different α 's (MATLAB file: Cartmf.m)

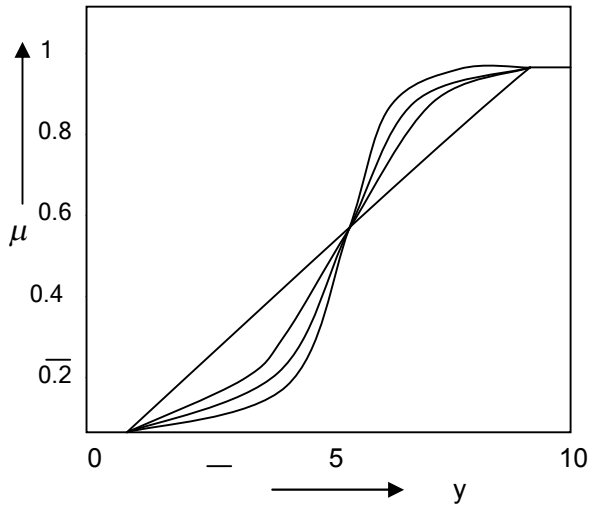

Fig ure 4 Extended S membership function with different γ 's γ =0.5
(MATLAB file: Cartmf.m)

Fig 3 and fig 4 shows the sigmoidal and extended S membership functions for the linguistic term $y \geq c$ (y is more than or equal to c).

Based on the fuzzy version of the rules in equation 11, one can derive another class of adaptive network for identifying the premise and consequent parameters of the underlying fuzzy inference system. This ANFIS architecture is depicted in fig 5.

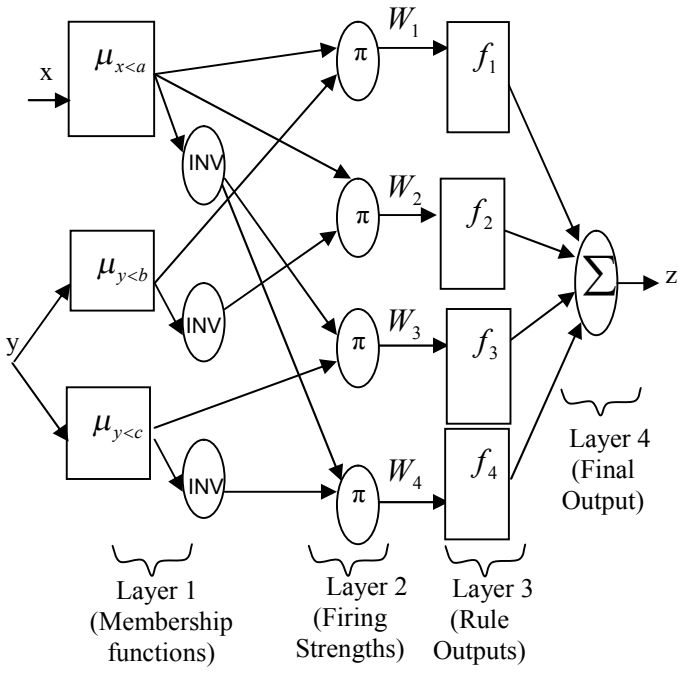

Figure 5 ANFIS architecture corresponding to the fuzzy version of the rule set in equation 11

Layer 1 calculates the membership functions (grades) of given input variables (INV nodes represent negation operators), Layer 2 multiplies the given membership functions (grades) to find the firing strength of each rule, Layer 3 computes the contribution of each rule based on given firing strengths, and Layer 4 finds the summation of incoming signals, which is equal to the overall output of this fuzzy inference system. Premise (antecedent) and consequent parameters are contained in layer 1 and layer 3, respectively; these parameters are fine tuned according to the fast hybrid learning rules or any of the other nonlinear parameter identification methods.

3.1 Implicit weight Normalization in a CART – constructed ANFIS

In converting a decision tree to a fuzzy inference system, (1) $\mu_{x>a}(x) + \mu_{x\leq a}(x) = 1,$ where x is any of the input variables and a is any of the splits of x , and (2) multiplication is used as the T-norm operator to calculate each rule's firing strength then the summation over each rules firing strength is always equal to unity.

Suppose that $\sum_{i=1}^{n} \omega_i = 1$ holds when $n = k$.

When $n = k+1$,one need to show that $\sum_{i=1}^{k+1} \omega_i = 1$ still holds. Without loss of generality, one can assume the newly generated rules are k and $k+1$, the result from splitting the previously terminal nodes k (or rule k). Consequently, one can have

$$\sum_{i=1}^{k+1} \omega_i = \sum_{i=1}^{k-1} \omega_i + \omega_i + \omega_{k+1}$$

$$= \sum_{i=1}^{k-1} \omega_i + \omega_k \left(\mu_{x<a}(x) + \mu_{x\geq a}(x)\right)$$

$$= \sum_{i=1}^{k-1} \omega_i + \omega_k$$

$$= 1$$

where ω_k is the firing strength of rule k before splitting.

The implicit weight normalization of the ANFIS architecture(T. Takagi and M. Sugeno 1985)[6] in fig 5 is maintained throughout training processes; this eliminates the need for another normalization layer and reduces training and application computation time as well as round-off errors.

In summary fuzzy modeling based on CART-ANFIS approach consists of two tasks (i) Structure identification: This is done by CART to find an initial set of crisp rules. (ii) Parameter identification: After fuzzifying the premise (antecedent) parts of the initial rules, one can construct an ANFIS architecture to fine tune the parameters.

The major advantage offered by this approach is that one can quickly determine the roughly correct structure of a fuzzy inference using CART, and then refine the membership functions and output functions via an efficient ANFIS architecture (M. F. Qureshi 2007)[10] that does not need a normalization layer. Note that CART can select relevant inputs and do tree partitioning of the input space, while ANFIS refines the regression and makes it every where continuous and smooth. Thus it can be seen that CART and ANFIS are complementary and their combination constitutes a solid approach to fuzzy modeling.

Thus this section presents the CART algorithm, a fast one-pass approach for multivariate analysis. CART is a popular non-parametric approach for both data classification and regression in statistics. Because CART can select relevant input variables and partition the input space effectively, it is an ideal tool for structure identification in ANFIS.

4. Superheater System Modeling and Simulation

In this paper one of the most common structure of neuro-fuzzy network called adaptive neuro-fuzzy inference system (ANFIS) tuned by classification and regression tree (CART) is proposed (M. M. Zaheri 2007)[1]. ANFIS is a scheme of a linear Sugeno type FIS. In this structure, antecedent of rules contains fuzzy sets (as membership functions) and consequent is a first order polynomial (a crisp function).

In this method, a fuzzy inference system is designed based on system specifications. This initial model is transformed to a neuro-fuzzy network and then trained by experimental recorded data of the system. The training procedure involves both gradient error back propagation (to adjust membership function co-efficient) and LSE (to adjust linear output parameters).

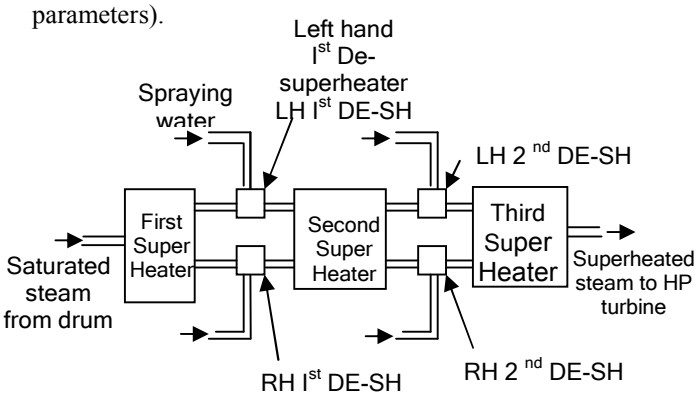

Figure 6 Superheating system of the power plant

In fuzzy inference systems (Earl Cox 1990)[4], fuzzy rules number is equal to number of membership functions powered by number of inputs. Sometimes, to cover all input space. So many rules are needed. Training such FIS's is too time consuming or practically impossible. In order to reduce fuzzy rules number with minimum accuracy loss, a method namely subtractive clustering is applied. In this method, rules with most probable antecedents in recorded data of actual system are selected. The model derived from subtractive clustering is used as initial model for training. LSE method is the optimum modeling method for linear systems for non linear plant I/O data based methods using CART algorithm based ANFIS model or CART-ANFIS model is proposed here. CART-ANFIS model is used for both structures as well as parameter identification. CART is used to generate a tree partitioning of input space.

The structure of a superheating system in a steam power generating plant (A. W. Ordys 1994)[5] is shown in fig 6. The steam flow enters to the Superheater and after passing through the heat exchangers it enters to the high pressure turbine. For normal operation of the plant and when the capacity of the power plant is over 30% of its normal value, the desired output temperature of Superheater is 540 C. This temperature is adjusted at the desuperheater by spraying water through spraying valves.

In this paper first order linear Sugeno type fuzzy inference system is used. The sigmoidal function and S-function of membership functions are used as given by equations 12, 13, 14 and shown in fig 3 and fig 4. The modeling is performed using a complete set of data, including 3000 data set of 'NTPC' power plant, the sampling time equals to 1 second. Additionally, 1500 sets of data are used as checking data.

In order to model the superheating system, for each subsystem a CART-ANFIS is constructed and trained by hybrid learning method of ANFIS based on CART. Superheating system consists of three superheaters and four de-superheaters. Since the first superheaters are single-inputs and multi-outputs (SIMO) systems and second superheaters are multi-inputs and multi-outputs (MIMO) systems, they are modeled as two parallel multi-inputs and single-outputs (MISO) systems. In total nine CART-ANFIS's are constructed and trained for seven superheating subsystem. Models have 7-12 (seven to twelve) inputs and one output. Then, all these components are put together as parallel or series elements, whereas in final run, many of inputs of subsystems model are outputs of preceding subsystems. In order to use recorded data for modeling, the following points are considered.

(a) Delays are included in modeling, for instance, it take 20 seconds to steam passes through a

superheater. Therefore, when the temperature of inlet steam is applied in modeling that superheater, 20 second delay should be considered.

(b) The algorithm for adjusting CART-ANFIS model depends on the magnitude of inputs data, therefore all inputs are normalized.

(c) To improve the convergence speed of parameters and co-efficient in CART-ANFIS model, their sensitivity to the variation of inputs signals should be increased. To do so elements of each column of training data are substituted with same elements subtracted from the mean value of elements in that column. It causes that the quantity (error/ data magnitude) increases, where, error in the numerator is the difference between outputs of the model and actual system.

(d) In order to classify the modeling process, a subsystem of superheating system, the left hand 2nd de-superheater (LH 2nd DE-SH) is selected. Modeling process for this subsystem is comprehensively offered.

4.1 LH 2nd DE-SH Modeling

Fig 7 shows the input and output signals of the LH 2nd DE-SH, where these inputs are defined below

T_b = Temperature before spraying water (inlet temperature)

V = Water mass rate

f = Steam mass rate

And output is:

T_a = temperature after spraying water

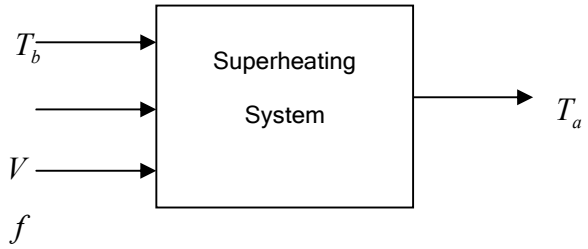

Figure 7 Inputs and Output of De-superheater

The steam mass rate (f) is summation of two other signals. The first is half of total mass flow of water entering the drum, after drum the steam flow is divided into two branches (Fig 8) and second signal is the first step spraying water mass rate which is added to main steam flow. The de-superheater system is influenced by both of these signals with delay. Fig 8 illustrates the input-output signals of the CART-ANFIS model for the de-superheater in the discrete domain. Here the values of T_b, V and f at present time their values at two steps (z^{-2}) before (for T_b and V) and one step before (z^{-1}) (for T_b, V and f) and

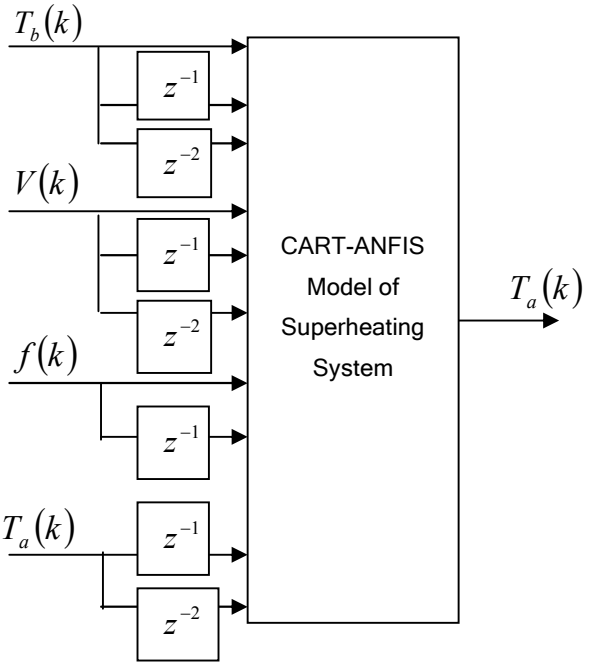

Figure 8 Input and output of de-superheater CART-ANFIS model

also the values of T_a at the past two time increments are all input signals. The output of the CART-ANFIS model is the output temperature of the de-superheater $T_a(k)$.

The relation between the ten inputs and outputs of fig 8 for each fuzzy rule is given by the following equation:

$$\begin{aligned} T_a(k) = {} & \alpha_1 T_b(k) + \alpha_2 T_b(k-1) + \alpha_3 T_b(k-2) \\ & + \alpha_4 V(k) + \alpha_5 V(k-1) + \alpha_6 V(k-2) \\ & + \alpha_7 f(k) + \alpha_8 f(k-1) \\ & + \alpha_9 T_a(k-1) + \alpha_{10} T_a(k-2) + \alpha_{11} \end{aligned} \quad \text{.....(15)}$$

where $(k-1)$ is one step before , $(k-2)$ two step before

Parameters α_i, i = 1….11 and co-efficient of sigmoidal and S membership functions of equation 12, 13, 14 for all associated fuzzy rules are adjusted in CART-ANFIS model. The equation15 is written for each rule, while for simplicity the subscript of the associated fuzzy rule is omitted in this equation. If left hand side of equation15 for j^{th} fuzzy rule

is shown by $T_a(k)$, then the output of CART-ANFIS model is :

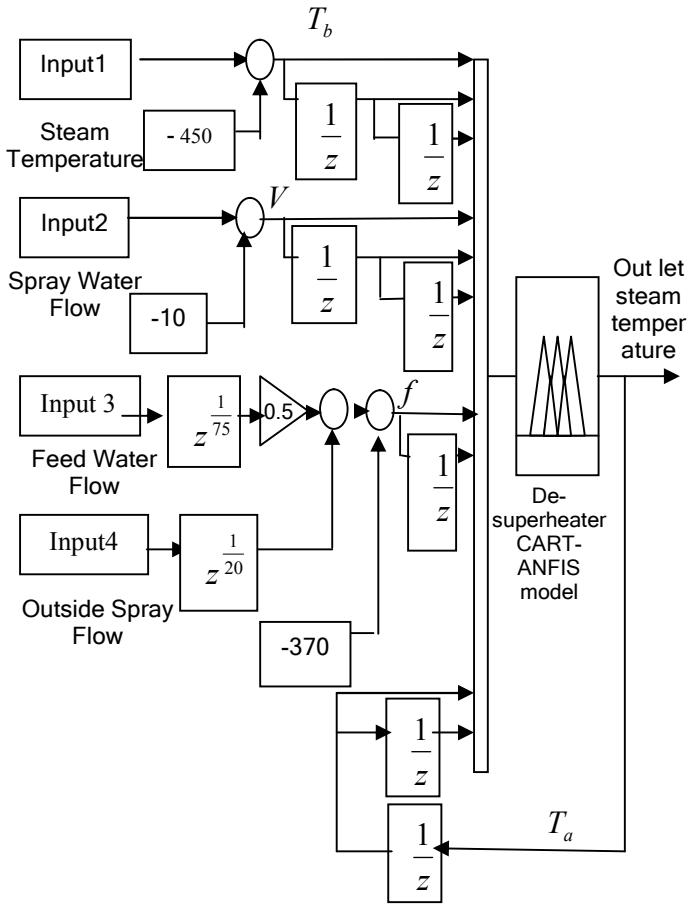

Figure 9 Input- Output Signals of CART-ANFIS model

$$T_a(k) = \frac{\sum_j \eta_j T_{aj}(k)}{\sum_j \eta_j} \qquad \text{.....(16)}$$

Where η_j is the firing strength of the j^{th} rule. For CART-ANFIS modeling, all quantities T_a, T_b, V and f are measured and put in common vectors.

Fig 9 shows the schematic diagram of this de-superheater CART-ANFIS model. Noting that the number of inputs in this model is 10, if only three linguistic variables i.e. positive (P), medium (M) or positive large (PL) are assigned for each input, the number of rules would result in 3^{10} rules. An alternative approach is subtractive clustering which reduces the number of rules to only 22 rules. Note that for each rule in addition to parameters α_i, i = 1….11, co-efficient in all membership functions of 10 inputs must be adjusted.

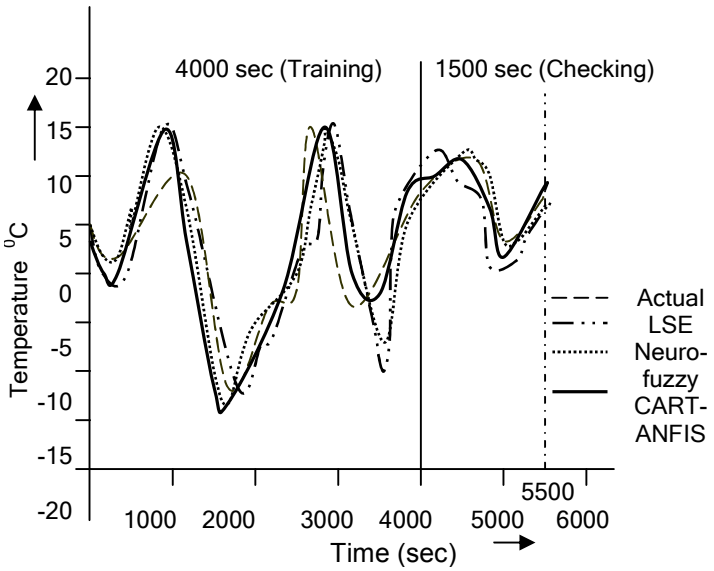

Figure 10 CART-ANFIS, neuro fuzzy and LSE modeling result both for training and checking area

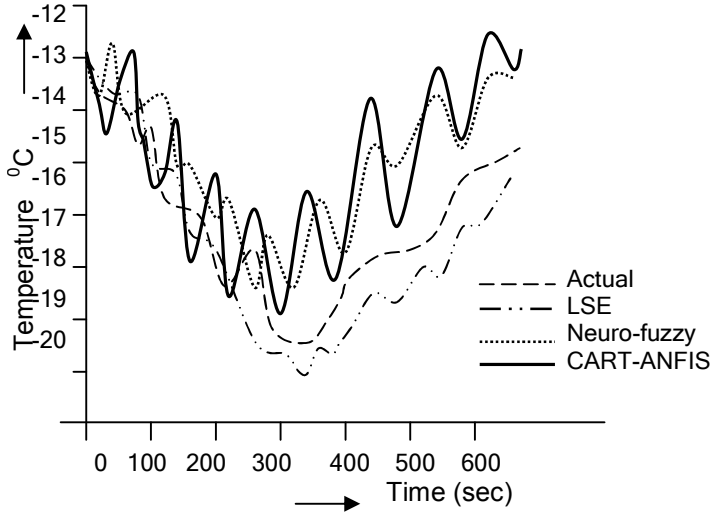

Figure 11 CART-ANFIS, Neuro fuzzy and LSE modeling result, under special condition

5. Discussion

Implementation of CART-ANFIS model for modeling the LH 2nd DE-SH of power generating plant is investigated first and then its implementation for whole superheating system is studied.

Fig10 illustrates the response of the LH 2nd DE-SH, obtained from recorded data of the actual plant. It also shows the comparison of the responses obtained from simulation results for LSE, neuro-fuzzy model and CART-ANFIS model. Fig11 shows similar responses of the actual plant and the models under special operating conditions. Both fig10 and 11 indicate that the CART-ANFIS model is more accurate than the neuro fuzzy model and LSE model, in the sense that, its response is closer to the response of the actual plant. Noting that the LSE method is optimum for modeling linear systems, the simulation results confirm that the de-superheater is a nonlinear subsystem of a power plant.

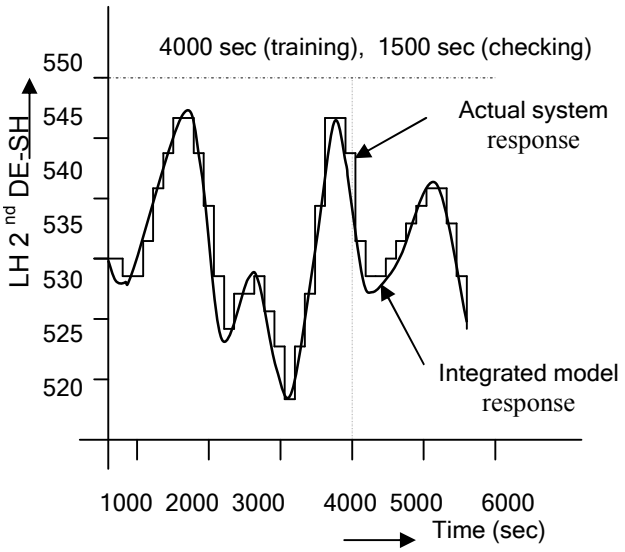

Figure 12 CART-ANFIS modeling result for integrated model (including nine sub-models)

Fig 12 shows the simulation result of whole model, formed by nine series and parallel CART-ANFIS models for both for training and checking areas.

6. Conclusion

In this piece of research work, CART-ANFIS modeling is performed for a power plant superheating system, including three superheaters and four de-superheaters. Then all these models are put together as a total model. In modeling, some significant notes are considered, such as time delays. After all considerations and using subtractive clustering, to reduce the number of fuzzy rule, a relatively good accuracy is achieved for this set of complex models. Many of inputs of total model elements are outputs of other elements or their own outputs at earlier times. Also, it is indicated that some of power plant subsystems are of a non linear nature, with comparison between LSE modeling, neuro-fuzzy modeling and CART-ANFIS modeling.

References

[1] M.M.Zaheri et al "Neuro fuzzy modeling of superheating system of a steam power plant" J. of Applied Math Sciences, Vol1,no 42, pp 2091-2099, 2007,

[2] J. Vieira, F. Morgado Dias, A. Mota "Artificial Neural Networks and Neuro-Fuzzy systems for modeling and controlling Real systems: A comparative study" J. of Engineering Applications of Artificial Intelligence, no. 17, pp 265-273, 2004,

[3] A. Afzalian, D.A. Linkens " Training of Neuro-fuzzy power systems stabilizers using genetic Algorithm " 22nd conference of electrical power and energy systems, pp 93-102, 2003,

[4] Earl Cox "The fuzzy system hand book, AP professional, 1990,

[5] A.W. Ordys et al " Modeling and Simulation of power system plants" springer-Verlag London, 1994

[6] T. Tagaki, m Sugeno "Fuzzy Identification of systems and its application to modeling and control" IEEE Trans on Syst, Man and Cybn, Vol15, no 1, pp 116-133, 1985,

[7] Yaochu Jin " Modeling of high dimensional systems, complexity reduction and interpretability improvement," IEEE Trans on fuzzy Syst. Vol8, no 2 , pp 212-220, 2000,

[8] J.R.S. Jang, C.T.Sun, E. Mizutani, "Neuro-fuzzy and soft computing, prentice hall India, 2004

[9] Qureshi M.F., Bharti I.C. et al, 'Improving dynamic and transient stability of power system using Natural logic Controller: A modified Mamdani's Fuzzy controller" AMSE journal, France, Advances 'C', Vol. 63 No4, pp50-63, 2008.

[10] Qureshi M.F., Bharti I.C. et al " Application of hybrid system control method for real time power system stabilization, Science direct , Elsevier, Fuzzy sets and systems 158,pp2687-2705 , 2007

[11] Qureshi M.F. M.Jha, I.C. Bharti, "Soft computing based governing control and excitation control for stability of power system" Advances 'C',AMSE journal, France, Vol. 63 No4, pp1-11, 2008

[12] Qureshi M.F. M.Jha, I.C. Bharti, "Application of multilayer perceptron tuned coactive neuro fuzzy inference system for governing control and excitation control of power system stability" Advances 'C', AMSE journal, France, Vol. 63 No3, pp62, 2008

Experimental Investigations of Gas-solid Fluidization of Spherical Food Material

S. Kumar
Department of Mechanical Engineering
Raipur Institute of Technology
Raipur – 492001 (India)
e-mail : saurabhkumar2002@gmail.com

A. Arora
Department of Mechanical Engineering
Bhilai Institute of Technology
Durg - 491001 (India)

H. Chandra
Department of Mechanical Engineering
Bhilai Institute of Technology, Durg – 491001 (Chhattisgarh)

Abstract

The present work covers an experimental study of pressure drop aspects of air - solid fluidization. The studied parameters are air velocity, bed height and particle density. Gas fluidization of solids is of comparatively recent origin and is finding an increasing number of applications in all industries in general and power plant industry in particular.

In the present work, an attempt has been made to explain air phase pressure drop for spherical food materials in granular bed considering air flow rate, bed height, and density of bed material as variables. Air and mustered, sago and sugar balls have been used as gas and solid phases respectively. The experimentations are carried out for air velocity v, static bed height h and solid density ρ_s.

Keywords- Fuidization, fixed bed, gas, solid, pressure drop, velocity

Broad Area- Mechanical engineering

Sub-Area- Two phase flow

1. Introduction

The proposed work is about the formulation of correlation for solid particles in gas system and application of these systems to the prediction of system behaviors. The history of this approach to fluidization research is presented here below.

The first experimental work on flow of fluid through a granular fixed bed was carried out by Darcy[3], who was a French municipal engineer concerned with the very practical problem of water supply and distribution in urban area. His experiments involved measuring the permeation. Rates of water through beds of sand, and led to the empirical relation.

$$\Delta P = K_D \mu_f L U$$

Where -
Δ P is the pressure drop across the bed, L is the thickness of the bed,
U is the average velocity of flow of the fluid through bed, μ_f is the viscosity of fluid, K_D is a constant depending on the physical properties of the bed and fluid.

This relates more appropriately to fluidized suspensions when dealing with flow through expanded beds. Dupuit [4] related the average fluid velocity with the velocity of fluid in granular bed. The general expression for flow through beds was first accepted in Kozeny's work [9] which was further modified by Carman [1]. Ergun and Orning [5] developed correlation for the pressure losses in fixed particle beds. For pressure drop in packed beds, Max Leva [11] developed generalized correlation for incompressible flow. In one of the earlier attempts to differentiate between the conditions leading to particulate and aggregative fluidization, Willhelm and Kwauk [16] suggested , using the value of the Froude number as a criterion of description. A theoretical justification for using the Froude number to distinguish between particulate and aggregative fluidization is provided in the work of Jackson [8]. For gas flow, substantial variation in gas density may be involved when the column pressure drop is high as in case of compressible flow. Work reported by Richrdson and Meikle [14] had suggested that the particles are free to adjust their orientations with respect to one another as in fluidization, the equation obtained for pressure drop in fixed beds overestimate the pressure drop. Rumpf [15] worked on the influence of porosity and particle size distribution during fluid flow through randomly packed beds. Geldart [7]

differentiated the type of fluidization and introduced one model for categorization of powdery material. Gibilaro [6] developed a unified model for the expansion of beds in fluidized state. In India, G.K.Roy [10] of National Institute of Technology, Rourkela contributed mainly with his work in the field of semifluidisation and liquid-solid flow systems in recent years.

2. Experimental Setup

The experimental setup consists of a perspex column of 44 mm diameter and 730 mm height. Perspex column is provided with a suitable distributor at the bottom of the inlet and outlet for air is provided at the top of the column respectively with pressure tapings at appropriate locations. The solid bed is suspended on 200BS mesh stainless steel sieve suitably fixed at bottom of the column.

Air is fed into the column by using a centrifugal blower through a pipe line of inner diameter of 44 mm. The air flow rate is controlled by the control valve. A calibrated orificemeter is used to measure the flow rate of air. For a uniform flow distribution the G.I. pipe line and column diameter is kept of same inner diameter. The pressure drops across column and orificemeter are measured by the manometer.

2.1 Pressure Drop Measurement

Initially of all blank runs for different air flow rates are taken and corresponding pressure drops are noted which represents the pressure losses for pipe and fittings at different floe rates. A known amount of solids is then loaded in the column and static bed height is noted. Now the air flow rate is progressively increased and corresponding pressure drops across the column are noted. The blank pressure drop (for pipe and fittings), is subtracted from air solid pressure drop in the bed. Because it is convenient to use ($\Delta h/L$) instead of actual pressure drop, the net pressure drop is divided by effective height of the column thus excluding height considerations. All air flow rates are converted into superficial velocity based on empty column thus excluding the height considerations. In the present study air is used as the gas phase and sago, mustered and sugar ball are used as solid phase. Parameters studied are air velocity v, static bed height h, and particle density ρ in the following range:

Sr	Parameters	Range of study
01	Velocity, v	0 -18 m/s
02	Bed height, h	10 -70 mm
03.	Particle Density, ρ_s	736.8- 788Kg/mtr^3

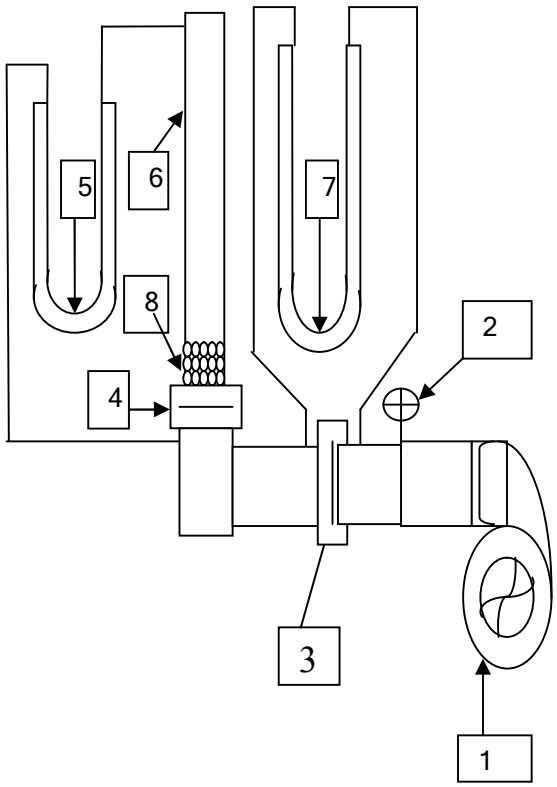

1 - Blower 2 - Control valve 3 - Orifice plate
4 - Distributor plate 5 - Manometer for column
6 - Perspex column 7 - Manometer for orifice meter
8 - Bed material

Figure 1. Line diagram of experimental set-up

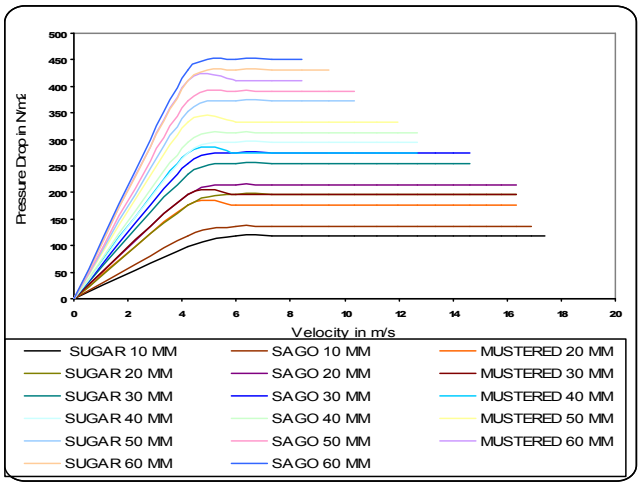

Figure 2. Column pressure drop vs. velocity in for all materials

3. Results and discussions

3.1 Gas phase pressure drop across column.

The air pressure drop across column for gas–solid systems is predicted in the following charts

(i) From Figure 2 it can be predicted that pressure drop increases initially with increase in air flow rate and finally pressure drop stabilizes and remains constant for all the selected materials and in the entire range of experimental bed heights.

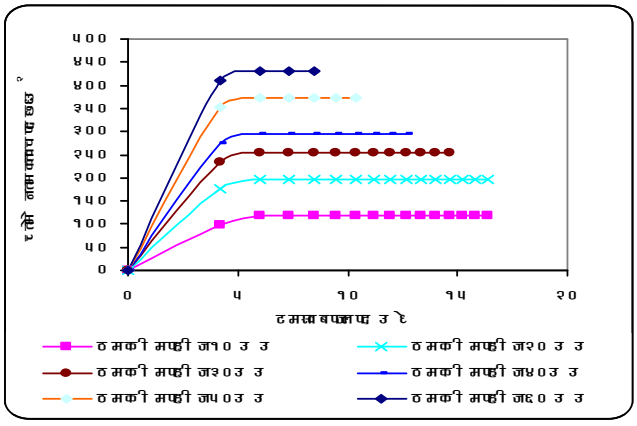

Figure 3. Effect of bed height on column pressure drop for sugar ball

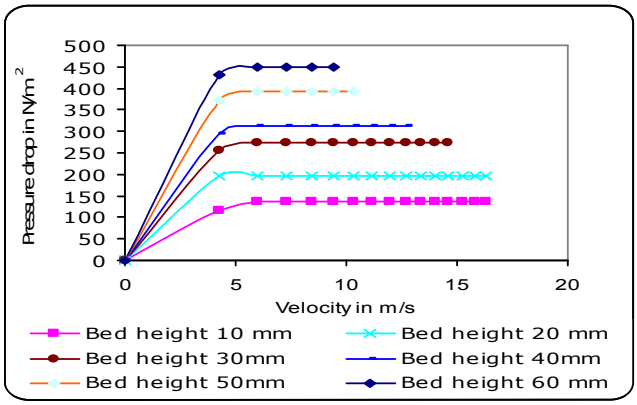

Figure 4. Effect of bed height on pressure drop for sago

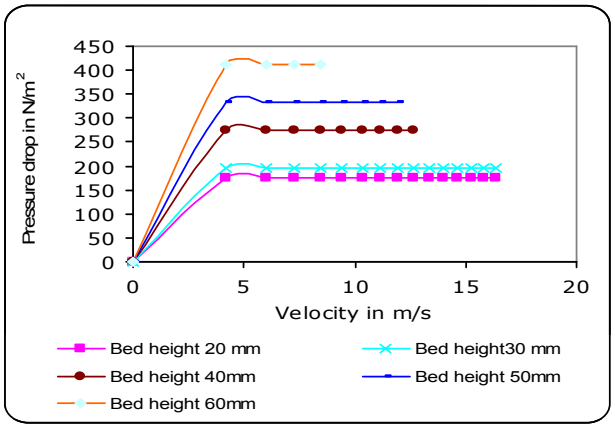

Figure 5. Effect of bed height on column pressure drop for mustered

(ii) From Figure 3, 4, 5, it is evident that pressure drop increases with increase in bed height. This pattern follows for all the selected materials. The effect of increasing bed height for constant air flow rates is to increase the solid concentration, thereby increasing the effective average density of the air and solid particles. Hence, an increase in bed height, under constant flow conditions will increase the pressure drop.

(iii) From the Figure 6, 7, 8, 9 it is found that pressure drop increases with increases in density as densities of the sugar ball, sago and mustered are 788, 773.4 and 736.4 kg/m3. Increased solid density will also result in an increase in the average density of solid – air which will ultimately increase pressure drop.

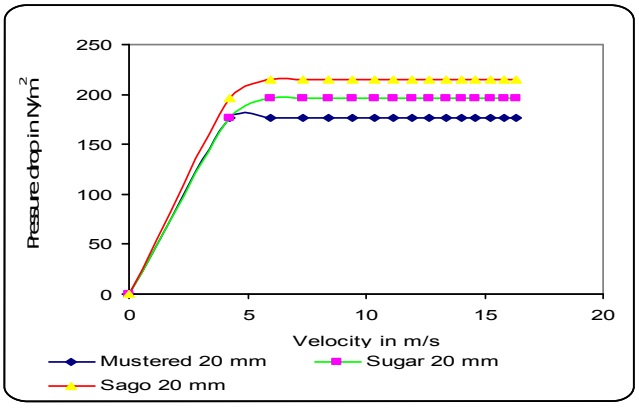

Figure 6. Effect of density on pressure drop for 20 mm bed height

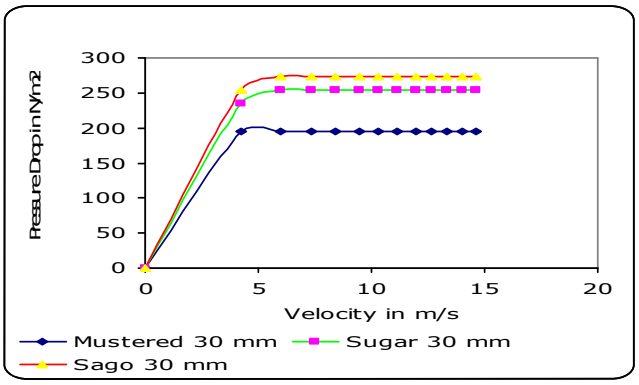

Figure 7. Effect of density on column pressure drop for 30 mm bed height

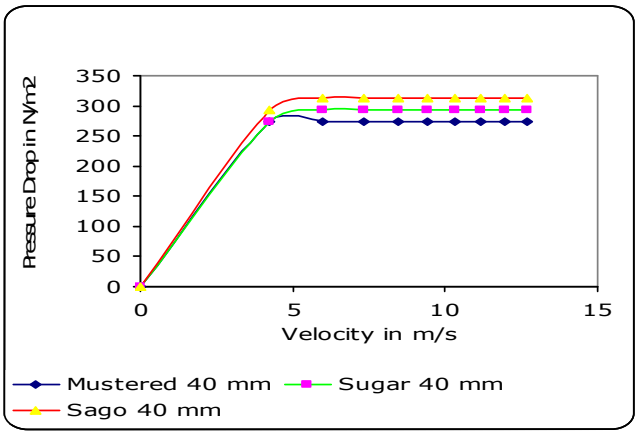

Figure 8. Effect of density on column pressure drop for 40 mm bed height

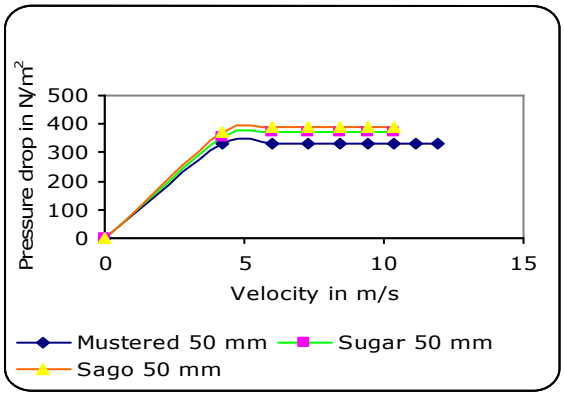

Figure 9. Effect of density on column pressure drop for 50 mm bed height

3.4 Correlation between column pressuredrop and system variables

From the system dynamic point of view the behavior of air pressure drop with respect to the systems variables may be considering as following :

$$(\Delta h / L) = \varphi_1(v, h, \rho_s, \rho_a, \mu, g, \sigma)$$

Under experimental conditions since g and σ_a are constant and variations in ρ_s was subjected to a qualitative analysis, the above equation reduces to :

$$(\Delta h / L) = \varphi_1(v, h, \rho_s, \mu)$$
$$(\Delta h / L) = \varphi_1(v, h, \rho_s/\mu)$$

Or

$$(\Delta h / L) \text{ œ } f(Re)$$

By dimensional analysis the functional relationship among the various system variables is found as :

$$(\Delta h/L) = m(Re)^n$$

Now experimental readings of pressure drops and flowrates for different material and bed height are reduced into (Δh/L) and Reynolds number (Re).Then plot (Δh/L) vs (Re) assuming Y = f (X) as in Figure 10.

Plotting all the data in MS Excel gives best fit curve as in above curve. The equation of the presented curve is calculated by the software as

$Y = 5E\text{-}07X^2 + 0.0002X - 0.0023$

So final correlation will be

$(\Delta h/L) = 5E\text{-}07(Re)^2 + 0.0002(Re) - 0.0023$

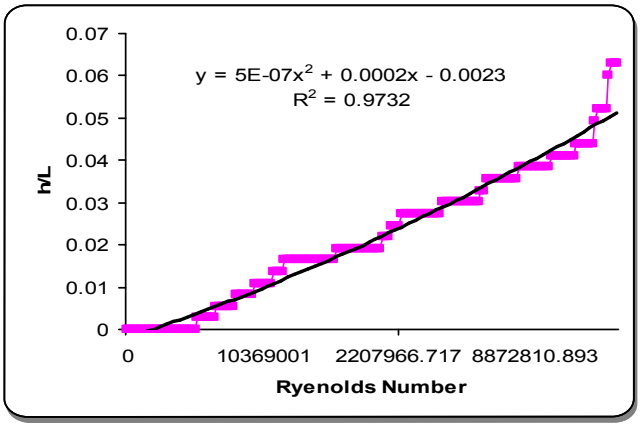

Figure 10. Correlation curve for (Δh/L) and Re

4. Conclusion

The presented pressure drop data of the gas - solid fluidization system for different bed height for different bed materials give the following conclusions.

(i) Air phase pressure drop in gas solid fluidization system increases at first with increasing air velocity and then becomes constant.

(ii) Air phase pressure drop in gas solid fluidization system has the same pattern for all the plots for selected material.

(iii) Air phase pressure drop in gas solid fluidization system increases with increasing bed height.

(iv) Air phase pressure drop in gas solid fluidization system increases with increasing solid density.

(v) The variation of air phase pressure drop with respect to variable parameters i.e. density, flow rate and bed height can be predicted by the following correlation.

$(\Delta h/L) = 5E\text{-}07(Re)^2 + 0.0002(Re) - 0.0023$

During uncertainty analysis it is found that the % error which is associated with the pressure drop is (+/-)2%. Further, % errors associated with the density of the selected material are different. It is found that % error for sago, mustered and sugar ball are (+/-) 2.99%, (+/-)1.99%, (+/-)2% respectively.

Nomenclature:

g Acceleration due to gravity, m/s^2
h Static bed height, m
K_D Constant of the physical properties of the bed and fluid, m^3/s
L Bed depth or height of packing, m
m Constant
Re Reynolds Number
U Superficial velocity
ΔP pressure drop across column, N/m^2
μ_f Viscosity of the fluid, Ns/m^2
ρ_a Density of air, kg/m^3
ρ_s Particle density, kg/m^3
ρ_w Density of water, kg/m^3

References

[1] Carman, P. C. (1937) : "Fluid flow through granular beds." Chemical Engineering Research and Design, Vol.75, Supl.1, pp.S32-S48, 1997.

[2] Coulson, J. M., Richardson, J. F., Backhurst, J.R. and Harker, J. H. (1996) : "Flow of fluid through granular beds and packed column." Particle technology & separation process, vol.2, pp. 133-171, edition 4,(1996).

[3] Darcy, H. P. G. (1830): "Les Fountaines publiques de la ville de", Dijon.

[4] Dupuit, A. J. E. J. (1863): Etudes theoriques sur le movement des eaux.

[5] Ergun, S. and Orning, A. A. (1949): Fluid flow through randomly packed columns and fluidized beds. Ind. Eng. Chem., vol.6, pp.1179, 1949.

[6] Foscolo,P.U.,Gibilaro,L.G. and Waldram,S.P. (1983):"A unified model for particulate expansion of fluidized beds." Chem. Eng. Sci., vol. 38, issue 8, pp.1251-1260.

[7] Geldart, D (1973) : "Types of fluidization." Powder Tecnology, vol.7, pp.225, 1973.

[8] Jackson, R. (1963): "The mechanisms of fluidized beds", Inst. Chem. Eng., vol.41, pp.13-22, 1963.

[9] Kozeny, J. (1933):Trans. Inst. Chem. Eng., vol.28(A), pp.54-56, 1933.

[10] Kumar, A., Roy, G. K. (2002) :" Influence of coaxial rod and coaxial blade baffles on bed expansion in gas solid fluidization" Powder Technology, vol. 126, pp.91, 2002.

[11] Leva, M., Grummer, M., Weintraub, M. and Pollchik, M. (1948) : " Fluidization of non-vesicular particles". Chem. Eng. Prog., vol.44, pp.619, 1948.

[12] Muthy, J. S. N., Roy, G. K., Sahu, G. N., Patra, P. (1987) : "Onset of fluidization in conical vessels" Journal of Institution of Engineers (India), vol.68, pp.13, 1987.

[13] Puncochar, M. and Drahos,J. (1993): "The tortuosity concept in fixed and fluidized bed".Chem. Eng. Sci., vol.48, isu.11, pp.2173-2175, 1993.

[14] Richardson, J. F. and Meikle, R. A.(1961):"Sedimentation & Fluidization ". Chemical Engineering Research and Design, vol.75, supl.1, pp.S32-S48, 1997.

[15] Rumpf, H. and Gupte, A. R. (1971) : "Influence of porosity and particle size distribution in resistance law of porous flow". Chem. Eng. Tech., vol.43, pp.367,1971.

[16] Wilhelm, R. H. and Kwauk, M. (1948): "Fluidisation of solid particles", Chem. Eng. Prog. Vol.44, pp.201, 1948.

Methodology of Evaluating the Overall Equipment Effectiveness in a Gear Industry Through TPM

Yash Dave
Manufacturing Engineering,
Dhar Polytechnic College
Dhar (M.P), India
Email:yash_megha@yahoo.co.in

Nagendra Sohani
Mechanical Engineering
Institute of Engineering and Technolgy, DAVV
Indore (M.P), India.
Email: nagendrasohani@yahoo.com

Abstract

Rapid machine breakdowns, low plant availability are a great threat to any industry as it increases overall costs of an industry. Many companies have adopted TPM to improve their Overall Equipment Efficiency and to get the competitive advantage in the world market in terms of cost and quality Total productive maintenance (TPM) has become one of the most popular maintenance techniques to ensure high machine availability. The objective of TPM is to create an active involvement of all employees in maintenance and production functions, including the operators who operate the machines and equipments. This paper examines the basic concepts of TPM and illustrates the procedure to calculate the Overall Equipment Effectiveness (OEE) at a gear manufacturing company framed within the framework of TPM (Total Productive Maintenance). A sample study was carried out in a company which manufactures gears used for automobile industry.

Keywords- Overall Equipment Effectiveness, TPM

Broad Area- Mechanical Engineering

1. Introduction

Any activity done on machine or equipment to increase the efficiency after or before breakdown is called maintenance. For industry to produce goods of the highest quality, it is essential that its machine or equipment must be able to operate efficiently and accurately. For every industry the main aim is to manufacture products with highest quality and gain maximum profit and this is only achieved by having an systematic maintenance system that increase availability by reducing machine downtime due to sudden stoppages. Without an effective and systematic maintenance system, equipment reliability becomes low and this leads to poor availability and increased downtime. TPM is a Japanese System, which has been developed from the PM concept. TPM is a maintenance management system that strongly emphasizes on improving equipment performance, productivity and eliminating all production losses. Total participation from all employees including top management and operators are most essential in TPM. More importantly, TPM improves the contribution of operators to achieve zero breakdowns, zero stoppages and safe working environment. Efficiency and effectiveness of equipment plays a major role in modern manufacturing industry to keep the performance of the plant at optimum level. TPM aims to reduce the 6 major equipment losses to zero has been recognized as necessary for corporate survival. Eight pillars of TPM are as follows:

1. Focused improvement (Kobetsu kaizen)
2. Autonomous maintenance (Jishu Hozen)
3. Planned maintenance
4. Quality maintenance
5. Initial flow control
6. Education and Training
7. Office TPM
8. Safety Health and Environment

2. Literature Review

Nakajima described that the word 'total' means total effectiveness, total maintenance system, and total participation of all employees. Historically, there are three eras of maintenance in Japan, where TPM originated. The first era, is known as preventive maintenance era (1950's) that emphasizes on establishing maintenance functions. The second era (1960's) is the introduction of productive maintenance, where maintenance prevention, reliability, maintainability engineering took place. The third era, total productive maintenance in 1970's put emphasis on total employee participation and strong support from top management. *K.D.P. Singh et al*, worked to eliminate losses in the oxygen plant by the application of Total Productive Maintenance (TPM) technique thereby improving the overall performance of the plant. Out of the 8 Pillars of T.P.M, two most important pillars i.e. Jishu-Hozen (Autonomous Maintenance) and Kobetsu-Kaizen (Focused Improvement) have been used by them for the investigations. According to *P.Sharma et.al* the aim of TPM is to bring together management, supervisors and trade

union members to take rapid remedial actions as and when required. Its main objectives are to achieve zero breakdowns, zero defects and improved throughputs. According to *Chan et.al,* Maintenance is accomplished through a 'team' effort, with the operator being held responsible for the ultimate care of his/her equipment. As defined by the Japan institute of plant maintenance: "TPM aims at maximizing equipment effectiveness with a total system of preventive maintenance covering the entire life of the equipment involving everyone in all departments and at all levels, it motivates people for plant maintenance through small-group and voluntary activities" (*Imai Masaaki*). The main advantage of Nakajima's indicators is their usefulness in verifying how the newly applied improvements affect equipment efficiency (*Santos J et al.). F. Ireland et al*, examines how TPM was implemented at three companies, with particular focus on the: TPM journey; TPM processes used; role of TPM co-coordinators; and the company's TPM goals. *S. Fore et al,* addressed the use of effective maintenance strategies to improve overall equipment effectiveness of production machines. *Lina Gozali et al*, reported the use of OEE toolkit 5.4 software to measure the performance of Total productive maintenance.

3. Fundamentals of OEE

According to Nakajima, the total time available for working, that is to say, the calendar time, must be reduced by the time required for scheduled shutdowns. This time includes, for instance, preventive maintenance tasks. The rest of the time is considered load time. Load time can be reduced because of six main types of time losses as shown in Table 2 which affect equipment efficiency:

Breakdowns: Time that the equipment is stopped for repairs.

Setup and changeovers: Time used to change between models or between products of the same model.

Idling and minor stoppages: Loss time caused by process randomness or worker machine cycle complexity.

Reduced speed: Decrease in working speed caused by the wear of components.

Defects and reworks: Faulty and low-quality products.

Start-up losses: Before reaching the stable operation state, machines occasionally produce defects.

Figure 1 shows the load time and how these six main losses are grouped, reducing the time to the real operation time of the equipment. Overall Equipment Effectiveness (OEE) is basic measure associated with TPM. This OEE highlights the actual capacity in an organization. It measures both efficiency and effectiveness of the equipment. It incorporates three basic factors of equipment performance and reliability. Thus OEE is a function of the three factors mentioned below and shown in figure 2:

1. Availability (A)
2. Performance efficiency (PE)
3. Quality Rate (QR)

Thus, **OEE = A x PE x QR**

4. Data Analysis

Data collected for the past one year. The operation is based on the three shifts per day every shift is for eight hours the planned standard allowance per day is three hours.

Number of Shifts	3
Working time per shift	8 hours
Break time for food	0.5 hours for each shift
Break time for Tea (Twice in a shift)	15 minutes
Meeting time	15 minutes for each shift

Data gathered for the equipment in a particular day:

Break down (A)	2 Hours
Setup and Adjustment (B)	2.5 Hours
Tool Change (C)	0.5 Hours
Startup Losses (D)	0.25 Hours
Management Losses (E)	3.75 Hours
Production Volume	750 Numbers
Defects	50 Numbers
Reworks	100 Numbers
Standard Cycle time	50 seconds

5. Methodology for calculation of overall equipment effectiveness

Planned Time = 3*8 = 24 hours

Loading Time = Planned Time-Standard Allowance

= Planned Time – (Break Time for Food + Tea + Meeting)

= 24 – (3*0.5 + 3*0.25 + 3*0.25)

= 24 – 3

= 21 Hours

Down Time = (A+B+C+D+E)

= 2.00 + 2.50 + 0.50 + 0.25 + 3.75 = 9.00 Hours

Availability = {(Loading time – Down time) / (Loading time)} *100

= {(21.00-9.00) / (21.00)}*100

= 57.14 %

Performance Rate = {(Cycle time * Prod. volume) / (Loading time- Down time)}*100

= {(50/3600) * (750) / (21.00-9.00)}*100

= {(50 * 750 / 12*3600)}*100

= 86.81%

Quality Rate = {(Prod. Volume – Defect - Reworks) / (Prod. Volume)} *100

= {(750-50-100) / (750)}*100

= {(600) / (750)}* 100

= 80.00 %

Table 1. Equipment Performance

Equipment's Performance	World - Class performance
57.14% Availability	>90% Availability
86.81% Performance efficiency	>95% Performance efficiency
80% Rate of quality	>99% Rate of quality
39.68% OEE	>85% OEE

OEE = (Availability * Performance Rate * Quality Rate)* 100

= (57.14 % * 86.81 % * 80.00 %) * 100 %

= (39.68) * 100 %

= 39.68 %

Table 2. Description of losses

Types of losses	Characteristics
Downtime/Breakdown (a)	Equipment failure – from breakdowns. These failures are due to chronic / sporadic losses Set-up and adjustment – from exchange of die in injection molding machines, etc
Speed losses (b)	Idling and minor stoppages – due to the abnormal operation of sensors, blockage of Work on chutes, etc. Reduced speed – due to discrepancies between designed and actual speed of equipment
Defect/Rework (c)	Process defects and rework – due to scraps and quality defects to be repaired Start-up loss (reduced yield) – from machine start-up to stable production
Notes: a Equipment availability; b performance efficiency; c quality rate	

(Source: Nakajima, 1988)

6. Conclusion

This paper deals with an illustration of a methodology to calculate the OEE for particular equipment in a gear industry. As data given in Table 1 it is very clear that lot of improvements has to be done so that equipment performance can be improved up to world class performance. As it is shown that there is a considerable setup time almost 2.5 hours which can be greatly reduced by applying systematically single minute exchange of dies (SMED) ,by doing this availability of equipment will be increased. Also by adopting firm TPM concepts such as Kobetsu Kaizen and Autonomous maintenance, breakdown can be greatly reduced. It is also clear from the equipments data that by giving full exposure of TPM and training to all employees or operators can be a better way to compensate the rework and defects loss simultaneously it would enhance quality rate of the equipment. In the end it is concluded that OEE can be a powerful tool under the purview of TPM which can enhanced the performance of all equipment by

implementing it thoroughly and in this process training of all operators is most essential.

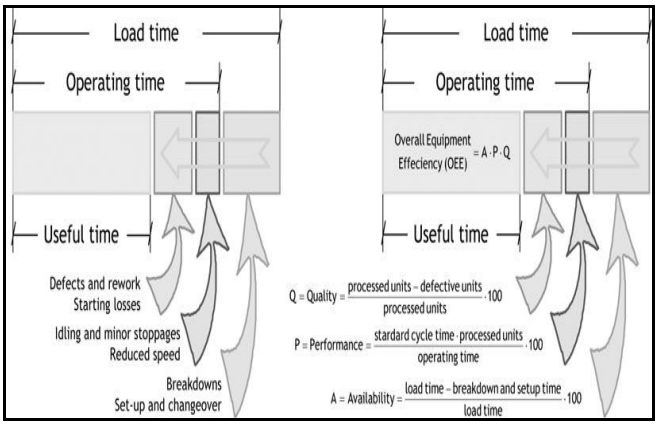

Figure 1. Losses and OEE rate calculation

(Source: J. Santos, 2007)

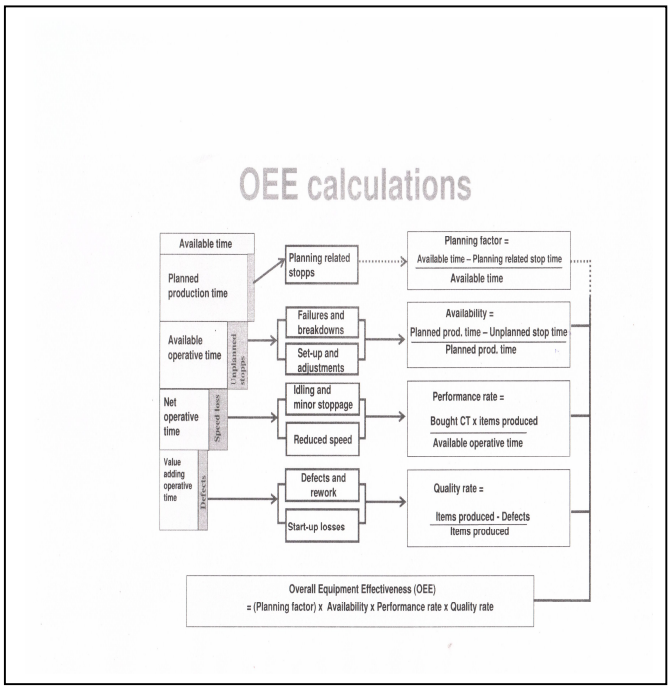

Figure 2. OEE Calculations preview

(Source: P. Sharma, 2010)

References

[1] Chan F.T.S, Lau H.C.W, Ip R.W.L, Chan H.K., Kong S., 2005, "Implementation of total productive maintenance: A case study." Int. Journal of Production Economics 95, pp 71–94.

[2] Gozali Lina, Widodo Lamto, Rusli Wijaja, 2009, "Measuring Performance Of Total Productive Manufacturing Using OEE Software At Pt. ABC", Proceeding, International Seminar on Industrial Engineering and Management, Bali, ISSN: 1978-774X

[3] Ireland F and Dale B.G., 2001, "A study of total productive maintenance implementation" Journal of Quality in Maintenance Engineering, Vol. 7 No. 3, pp. 183-191.

[4] Imai Masaaki, 1986. "KAIZEN-The key to Japan's competitive success". Random House Business Division, First edition, New York.

[4] Nakajima S. Introduction to TPM. Cambridge, MA: Productivity Press; 1988

[5] Santos J, Serrats G, Arcelus M, (2007), "Implementation of the OEE rate as a participative improvement tool", Proceeding, Innovative production machines and systems.

[6] Santos J, Wysk R. Torres JM, 2006, "Improving with Lean Thinking", John Wiley & Sons Inc. Hoboken New York

[7] S. Fore, L. Zuze, 2010, "Improvement of Overall Equipment Effectiveness through Total Productive Maintenance" World Academy of Science, Engineering and Technology 61

[8] Sharma P, Bhave Vishwas, Khurasia H.B., Shikari B, 2010"Enhancing Overall Equipment Effectiveness through TPM"

[9] Singh K.D.P.and Patha A.K., 2009, "Reduction of Losses in Oxygen Plant through Total Productive maintenance" ARISER Vol. 5 No. 2, pp 119-130, ISSN 1994-3253